T-2467

Synthetic Electric Sounding Surveys

Over

Known Oil Fields

(Southern portion of San Joaquin Valley, Kern County, California; Payne, Logan and Lincoln Counties, Oklahoma and Lance-Creek Field, Niobrara County, Wyoming)

By

Nek R. Garg

A thesis submitted to the Faculty and the Board of Trustees of the Colorado School of Mines in partial fulfillment of the requirements for the degree of Master of Science in Geophysical Engineering.

Golden, Colorado

Date April 22, 1981

Signed NRGarg

Nek R. Garg

Golden, Colorado

Date Apr. 22, 1981

Approved: George V. Keller

Dr. G.V. Keller
Advisor and Head,
Geophysics Department

Dedicated to that Almighty Great Lord

ABSTRACT

Average geoelectrical parameters determined from the study of electrical well-logs obtained from several oil fields characterized by different geoelectrical sections. The DC anomaly due to the presence of an oil-layer embedded between first and second layer depends upon the type of geoelectrical section and the geometrical array employed. The radial-dipole array gives the largest anomaly values, and is followed by other DC arrays such as the equatorial-dipole, Schlumberger and Wenner arrays. The maximum anomaly value over a given model in an H-type of environment for radial-dipole is almost the same as the transverse resistance contrast ratio of the oil-layer to the first layer. The finite areal extent of the oil-layer does not have any significant effect on the anomaly value due to an infinite layer, if the dimensions are about four times the depth and the geometrical array used is the radial-dipole. Moreover, a buried current electrode in the vicinity of the oil-layer increases the anomaly value; the maximum anomaly value appears at a separation comparable to its depth.

TABLE OF CONTENTS

	PAGE
ABSTRACT	iv
List of Figures	vi
List of Table	xii
Acknowledgements	xiii
Introduction	1
General Background	6
Present Study: General Discussion	12
Southern Portion of the San Joaquin Valley, California	12
Payne, Logan, Lincoln Counties, Oklahoma	13
Lance Creek Field, Wyoming	13
Southern Portion of the San Joaquin Valley, Kern County, California	21
Anomaly Curve due to the Presence of Possible Oil/Gas Layer Picked Up from Well-Log #10	39
Payne, Logan, and Lincoln Counties, Oklahoma	45
Anomaly Due to the Presence of Actual Oil-Layer .	61
Lance Creek Field, Wyoming	67
Finite Oil-Layer Effect Over Anomaly	85
Conclusions	105
References	107
Appendix 1: Integral resistivity plots and geoelectrical parameters corresponding to individual well-logs, California	108
Appendix 2: Integral resistivity plots and geoelectrical parameters corresponding to individual well-logs, Oklahoma	129
Appendix 3: Integral resistivity plots and geoelectrical parameters corresponding to individual well-logs, Wyoming	156

LIST OF FIGURES

FIGURE NO.		PAGE
1	Locations of wells studied in the present work, Southern portion of the San Joaquin, Valley, Kern County, California	3
2	Locations of wells studied in the present work, Payne, Logan & Lincoln Counties, Oklahoma	4
3	Locations of wells studied in the present work, Lance Creek Field, Niobrara County, Wyoming	5
4	Column from a layered sequence of rocks used in defining average longitudinal resistivity, average transverse resistivity, and anisotropy arising from layering . . .	7
5	Anomaly in transverse resistance as a function of oil-saturation and pay-zone thickness to overburden thickness. The shaded zone represents oil saturation of most interest (Keller, 1968)	10
6	Different DC geometrical-arrays considered in the present study	18
7	Average longitudinal resistivity contours in ohm-m. First unit, California	22
8	Average longitudinal resistivity contours in ohm-m. Second unit, California	23
9	Average longitudinal resistivity contours in ohm-m. Third unit, California	24
10	Apparent resistivity plot	26
11	Apparent resistivity plot	27
12	Apparent resistivity plot	28
13	Apparent resistivity plot	29

LIST OF FIGURES (CONT'D.)

FIGURE NO.		PAGE
14	Anomaly plot for varying transverse resistance contrast (T_{oil}/T_{over}) in %	31
15	Plot of maximum anomaly for varying transverse resistance contrast (T_{oil}/T_{over}) . . .	32
16	Anomaly plot for varying transverse resistance contrast (T_{oil}/T_{over}) in %	33
17	Plot of maximum anomaly for varying transverse resistance contrast (T_{oil}/T_{over}) . . .	34
18	Anomaly plot for varying transverse resistance contrast (T_{oil}/T_{over}) in %	35
19	Plot of maximum anomaly for varying transverse resistance contrast (T_{oil}/T_{over}) . . .	36
20	Anomaly plot for varying transverse resistance contrast (T_{oil}/T_{over}) in %	37
21	Plot of maximum anomaly for varying transverse resistance contrast (T_{oil}/T_{over}) . . .	38
22	Anomaly plot over possible oil/gas layer picked up from well-log #10	41
23	Anomaly plot over possible oil/gas layer picked up from well-log #10	42
24	Anomaly plot over possible oil-gas layer picked up from well-log #10	43
25	Anomaly plot over possible oil/gas layer picked up from well-log #10	44
26	Average longitudinal resistivity contours in ohm-m. First unit, Oklahoma	46
27	Average longitudinal resistivity contours in ohm-m. Second unit, Oklahoma	47
28	Apparent resistivity plot	49

LIST OF FIGURES (CONT'D.)

FIGURE NO.		PAGE
29	Apparent resistivity plot	50
30	Apparent resistivity plot	51
31	Apparent resistivity plot	52
32	Anomaly plot for varying transverse resistance contrast (T_{oil}/T_{over}) in %	53
33	Plot of maximum anomaly for varying transverse resistance contrast (T_{oil}/T_{over}) . .	54
34	Anomaly plot for varying transverse resistance contrast (T_{oil}/T_{over}) in %	55
35	Plot of maximum anomaly for varying transverse resistance contrast (T_{oil}/T_{over}) . .	56
36	Anomaly plot for varying transverse resistance contrast (T_{oil}/T_{over}) in %	57
37	Plot of maximum anomaly for varying transverse resistance contrast (T_{oil}/T_{over}) . .	58
38	Anomaly plot for varying transverse resistance contrast (T_{oil}/T_{over}) in %	59
39	Plot of maximum anomaly for varying transverse resistance contrast (T_{oil}/T_{over}) . .	60
40	Anomaly plot over possible oil/gas layer picked up from well-log #5	63
41	Anomaly plot over possible oil/gas layer picked up from well-log #5	64
42	Anomaly plot over possible oil/gas layer picked up from well-log #5	65
43	Anomaly plot over possible oil/gas layer picked up from well-log #5	66
44	Average longitudinal resistivity contours in ohm-m. First unit, Wyoming	69

LIST OF FIGURES (CONT'D.)

FIGURE NO.		PAGE
45	Average longitudinal resistivity contours in ohm-m. Second unit, Wyoming	70
46	Average longitudinal resistivity contours in ohm-m. Third unit, Wyoming	71
47	Apparent resistivity plot	73
48	Apparent resistivity plot	74
49	Apparent resistivity plot	75
50	Apparent resistivity plot	76
51	Anomaly plot for varying transverse resistance contrast (T_{oil}/T_{over}) in %	77
52	Plot of maximum anomaly for varying transverse resistance contrast (T_{oil}/T_{over}) . .	78
53	Anomaly plot for varying transverse resistance contrast (T_{oil}/T_{over}) in %	79
54	Plot of maximum anomaly for varying transverse resistance contrast (T_{oil}/T_{over}) . .	80
55	Anomaly plot for varying transverse resistance contrast (T_{oil}/T_{over}) in %	81
56	Plot of maximum anomaly for varying transverse resistance contrast (T_{oil}/T_{over}) . .	82
57	Anomaly plot for varying transverse resistance contrast (T_{oil}/T_{over}) in %	83
58	Plot of maximum anomaly for varying transverse resistance contrast (T_{oil}/T_{over}) . .	84
59	Anomaly plot over infinite (IL) & finite oil-layer (FL) for varying transverse resistance contrast (T_{oil}/T_{over}) ratio in % .	86

LIST OF FIGURES (CONT'D.)

FIGURE NO. PAGE

60. Anomaly plot over infinite (IL) & finite oil-layer (FL) for varying transverse resistance contrast (T_{oil}/T_{over}) ratio in % . 88

61 Anomaly plot over infinite (IL) & finite oil-layer (FL) for varying transverse resistance contrast (T_{oil}/T_{over}) ratio in % . 89

62 Anomaly plot over infinite (IL) & finite oil-layer (FL) for varying transverse resistance contrast (T_{oil}/T_{over}) ratio in % . 90

63 Anomaly plot over infinite horizontal (IHL) & finite dipping oil-layer (FDL) for varying transverse resistance contrast (T_{oil}/T_{over}) ratio in % 91

64 Anomaly plot over infinite horizontal (IHL) & finite dipping oil-layer (FDL) for varying transverse resistance contrast (T_{oil}/T_{over}) ratio in % 92

65 Anomaly plot over finite oil-layer for fixed buried current electrode at x =0 & z = 10 m and moving potential electrode pair for varying T_{oil}/T_{over} ratio in % . . 94

66 Anomaly plot over finite oil-layer for fixed buried current electrode at x=0 & z=500 m and moving potential electrode pair for varying T_{oil}/T_{over} ratio in % . . 95

67 Anomaly plot over finite oil-layer for fixed buried current electrode at x=0 & z=700 m and moving potential electrode pair for varying T_{oil}/T_{over} ratio in % . . 96

68 Composite anomaly plot over finite oil-layer for varying buried current electrode depth at x=0 and moving potential electrode pair for varying T_{oil}/T_{over} ratio in % 97

LIST OF FIGURES (CONT'D.)

FIGURE NO.		PAGE
69	Anomaly plot over finite oil-layer for fixed buried current electrode at x= -750 m & z=10 m and moving potential electrode pair on lefthand (LH) & right-hand (RH) side of current electrode for varying T_{oil}/T_{over} ratio in %	98
70	Anomaly plot over finite oil-layer for fixed buried current electrode at x= -750 m & z=500 m and moving potential electrode pair on lefthand (LH) & right-hand (RH) side of current electrode for varying T_{oil}/T_{over} ratio in %	99
71	Anomaly plot over finite oil-layer for fixed buried current electrode at x= -750 m & z=700 m and moving potential electrode pair on lefthand (LH) & right-hand (RH) side of current electrode for varying T_{oil}/T_{over} ratio in %	100
72	Anomaly plot over finite oil-layer for fixed buried current electrode at x= -1250 m & z=10 m and moving potential electrode pair on lefthand (LH) & right-hand (RH) side of current electrode for varying T_{oil}/T_{over} ratio in %	102
73	Anomaly plot over finite oil-layer for fixed buried current electrode at x= -1250 m & z=500 m and moving potential electrode pair on lefthand (LH) & right-hand (RH) side of current electrode for varying T_{oil}/T_{over} ratio in %	103
74	Anomaly plot over finite oil-layer for fixed buried current electrode at x= -1250 m & z=700 m and moving potential electrode pair on lefthand (LH) & right-hand (RH) side of current electrode for varying T_{oil}/T_{over} ratio in %	104

LIST OF TABLE

Table No.		Page
1	Approximate details about depths of different ages, lithology, thickness and effective pay zone of Lance Creek Field, Niobrara County, Wyoming (Wyoming Oil and Gas Fields, 1957).	15

ACKNOWLEDGEMENTS

I take this opportunity to thank Dr. George V. Keller for his guidance, help, and stimulating discussions throughout the present work. I am also thankful to Dr. C. H. Stoyer and Dr. A. A. Kaufman for serving as my committee members and helping me whenever I needed them.

I gratefully acknowledge the support provided by Dr. G. V. Keller from the Geophysics Fund and by the Government of India for the present study.

INTRODUCTION

In recent years, there has been a search for exploration techniques which may detect the contrast in physical properties directly associated with the presence of oil in rock. One of these techniques is the electrical method in view of the high resistivity of an oil-bearing formation compared to its environment. However, before electrical methods can find a place in petroleum exploration programs, it seems most important to analyze some of the problems associated with their use. One of the very important problems which may be evaluated without the expense of undertaking field operations with large scale electrical surveys is the estimation of the size and detectibility of anomalies associated with oil occurrence. Other problems are involved in interpretation keeping in mind the size of an anomaly and geological noise.

Keller (1968) has discussed the role of electrical methods and associated problems very extensively. Garg (1976) has computed the electrical response over theoretical hydrocarbon reservoirs. In this study, I will consider only the first problem in actual field environments. This important problem in the present study was analyzed using well-logs as a basis for computing synthetic electric soundings. About 75 well-logs were chosen from three oil fields, namely from the southern portion of the San Joaquin Valley, California (Figure 1), Payne, Logan and Lincoln Counties, Oklahoma (Figure 2), and Lance Creek Field, Wyoming (Figure 3). According to Keller (1968), the least oil field which we wish to find in exploration is characterized by a thickness of several feet per thousand feet of burial, an areal extent of three quarters steradian, and a transverse resistance contrast with overlying rocks of at least several percent. All these factors were taken into consideration in the present study at the time of analyzing the electrical anomaly due to the presence of an oil bed. I will pay attention only to size and detectability of the anomaly arising due to the presence of an oil/gas layer in the actual environment.

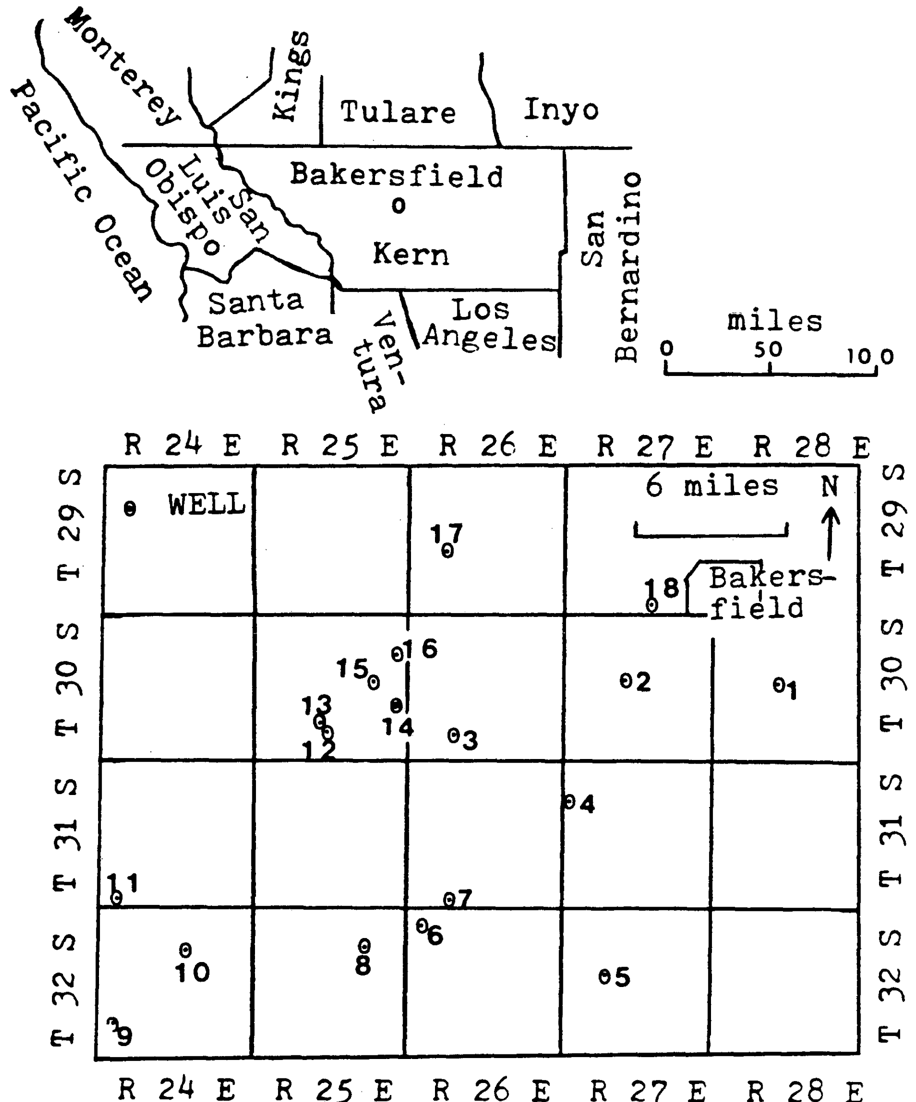

Figure 1 Locations of wells studied in the present work, Southern Portion of San Joaquin Valley, Kern County, California.

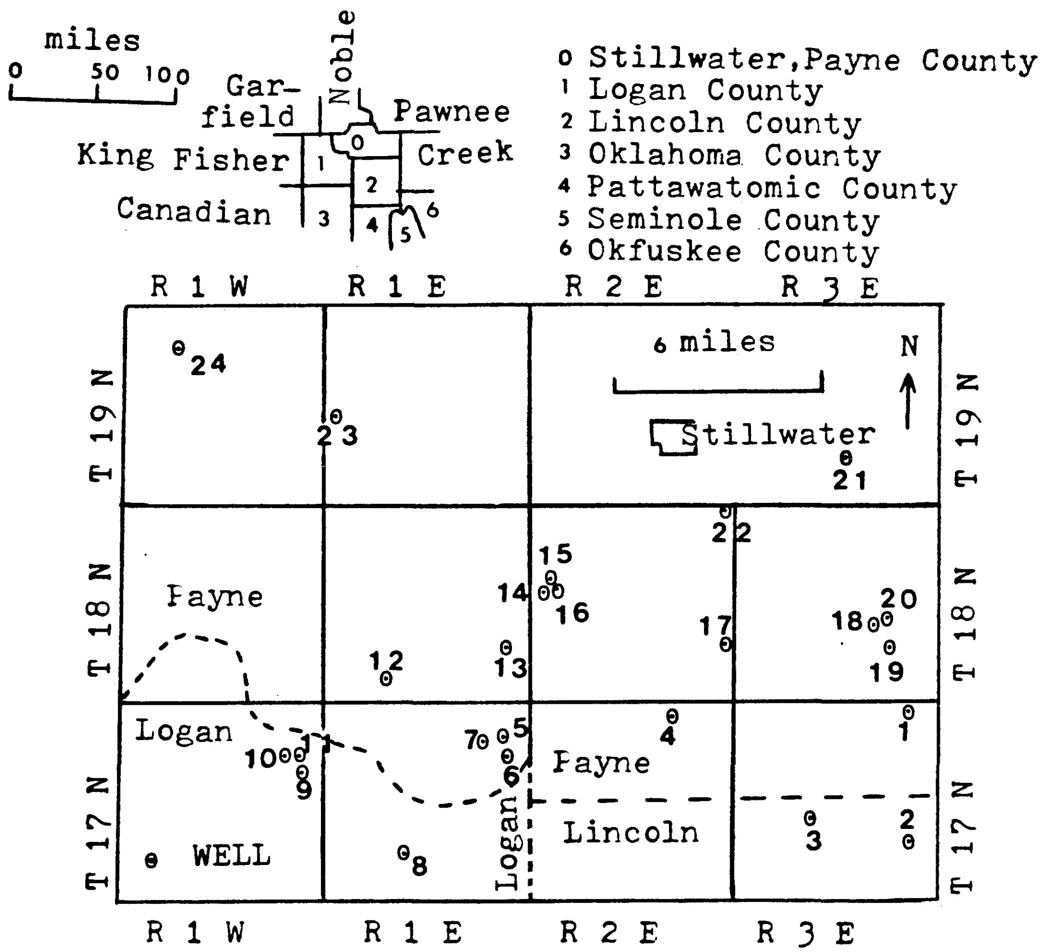

Figure 2 Locations of wells studied in the present work,Payne,Logan & Lincoln Counties, Oklahoma.

Figure 3 Locations of wells studied in the present work, Lance Creek Field, Niobrara County, Wyoming.

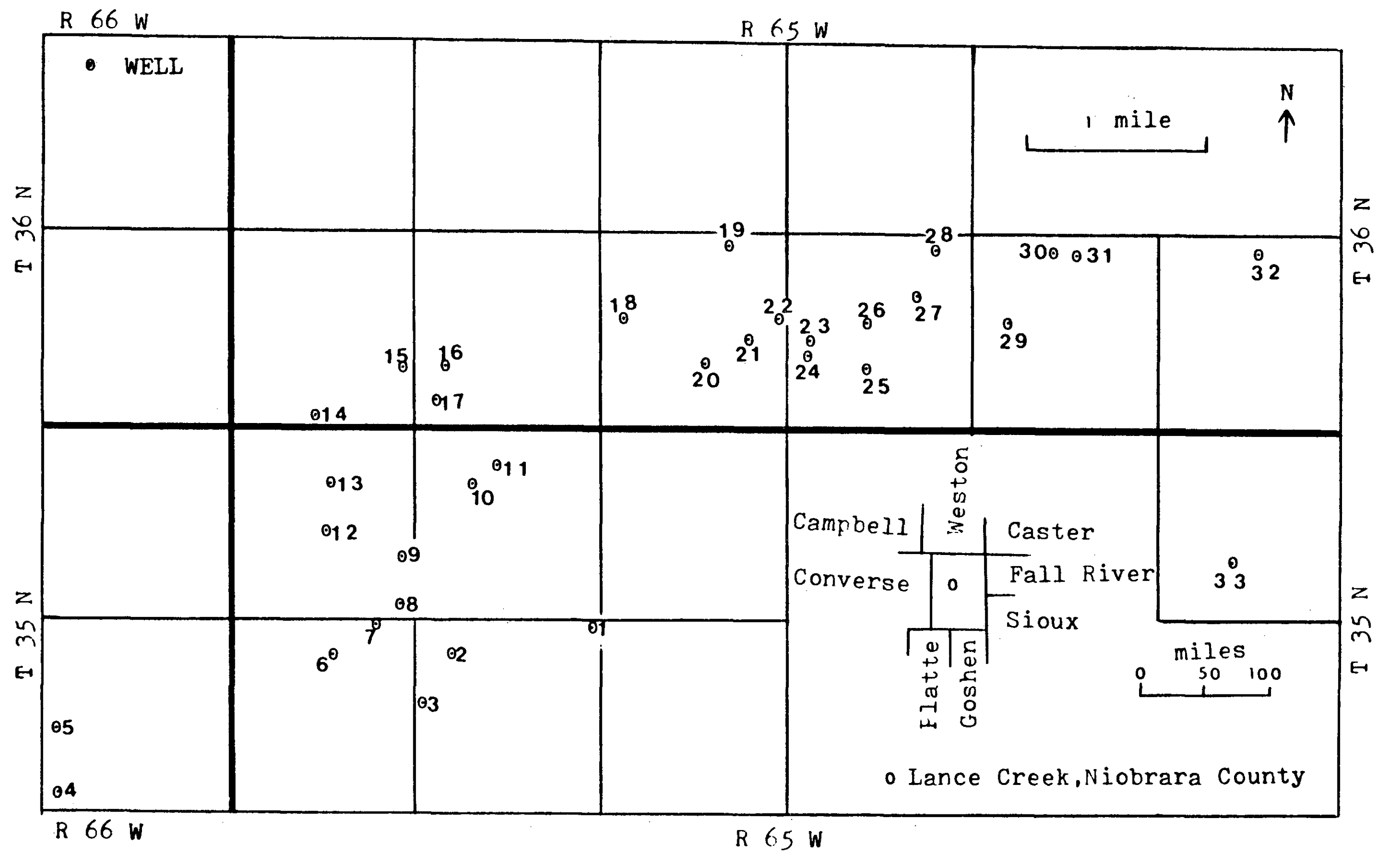

GENERAL BACKGROUND

The large number of individual layers apparent on an electric log cannot be resolved with any of the surface-based electrical prospecting methods. And so, it is necessary to devise a realistic way of defining the average resistivity of an assemblage of relatively thin beds (Keller, 1968). The average electrical properties for a finely layered sequence may be described with a set of 5 parameters, these parameters being defined in terms of a column of rock one meter square cut from the sequence of layers. This column consists of n horizontal beds, each with its own characteristic resistivity ρ_i and thickness h_i as shown schematically in Figure 4.

These parameters are defined by considering the resistance to current, flowing either vertically or horizontally through the column. The total resistance to current flowing vertically through the column is found by adding in series the resistance contributed by each layer:

$$R_T = \Sigma_{i=1}^{n} \rho_i h_i \quad \text{Ohm} \tag{1}$$

The average transverse resistivity for current flowing vertically is

$$\rho_{tr} = \frac{R_T}{H} = \frac{\Sigma_{i=1}^{n} \rho_i h_i}{H} \text{ Ohm - m} \tag{2}$$

where $H = \Sigma_{i=1}^{n} h_i$

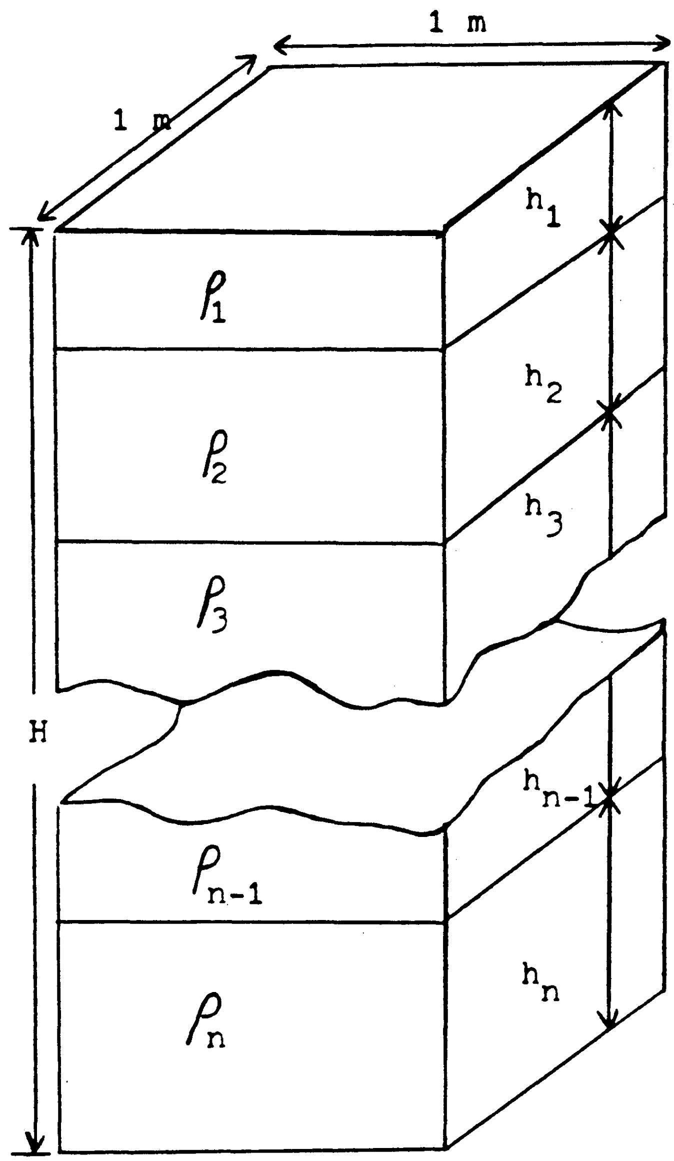

Figure 4 Column from a layered sequence of rocks, used in defining average longitudinal resistivity, average transverse resistivity and anisotropy arising from layering.

The conductance for current flowing horizontally through the column of rock, S_T, is found by assuming the conductance through each individual layer:

$$S_T = \Sigma_{i=1}^{n} \frac{h_i}{\rho_i} \text{ mho} \quad (3)$$

The average longitudinal resistivity for current flowing horizontally is:

$$\rho_{lr} = \frac{H}{S_T} = \frac{H}{\Sigma_{i=1}^{n} h_i/\rho_i} \text{ Ohm - m} \quad (4)$$

A coefficient of anisotropy, λ, may be defined by taking the square root of the ratio of resistivities measured in the two principle directions, along the bedding planes and across the bedding planes:

$$\lambda = (\rho_{tr}/\rho_{lr})^{1/2} \quad (5)$$

In evaluating the sensitivity of surface-based electrical exploration techniques in petroleum exploration program, the transverse resistance of an oil-bed, defined as the product of its resistivity and thickness, is a description parameter needed in the theoretical development. If we assume an extremely simplified model in which the oil zone is contained in a rock that is completely uniform in resistivity, having the resistivity the oil zone would have and the surrounding rock is similar differing only in that it is fully saturated with water with its resistivity, then the transverse resistance contrast of oil-layer T_2 to the overlying layer T_1

$$\frac{T_2}{T_1} = (1 - S_o)^{-n} \frac{h}{h_1}$$

Where h_1 is the depth to the oil-layer, h being the thickness of the pay zone, S_o is the fraction of pore spaces filled with oil and n is an empirical constant (Keller, 1968).

The relative contrast in transverse resistance given by the above equation is plotted in Figure 5 as a function of the ratio of the thickness of the pay zone to the thickness of the overlying rock, and as a function of oil saturation. Usually an oil reservoir must have an oil saturation in excess of 50 percent to be developable. Even with favorable drilling conditions, the thickness of the pay zone should be at least 10 feet at a depth of 10,000 feet, in order to provide a marginally profitable well. These considerations provide a lower limit for the ratio $T_2{:}T_1$, which is required for an economic oil field. This is indicated by the crosshatched area in Figure 5. It appears that the lowest ratio $T_2{:}T_1$ that might represent a worthwhile oil field is 1.01 (a one percent contrast). Larger values for $T_2{:}T_1$ would be associated with larger oil fields.

A second factor to be considered in formulating an electrical model for a minimum size oil field of commercial

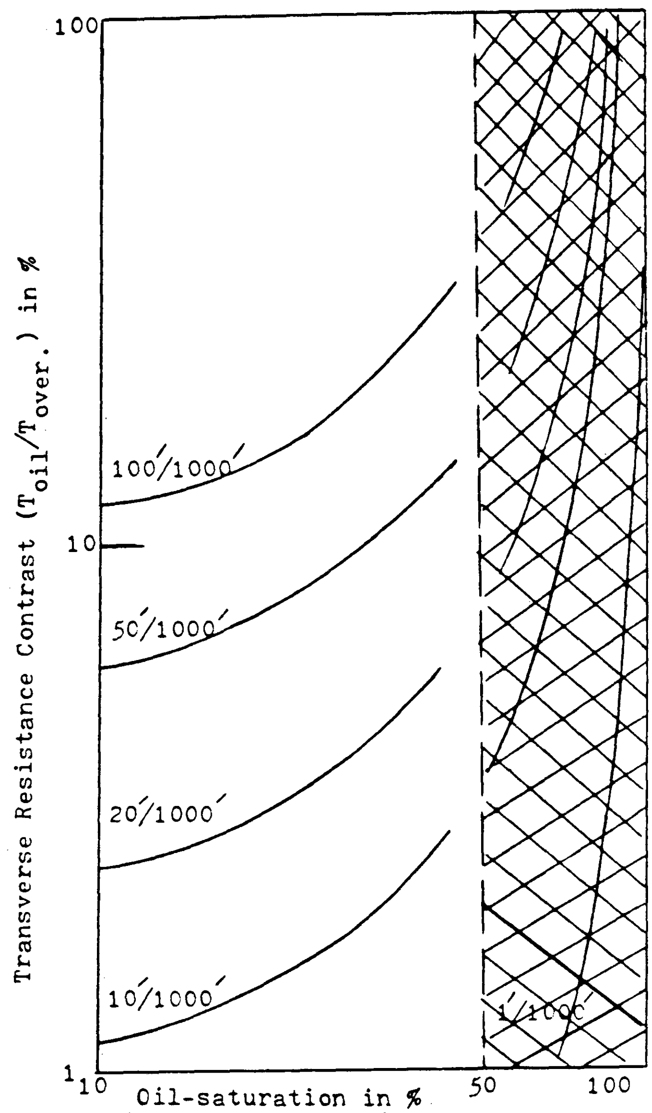

Figure 5 Anomaly in transverse resistance as a function of oil-saturation and pay-zone thickness to overburden thickness.The shaded zone represents oil saturation of most interest.(Keller,1968)

interest is its areal extent. In terms of the solid angle subtended when viewed from the surface directly over the field, the least of oil fields would occupy an area of three quarters steradian (Keller, 1968).

In summary, the least oil field which we wish to find in exploration is characterized by a thickness of several feet per thousand feet of burial, an areal extent of three quarters steradian, and a transverse resistance contrast with overlying rocks of at least several percent.

PRESENT STUDY: GENERAL DISCUSSION

For the present study, three areas were selected, namely, the southern portion of the San Joaquin Valley, Kern County, California (Figure 1), Payne, Logan and Lincoln Counties, Oklahoma (Figure 2), and Lance Creek, Niobrara County, Wyoming (Figure 3). There were no specific reasons for selecting these areas; however, preference was given where it was easy to get good quality well-logs.

Southern Portion of the San Joaquin Valley (California):

This area lies between Township T32S-T29S and Range R24E-R28E, Kern County, Figure 1. In this field, oil occurs largely in the Pliocene, Miocene, and Eocene with lesser amounts in the Pleistocene and Oligocene and very minor amounts in the Cretaceous and Jurassic. All the dry gas and a very large part of the oil are found in sands, sandstones, or simply shales. A minor amount of oil occurs in fractured shales and in schist. No limestone production has been found. A high percentage of oil and dry gas occurs in anticlines or domes. However, nearly every other known type of structure is present. Faulting is found in almost all fields and in many cases is an important factor in the control of accumulation. In numerous instances, it is in fact the entire means of closure (California Oil and Gas Fields, 1960).

Payne, Logan, Lincoln Counties, Oklahoma:

This area lies between Township 17-19 N and Range 1W-3E, Figure 2. The surface is covered with weathered red clay shale of the Stillwater formation. Massive red sandstone members of this formation crop out in many of the Stream valleys. The formations present are Permian, Pennsylvanian, Mississipian, Silluo-Devonian, and Ordovician. At present, the only producing formation in the Ramsey pool is the first "Wilcox" sand. It is the first sand body in the Simpson group of Ordovician age and is believed to average about 14 m in thickness over the entire structure. The sand is remarkably clean and uniform lithologically and has an average porosity of 20 percent. The sand is very soft and round grained and varies from medium to coarse in texture. There is one persistent break in the sand body. It consists of shale with dolomite and limestone stringers, ranging from about 1 to 5 m in thickness, occurring from about 0.5 to 2 m below the top of the sand over the entire pool. This shale break seems to serve as a cap rock as the principal oil-producing bed is invariably found immediately beneath it (Frost, 1940).

Lance Creek Field, Wyoming:

This area lies between Township 35-36 N and Range 65-66 W, Niobrara County, Figure 3. In this field, oil occurs in rocks of Cretaceous, Jurrassic, and Pennsylvanian ages. The structure is an anticline. Oil is present in porous dolomite, limestone, sandy limestone, and thin sandstone. Details about depths of different ages, lithology, thickness, and effective pay zone are given in Table 1 (Wyoming Oil and Gas Fields, 1957).

A simple procedure of determining the average resistivity described previously was used. Electric logs are a record of a value of apparent resistivity which is a continuous function of depth, rather than a function which varies stepwise from bed to bed. In averaging the apparent resistivity values recorded on a continuous electric log, the approximation is made that the sedimentary column consists of a large number of beds, each with the same thickness Δh (digitizing interval, 10 feet in the present work) and each having a constant resistivity equal to the resistivity read from the electric log at that digitizing interval in the assumed bed. The assumption of a sedimentary column consisting of beds of equal thickness simplifies computation; instead of using equations 2 and 4, these equations become:

$$\rho_{tr} = \frac{\Delta h}{H} \Sigma_{i=1}^{n} \rho_i \quad \text{Ohm - m}$$

and $$\rho_{lr} = \frac{H}{\Delta H \ \Sigma_{i=1}^{n} \ (1/\rho_i)} \quad \text{Ohm - m}$$

Table 1: Approximate details about depths of different ages, lithology, thickness and effective pay zone of Lance Creek Field, Niobrara County, Wyoming (Wyoming Oil and Gas Fields, 1957).

	Formation	Formation	Formation	Formation	Formation	Formation	Formation	Formation
Age	Frontier Cretaceous	Muddy Cretaceous	Dakota Cretaceous	Lakota Cretaceous	Morrison Cretaceous	Sundance Jurassic	Converse Pennsylv.	Leo Pennsylvanian
Average Depth (in m)	686	920	991	1012	1067	1158	1402	1615
Date of Discovery	1918	1918	1918	1918	1955	1930	1936	1937
Sub-Surface Closure (in m)	183	183	183	183	183	183	183	183
Lithology	Sandstone	Sandstone	Sandstone	Sandstone	Sandstone	Sandstone	Sandstone	Sandstone
Thickness (in m)	24	6	15-30	61	15	27		30
Effective Pay (in m)		3-6	6-9	14	11	17	9	30
Porosity %					11	20-30	16	8-23
Permeability (md)					0-400	0-1250	3	0.5-324
Average Gas/Oil Ratio (ft^3/bbl)					560			900

Corrections may be made for different types of errors in determining average resistivity. However, for the present study, it is reasonable to use the electrical well-logs which have minimum correction with a view that if the errors are consistent, comparison between sets of resistivity integral curves may be made with some confidence. So at the time of selecting well-logs, preference was given to focused current logs, followed by induction logs if the rock is of low resistivity. In the case of logs run before these methods become available, as very often was the case in present study, short normal spacing logs were chosen. For the present study, 75 well-logs were selected, namely, 18 from southern portion of San Joaquin Valley, California (Figure 1), 24 from Payne, Logan, Lincoln Counties, Oklahoma (Figure 2), and 33 from Lance Creek, Wyoming (Figure 3). The longitudinal resistivity value is less subject to error than the transverse resistivity value. However, for very small values of resistivity, which could not be read accurately from the well-logs, a minimum value was assigned on the basis of general low resistivity value in a particular area.

For calculating the above-defined electrical parameters, we have to know geoelectrical boundaries on the well-logs. For locating these boundaries, resistivity integral curves were plotted for all well-logs except well-log #18 and 20, Wyoming, (there was not a sufficient continuous length of record on these two). The results are shown in Appendices 1, 2, and 3. For calculating the above parameters approximate electrical boundaries were identified by changes in slope on the cumulative resistivity and conductivity plots. However, to make the error more consistent and to reduce the uncertainty corresponding to these boundaries, more exact boundaries were then located from the original well-logs. Also, at the time of plotting cumulative resistivity and conductivity vs. depth curves, inasmuch as the upper limit of the cumulative sums was not known and because this limit and depth of section was different for different plots, the curves were plotted to different horizontal and vertical scales. Due to this reason, sometimes when the scale is very small, a local change in the character of a bed looks like a major boundary. However, at the time of picking the electrical boundaries, only major units were selected which are possible to detect using surface-based electrical methods.

For calculating and plotting the synthetic sounding curves corresponding to four DC resistivity configurations, namely, the Schlumberger, Wenner, Radial and Equatorial dipole arrays (Figure 6), the longitudinal resistivity was used for the reason stated above. The resistivity and thickness corresponding to an electrical unit were calculated by taking an

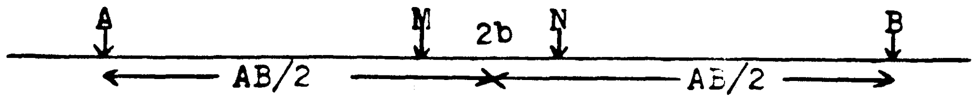

(Schlumberger-array)

$$G_S = (\pi\, AB/2^2)/2b$$

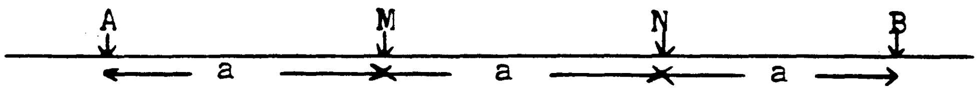

(Wenner-array)

$$G_W = 2\pi a$$

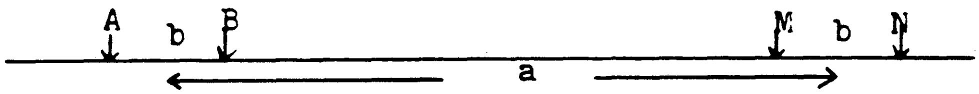

(Radial-dipole)

$$G_R = \pi\, a^3/b^2$$

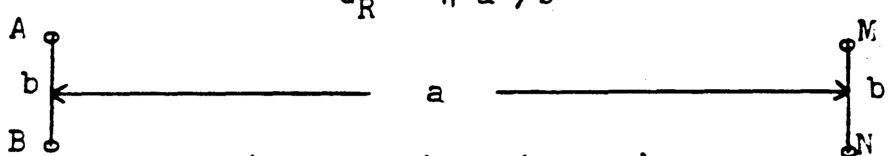

(Equatorial-dipole)

$$G_E = 2\pi a^3/b^2$$

Figure 6 Different DC geometrical-arrays considered in the present-study.

arithmetic average of the values corresponding to different well-log sites in a particular area. Well-logs are generally recorded only from a casing seat to the bottom of a well. Due to this reason, at the time of computing apparent resistivity curves and synthetic soundings, it was assumed that the top layer extends up to the earth-surface and bottom layer down to infinite depth. Also, the horizontal layers were assumed to be infinite in areal extent, homogeneous and isotropic. As in practice, the areal extent of oil-field is limited, an attempt was also made to give a feeling of the error caused by the finite areal extent of oil-layer using Whan's computer program (1979).

Anomaly responses were computed by introducing the oil-layer between layer 1 and 2 for varying transverse resistance contrast ratio of the oil-layer to the first layer. Sometimes anomaly curves also show negative values. So, a discontinuity is apparent on the plots when they show both negative and positive anomalies inasmuch as a zero anomaly value cannot be plotted on a logarithmic scale. In the present study, we will talk only of the DC anomaly. An attempt was also made to use actual oil-layer parameters, if it was possible to identify them from the well-logs. In the Wyoming area, it was not possible to specify these from well-logs. Only in the California and Oklahoma cases were anomaly curves computed for actual oil-layer parameters. Curves relating the transverse resistance contrast to the maximum anomaly values were also plotted to provide a quick idea about maximum anomaly values.

SOUTHERN PORTION OF THE SAN JOAQUIN VALLEY, KERN COUNTY, CALIFORNIA

The average transverse and logitudinal resistivity and coefficient of anisotropy corresponding to all individual wells are tabulated in Appendix 1. Three major units are detectable and their resistivities and thicknesses are:

$$\rho_1 = 6.36 \text{ Ohm - m}, \ h_1 = 881 \text{ m}$$

$$\rho_2 = 1.69 \text{ Ohm - m}, \ h_2 = 1728 \text{ m}$$

$$\text{and } \rho_3 = 4.5 \text{ Ohm - m}$$

which correspond to an H-type curve. The minimum and maximum depth available from well-logs study are about 27 and 4368 m, respectively. The coefficient of anisotropy of the first unit, corresponding to well-logs #12, 13, 14, 16, and 17 is about 15%. The anisotropy is high for well-log #10 probably due to the presence of a local resistive unit. The second unit does not show significant anisotropy, being below about 8% except for well-logs #5, 8, and 10 where it is about 12%. For the third unit, it ranges from 10% to 20-30%. The average longitudinal resistivity contours corresponding to all three units are shown in Figures 7, 8, and 9. The contours corresponding to unit one show high resistivity values in the right half of the area compared to the left half. Again, for the unit second, they

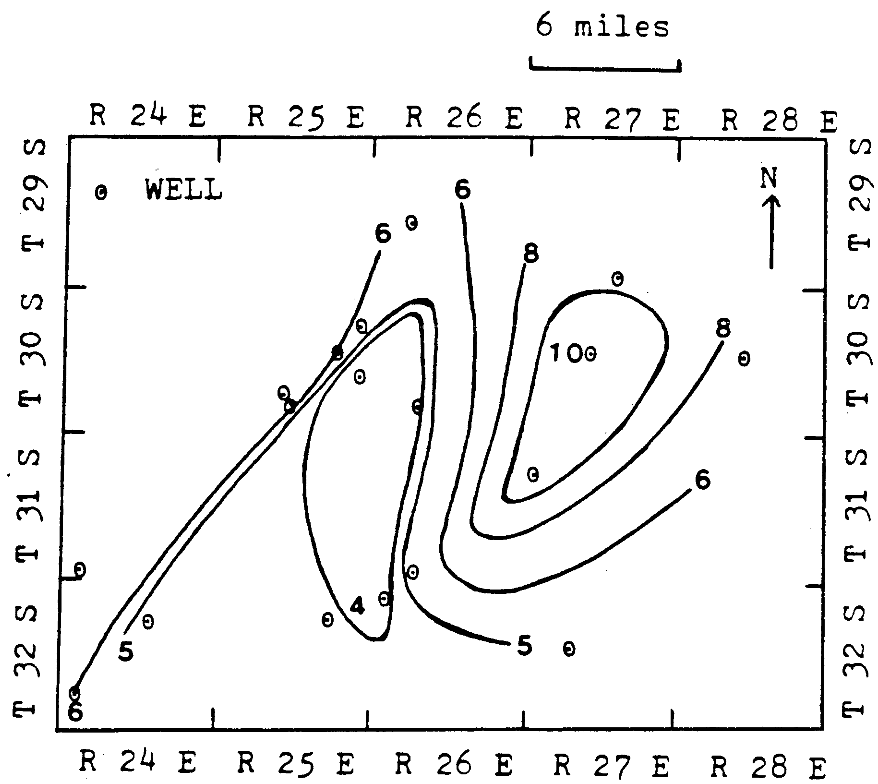

Figure 7 Average Longitudinal Resistivity Contours in ohm- m., First-unit, California.

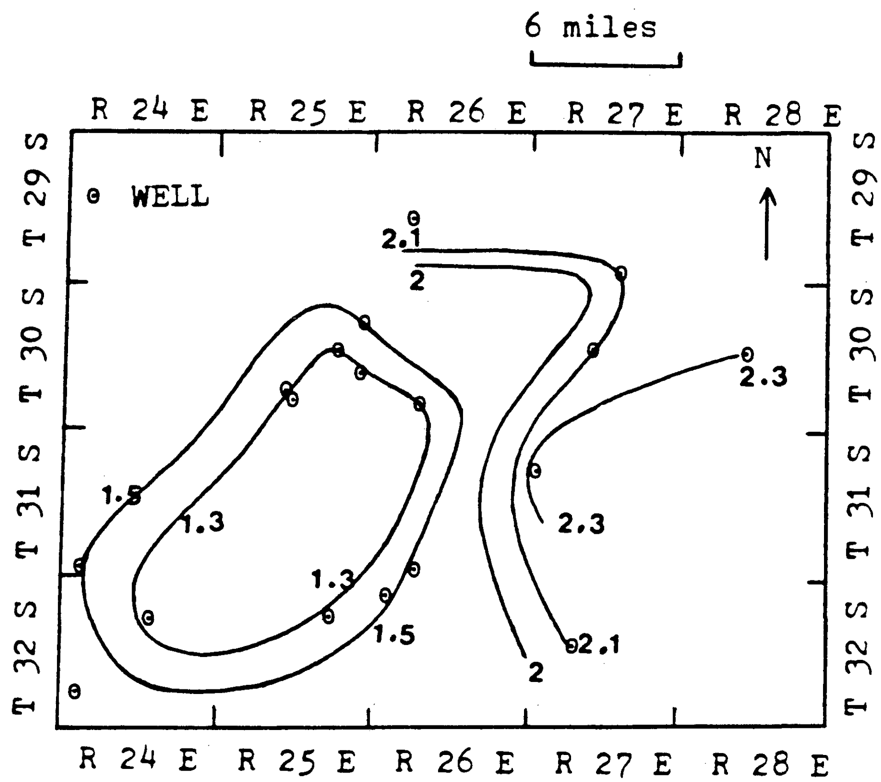

Figure 8 Average Longitudinal Resistivity Contours in ohm- m ., Second-unit, California.

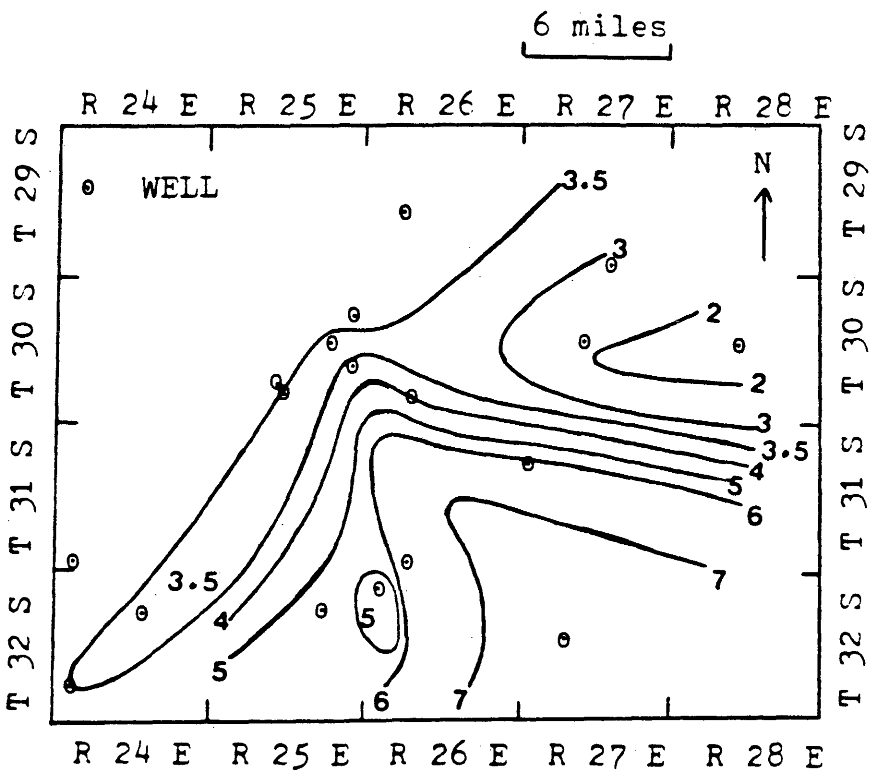

Figure 9 Average Longitudinal Resistivity Contours in ohm- m ., Third-unit, California.

show pretty much the same behavior. For the third unit, there is a local patch of 5 ohm-m resistivity value in the SW quadrant. For this unit, the contours have higher values in the SE quadrant compared to the rest of the area.

For computing resistivity curves, the Ghosh convolution method (1971) was used. In terms of speed and economy, this method gives good results within 1% accuracy. The apparent resistivity curves corresponding to all four DC arrays are shown in Figures 10, 11, 12, and 13. For the Schlumberger array, the curve is plotted as ρ_a/ρ_1 vs. the ratio of half of the distance between current electrodes to the thickness of the first layer, $AB/2h_1$; for the Wenner array as ρ_a/ρ_1 vs. distance between two consecutive electrodes, a/h_1; and for the radial and equatorial dipole arrays, as ρ_a/ρ_1 vs. distance between the center of the current and the potential dipoles, a/h_1. For computing the anomaly curve, it was assumed that the oil-layer is embedded between the first and second layers. Also, the resistivity of the oil-layer is 10 times the first layer resistivity. Keeping the oil-layer resistivity fixed, anomaly curves were computed for different transverse resistance contrast ratios of the oil-layer to the first layer (T_{oil}/T_{over}), which in later text is denoted by simple letter T. This ratio was 1, 5, 10, 15, 30, 50, 75,

Figure 10 Apparent Resistivity Plot.

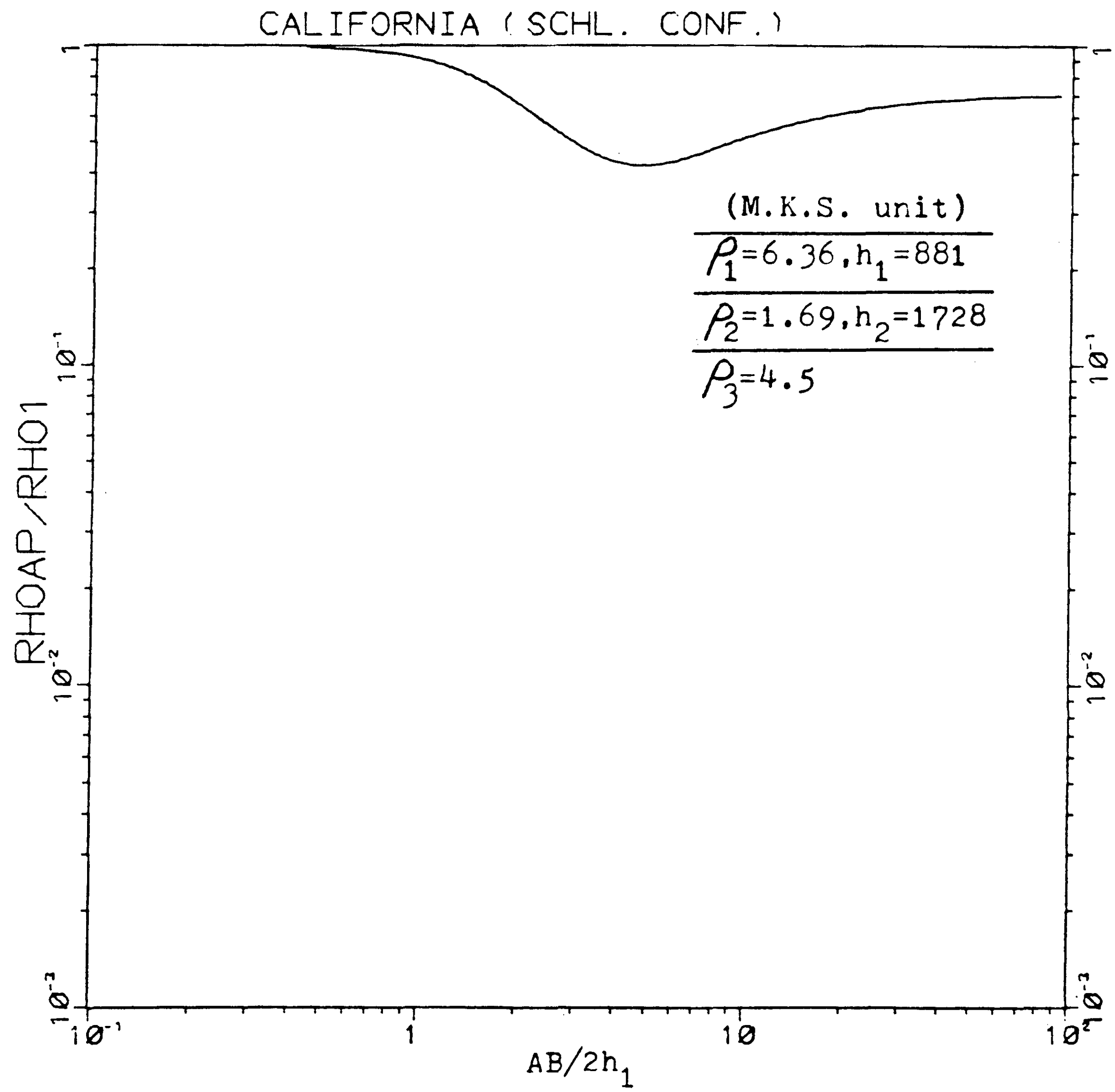

Figure 11 Apparent Resistivity Plot.

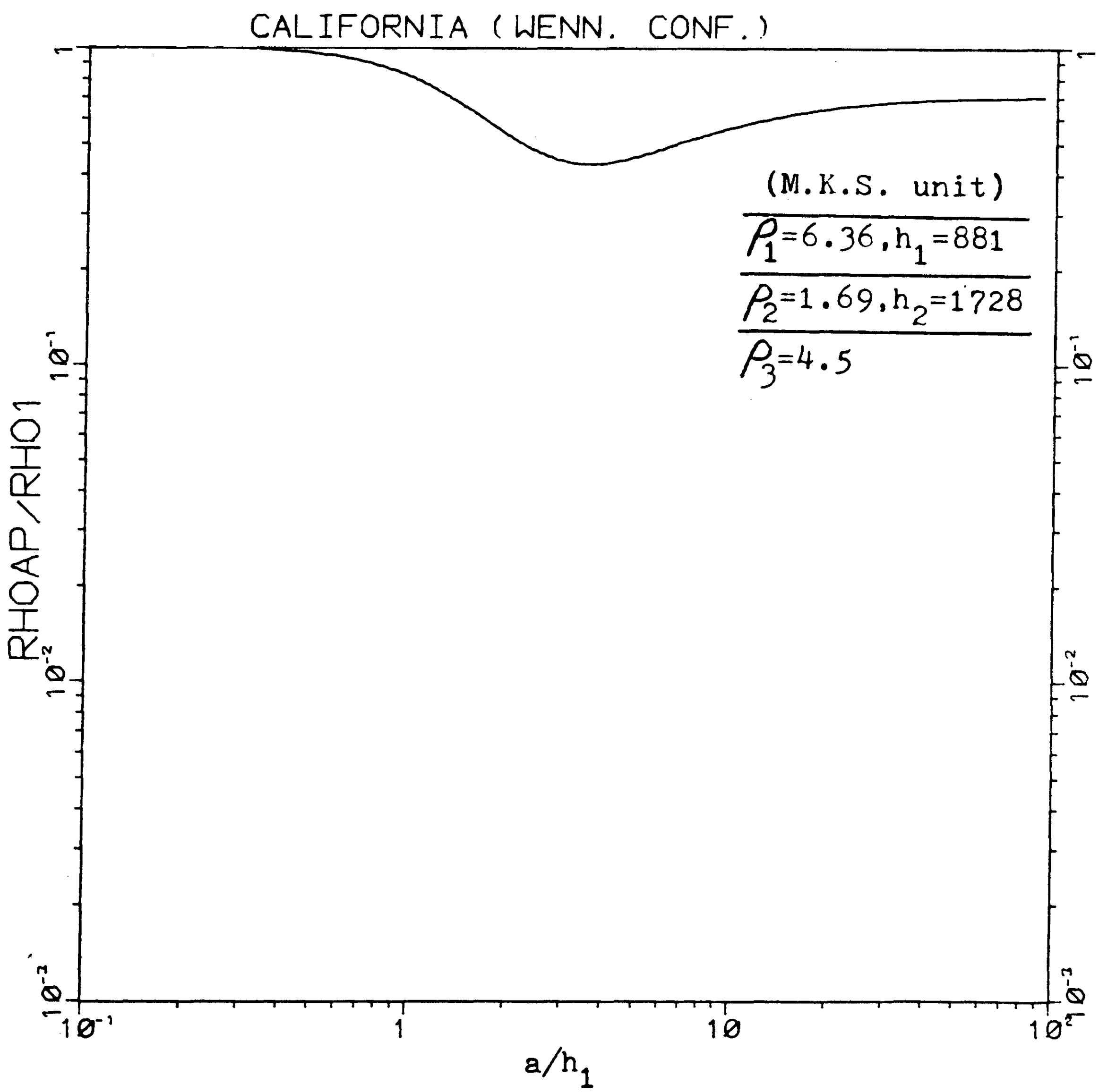

Figure 12 Apparent Resistivity Plot.

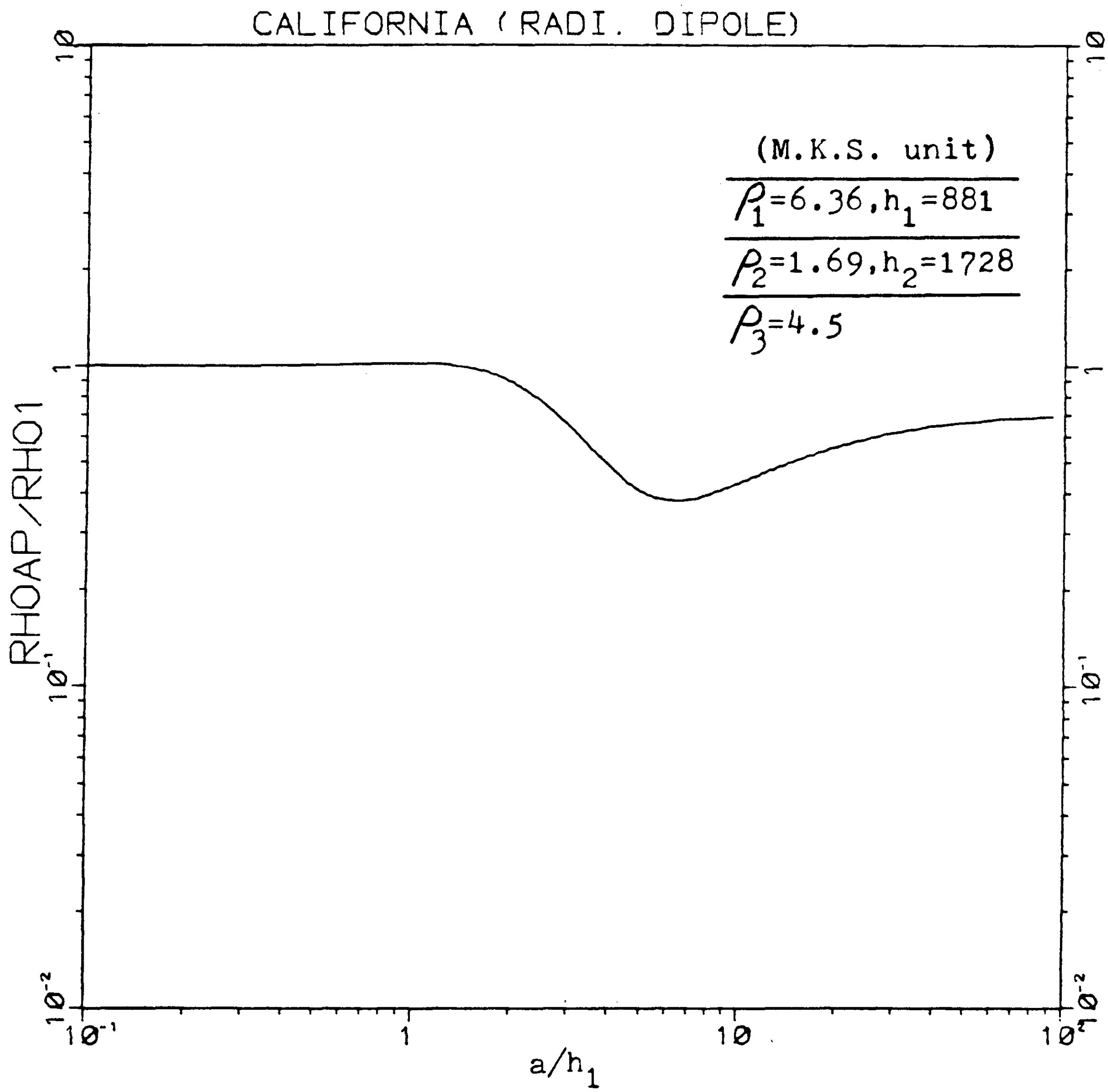

Figure 13 Apparent Resistivity Plot.

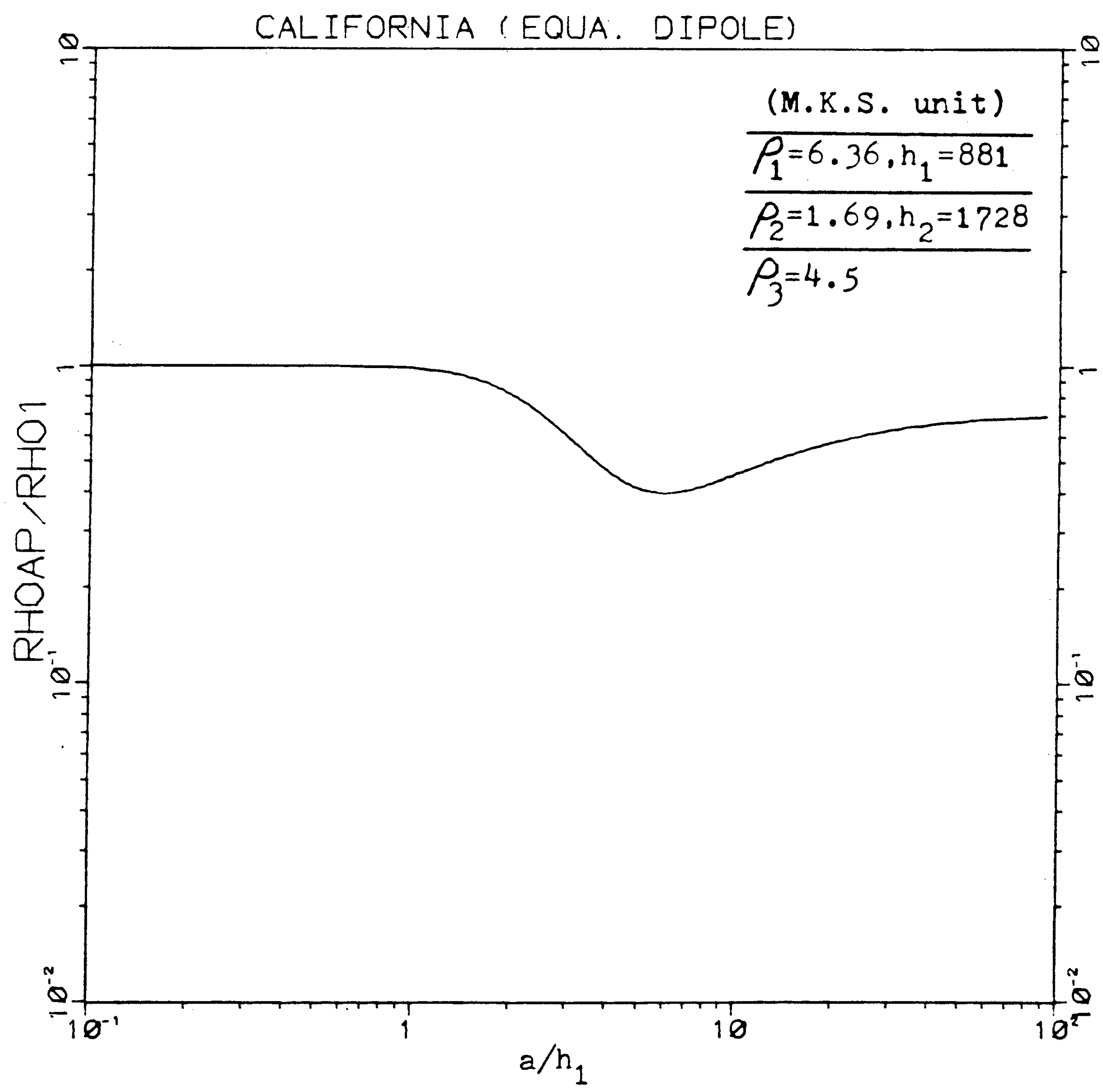

and 100%. The anomaly in the present study was defined as

$$\text{Anomaly \%} = \frac{(\rho_a)_{\text{with oil-layer}} - (\rho_a)_{\text{environment}}}{(\rho_a)_{\text{environment}}} * 100$$

Again, the anomaly curves were computed for all four DC arrays vs. the same spacing defined above; the results are shown in Figures 14, 16, 18, and 20. The relationships between maximum anomaly values and transverse resistance contrast are plotted in Figures 15, 17, 19, and 21. The anomaly curves were computed only for limited electrode separation due to the reason that for very small or large separations compared to the oil-layer depth, there will be little or no anomaly. In computing anomaly curves, the Ghosh convolution approach (1971) was used. Sometimes the anomaly curves were not smooth for anomaly values less than 1% due to the inaccuracy of the method used. In Figures 14 and 16, the anomaly curves for Schlumberger and Wenner arrays are quite smooth except when the anomaly is less than 1%. The maximum anomaly value with the Schlumberger array varies from about 0.9 to 80% for T = 1 to 100%. With the Wenner array, it varies from 0.84-74%, and is about 93% of that found for the Schlumberger array for both T values. For the radial-dipole array it is about 1.2 to 110%, and for the equatorial-dipole array, it is 1.1 to 96%. The radial-dipole anomaly is about 135 and 111% of the anomaly for the Schlumberger and the equatorial-dipole arrays, respectively. So, in the case of

Figure 14 Anomaly plot for varying Transverse Resistance Contrast($T_{oil}/T_{over.}$) in %.

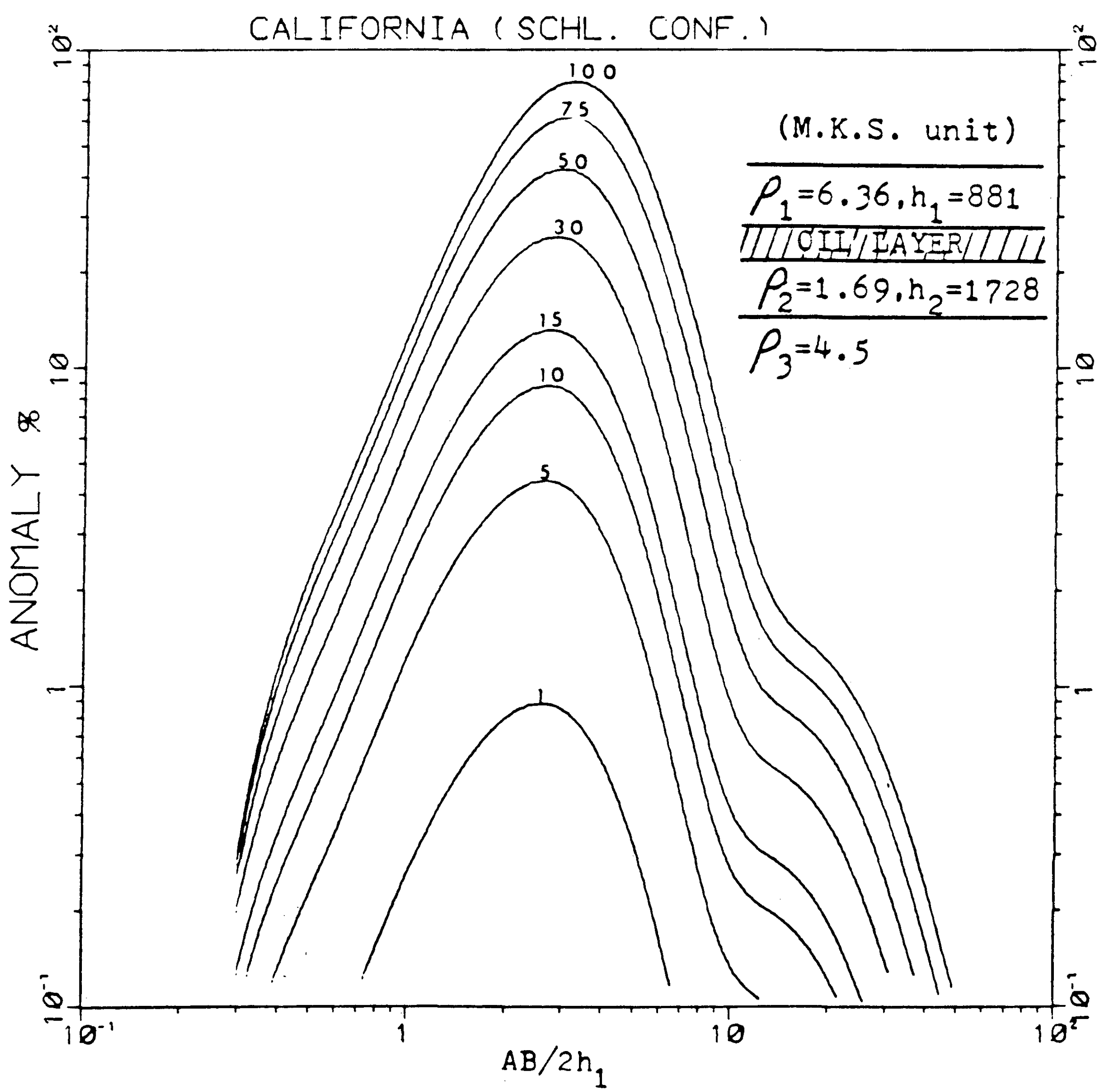

Figure 15 Plot of maximum anomaly for varying Transverse Resistance Contrast ($T_{oil}/T_{over.}$).

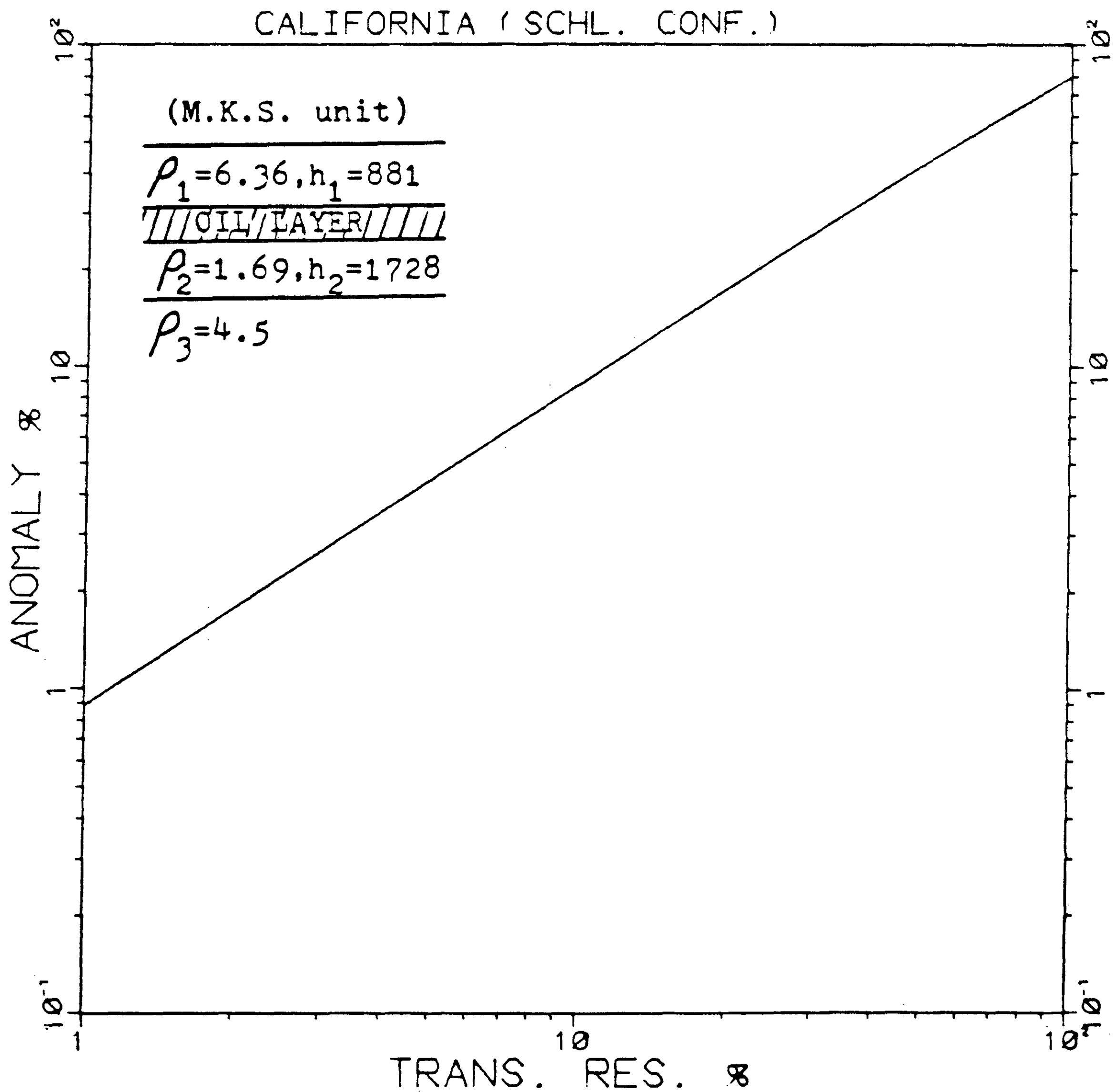

Figure 16 Anomaly plot for varying Transverse Resistance Contrast($T_{oil}/T_{over.}$) in %.

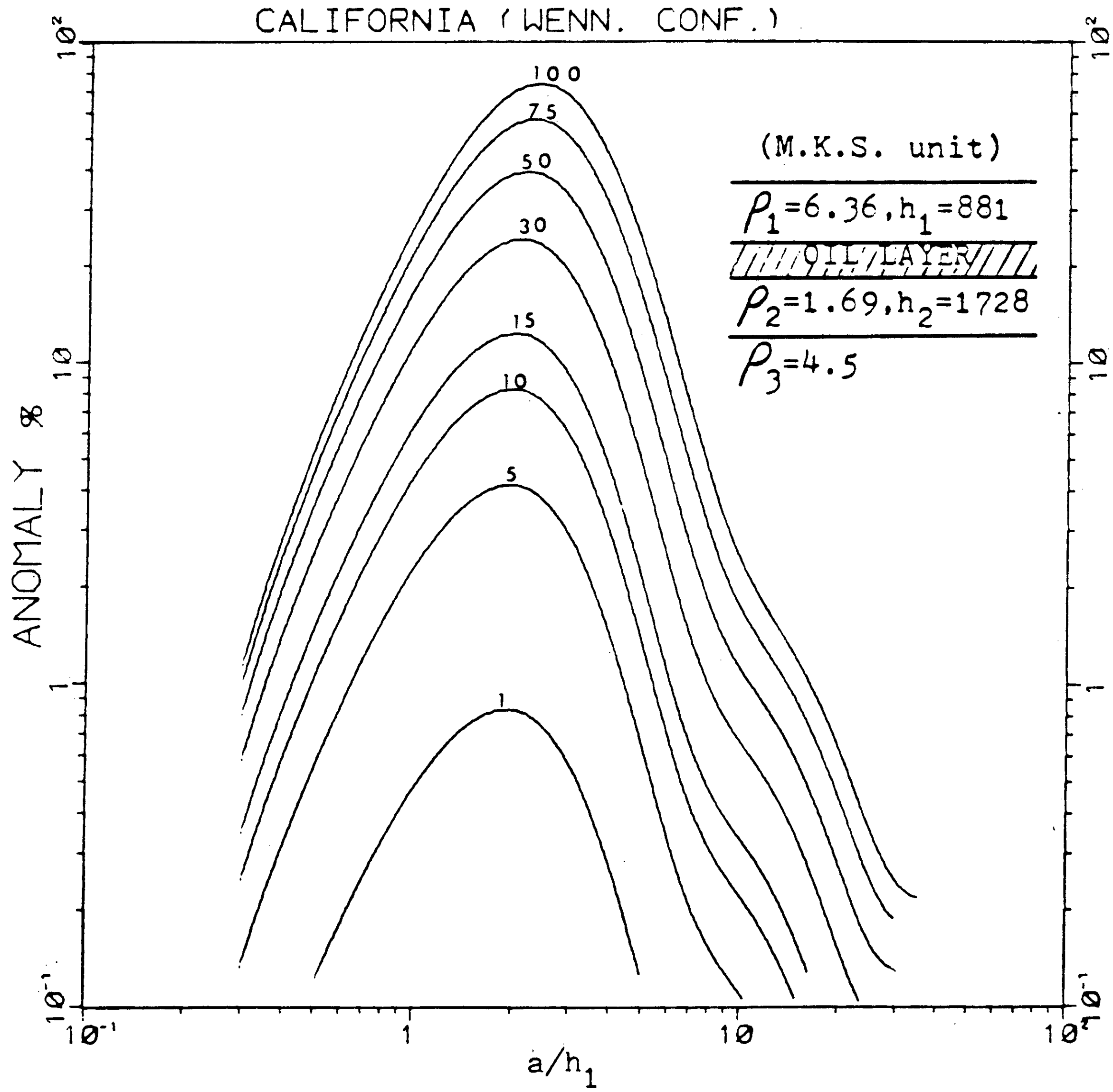

Figure 17 Plot of maximum anomaly for varying Transverse Resistance Contrast ($T_{oil}/T_{over.}$).

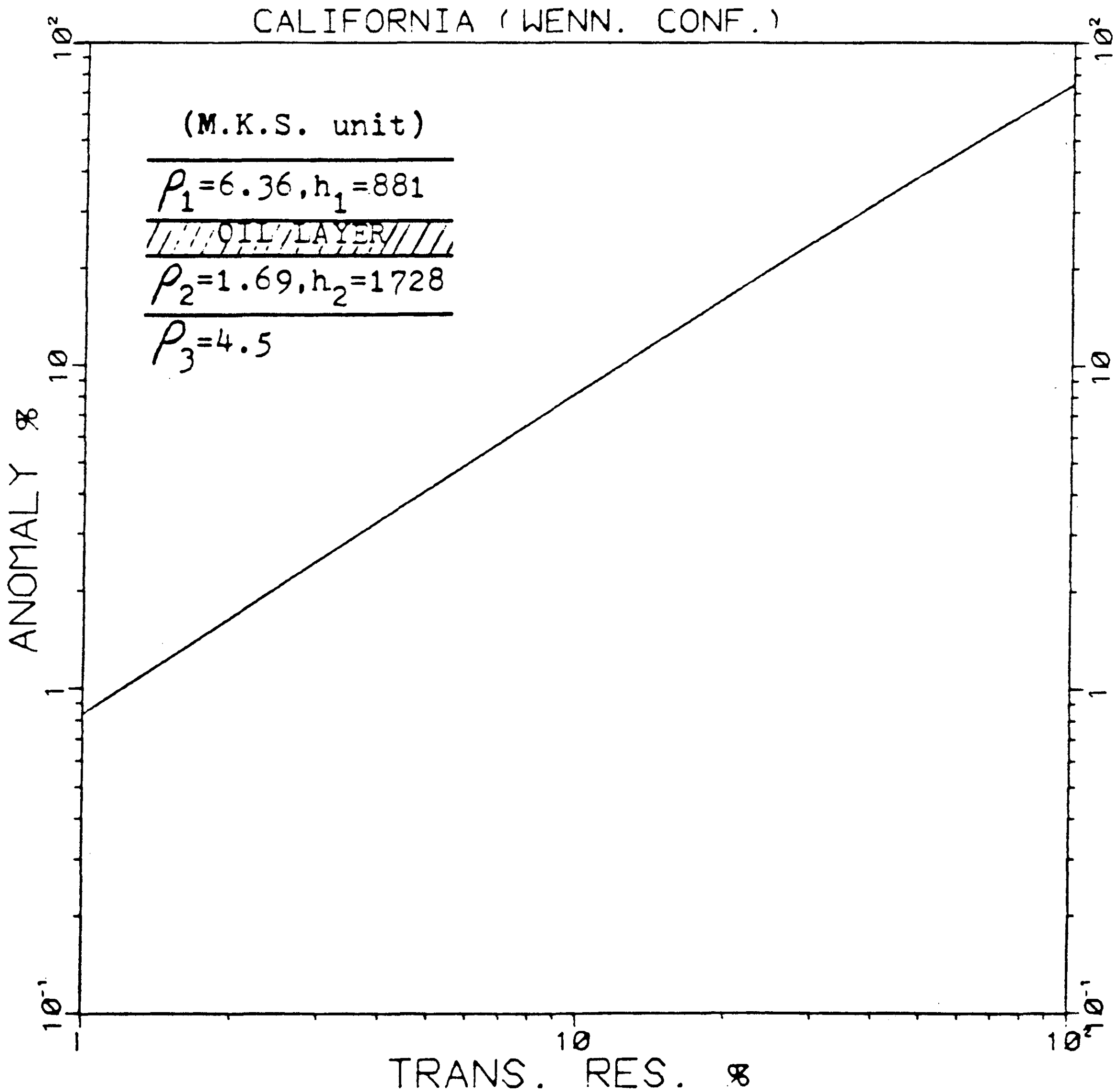

Figure 18 Anomaly plot for varying Transverse Resistance Contrast($T_{oil}/T_{over.}$) in %.

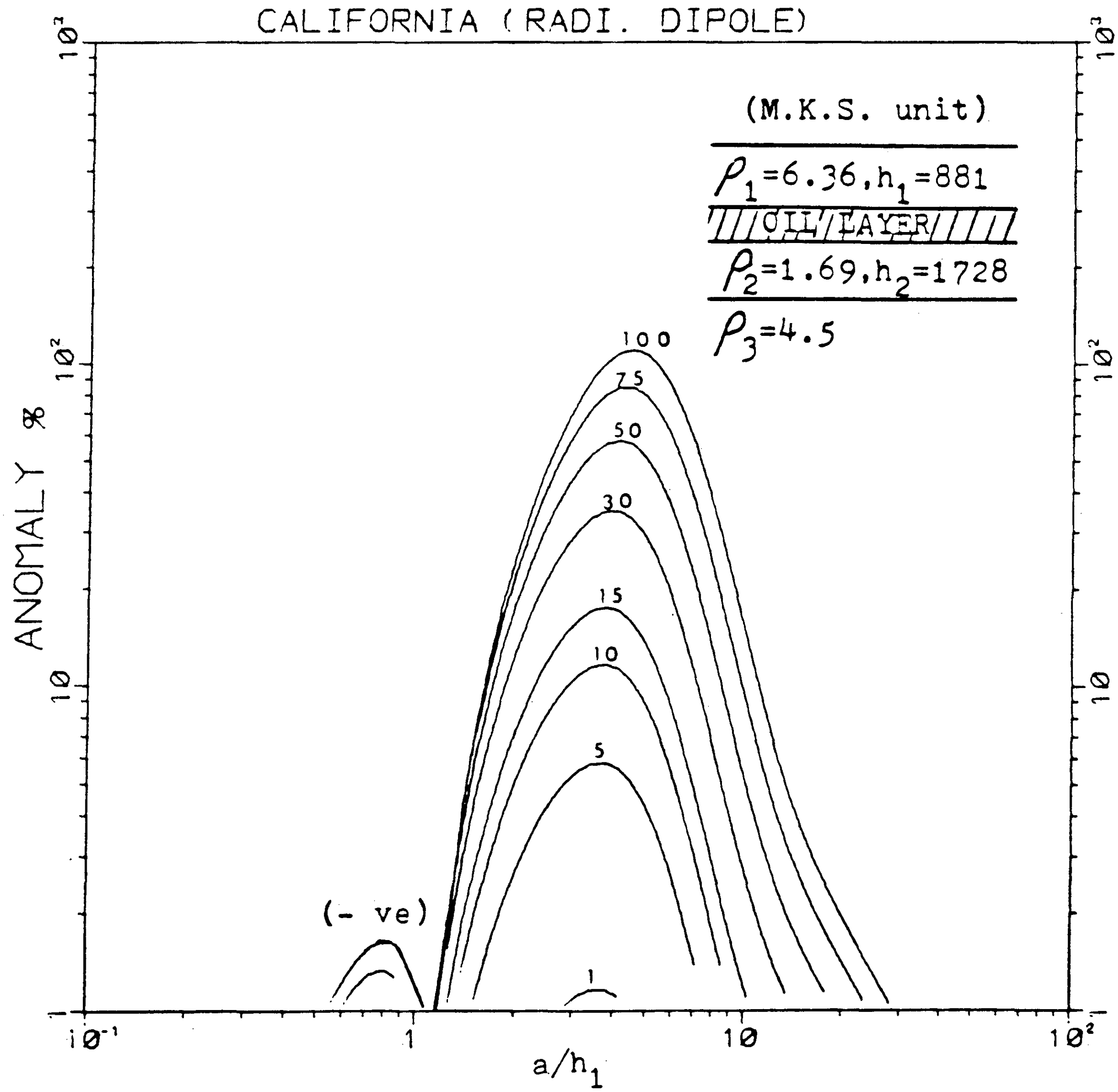

Figure 19 Plot of maximum anomaly for varying Transverse Resistance Contrast ($T_{oil}/T_{over.}$).

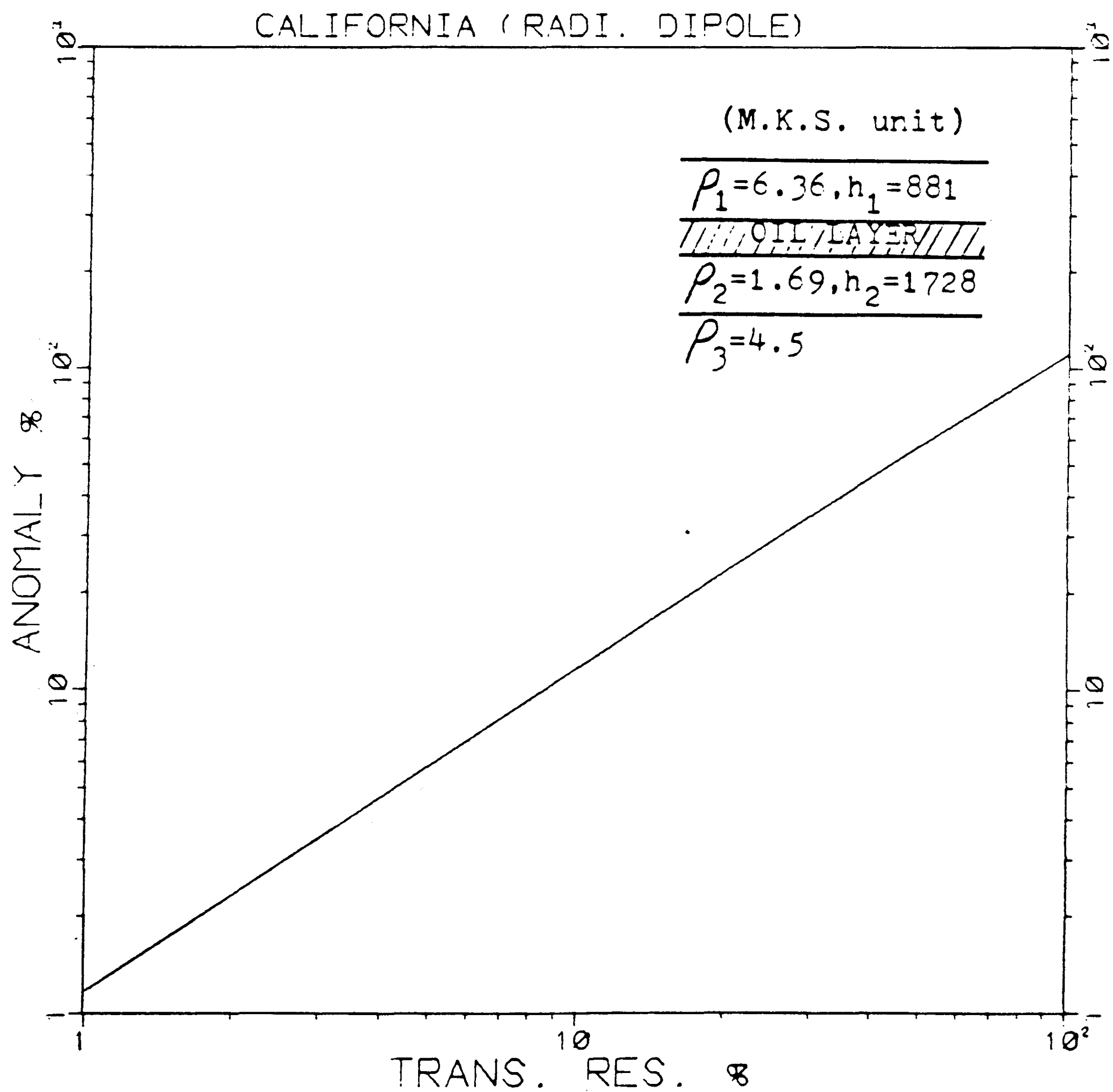

Figure 20 Anomaly plot for varying Transverse Resistance Contrast($T_{oil}/T_{over.}$) in %.

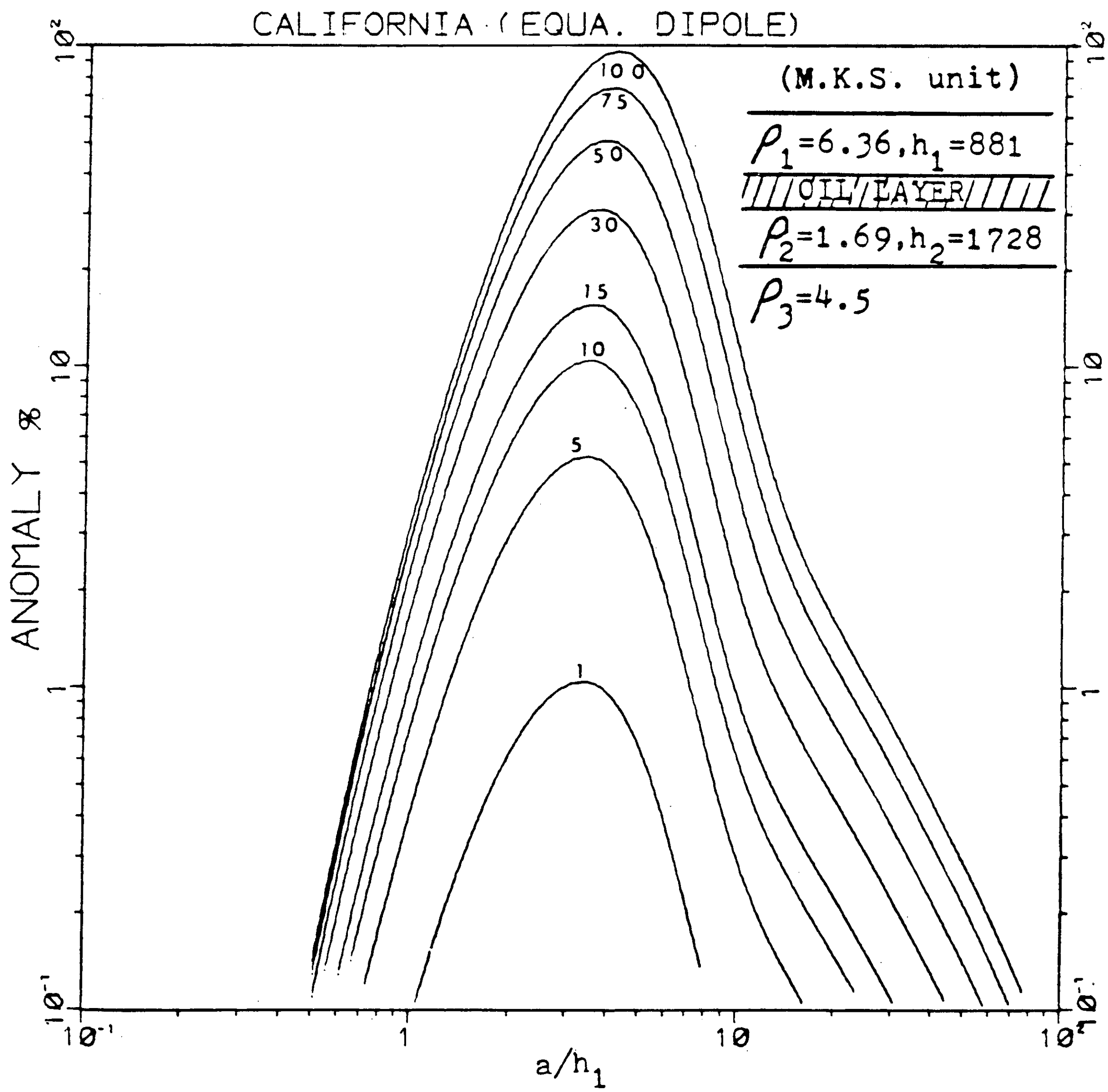

Figure 21 Plot of maximum anomaly for varying Transverse Resistance Contrast ($T_{oil}/T_{over.}$).

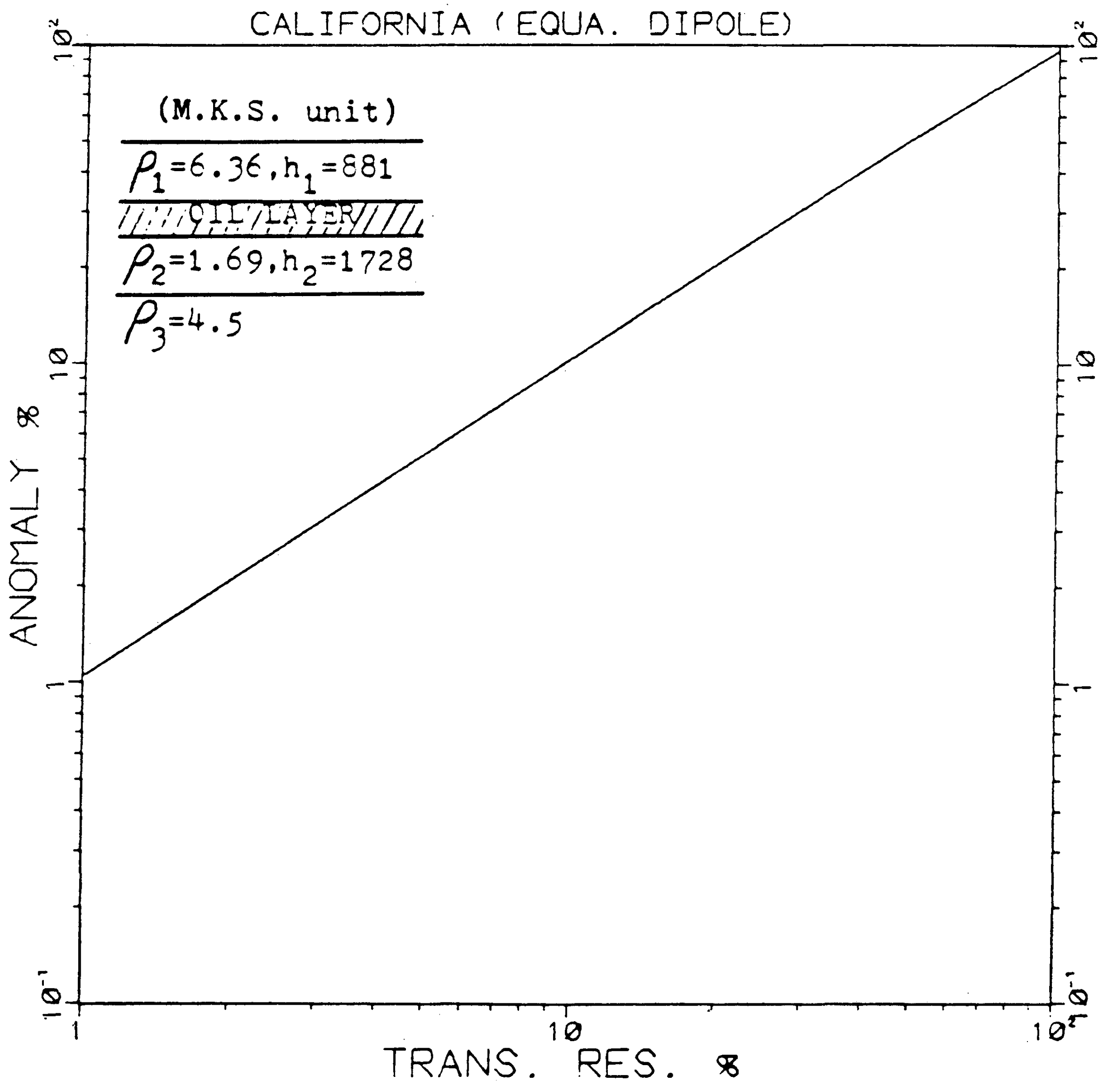

the radial-dipole, it is maximum compared to the other three arrays over the same model. However, using the radial-dipole array, it also shows a negative anomaly at small separations. We can say that sometimes the computed ρ_a with an oil-layer present is less in comparison to the case without an oil-layer ρ_a for these separations. Also, the maximum anomaly value appears at a smaller a/h_1 value for the Wenner array than for the Schlumberger array. This is due to the fact that the depth of penetration in the Wenner array is a bit more for the same a and AB/2 as the distance between two extreme current electrode in the Wenner array is more than in the Schlumberger array. Also, when we compare the radial and equatorial-dipole arrays again, the maxima appears at shorter spacings for the equatorial-dipole array. This is due to the same reason; the actual distance between the center of the current and potential dipole is more than for equatorial-dipole array. From an overall review, the radial-dipole array gives the best anomaly value over a given model. The anomaly varies from about more than 1% to 110% for T values from 1 to 100%, which is very encouraging.

Anomaly Curve due to the Presence of Possible Oil/Gas Layer Picked Up from Well-Log #10:

It is usually difficult to locate an oil/gas zone on a well-log. However, for well-log #10, a possible oil/gas zone is demarcated at a depth of 743 m. Its thickness is 3.66 m and the average longitudinal resistivity is 2.06 ohm-m, i.e., transverse resistance is 7.53 ohm. As the previous anomaly curves were computed assuming that the oil-layer is embedded between layer one and two with a resistivity 10 times that of the first layer. If we move this layer to the same position with resistivity $10\rho_1$, then its calculated thickness by keeping the same transverse resistance is 0.118 m and the transverse resistance contrast ratio of the oil-layer to first layer is only 0.134%. The actual model is as below:

$$\rho_1 = 6.36 \text{ ohm-m}, \; h_1 = 881 \text{ m}$$
$$\rho_o = 63.6 \text{ ohm-m}, \; h_o = 0.118 \text{ m}$$
$$\rho_2 = 1.69 \text{ ohm-m}, \; h_2 = 1728 \text{ m}$$
$$\text{and } \rho_3 = 4.5 \text{ ohm-m}$$

The anomaly curves for all four DC arrays for the above model are shown in Figures 22, 23, 24, and 25. Again, as before, the maximum anomaly value corresponds to the radial-dipole array. However, it is only 0.16% and there is a negative anomaly which is about 0.003%. However, as mentioned in the early discussion, a commercial field should have a transverse resistance contrast at least several percent, and so, we can say that the above example is merely of academic interest.

Figure 22 Anomaly plot over possible oil/gas layer picked-up from well-log # 10.

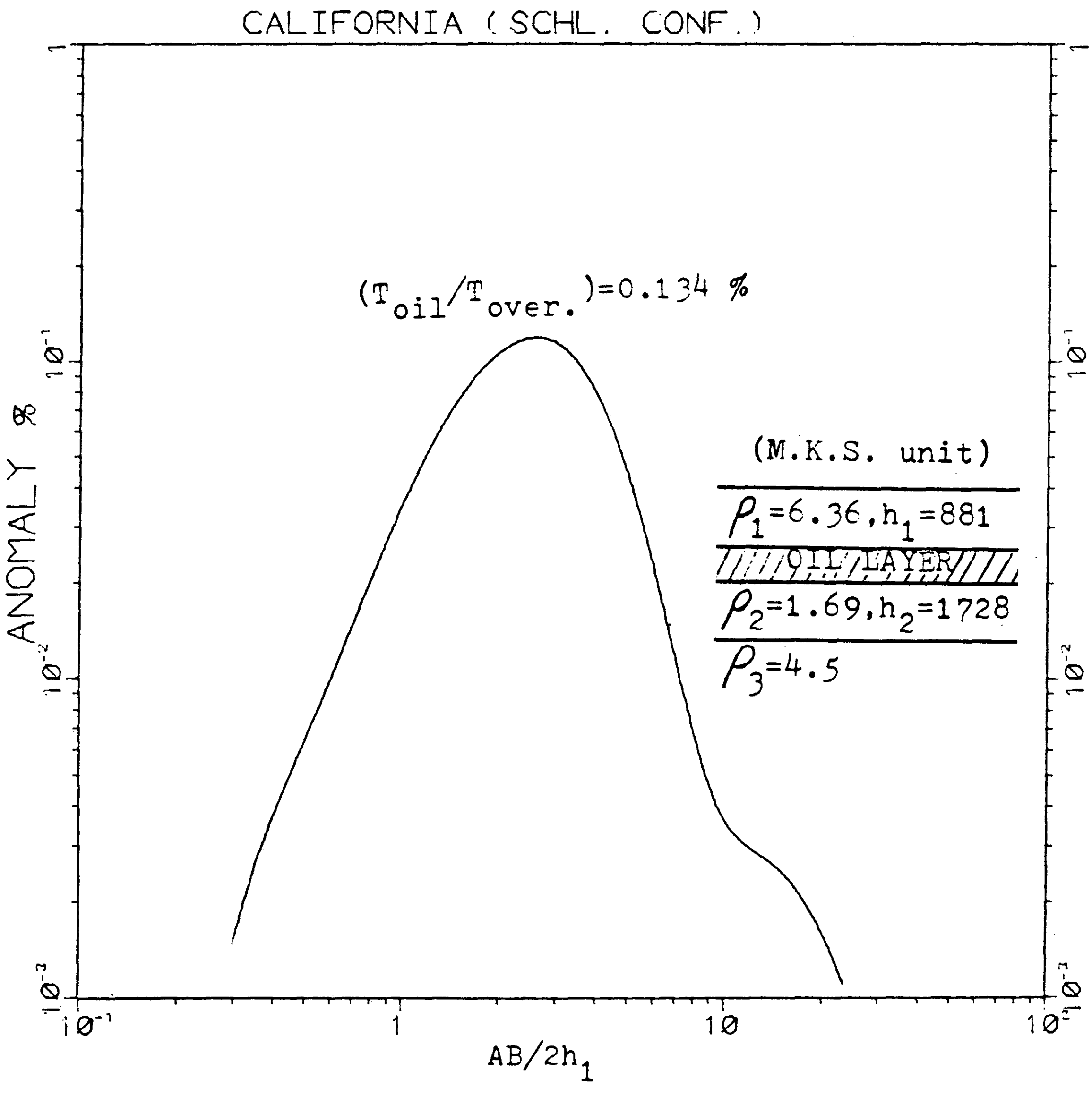

Figure 23 Anomaly plot over possible oil/gas layer picked-up from well-log # 10.

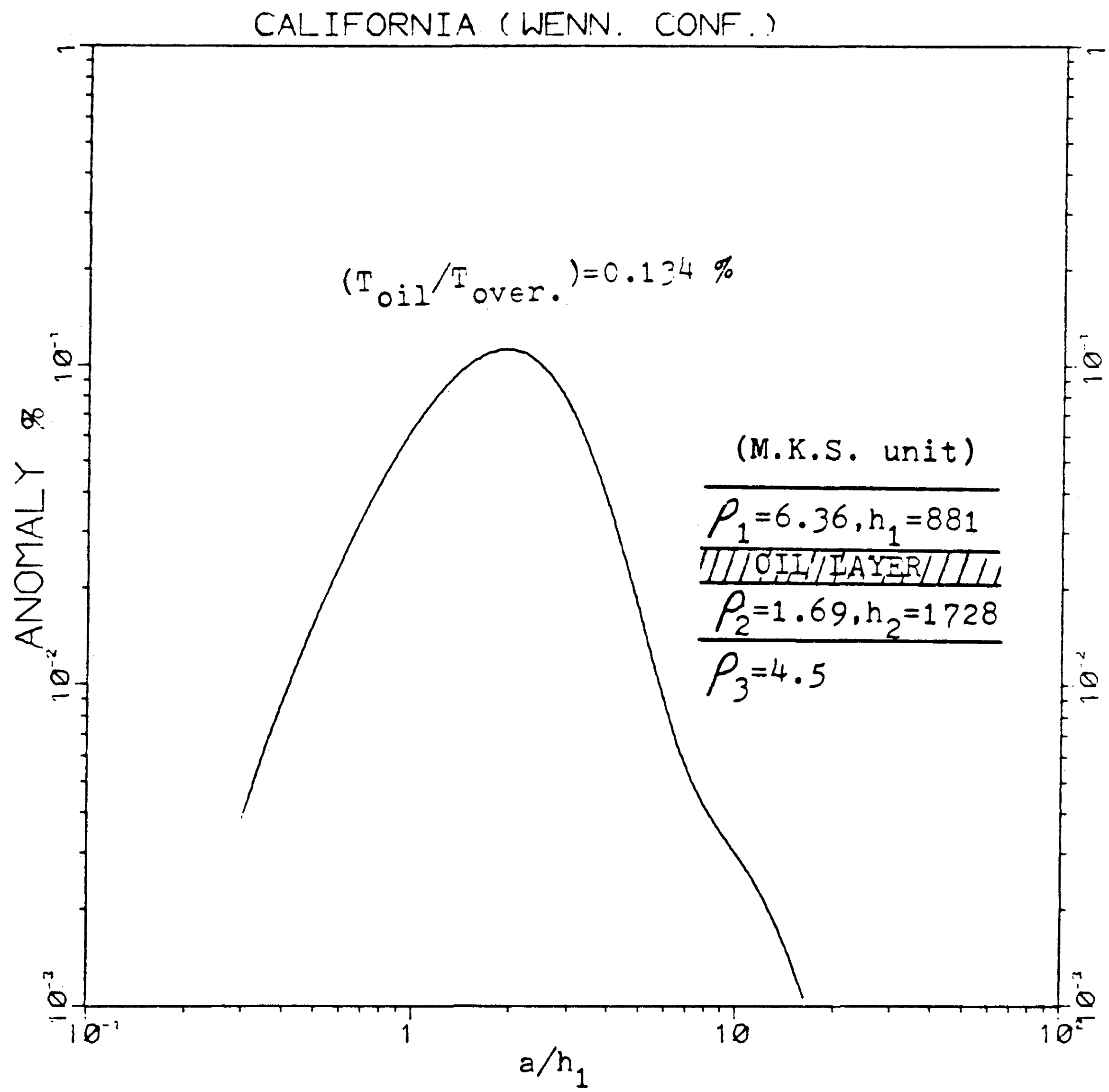

Figure 24 Anomaly plot over possible oil/gas layer picked-up from well-log # 10.

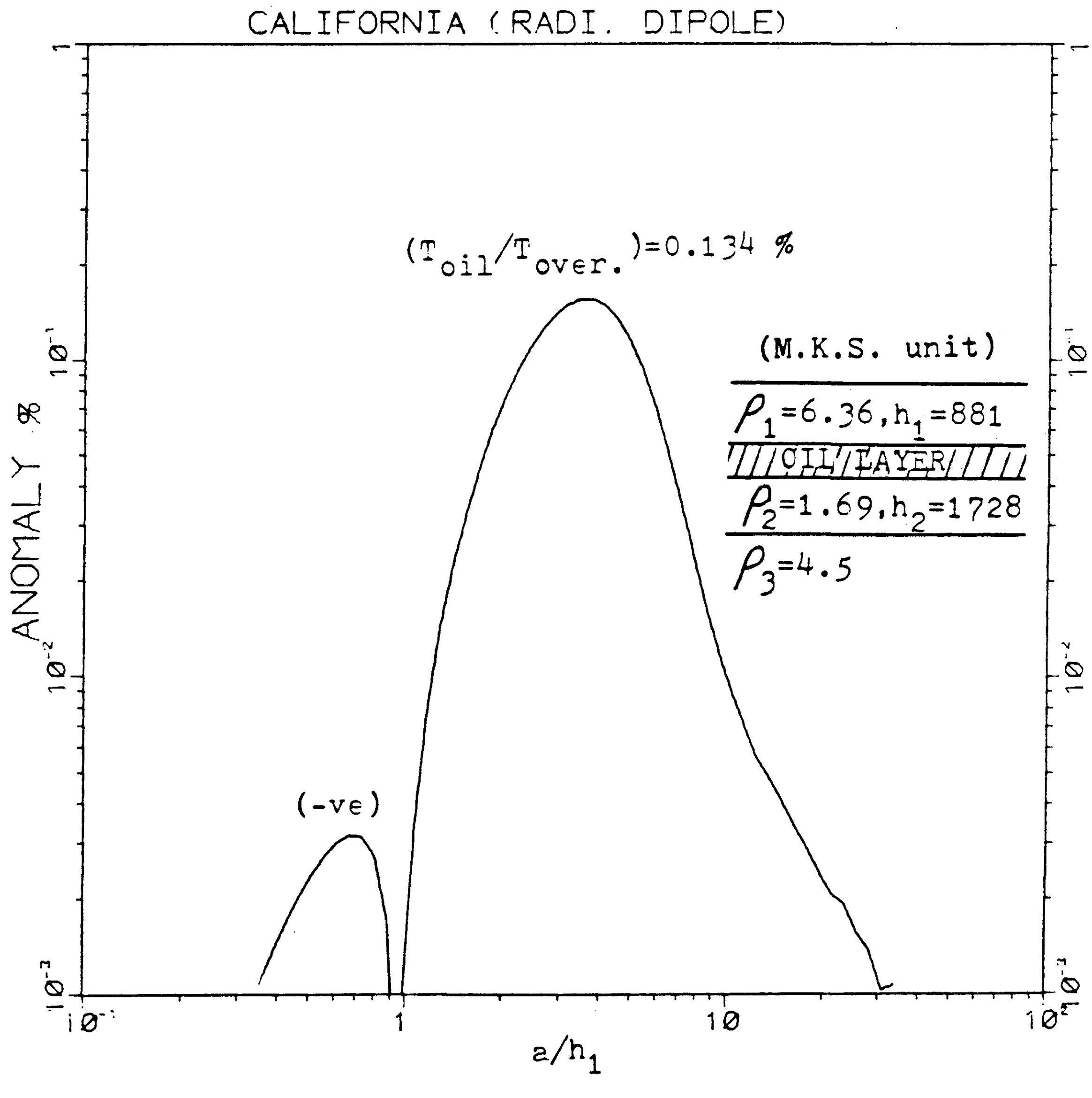

Figure 25 Anomaly plot over possible oil/gas layer picked-up from well-log # 10.

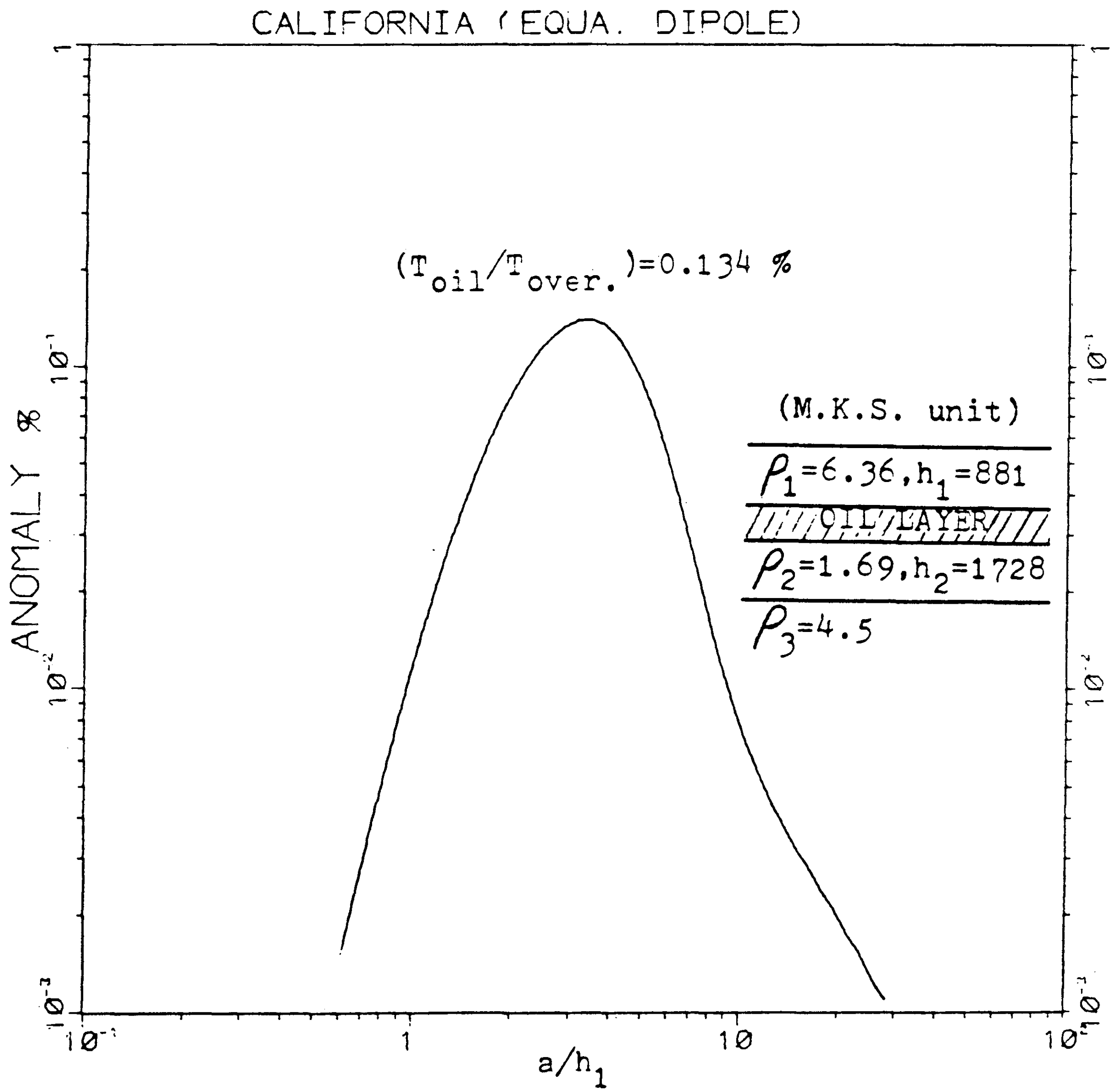

PAYNE, LOGAN, AND LINCOLN COUNTIES, OKLAHOMA

The average longitudinal resistivities and thicknesses computed from the well-logs are as below:

$\rho_1 = 4.8$ ohm-m, $h_1 = 1202$ m

and $\rho_2 = 12.55$ ohm-m

The above geoelectrical parameters correspond to a two-layer ascending type of curve (Type A). Average transverse and longitudinal resistivity values and the coefficient of anisotropy corresponding to all individual well-logs are tabulated in Appendix 2. Only two units are recognizable. The minimum and maximum depths available from well-logs were 30 and 1594 m, respectively. The coefficient of anisotropy corresponding to the first unit ranges between 10-30%. However, for the second unit, it is sometimes high, being about 90%. This might be due to the presence of resistive units like limestone, anhydrite, etc.

The average longitudinal resistivity contours for both units are shown in Figures 26 and 27. The resistivity contours corresponding to the first unit show a local patch of resistivity of 5 ohm-m. For the extreme eastern part of the area, the contours are very close. The resistivity for well #18 is low compared to well-logs # 19 and 20; this might be due to the presence of some

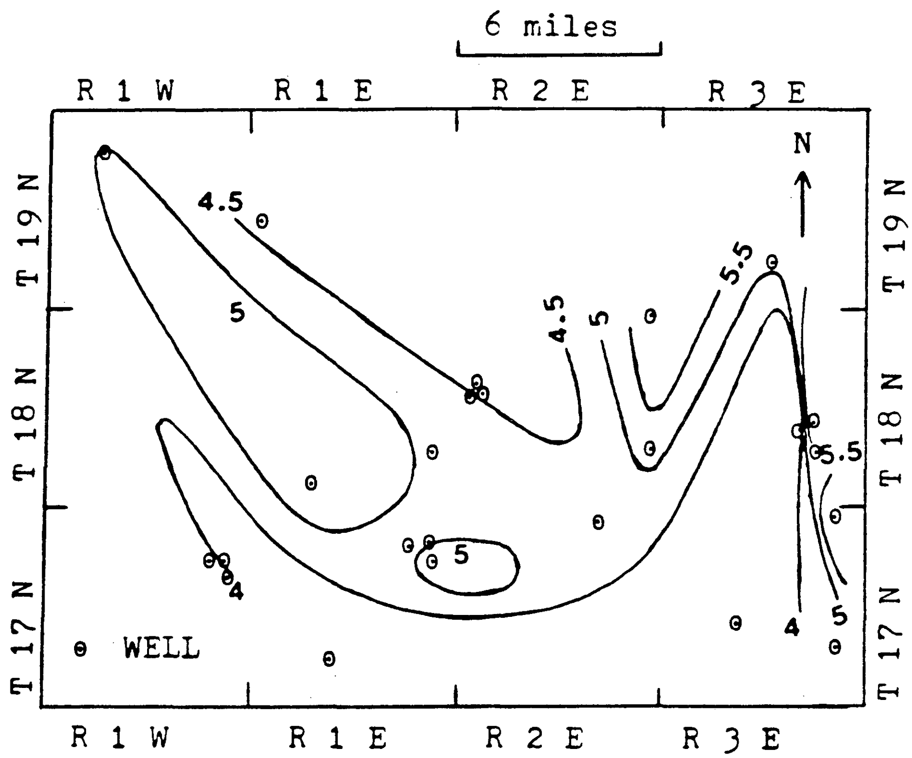

Figure 26 Average Longitudinal Resistivity Contours in ohm- m ., First-unit, Oklahoma.

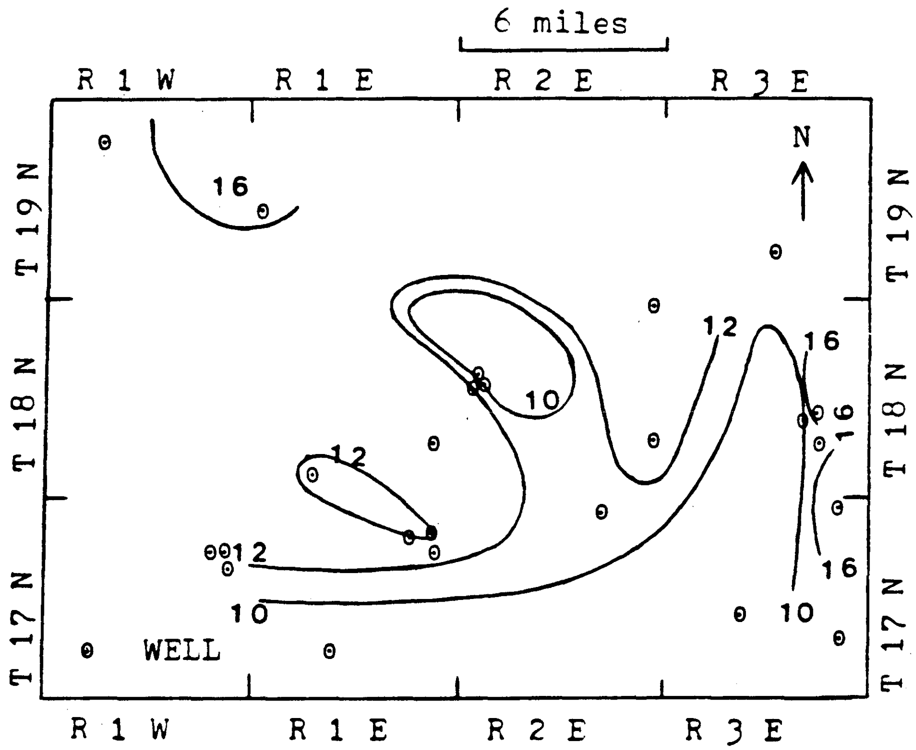

Figure 27 Average Longitudinal Resistivity Contours in ohm- m ., Second-unit, Oklahoma.

local low resistivity patch. The behavior of the resistivity contours corresponding to the second unit is pretty similar to those for the first unit. The apparent resistivity curves from the above model are shown in Figures 28, 29, 30, and 31 for all four DC arrays previously mentioned. For computing these curves, the same assumptions and methods were used as before. For calculating the electrical anomaly due to the presence of an oil-layer in the above environment, again, it was assumed that it is embedded between layer one and two with resistivity 10 times that of the first layer resistivity for different transverse resistance contrast ratios T = 1, 5, 10, 15, 30, 50, 75, and 100%. The anomaly curves were computed for all four DC arrays and are plotted in Figures 32, 34, 36, and 38. The maximum anomaly values corresponding to fixed T values are also plotted in Figures 33, 35, 37, and 39. The anomaly plots for the Schlumberger and Wenner arrays are similar to one another and do not show negative anomalies. However, in the case of the radial-dipole array, there is a negative anomaly. The negative anomaly corresponding to T = 100% is comparable to the positive anomaly for T = 5%. The maximum anomaly corresponding to T ratios of 1 and 100% are about 0.07 and 6.3%, respectively, for both the Schlumberger and Wenner arrays. However, strictly speaking, the maximum anomaly value is a bit more in

Figure 28 Apparent Resistivity Plot.

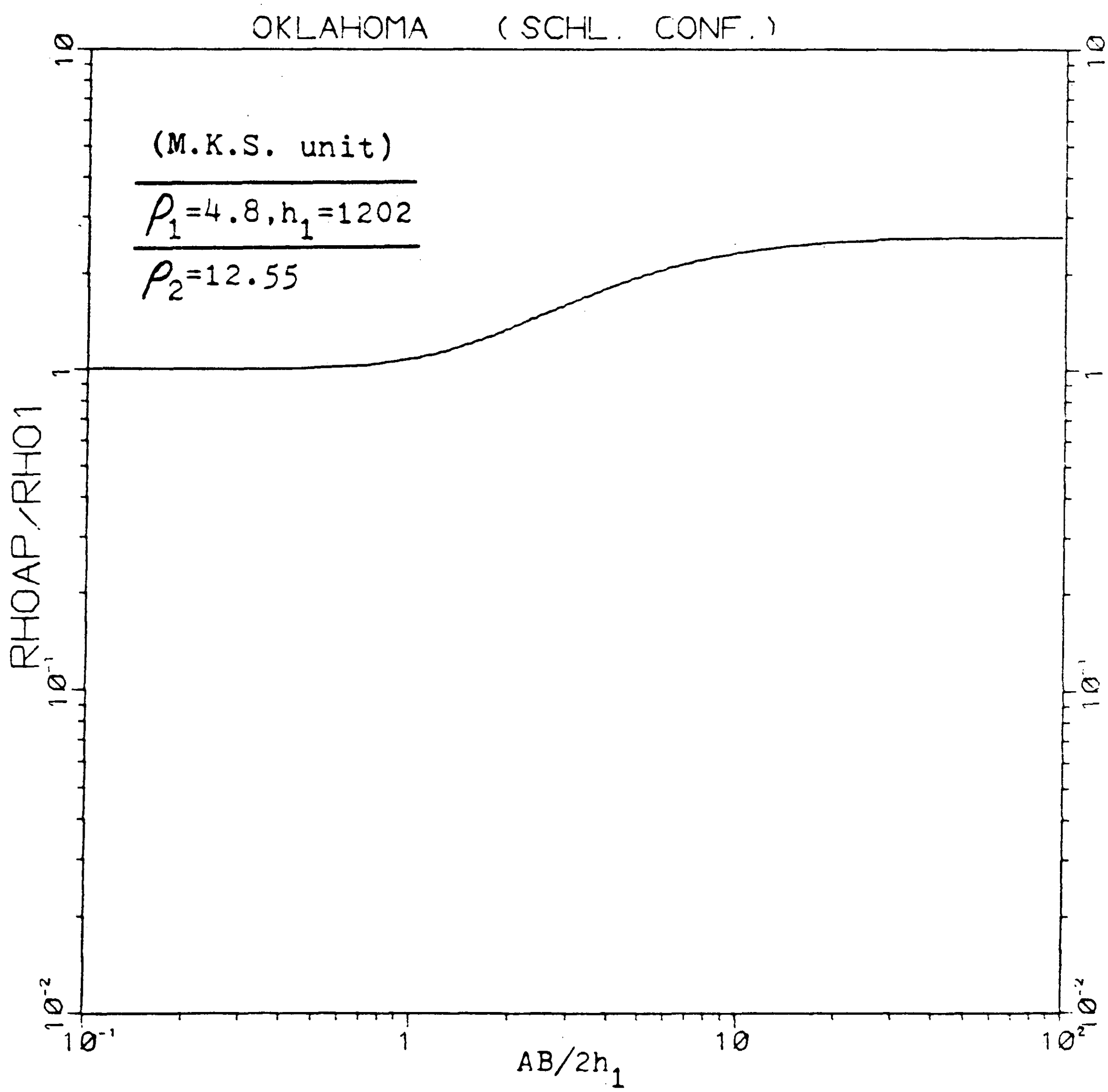

Figure 29 Apparent Resistivity Plot.

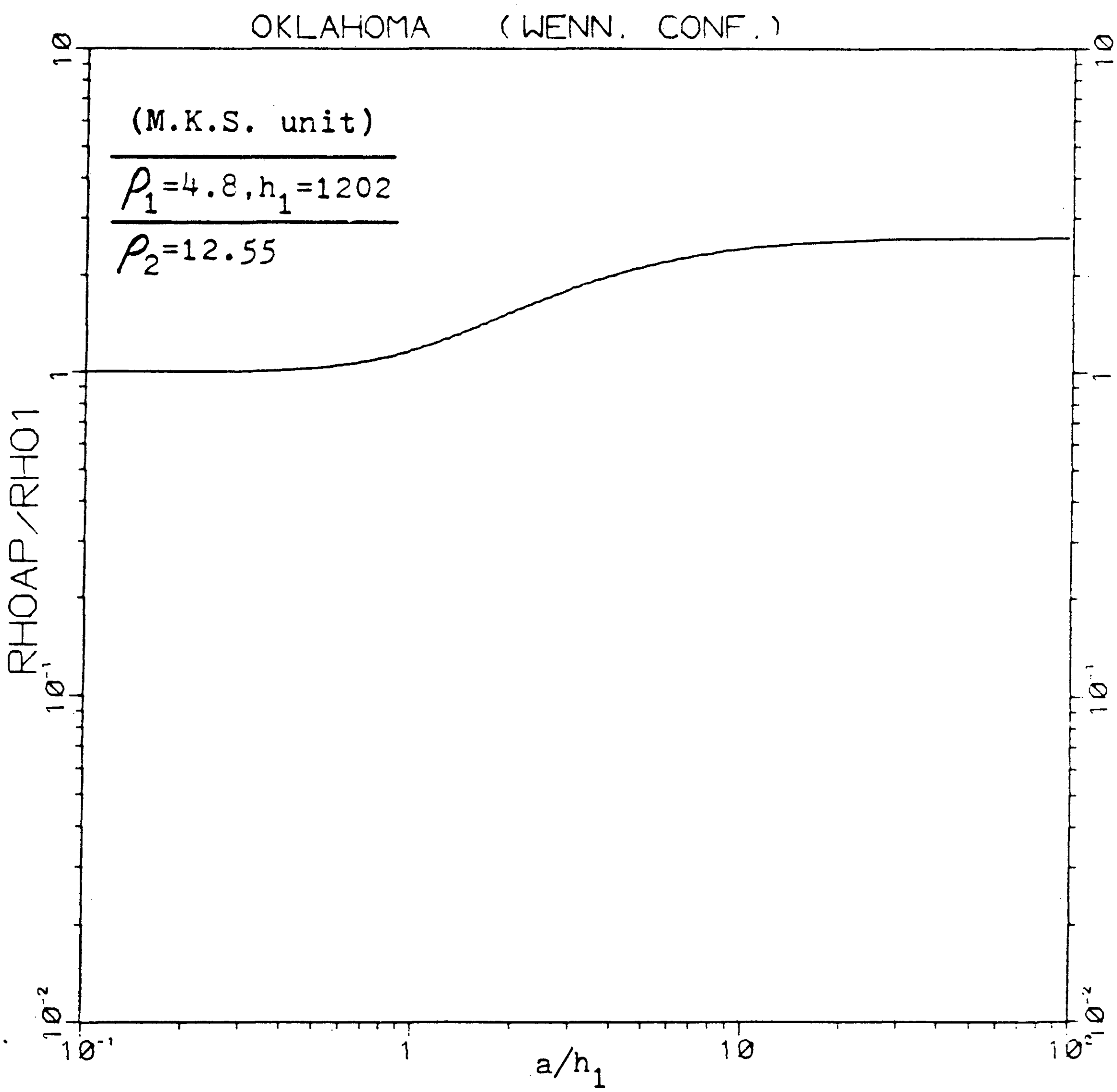

Figure 30 Apparent Resistivity Plot.

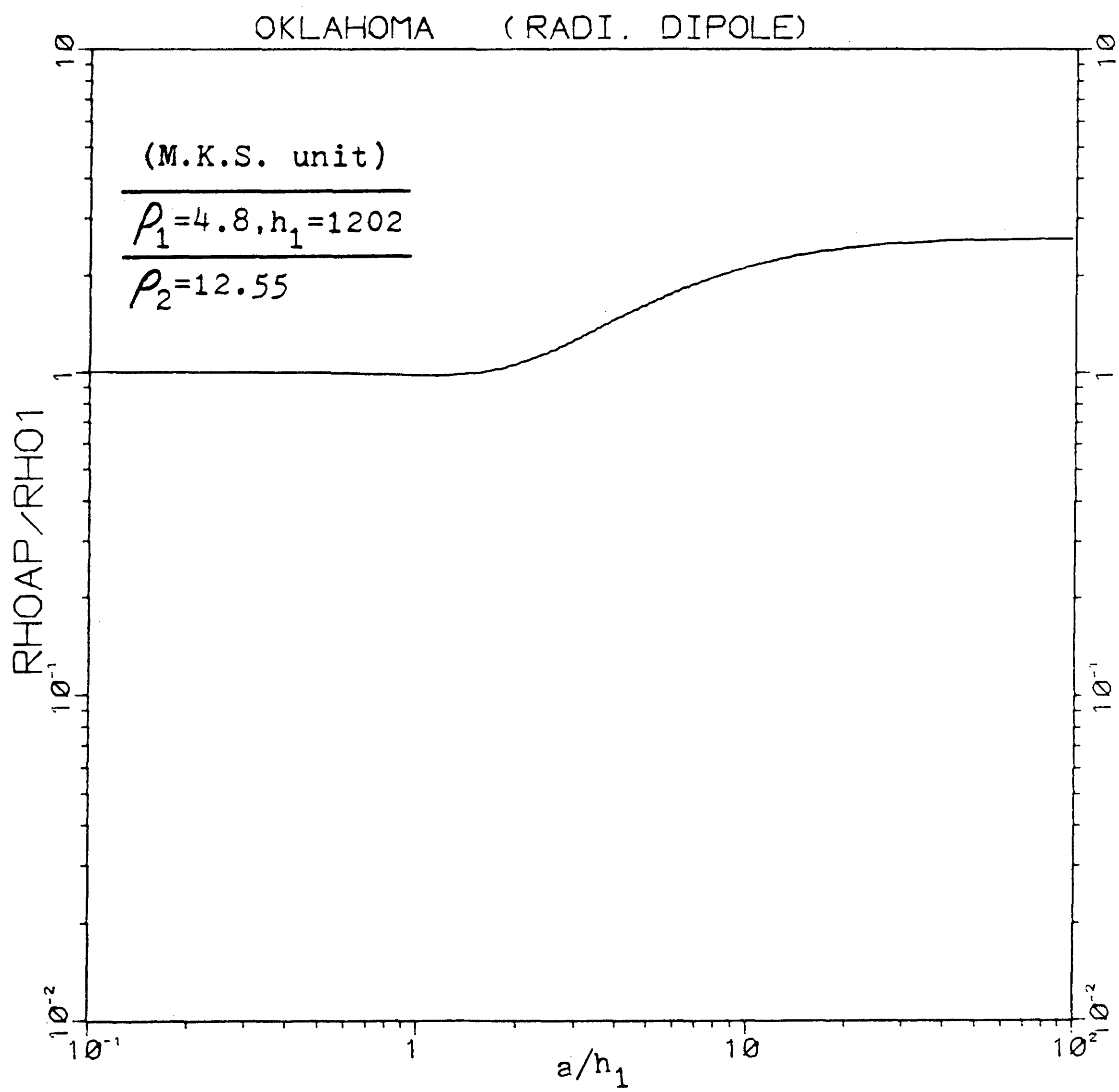

Figure 31 Apparent Resistivity Plot.

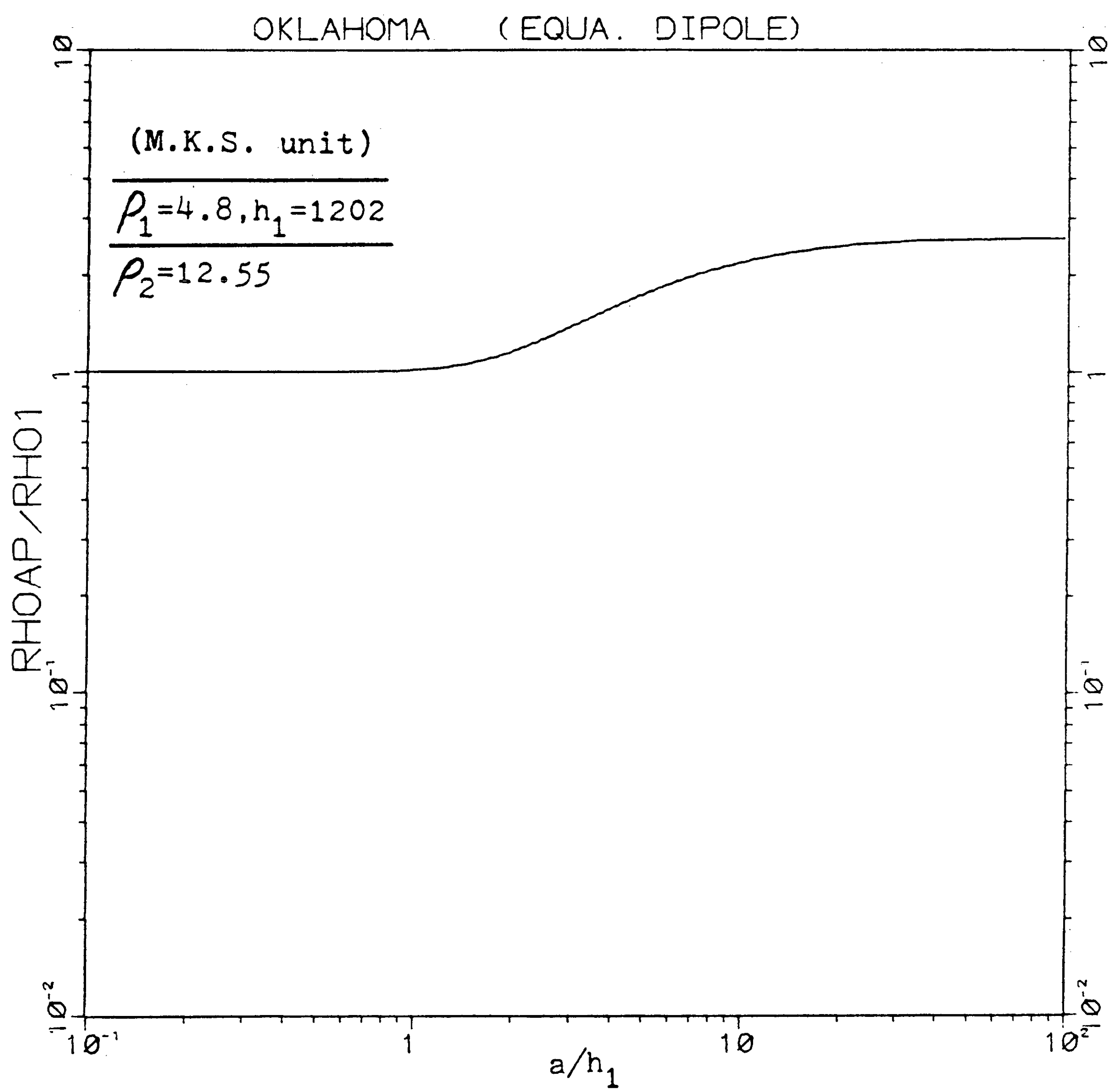

Figure 32 Anomaly plot for varying Transverse Resistance Contrast($T_{oil}/T_{over.}$) in %.

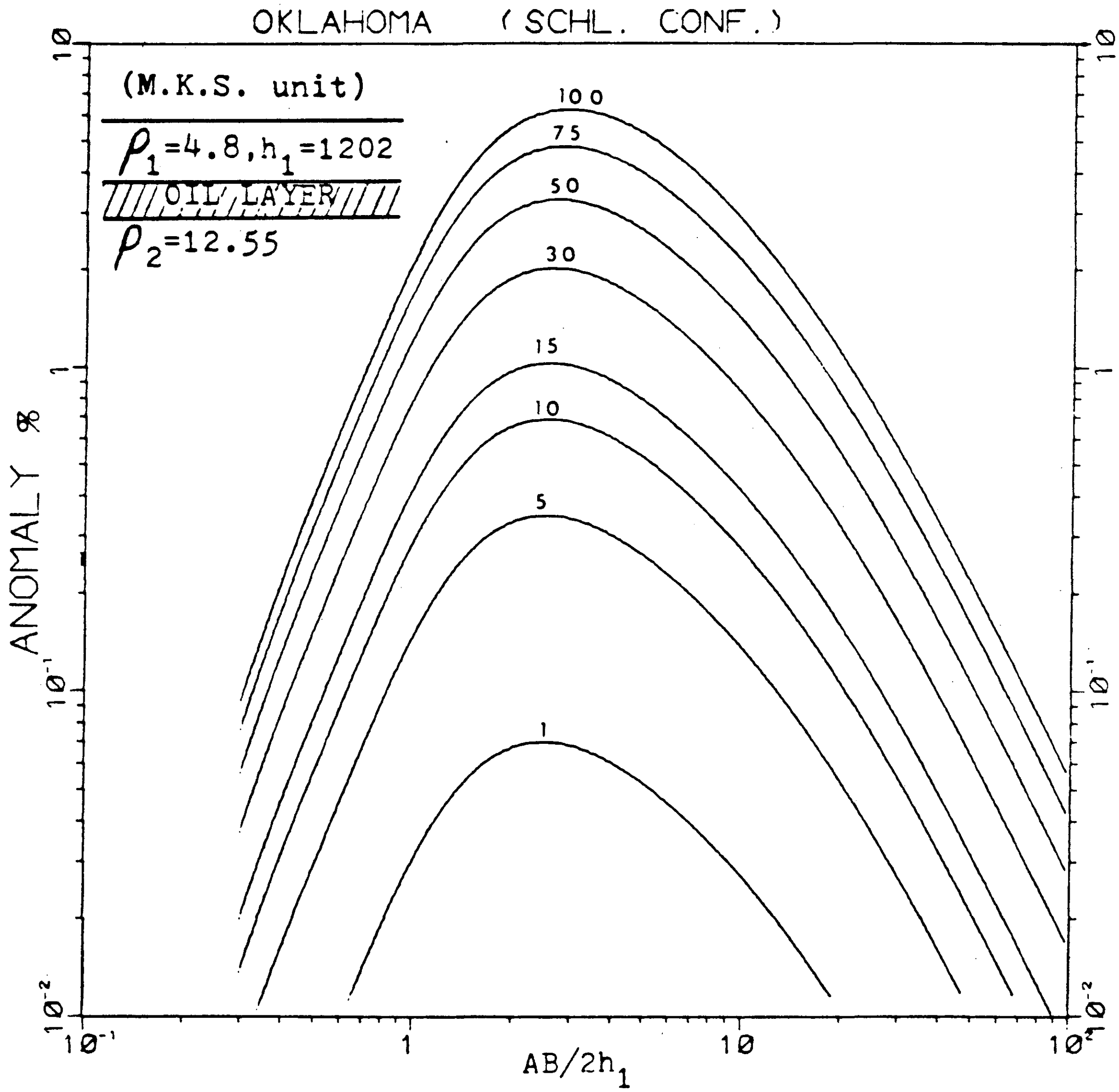

Figure 33 Plot of maximum anomaly for varying Transverse Resistance Contrast ($T_{oil}/T_{over.}$).

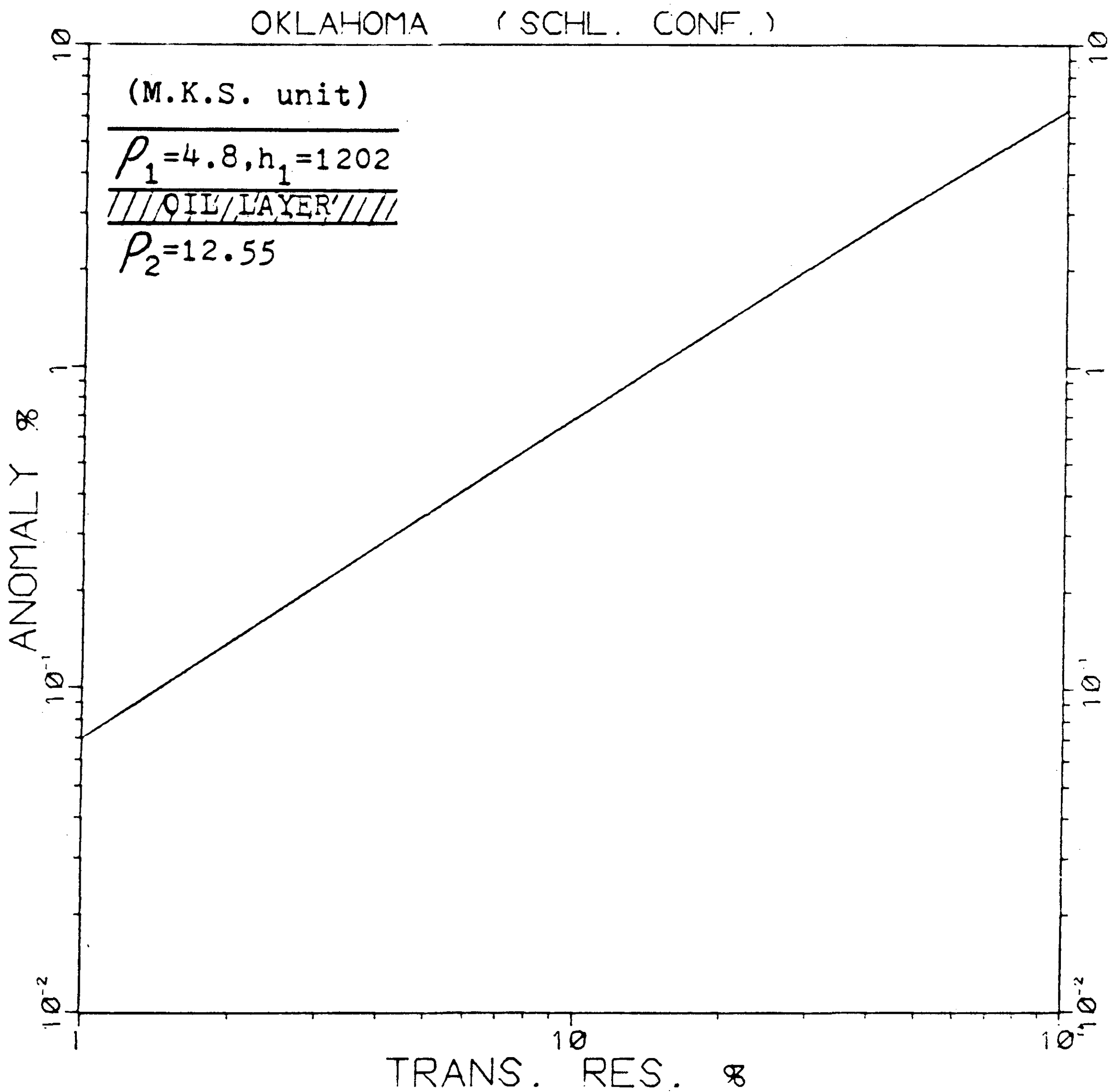

Figure 34 Anomaly plot for varying Transverse Resistance Contrast($T_{oil}/T_{over.}$) in %.

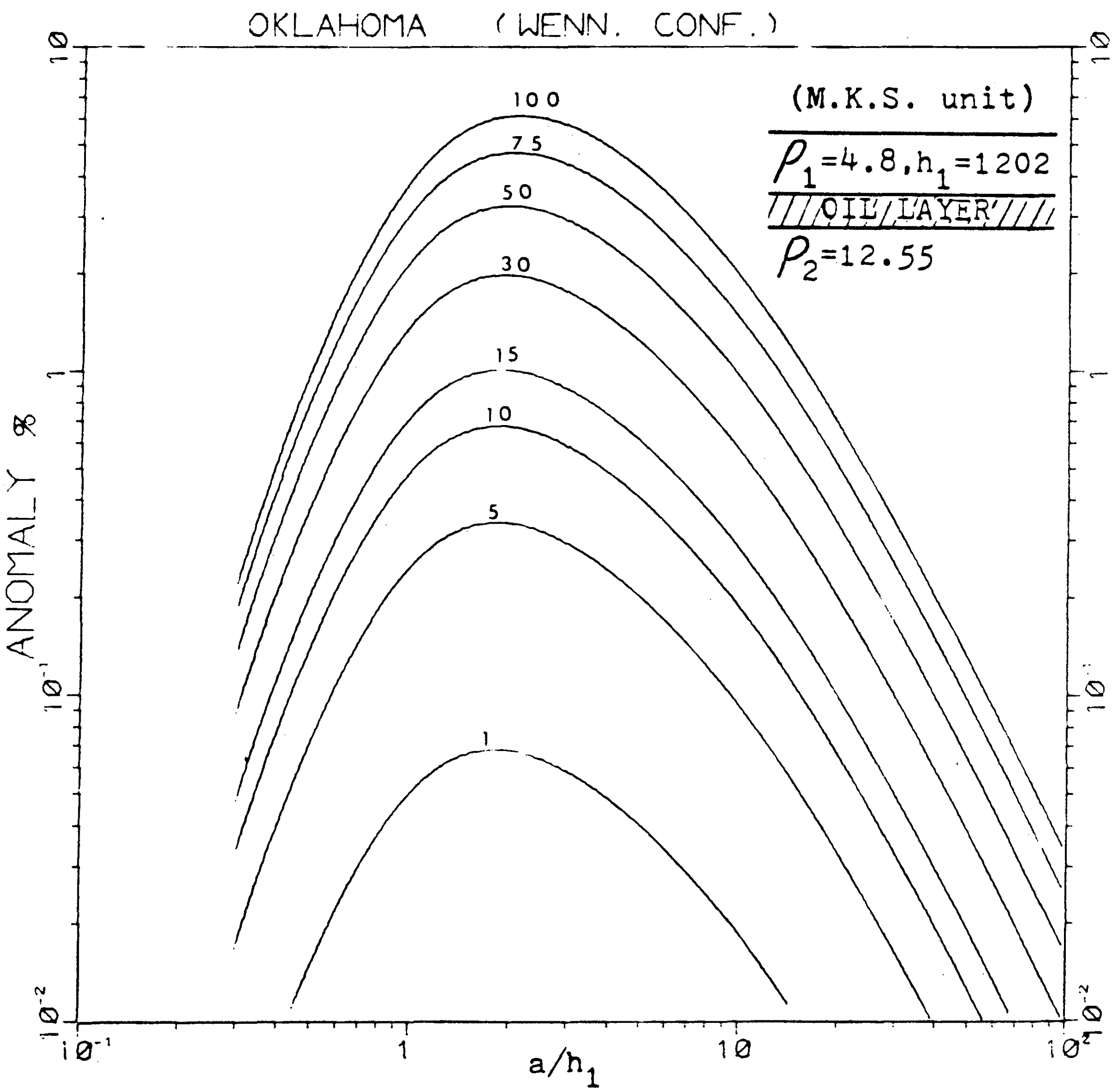

Figure 35 Plot of maximum anomaly for varying Transverse Resistance Contrast ($T_{oil}/T_{over.}$).

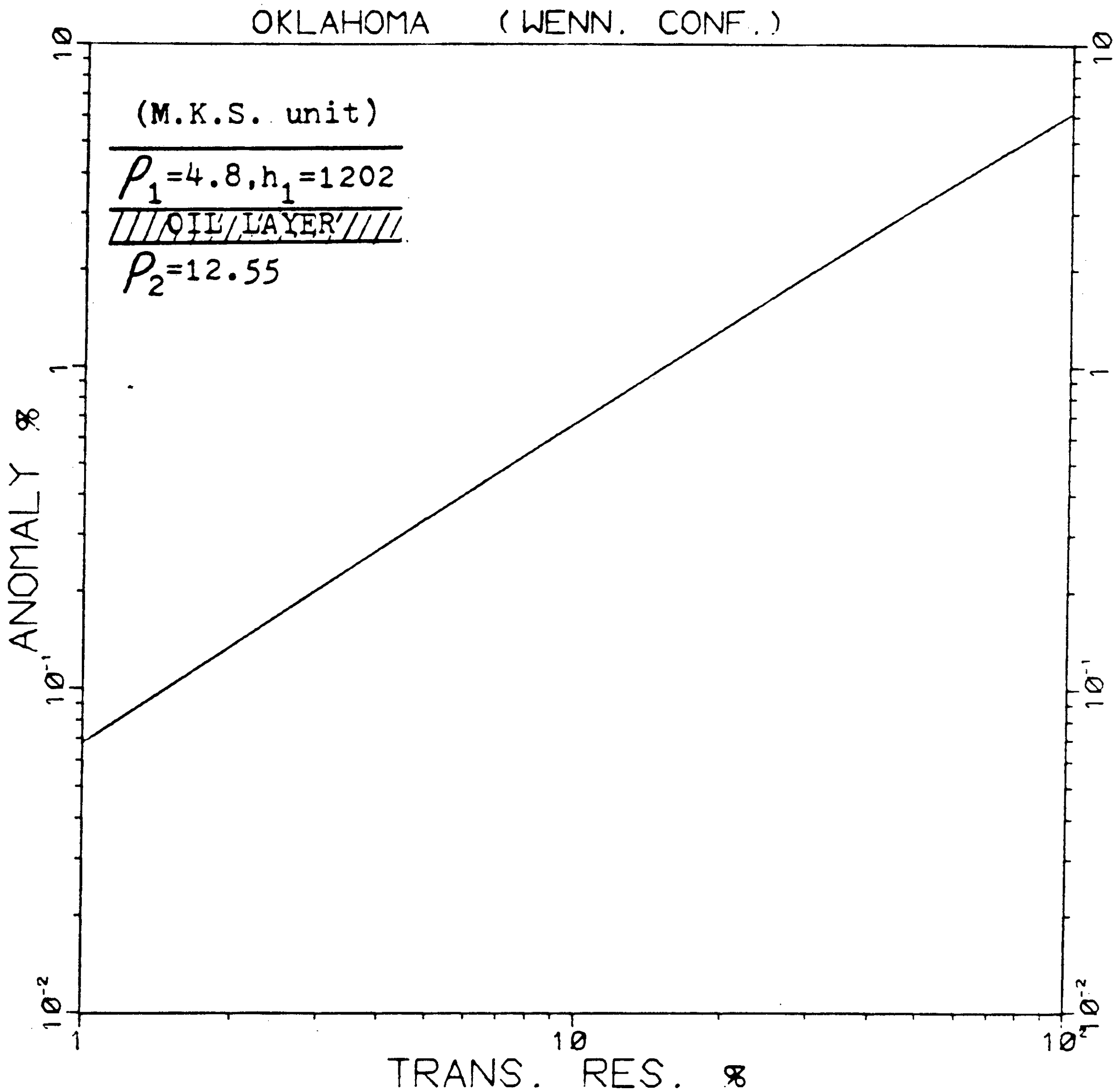

Figure 36 Anomaly plot for varying Transverse Resistance Contrast($T_{oil}/T_{over.}$) in %.

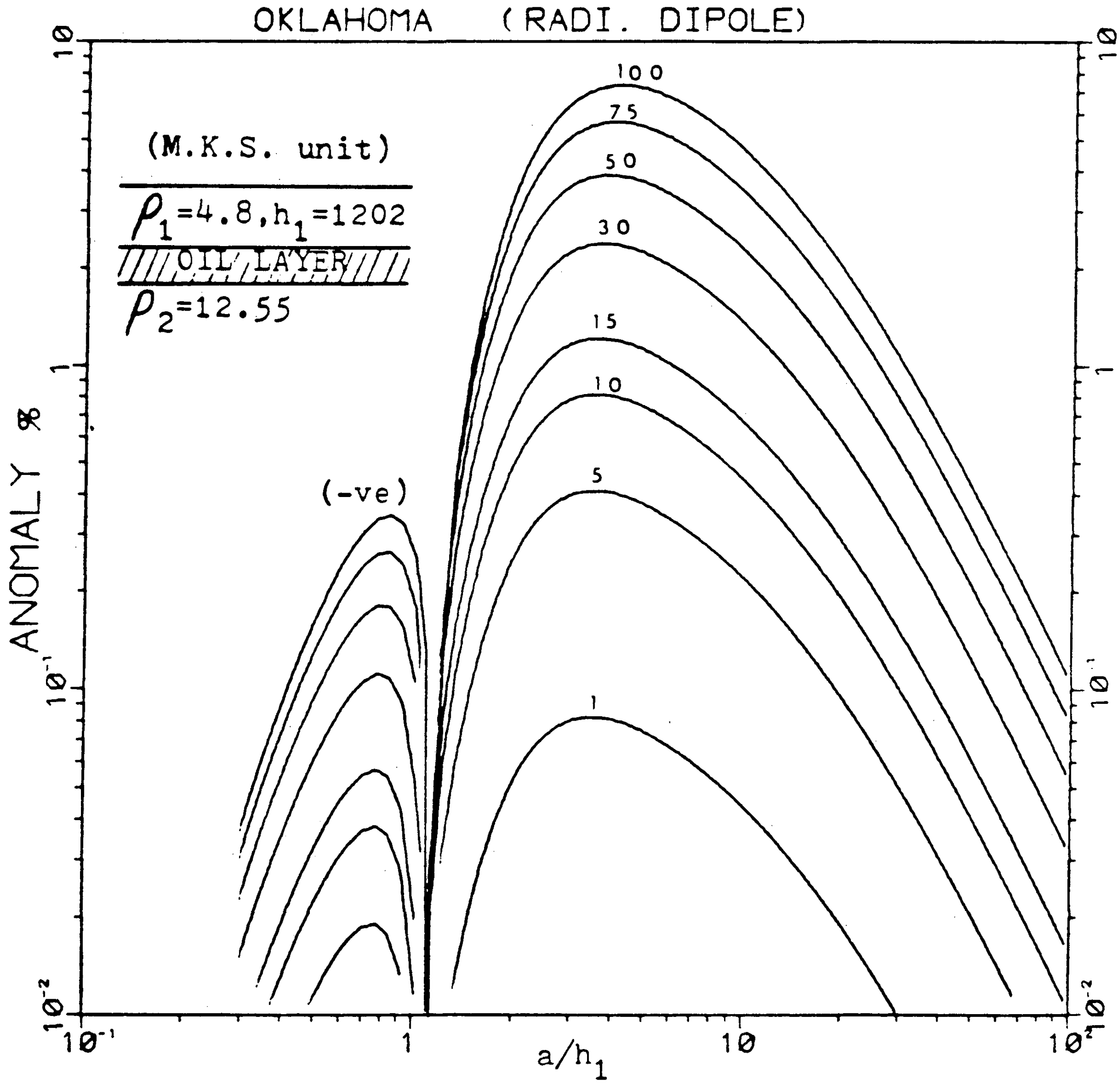

Figure 37 Plot of maximum anomaly for varying Transverse Resistance Contrast ($T_{oil}/T_{over.}$).

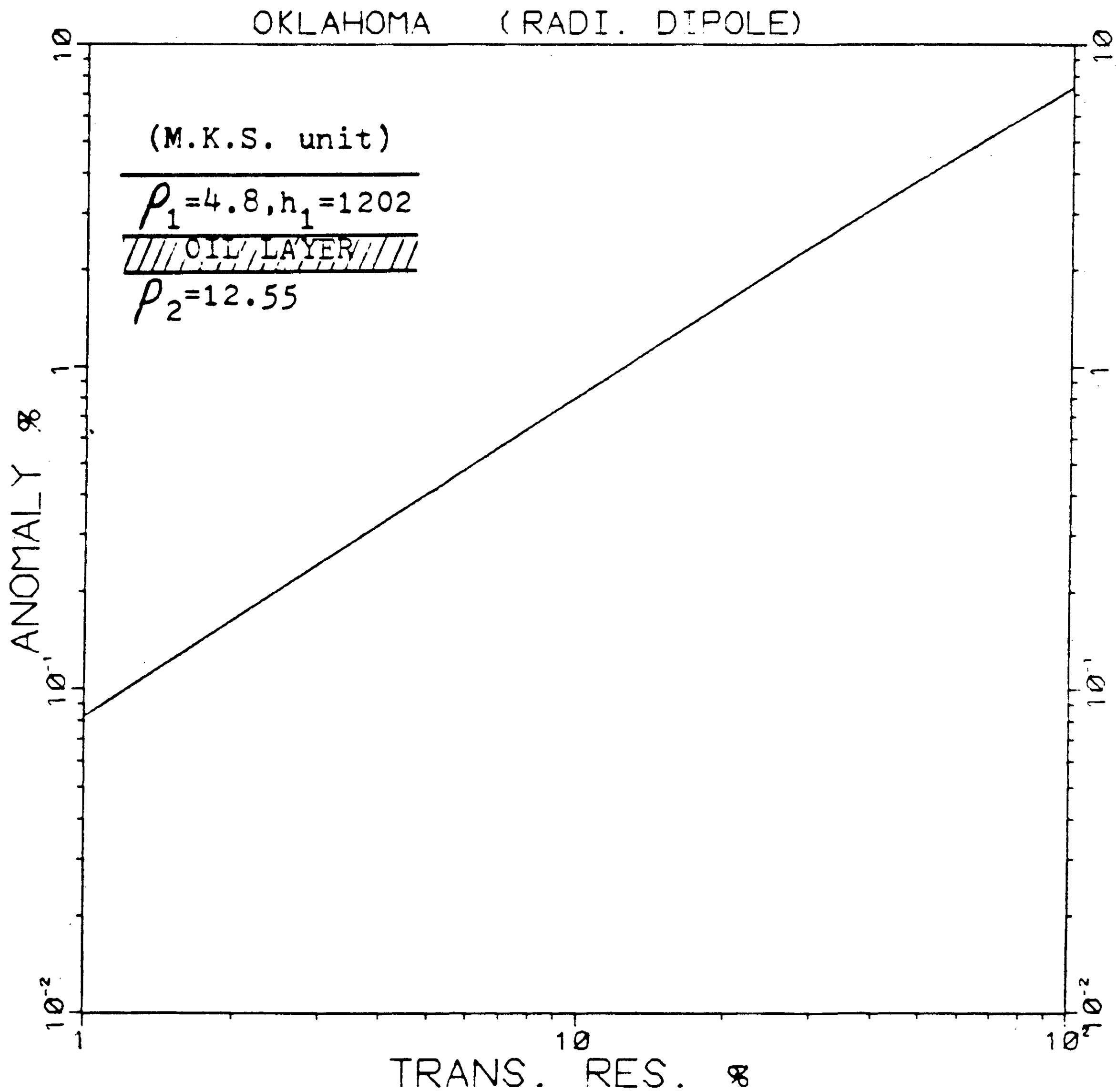

Figure 38 Anomaly plot for varying Transverse Resistance Contrast($T_{oil}/T_{over.}$) in %.

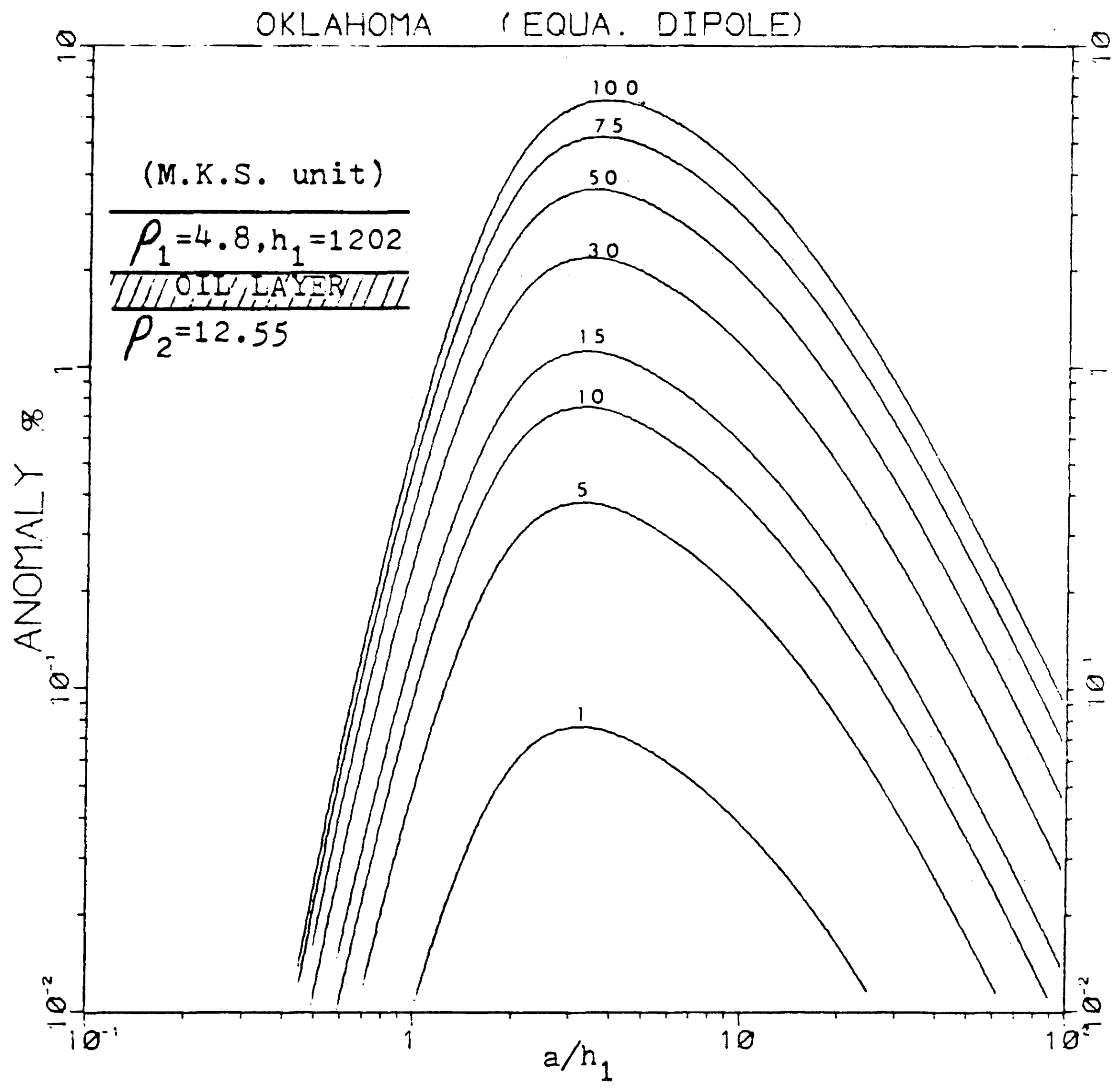

Figure 39 Plot of maximum anomaly for varying Transverse Resistance Contrast ($T_{oil}/T_{over.}$).

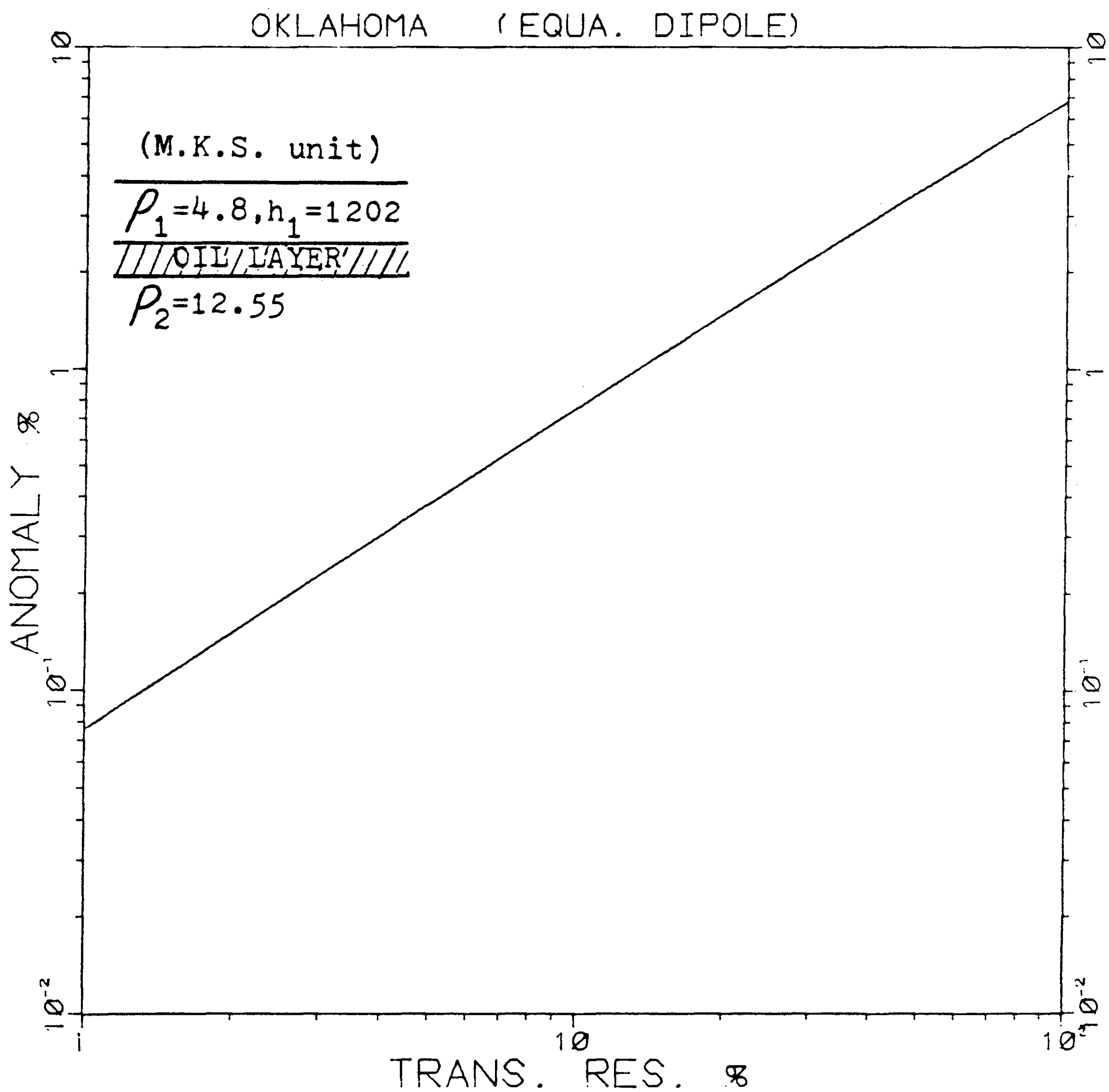

the case of the Schlumberger array than for the Wenner array. For the radial and equatorial dipole arrays, it is higher than for the other two arrays. It is maximum for the radial-dipole array, compared to the rest of the three arrays and is about 0.083 and 7.3%, respectively for the same T values, which is about 118 and 116% of the Schlumberger array anomaly for T = 1 and 100%, respectively, and about 108% for both T values of equatorial-dipole anomaly. From an overall review, again, the radial-dipole gives the best results. However, in this type of environment, the maximum anomaly value is less than 10%, while in the environment corresponding to Kern County, California, it was about 110% for the same T value.

Anomaly Due to the Presence of Actual Oil-Layer:

For well-log #5, a possible oil-gas-saturated bed of about 3.05 m thickness is demarcated at a depth of 1319 m; it has an average longitudinal resistivity of 20.66 ohm-m, which gives a transverse resistance of 62.97 ohm. As the above anomaly curves were computed assuming that the oil-layer is embedded between layer one and two, again, the same model was assumed; however, this time, actual transverse resistance value corresponding to the oil-layer was used, which gives a transverse resistance contrast ratio 1.09% of oil-layer to the first layer. Again if we assume the resistivity of oil-layer $10\rho_1$, it reduces the oil-layer thickness to 1.31 m. The final model is as below:

$$\rho_1 = 4.8 \text{ ohm-m}, \; h_1 = 1202 \text{ m}$$
$$\rho_o = 48 \text{ ohm-m}, \; h_o = 1.31 \text{ m}$$
and $\rho_2 = 12.55$ ohm-m

The anomaly curves were computed for all four DC arrays and are shown in Figures 40, 41, 42, and 43. Again, the maximum anomaly corresponded to the radial-dipole array and is about 0.092%. Again, it also shows negative anomaly with a maximum value is 0.004% for the same array. Again, as the transverse resistance contrast is only 1.09%, the above field is not of practical interest. However, if this field were to appear in the California geoelectrical environment, it could have given more than the 1% anomaly; in the present environment it is less than 0.1%.

Figure 40 Anomaly plot over possible oil/gas layer picked-up from well-log # 5.

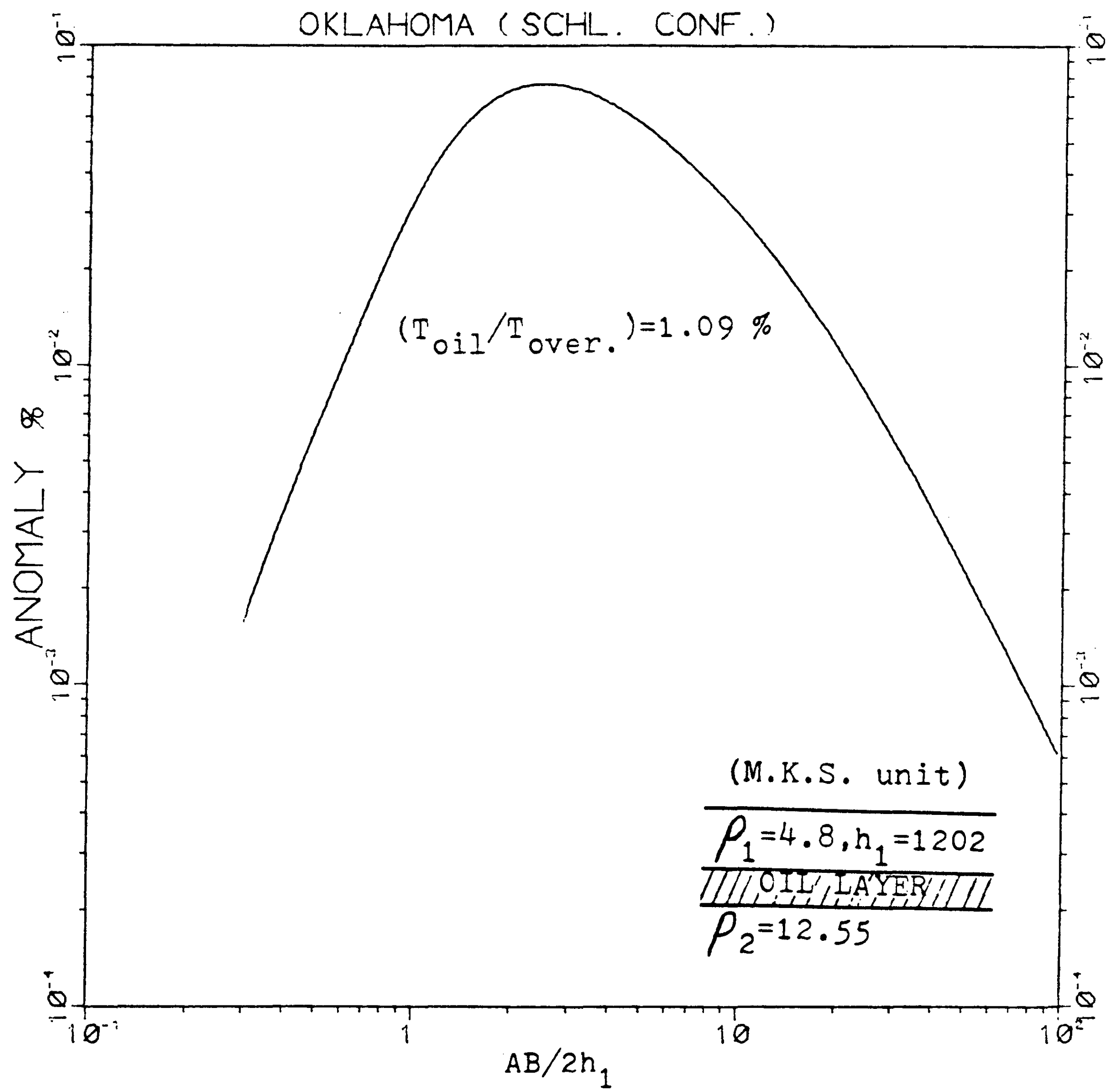

Figure 41 Anomaly plot over possible oil/gas layer picked-up from well-log # 5.

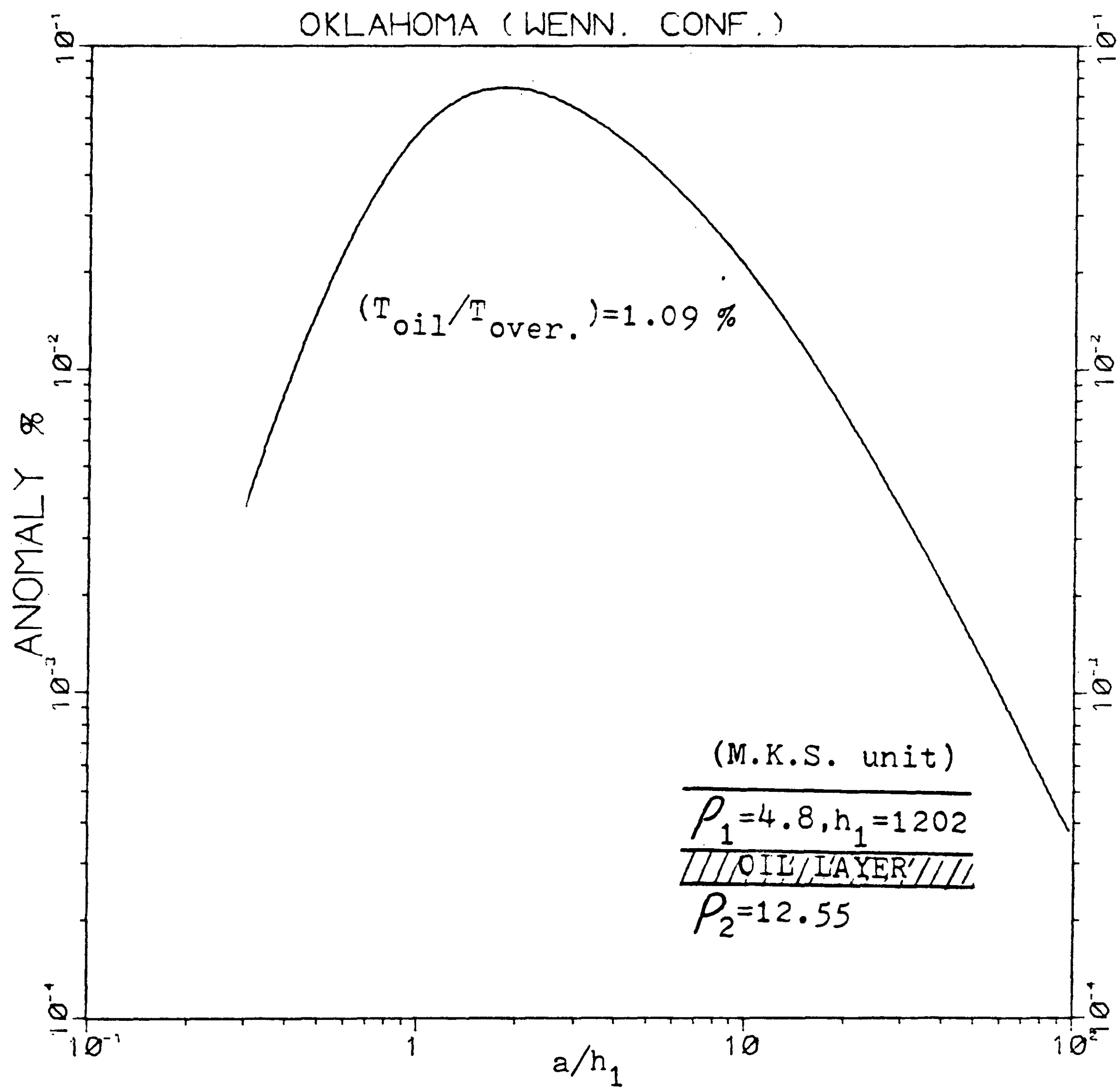

Figure 42 Anomaly plot over possible oil/gas layer picked-up from well-log # 5.

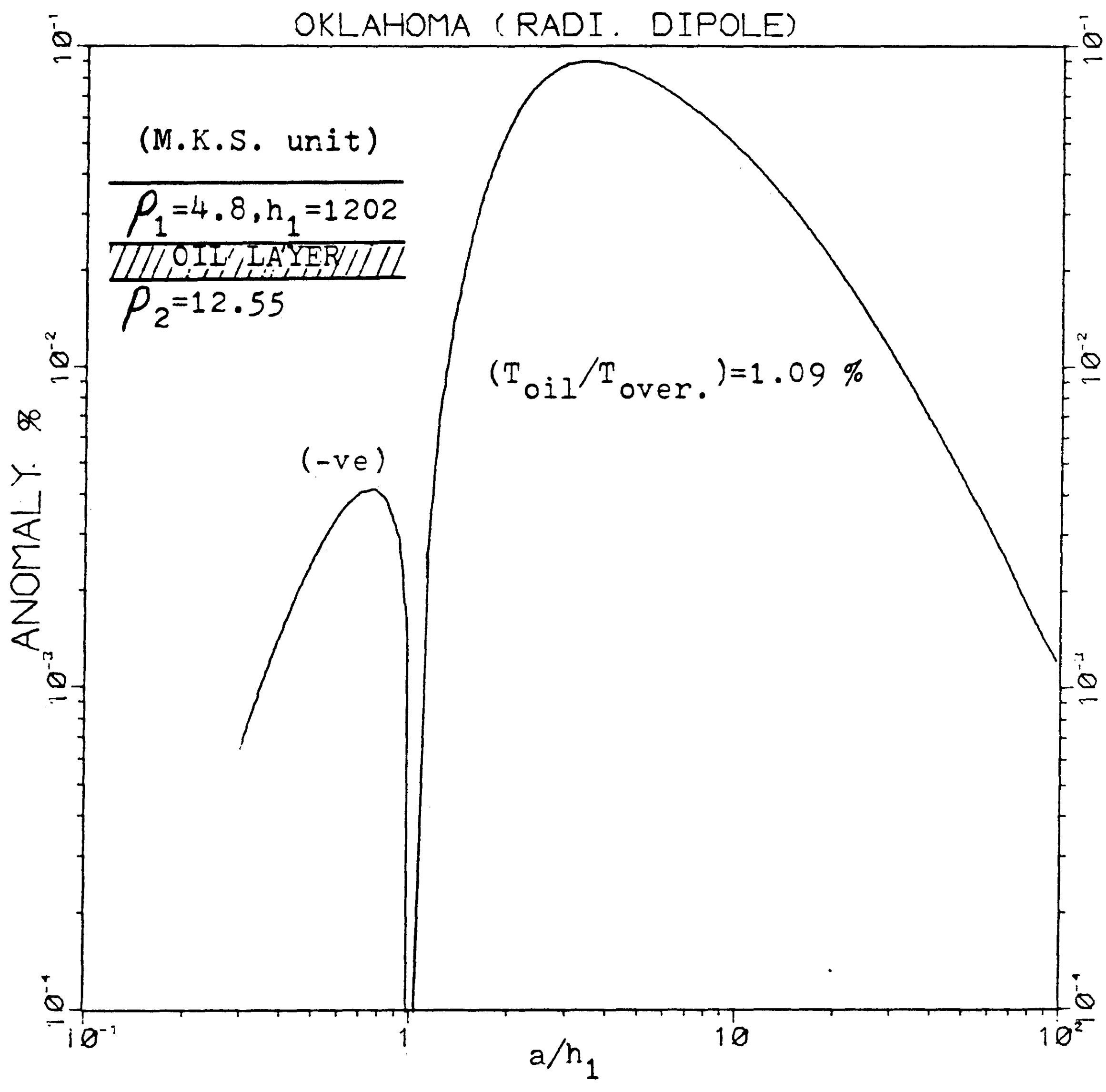

Figure 43 Anomaly plot over possible oil/gas layer picked-up from well-log # 5.

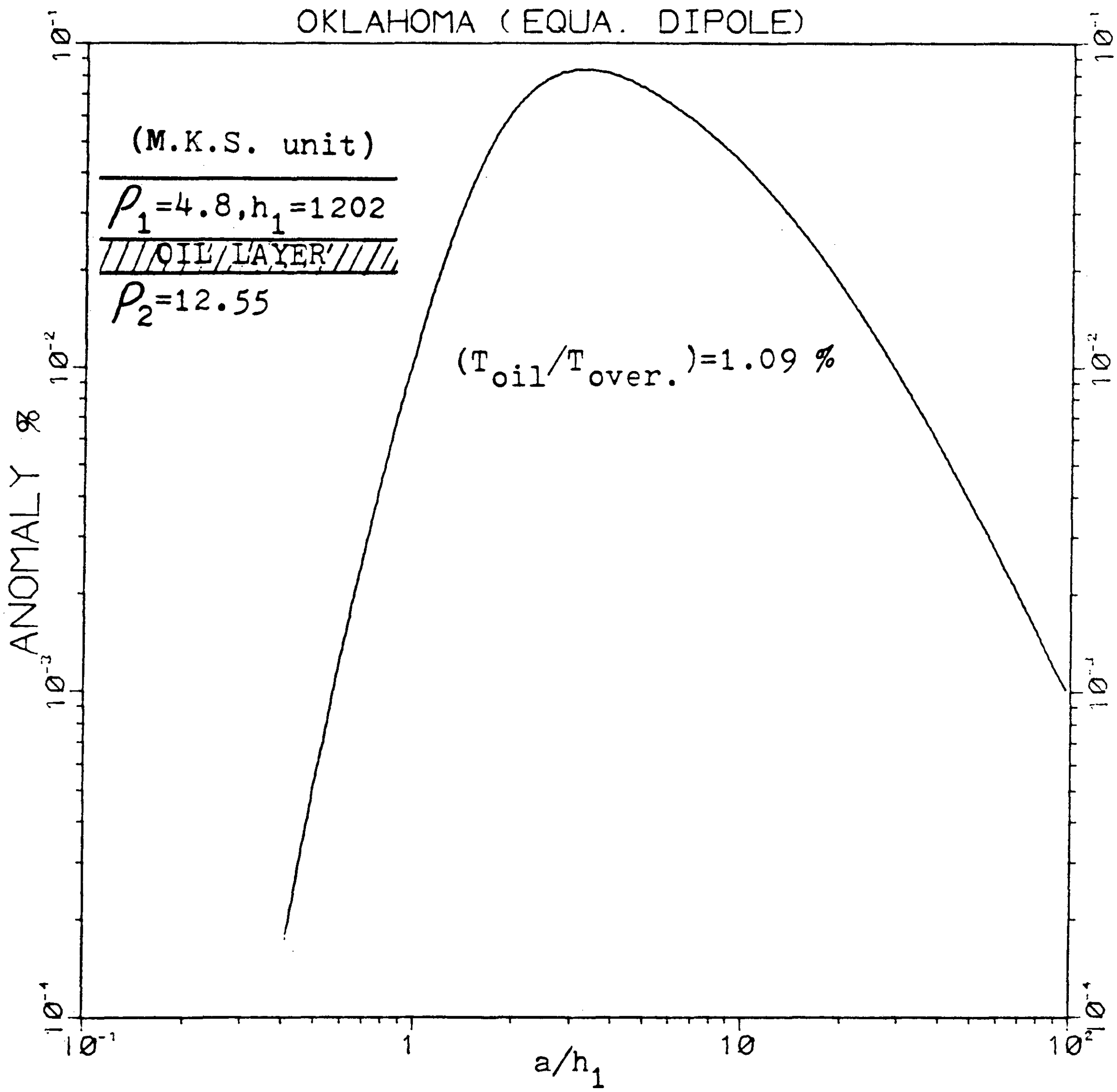

LANCE CREEK FIELD, WYOMING

From the well-logs, three units are recognizable; their average longitudinal resistivities and thicknesses are as follows:

$$\rho_1 = 4.24 \text{ ohm-m}, \; h_1 = 1063 \text{ m}$$
$$\rho_2 = 9.88 \text{ ohm-m}, \; h_2 = 274 \text{ m}$$
$$\text{and } \rho_3 = 56.22 \text{ ohm-m}$$

which correspond to the category of an A-type curve. The average transverse and longitudinal resistivities and coefficient of anisotropy for individual well-logs are tabulated in Appendix 3. The coefficient of anisotropy for unit one is low, about 6%, except for well-logs #4, 5, and 20, where it is about 15%. For the second and third units, it is generally below 40%; sometimes it rises to 50-60%. The high values are probably due to the presence of resistive units, such as limestone, anhydrite, etc. The minimum and maximum depth available from well-logs are 52 and 3353 m, respectively. Actually, the maximum depth available from well-logs, except well #5, is 1676 m. The integral resistivity plot for well #5 is different in character compared to the other integral plots in the same area. However, as we are interested in the average behavior of the resistivity in the overall area, only the first three units were considered from this plot for calculating average geoelectrical parameters. If we compare the average geoelectrical parameters of this area with those for the Oklahoma area, the first unit is much the same. Also, the second unit matches well with the second unit in the Oklahoma area. However, in the Wyoming area, we observe one more unit which has a high resistivity (56 ohm-m).

The average longitudinal resistivity contours are shown in Figures 44, 45, and 46 for all three units. The contours for the first unit show sudden changes in resistivity values in the central part of the area. The average resistivity value in the east and extreme S-W is about 3 ohm-m, while in the rest of the area, it is about 5 ohm-m. Resistivity contours corresponding to the second unit are smooth, except for one or two local patches in the NE. The resistivity value to the west is high, being about 11-15 ohm-m, while in the rest of the area, it is about 7-9 ohm-m. The third unit, shows high resistivity in the west. But this time, in the far NE quadrant, it shows an increasing trend in resistivity while in the second unit, there is a decreasing trend.

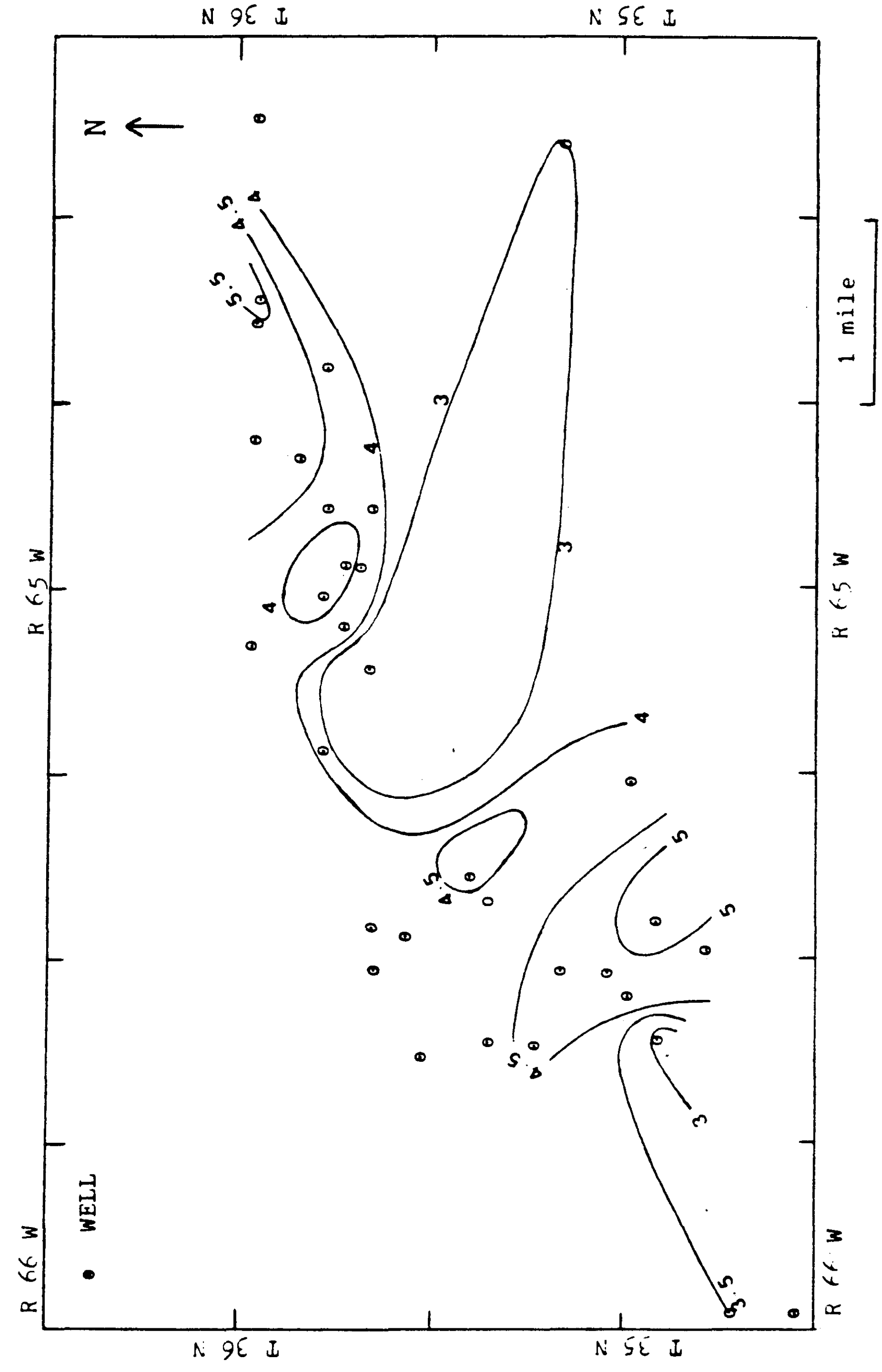

Figure 4.4 Average Longitudinal Resistivity Contours in ohm-m., First-unit, Wyoming.

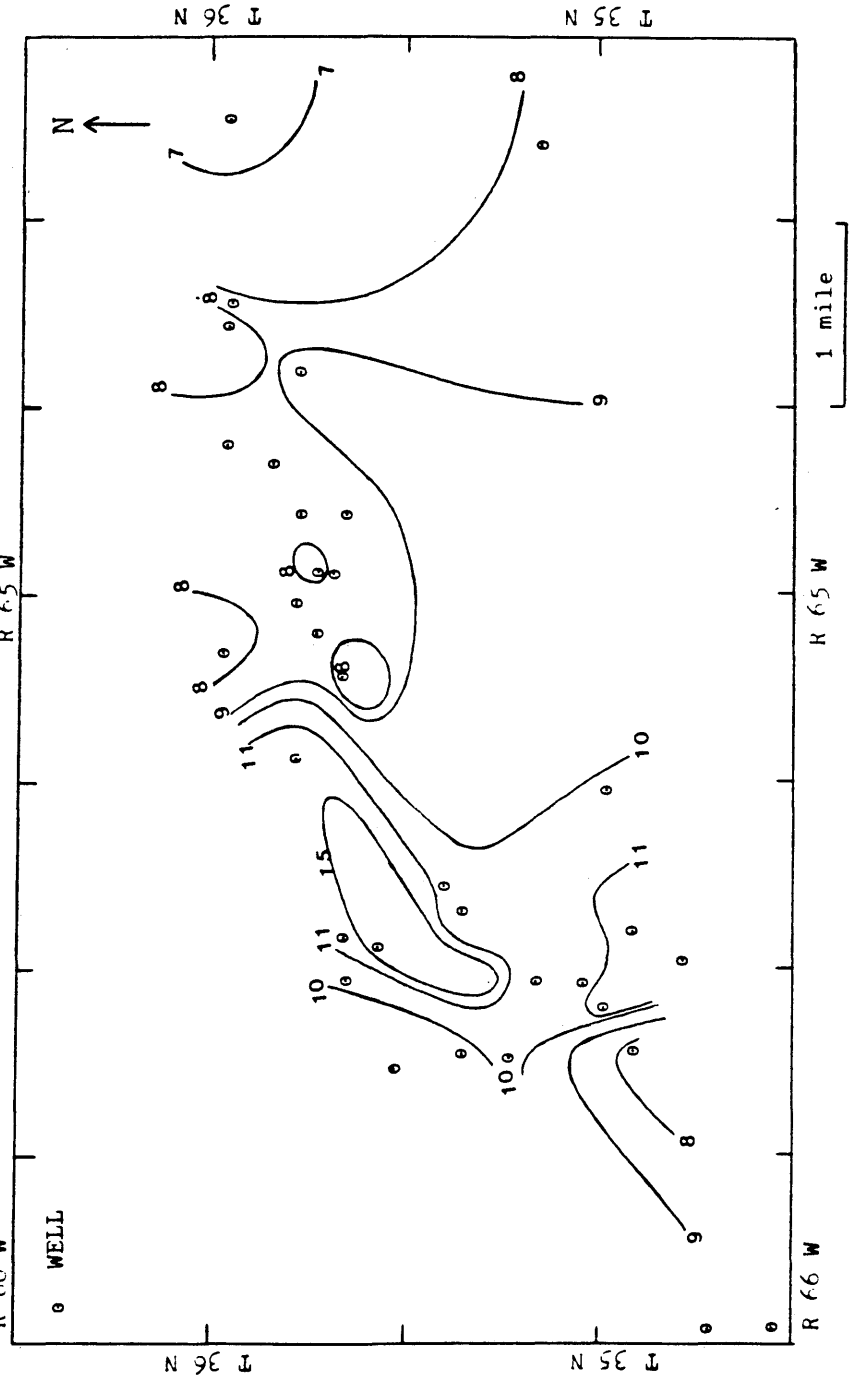

Figure 4.5 Average Longitudinal Resistivity Contours in ohm- m., Second-unit, Wyoming.

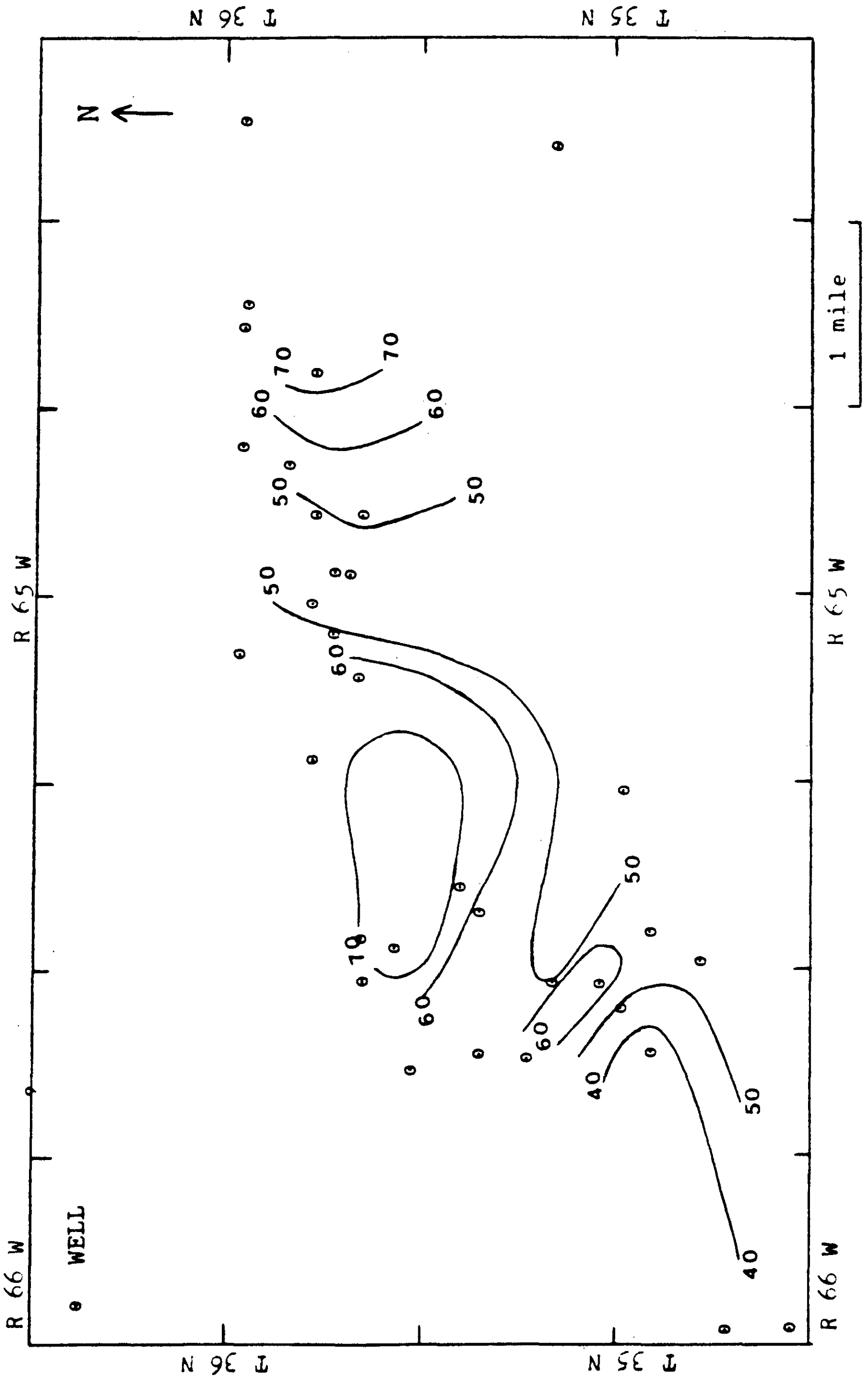

Figure 46 Average Longitudinal Resistivity Contours in ohm- m., Third-unit, Wyoming.

The apparent resistivity and anomaly curves for all four DC arrays are shown in Figures 47, 48, 49, 50, 51, 53, 55, and 57 with the same assumptions and using the same computing technique as before. The maximum anomaly vs. transverse resistance contrast curves are shown in Figures 52, 54, 56, and 58. Again, the radial-dipole array gives the best anomaly values. However, this time all arrays show a negative anomaly for large separations and the radial-dipole array shows negative anomalies for both small and large separations. The maximum anomaly for the radial-dipole array is less than 2% for T = 100%. For T = 1%, it is only 0.023%. The results are not encouraging and it seems difficult to detect an oil-layer in such an environment.

Figure 47 Apparent Resistivity Plot.

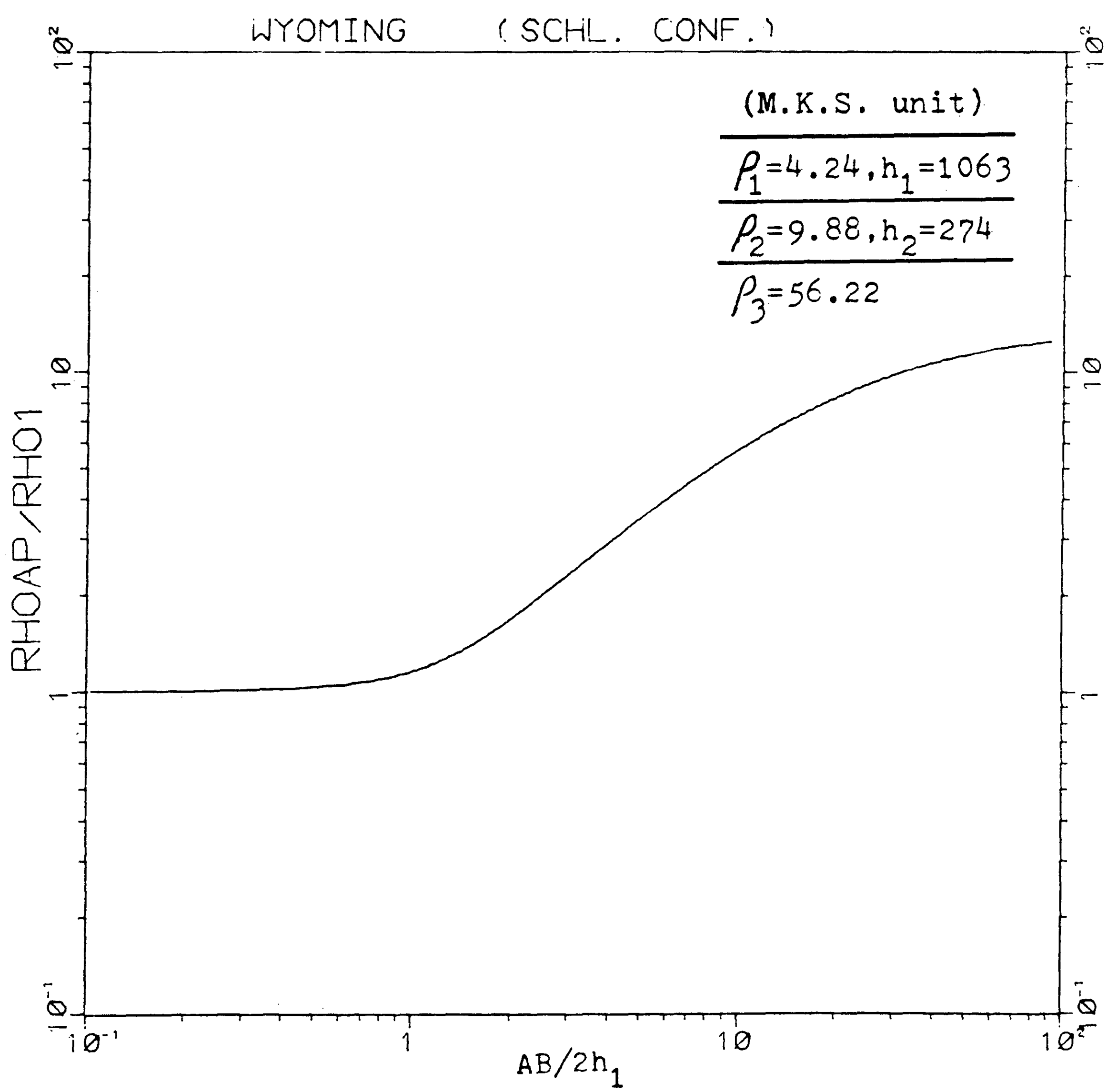

Figure 48 Apparent Resistivity Plot.

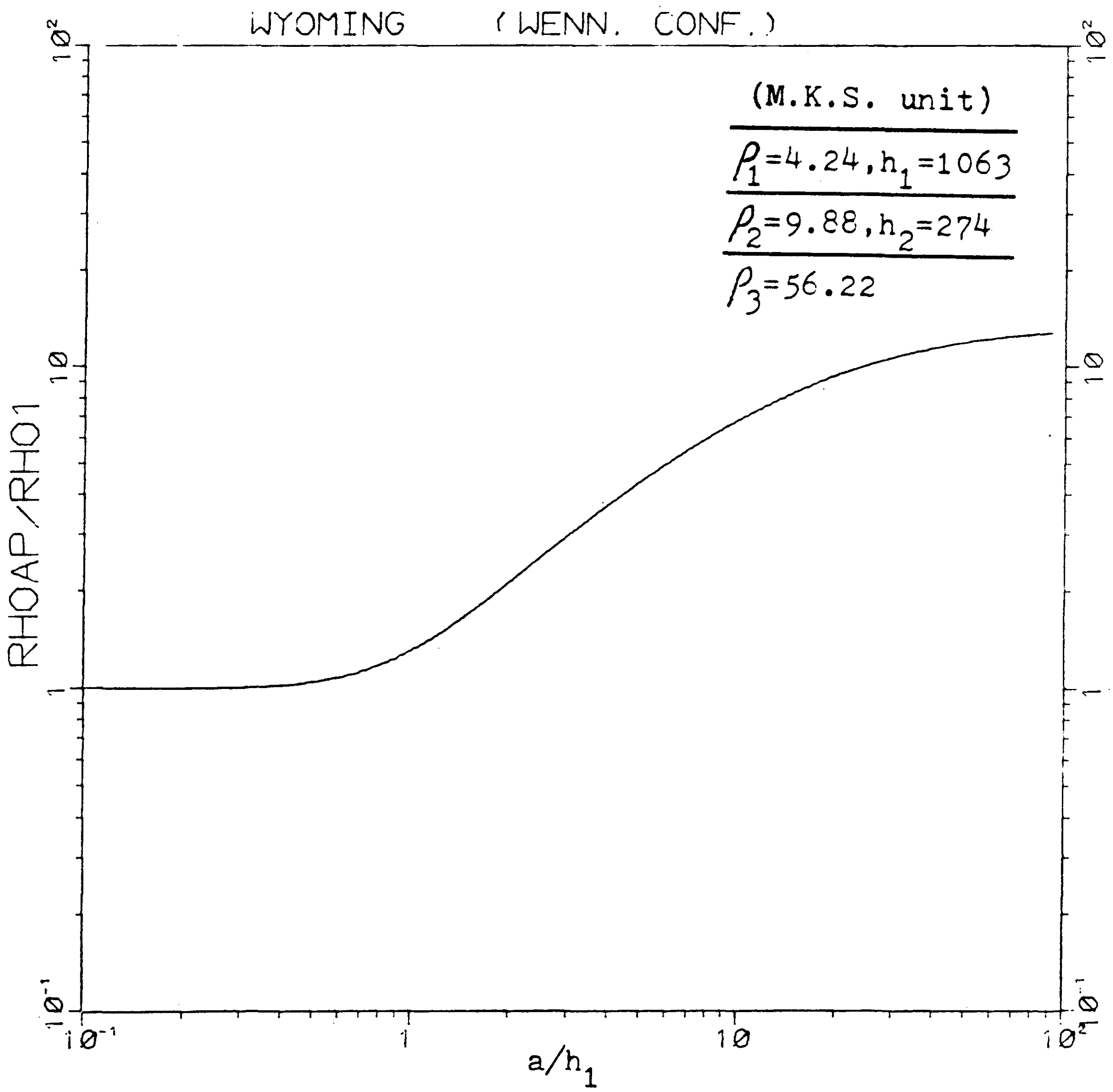

Figure 49 Apparent Resistivity Plot.

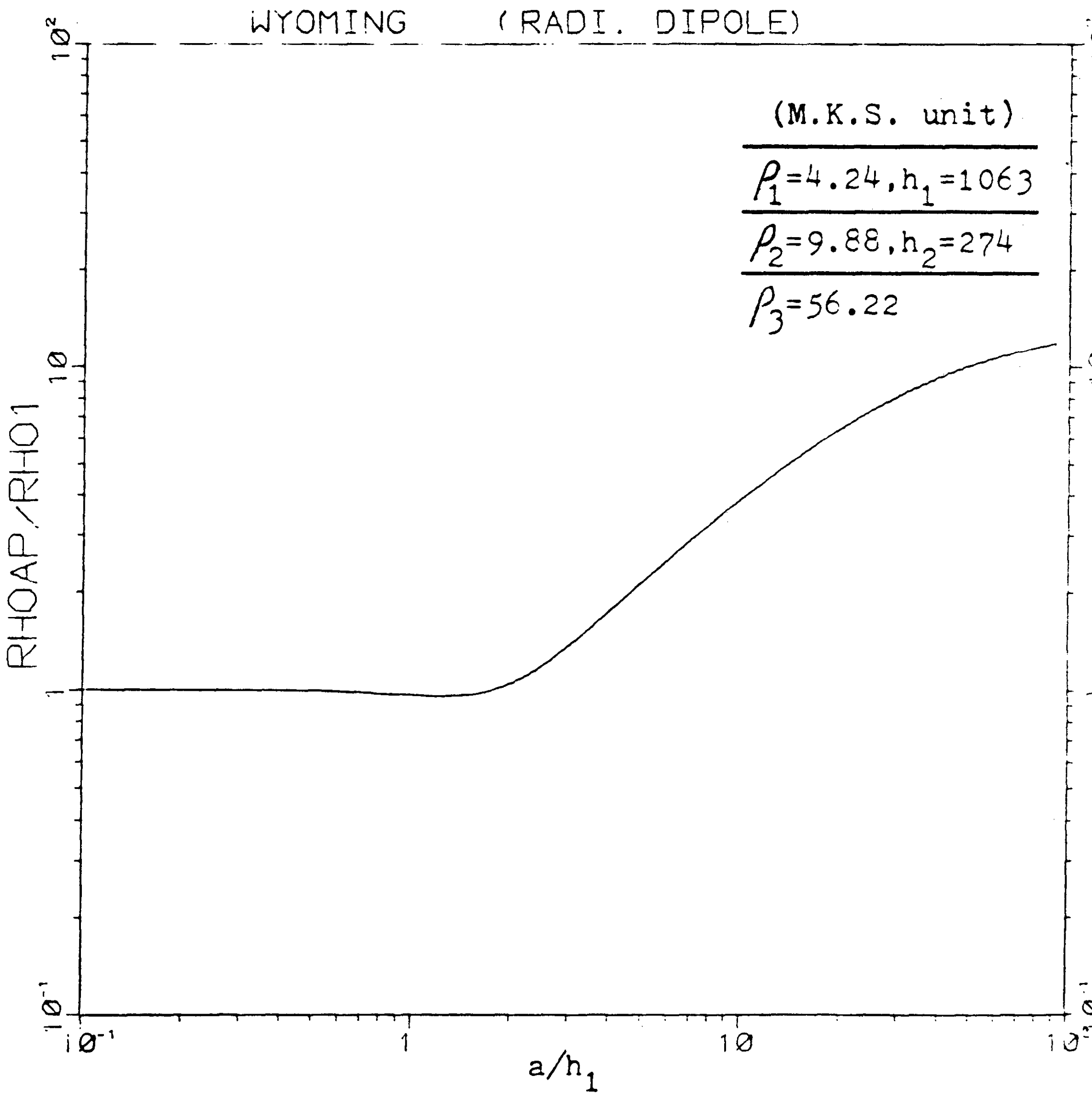

Figure 50 Apparent Resistivity Plot.

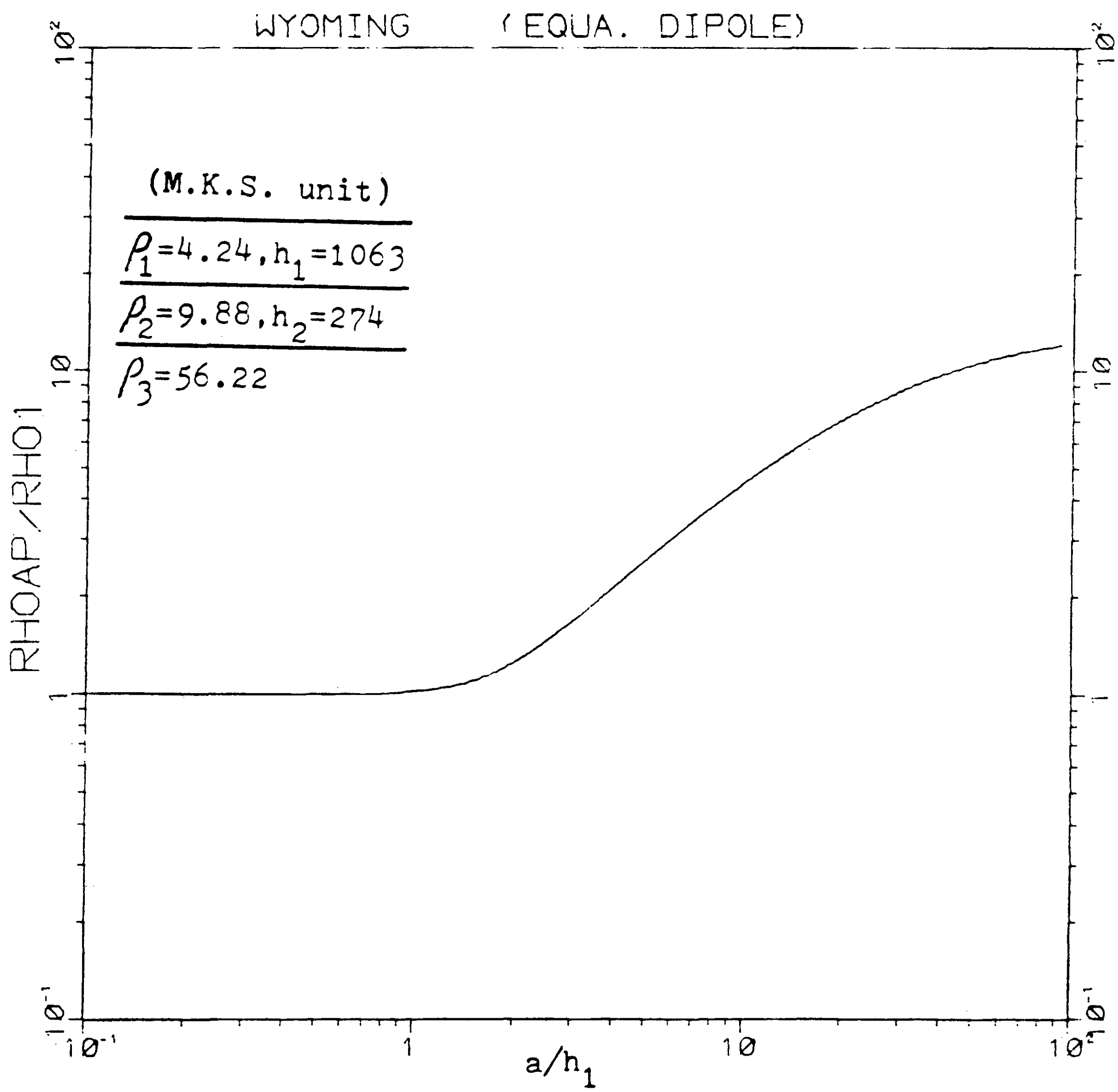

Figure 51 Anomaly plot for varying Transverse Resistance Contrast($T_{oil}/T_{over.}$) in %.

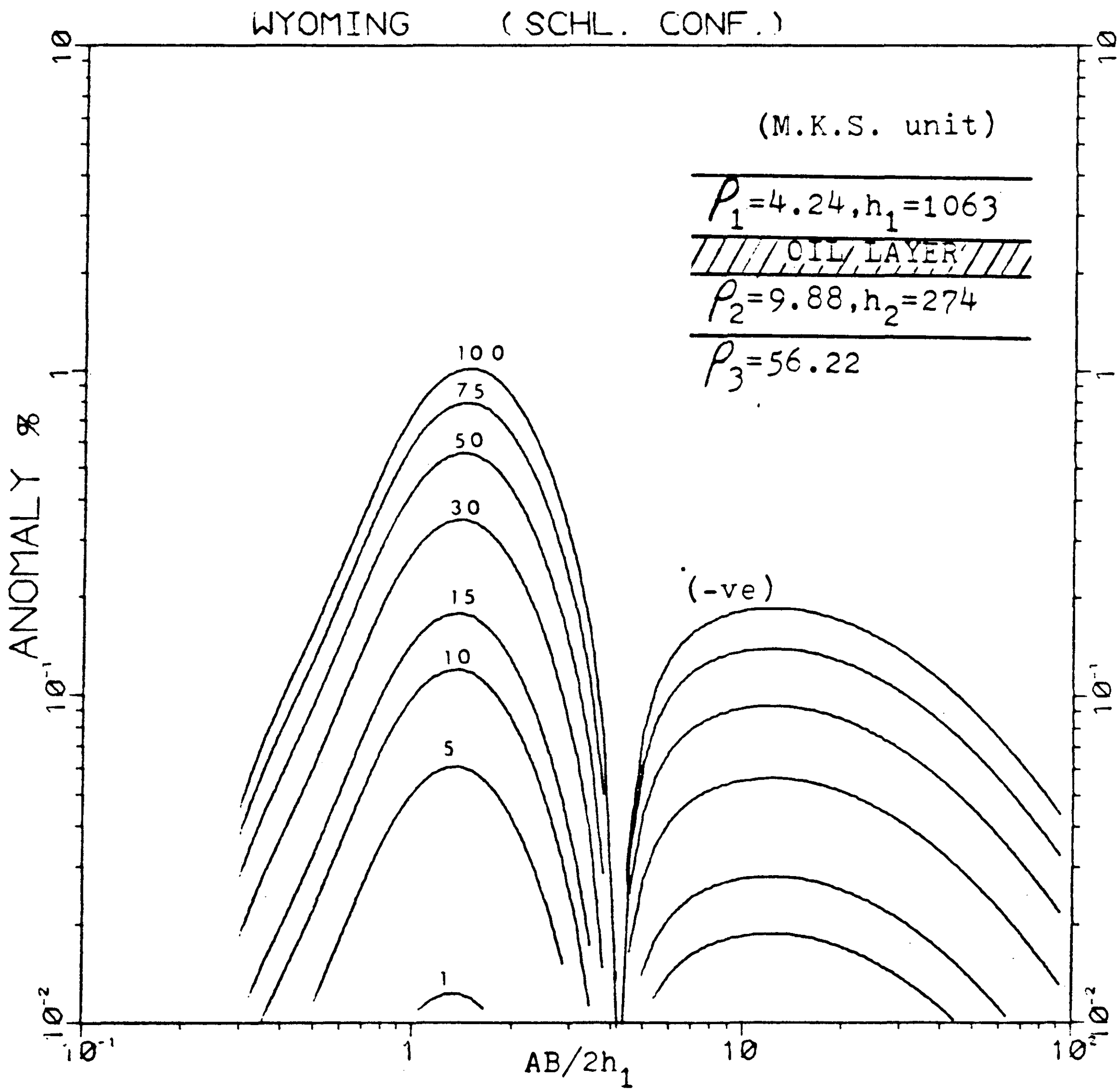

Figure 52 Plot of maximum anomaly for varying Transverse Resistance Contrast ($T_{oil}/T_{over.}$).

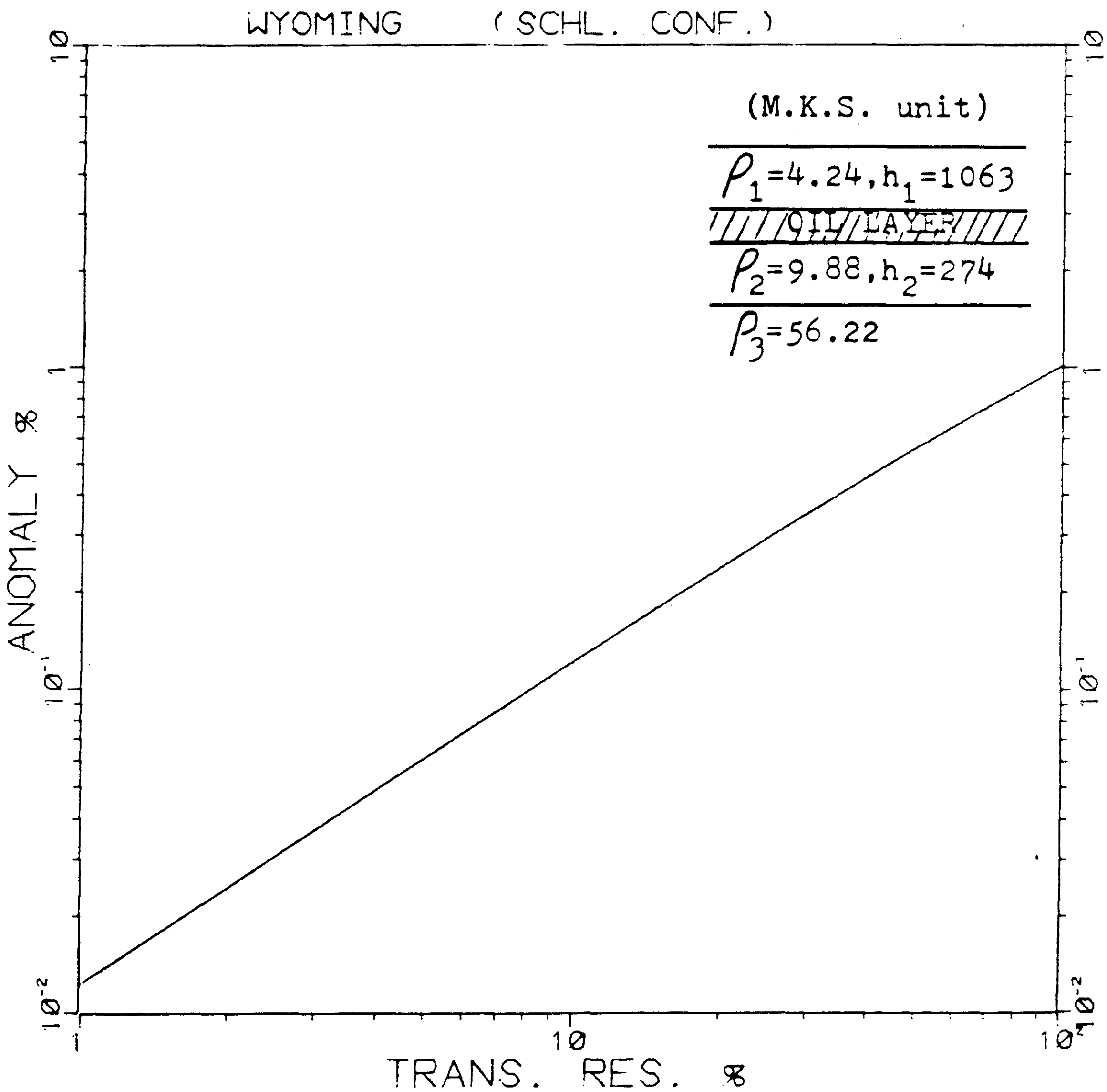

Figure 53 Anomaly plot for varying Transverse Resistance Contrast($T_{oil}/T_{over.}$) in %.

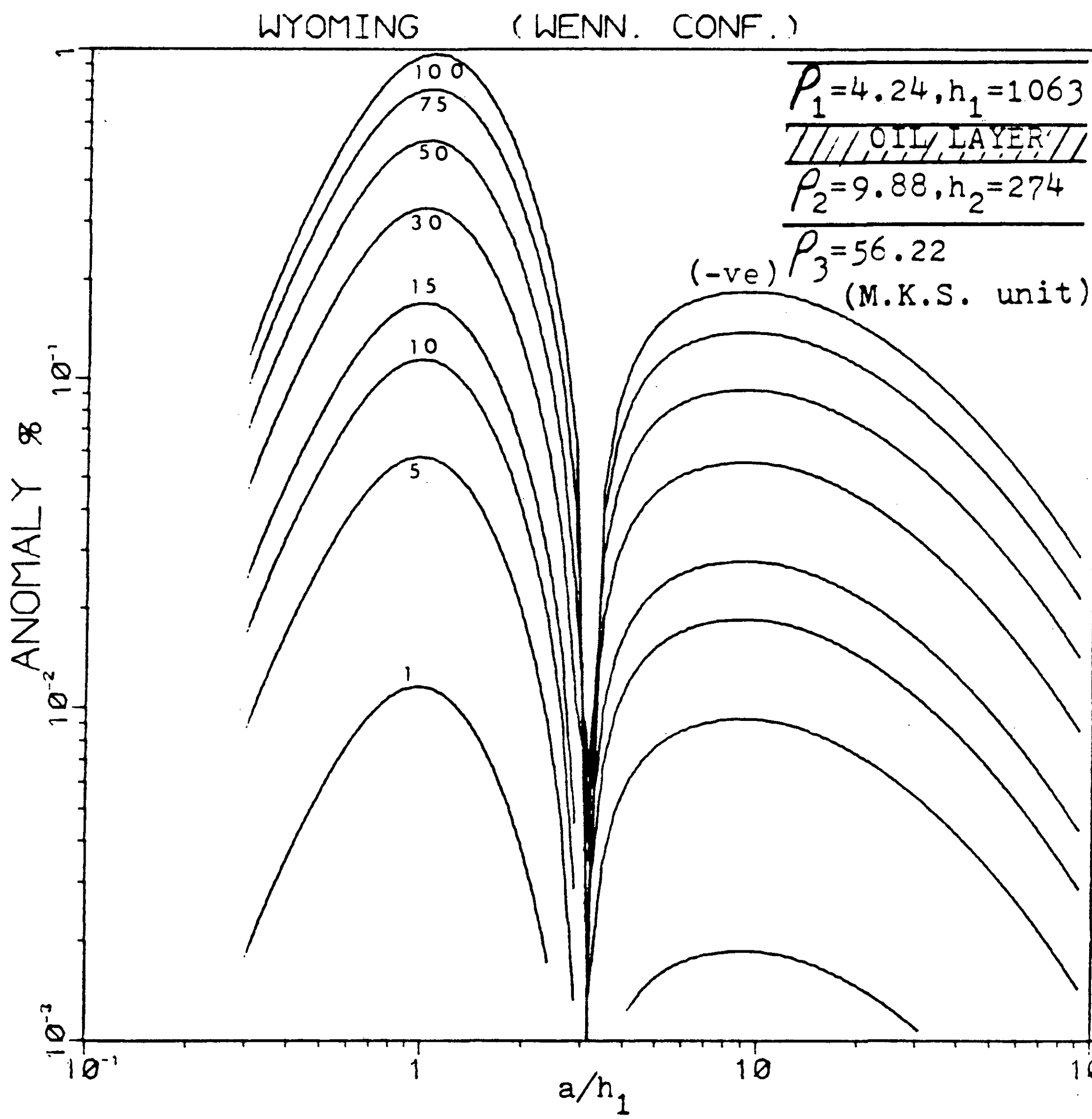

Figure 54 Plot of maximum anomaly for varying Transverse Resistance Contrast ($T_{oil}/T_{over.}$).

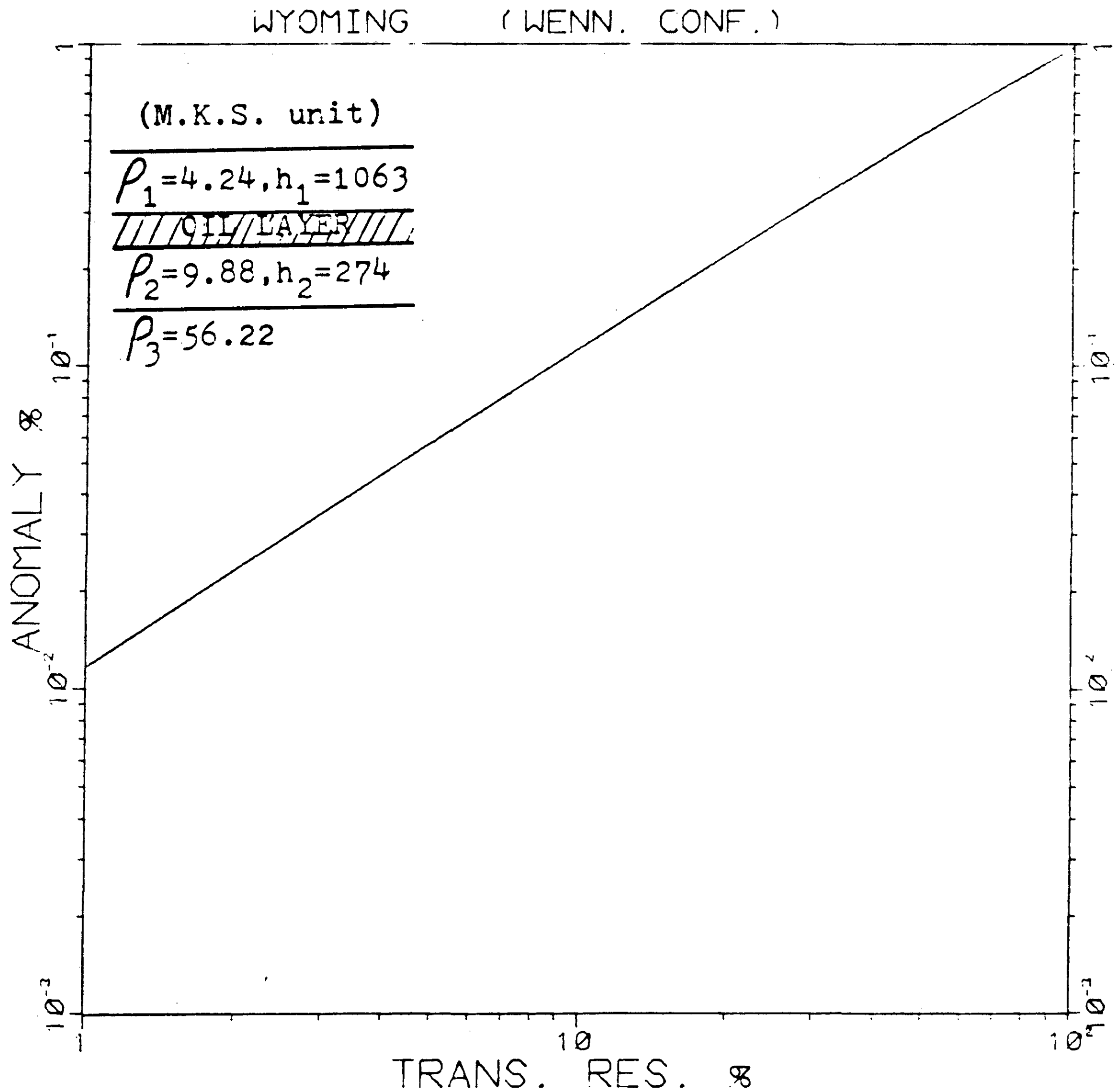

Figure 55 Anomaly plot for varying Transverse Resistance Contrast($T_{oil}/T_{over.}$) in %.

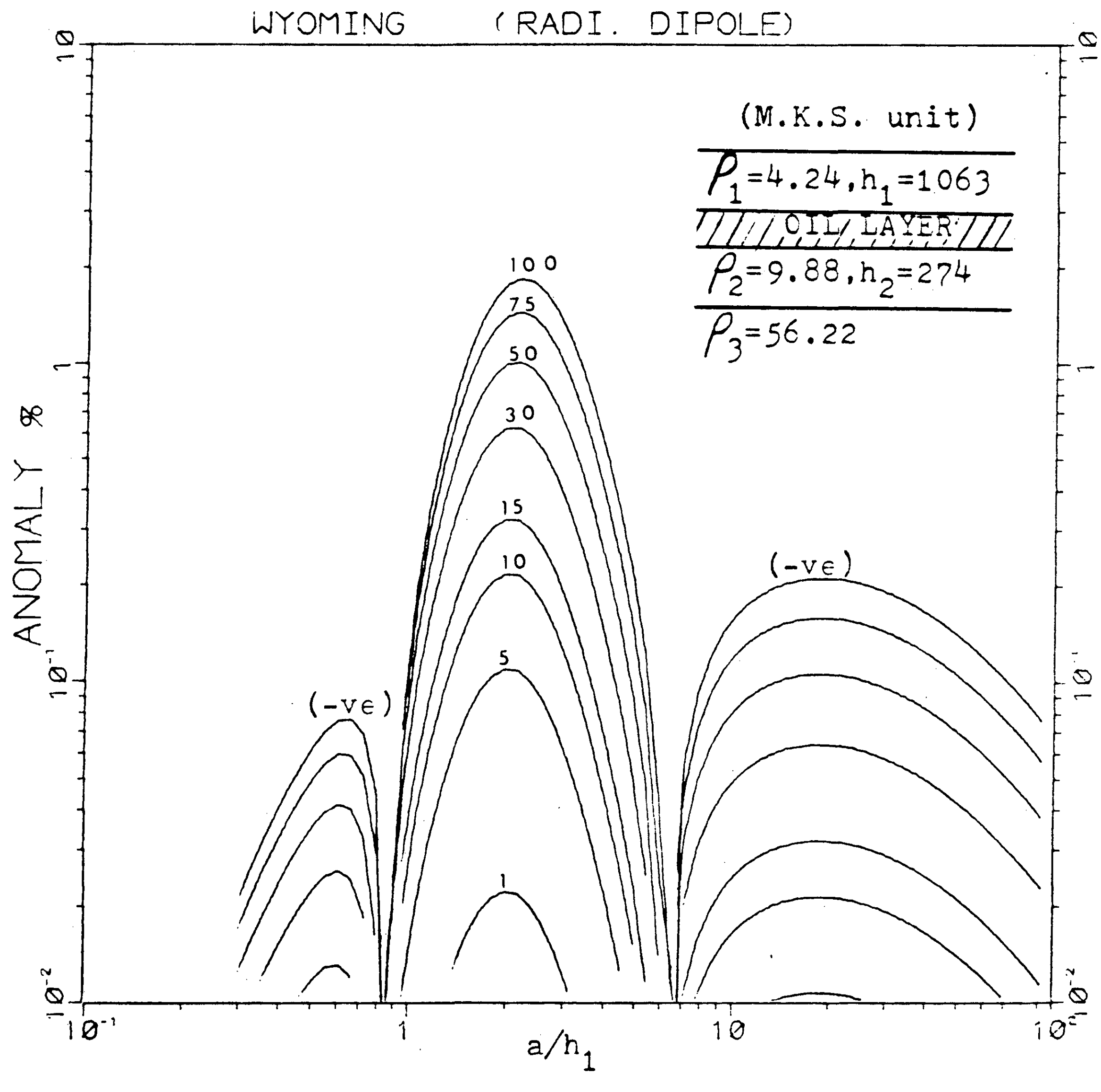

Figure 56 Plot of maximum anomaly for varying Transverse Resistance Contrast ($T_{oil}/T_{over.}$).

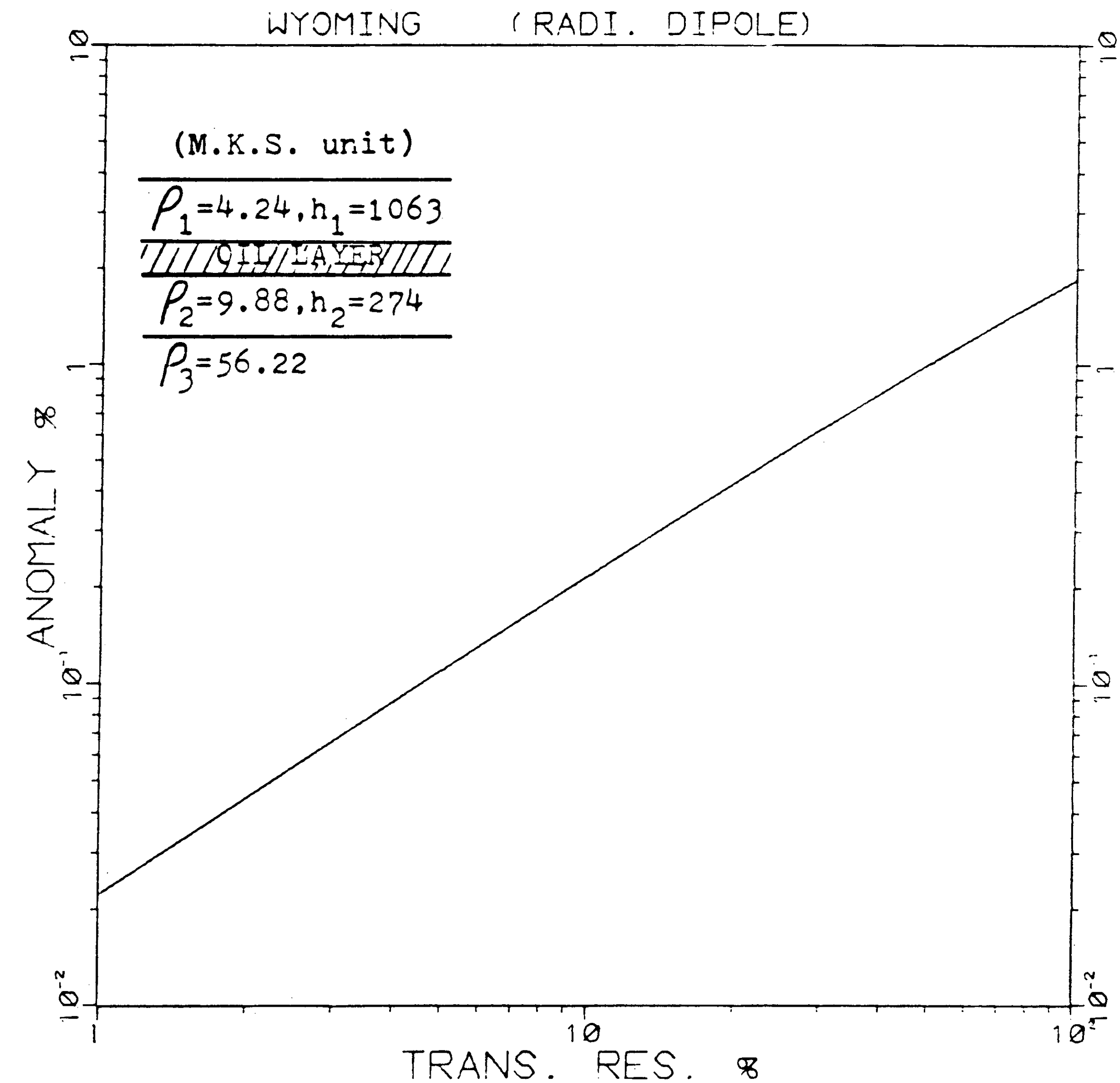

Figure 57 Anomaly plot for varying Transverse Resistance Contrast($T_{oil}/T_{over.}$) in %.

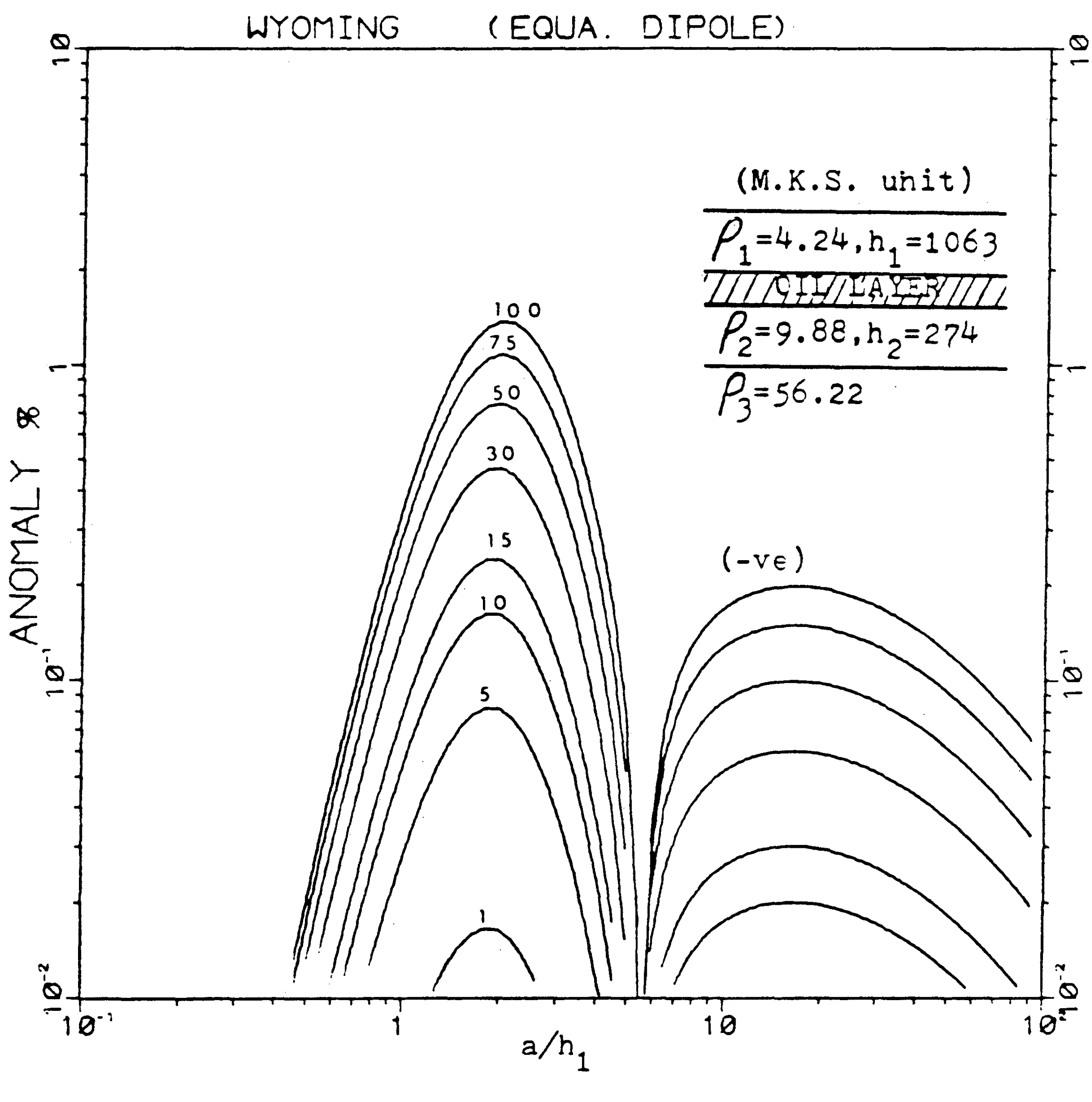

Figure 58 Plot of maximum anomaly for varying Transverse Resistance Contrast ($T_{oil}/T_{over.}$).

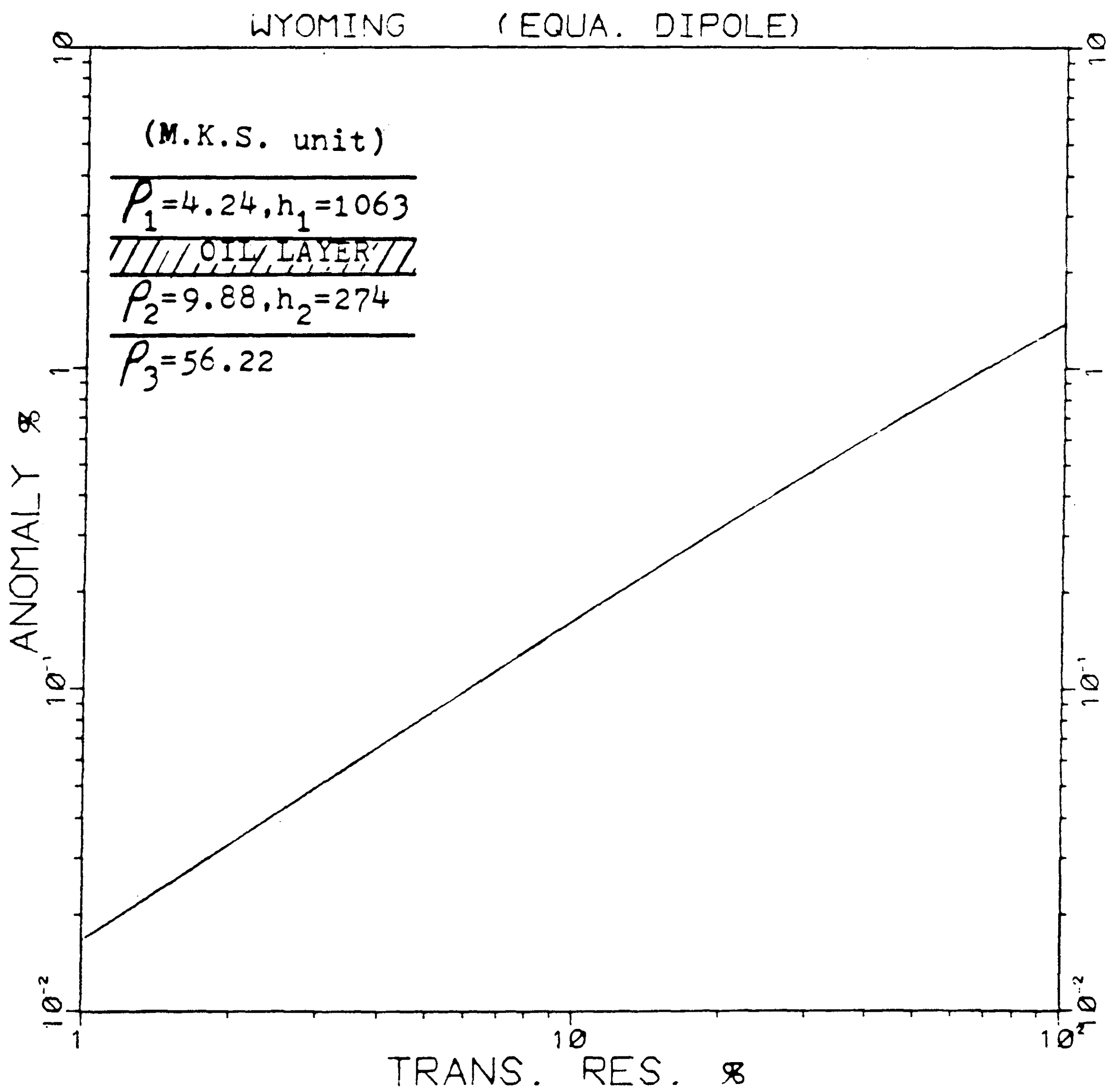

FINITE OIL-LAYER EFFECT OVER ANOMALY

As already mentioned, the previous anomaly curves were computed assuming that the oil-layer is infinite in areal extent. However, in practice, it has a finite areal extent. To have some idea about how the anomaly values differ over a finite oil-layer in comparison with an infinite layer, Whan's computer program (1979) was used. In the first model, it was assumed that the finite oil-layer is buried at a depth of 1,000 m in a half-space with areal extents of 2,000 and 1,600 m in the x and y directions, respectively. The anomaly curves were computed over both infinite and finite oil-layers for the Schlumberger array for transverse resistance contrast (T) between the oil-layer and the overburden of 100 and 1%; the results are plotted in Figure 59. The anomaly over an infinite-layer is about 24 and 0.3% for T = 100 and 1%, respectively. However, for the finite layer it is about 10 and 23% of latter said anomaly, respectively. The anomaly curve for T = 1% over a finite-layer model is not smooth due to numerical errors as the maximum response is smaller than 0.1%. If we increase the size of the finite-layer, the anomaly should increase. The same finite-layer model was assumed with twice the areal extent at the same depth of 1,000 m.
The anomaly curves over infinite and finite layer

Figure 59 Anomaly plot over infinite(IL) & finite oil-layer(FL) for varying Transverse Resistance Contrast($T_{oil}/T_{over.}$) ratio in %.

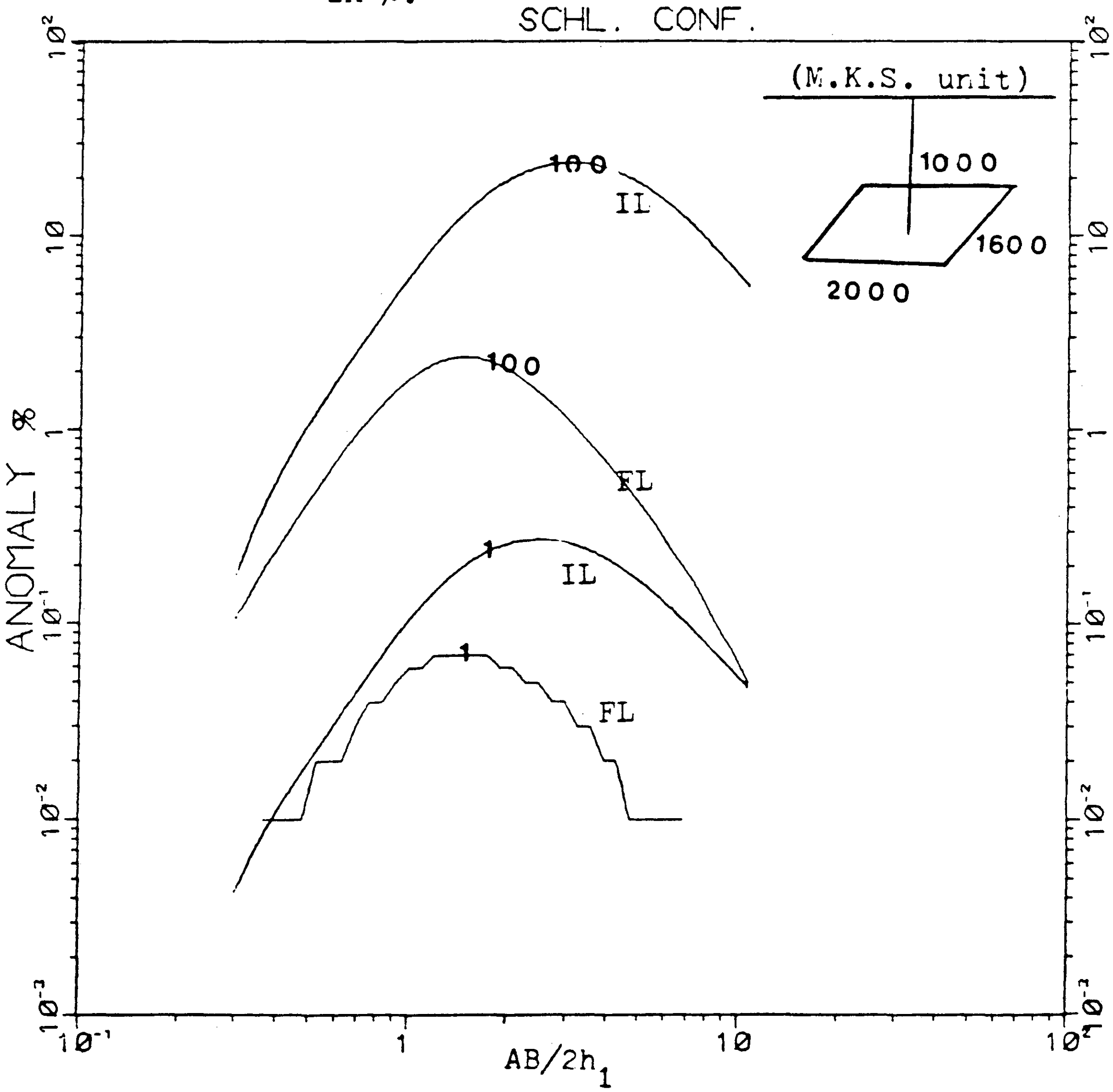

models are plotted in Figure 60. The anomaly over the finite-layer is about 50 and 67% of the anomaly over an infinite oil-layer for T = 100 and 1%, respectively. Also, the anomaly curve over a finite oil-layer is smoother than the first model anomaly curve due to the increase in anomaly value.

The anomaly curves were also computed over the same models for the radial-dipole array and are plotted in Figures 61 and 62. The anomaly for the first model is about 5 times that obtained for the Schlumberger array. The anomaly curve over the second model is close to the anomaly curve over the infinite areal-extent model. So, the radial-dipole array gives better results than the Schlumberger array over a finite oil-layer. There are negative anomalies for both infinite and finite layer models using the radial-dipole array.

Curves were also computed for a dipping finite-layer. It was assumed that the finite layer in the first model is dipping at $+30^{\circ}$ with respect to the x-axis. The anomaly curves over finite dipping and infinite horizontal layer for both the Schlumberger and radial-dipole arrays are plotted in Figures 63 and 64. The Schlumberger anomaly curve over a finite dipping layer first shows a positive anomaly, then negative, and again, positive. However, the radial-dipole anomaly curve trend is the opposite. Again, using the radial-dipole array, the maximum anomaly value is much better than that found for the Schlumberger array.

Figure 60 Anomaly plot over infinite(IL) & finite oil-layer(FL) for varying Transverse Resistance Contrast($T_{oil}/T_{over.}$) ratio in %.

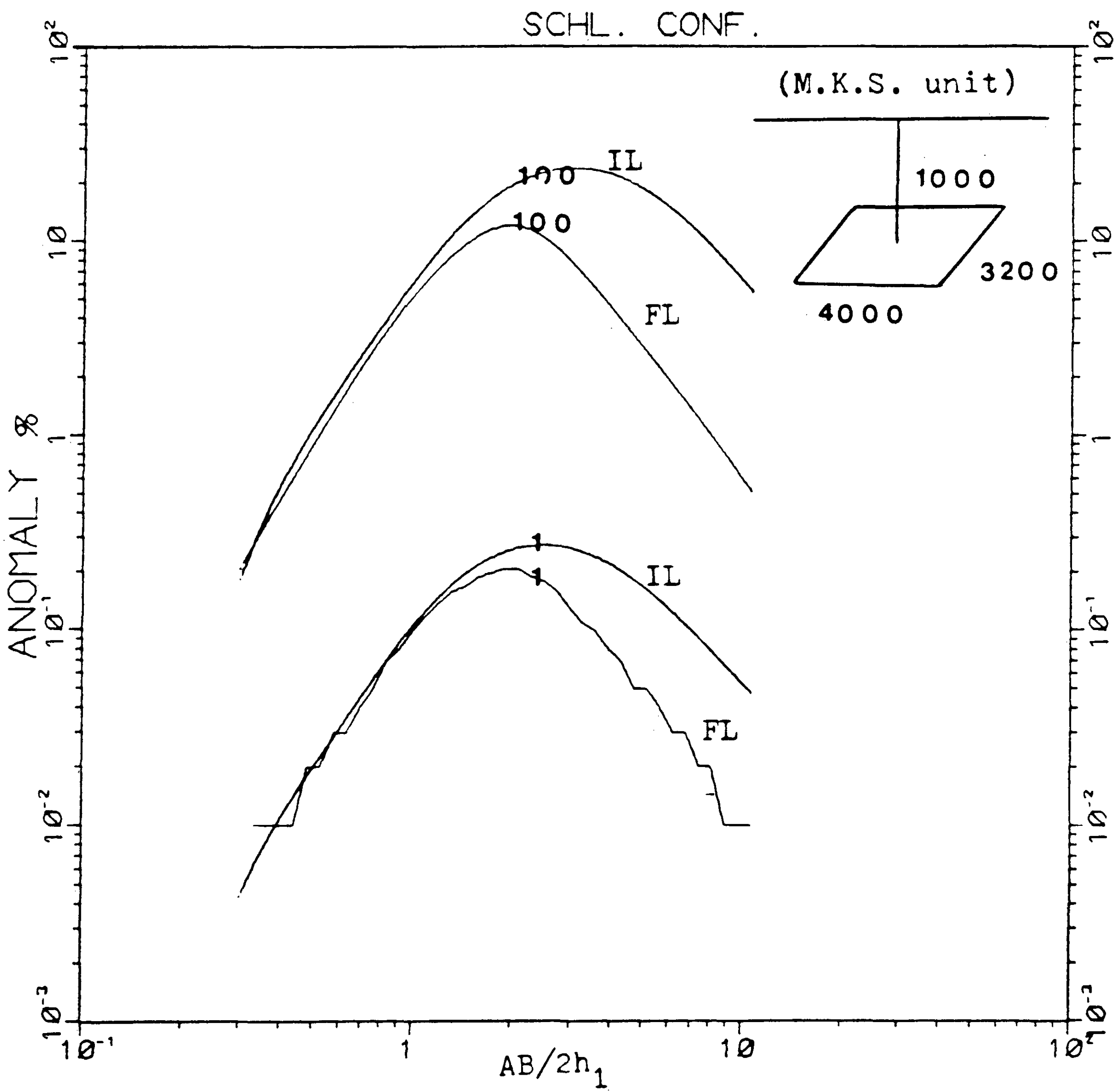

Figure 61 Anomaly plot over infinite(IL) & finite oil-layer(FL) for varying Transverse Resistance Contrast($T_{oil}/T_{over.}$) ratio in %.

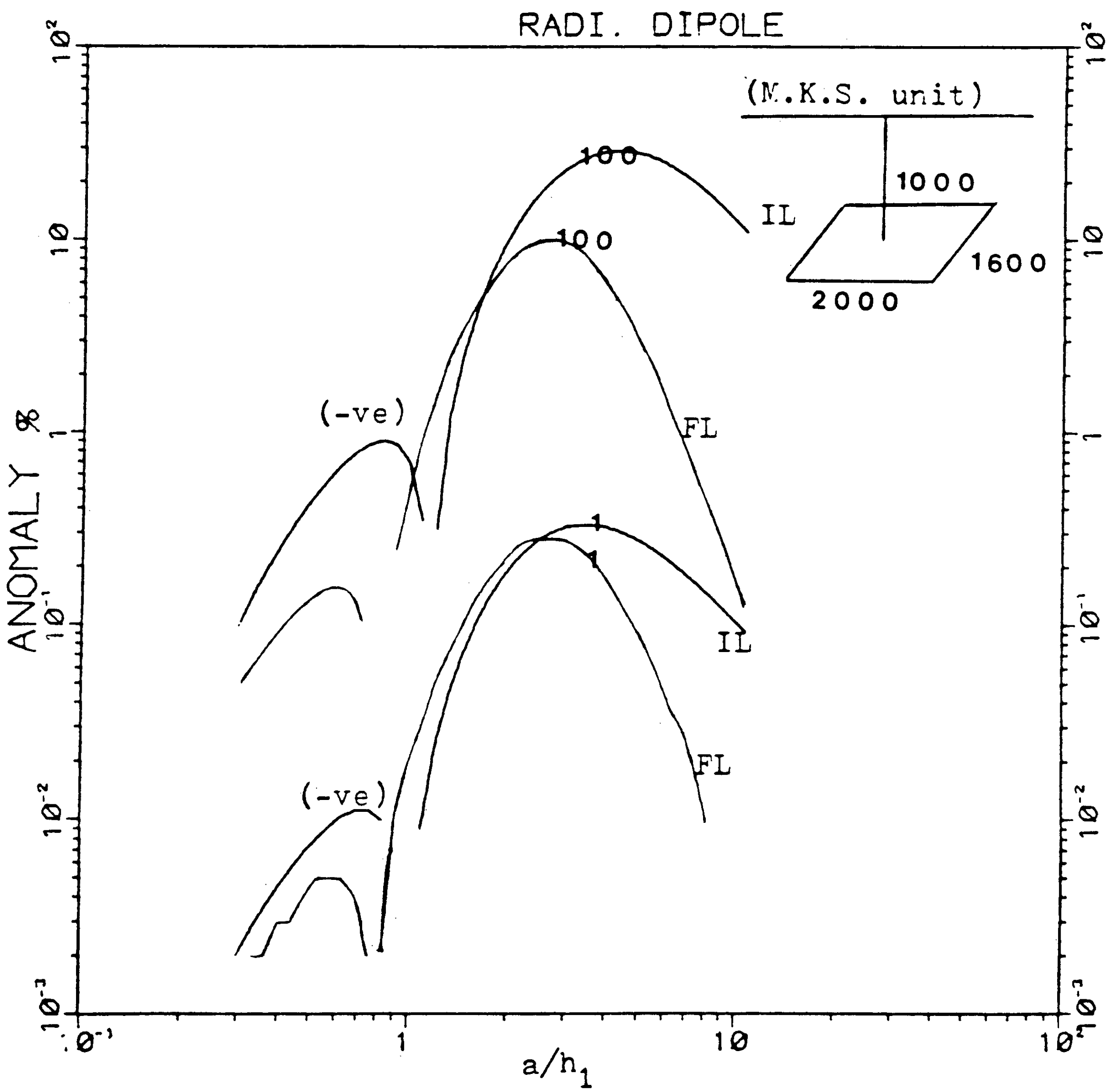

Figure 62 Anomaly plot over infinite(IL) & finite oil-layer(FL) for varying Transverse Resistance Contrast($T_{oil}/T_{over.}$) ratio in %.

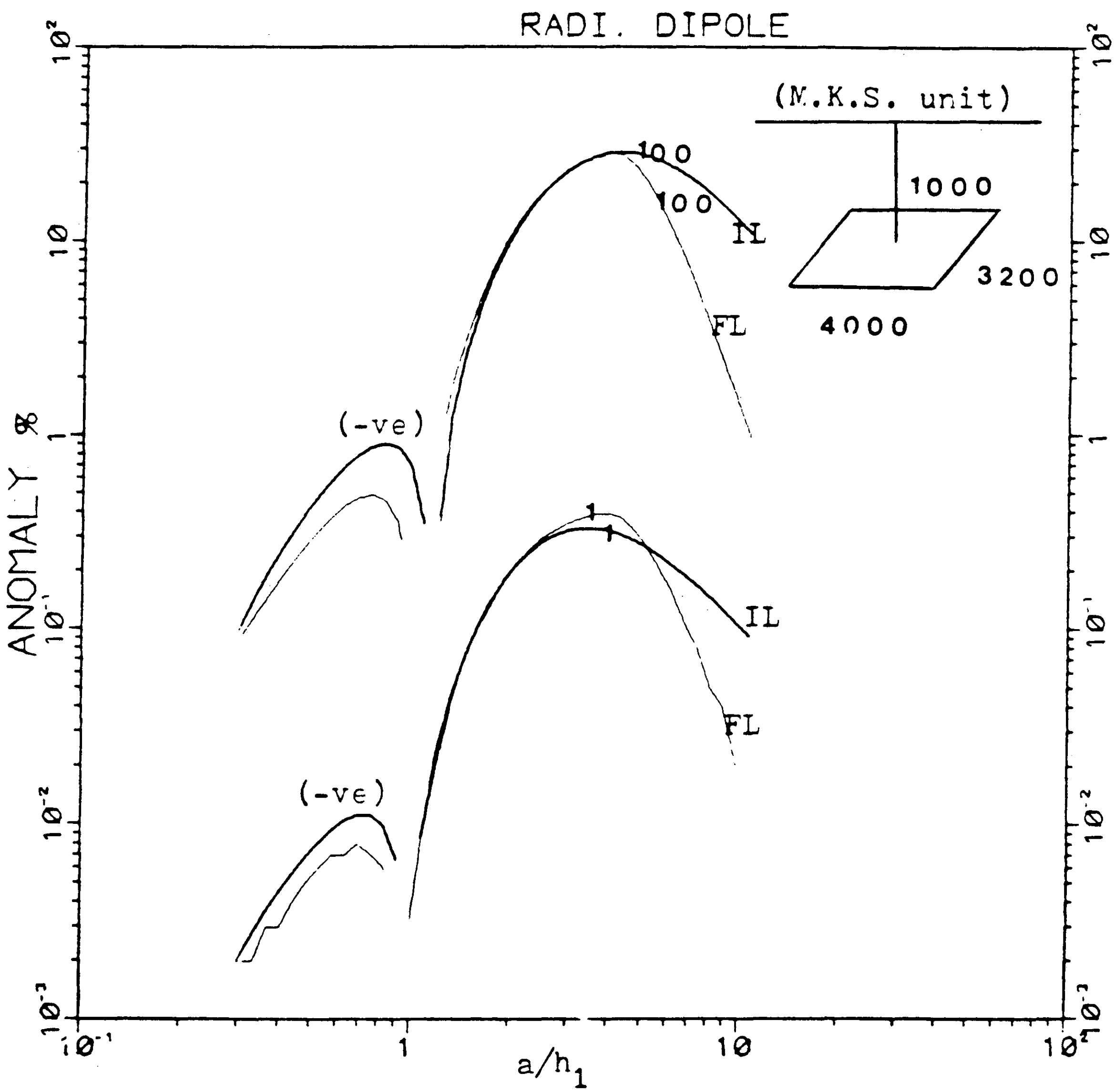

Figure 63 Anomaly plot over infinite horizontal (IHL) & finite dipping oil-layer(FDL) for varying Transverse Resistance Contrast($T_{oil}/T_{over.}$) ratio in %.

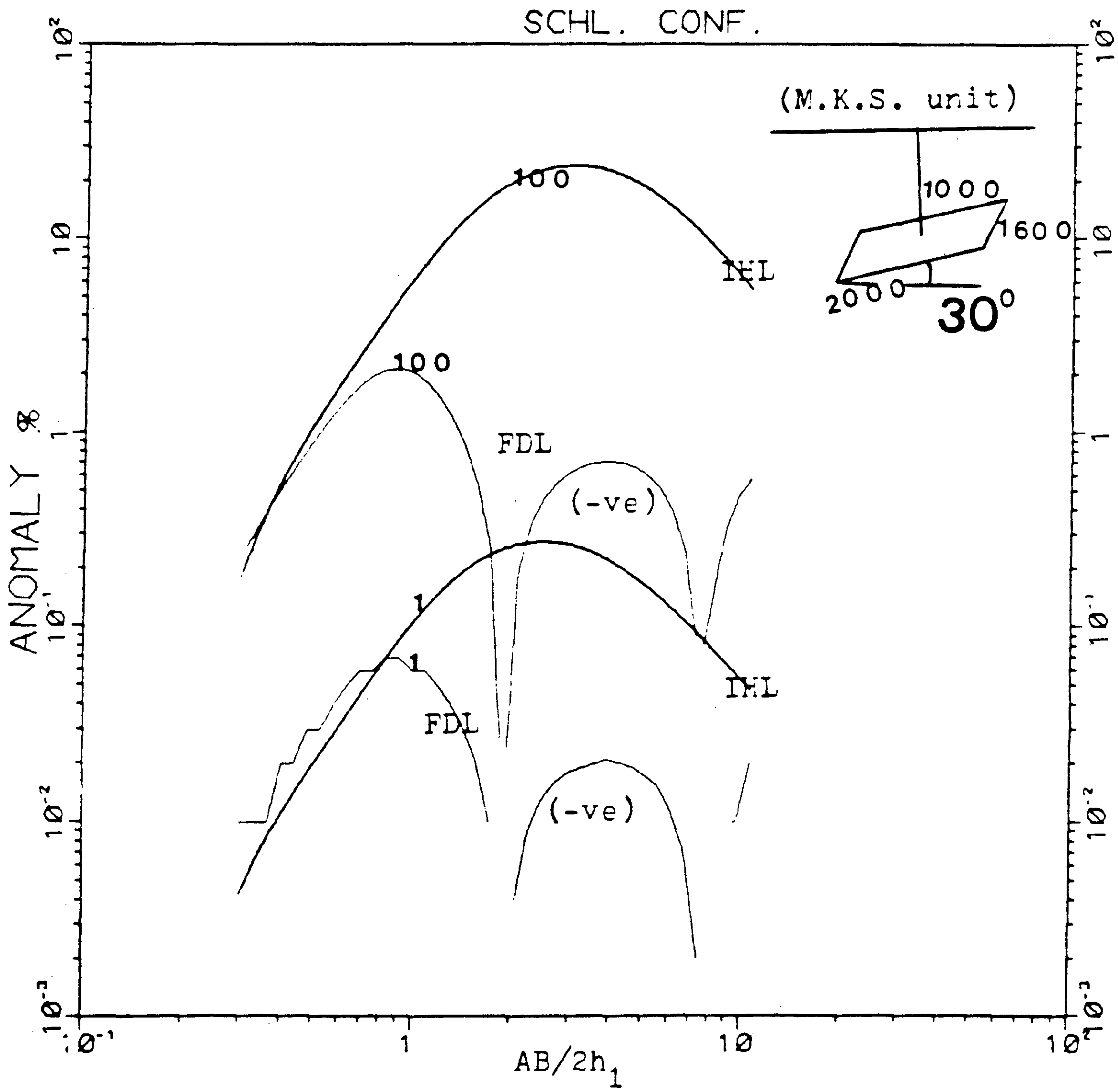

Figure 64 Anomaly plot over infinite horizontal (IHL) & finite dipping oil-layer(FDL) for varying Transverse Resistance Contrast($T_{oil}/T_{over.}$) ratio in %.

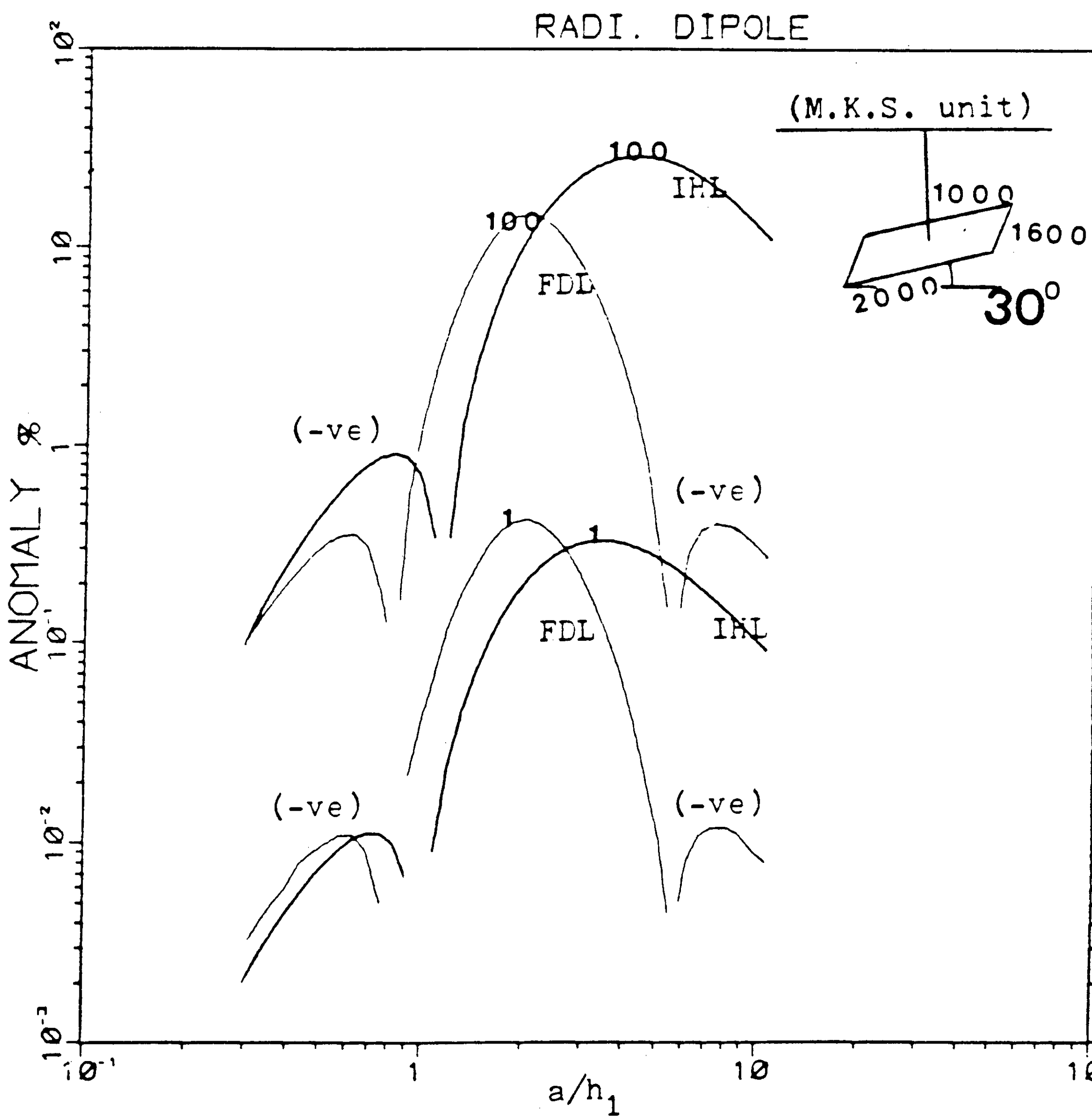

The anomaly curves were also computed for the case in which the finite-layer makes a -30° angle with x-axis. However, the results were exactly the same as before. So, the dip direction does not have any effect on the anomaly curves.

Anomaly curves were also computed for the first model for a buried current electrode. It was assumed that the current electrode is buried at the center of the finite-layer ($x = 0$) at depths, $Z = 10$, 500, and 700 m, and the potential electrode pair is moved along the surface. These curves are plotted in Figures 65, 66, and 67 as a function of separation between current electrode and potential electrode pair (a). Study of the results shows that as the depth of the buried electrode increases, the maximum anomaly increases. For a depth $Z = 700$ m, it is about 114 and 117% for $T = 100$ and 1%, respectively, of the anomaly computed for a radial-dipole array at the earth's surface. Also, one more interesting feature is that the maxima appears at small electrode separations. So, we do not need to make measurements up to long separations. A composite plot corresponding to all three burial depths is shown in Figure 68 just to provide insight about the behavior of the anomaly with increasing current electrode depth. Anomaly curves when the current electrode was buried away from the center of the finite-layer at $x = -750$ m for all three above depths are plotted in Figures 69, 70, and 71. At this time, the

Figure 65 Anomaly plot over finite oil-layer for fixed buried current electrode at x=0 & z=10 m and moving potential electrode pair for varying $T_{oil}/T_{over.}$ ratio in %.

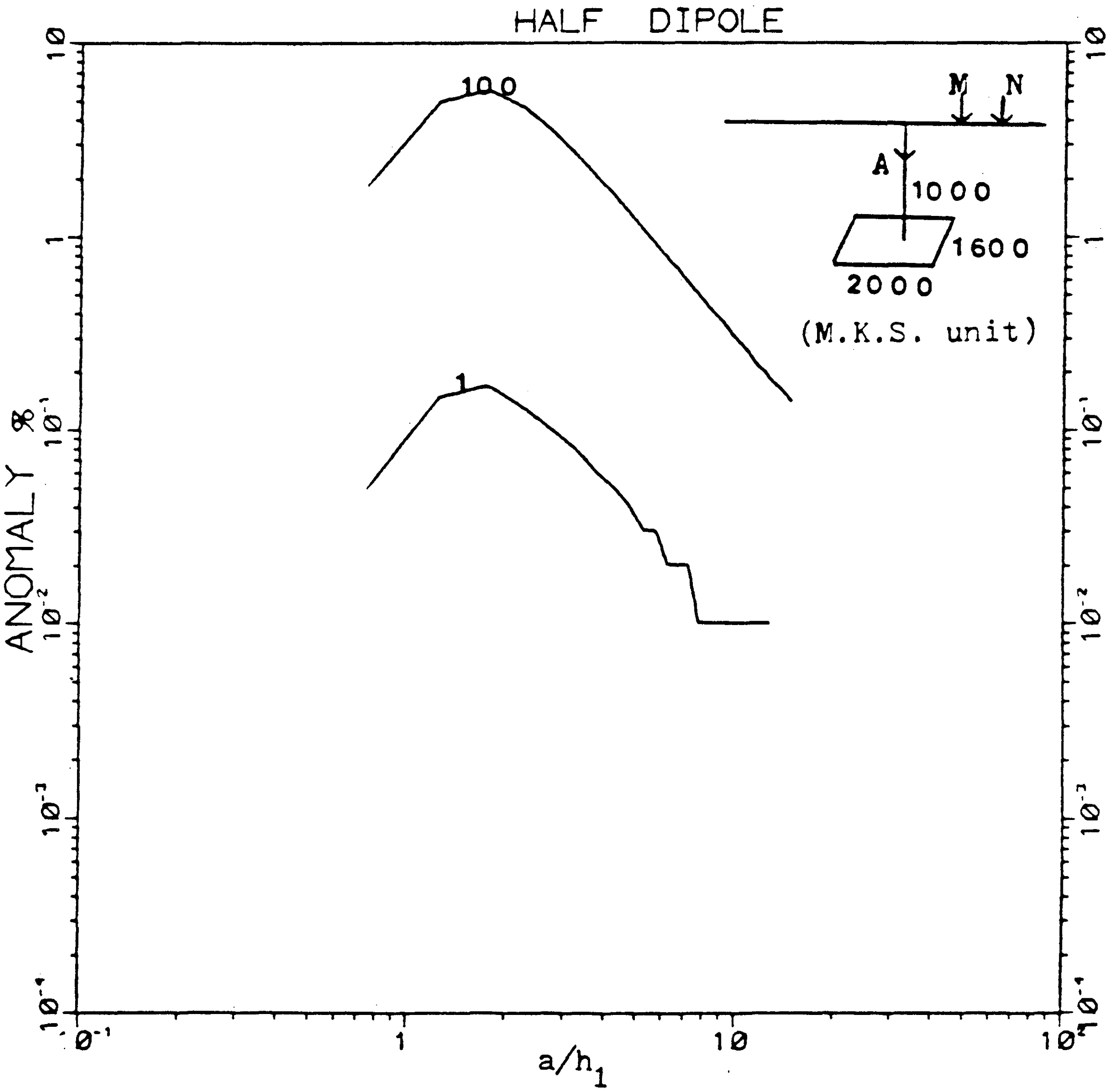

Figure 66 Anomaly plot over finite oil-layer for fixed buried current electrode at x=0 & z=500 m and moving potential electrode pair for varying $T_{oil}/T_{over.}$ ratio in %.

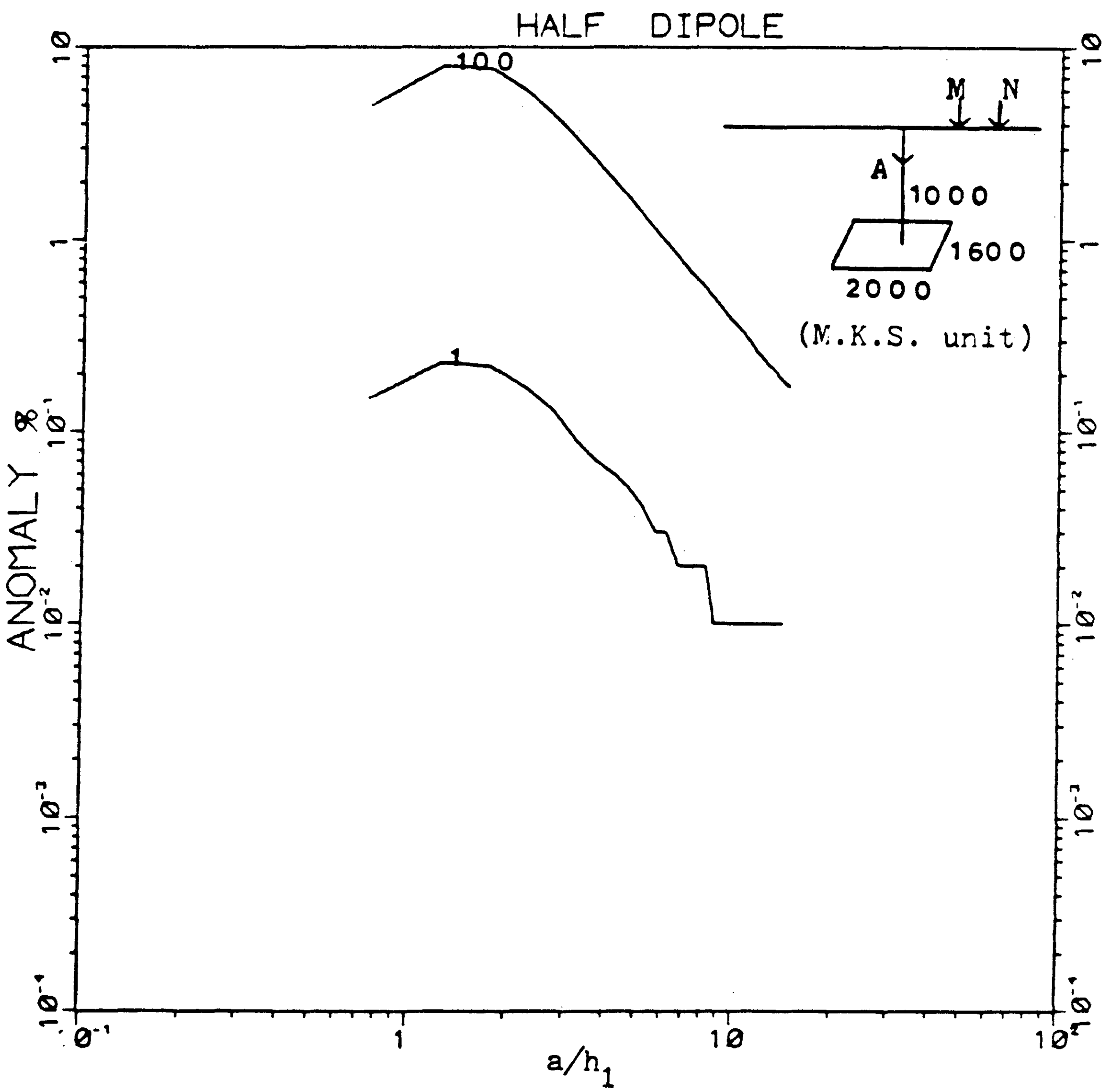

Figure 67 Anomaly plot over finite oil-layer for fixed buried current electrode at x=0 & z=700 m and moving potential electrode pair for varying $T_{oil}/T_{over.}$ ratio in %.

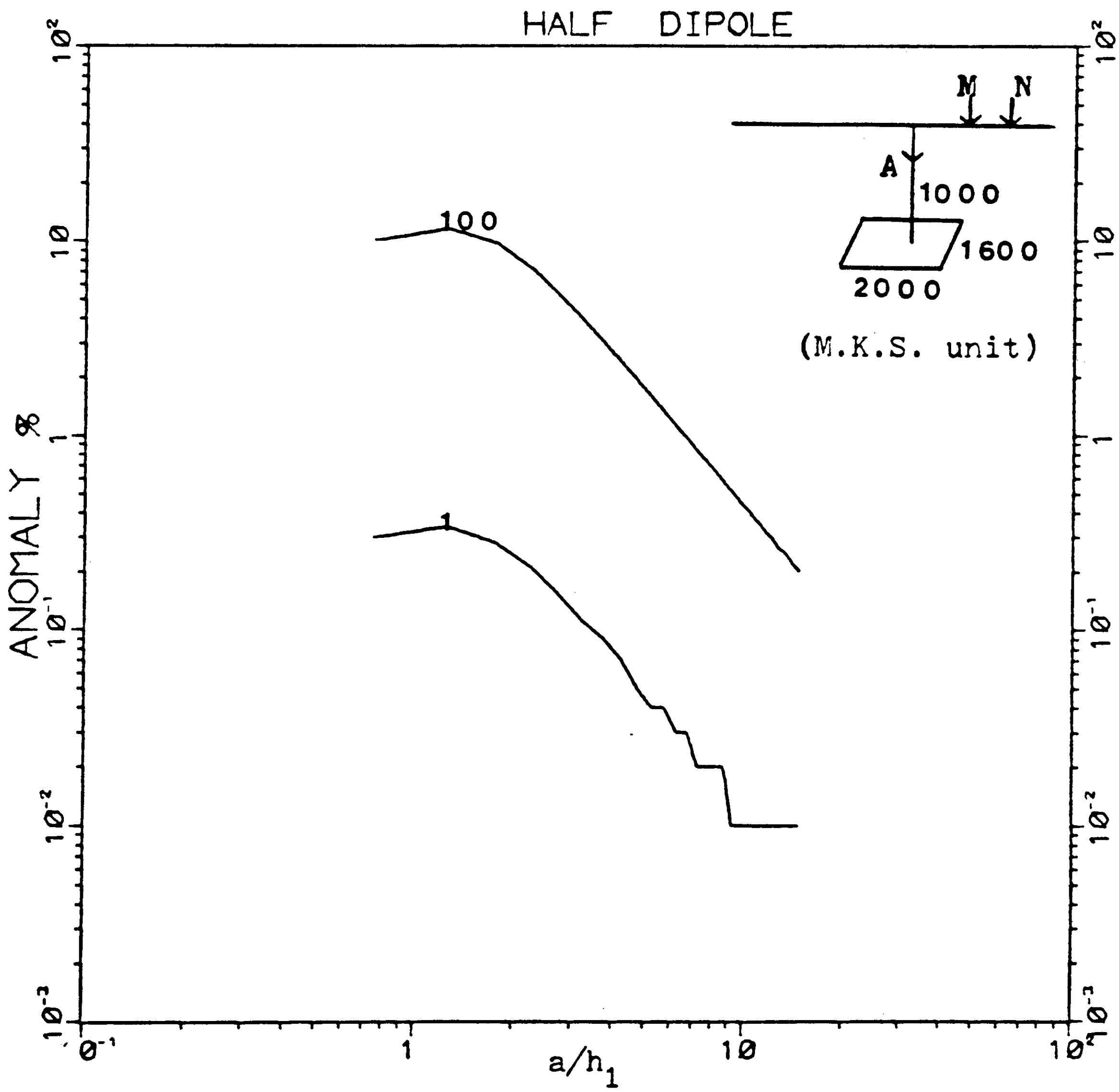

Figure 68 Composite anomaly plot over finite oil-layer for varying buried current electrode depth at x=0 and moving potential electrode pair for varying $T_{oil}/T_{over.}$ ratio in %.

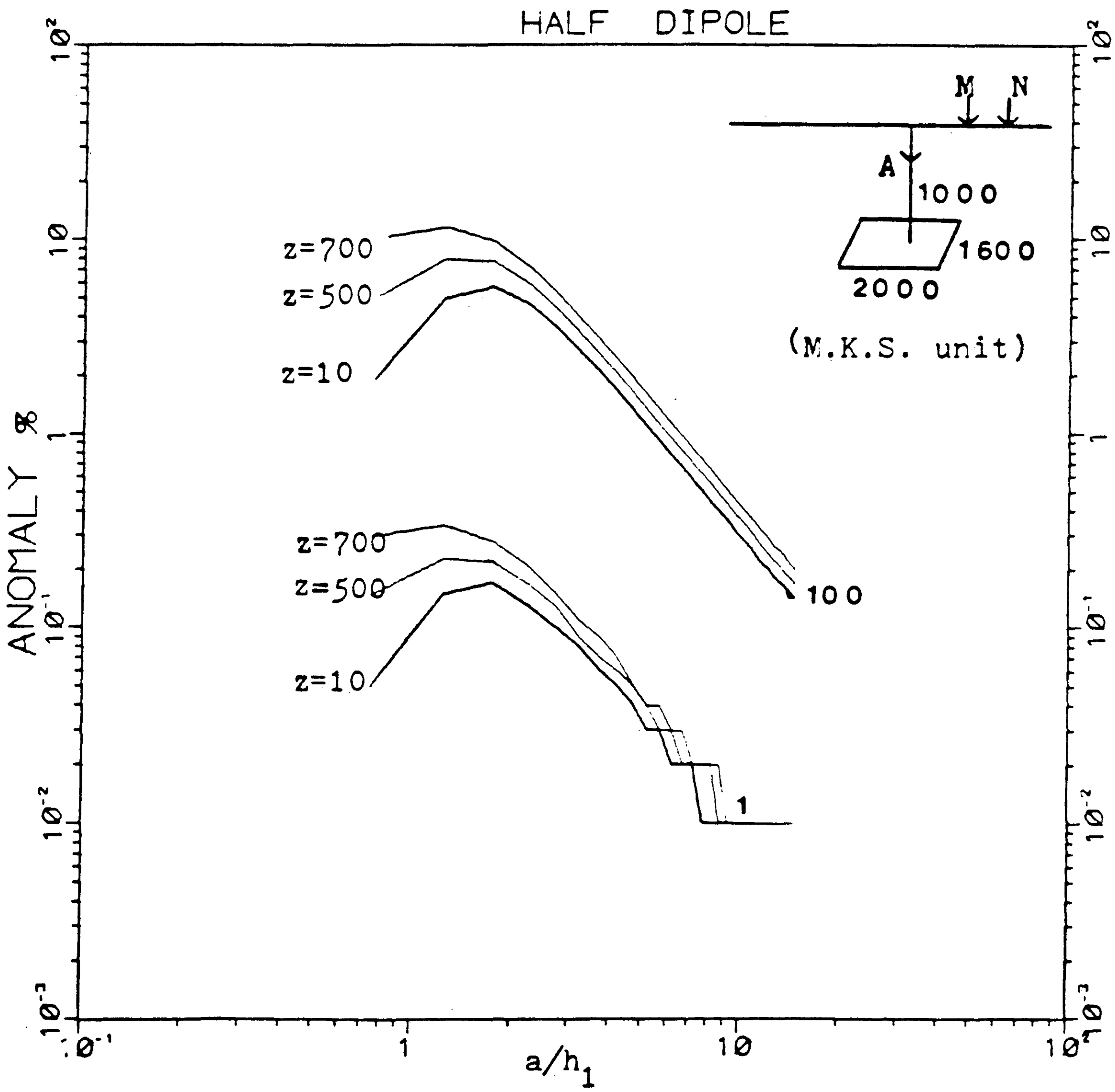

Figure 69 Anomaly plot over finite oil-layer for fixed buried current electrode at x= -750 m & z=10 m and moving potential electrode pair on Left-hand(LH) & Right-hand(RH) side of current electrode for varying $T_{oil}/T_{over.}$ ratio in %.

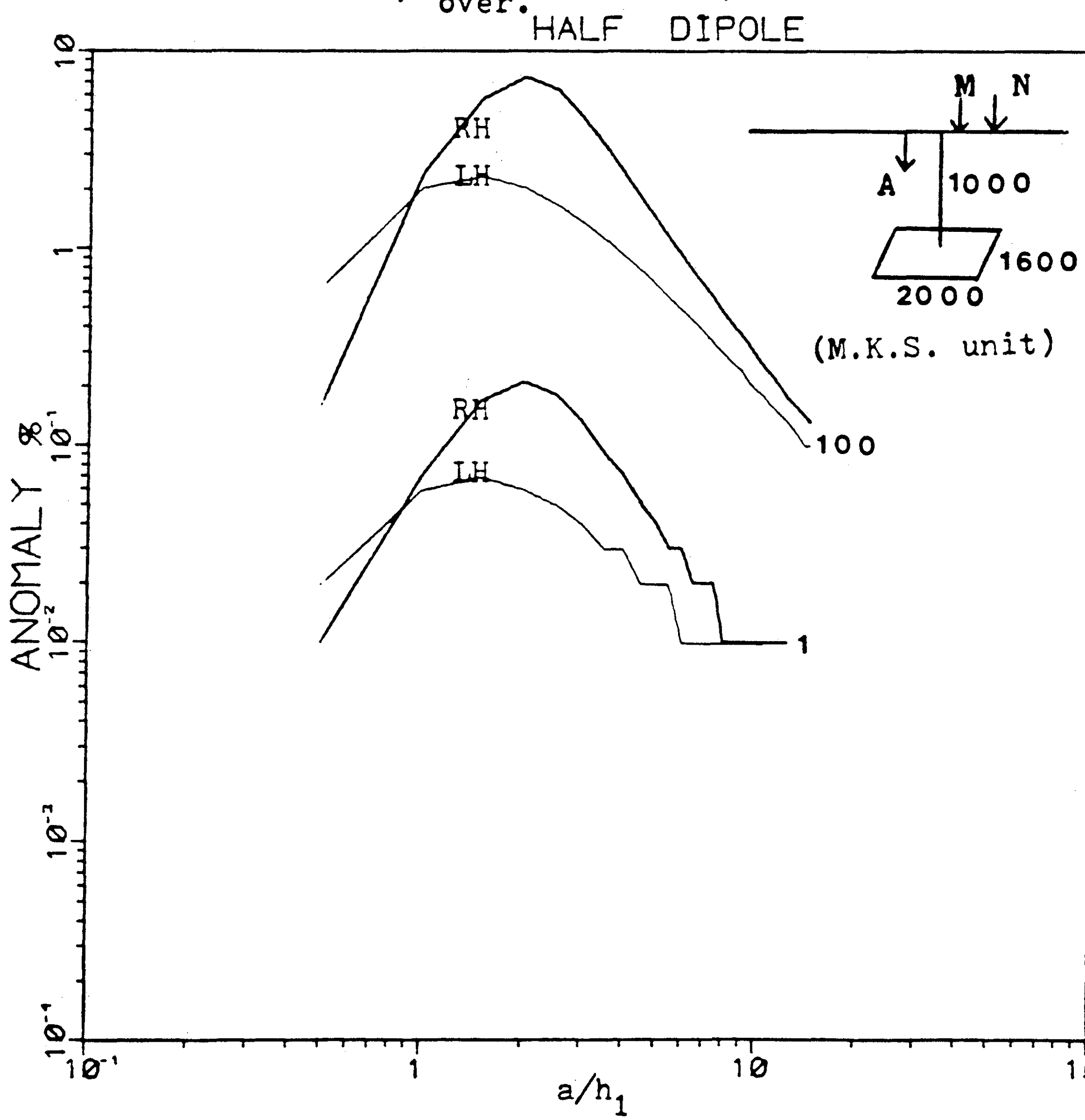

Figure 70 Anomaly plot over finite oil-layer for fixed buried current electrode at x= -750 m & z=500 m and moving potential electrode pair on Left-hand(LH) & Right-hand(RH) side of current electrode for varying T_{oil} $/T_{over.}$ ratio in %.

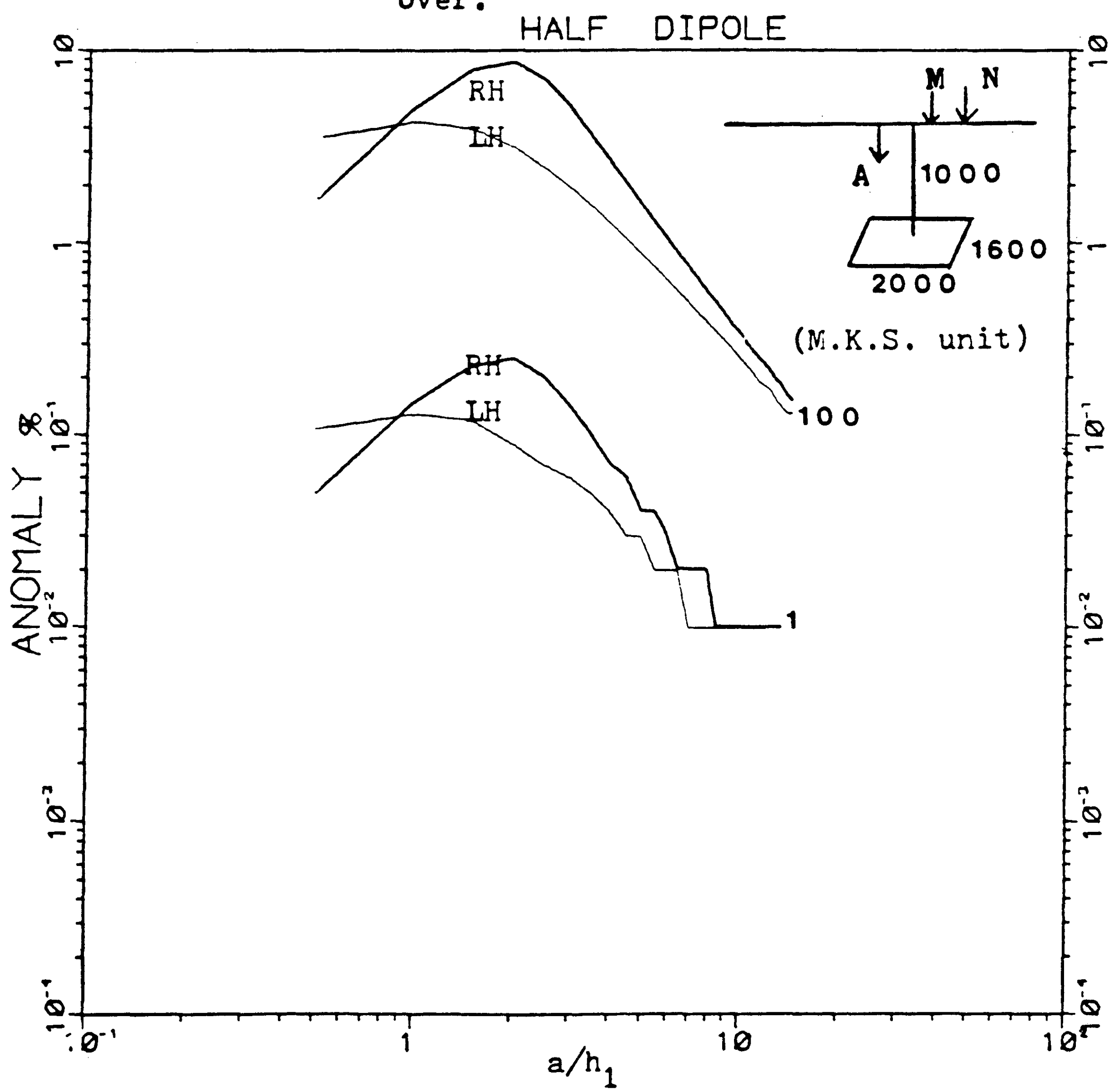

Figure 71 Anomaly plot over finite oil-layer for fixed buried current electrode at x= -750 m & z=700 m and moving potential electrode pair on Left-hand(LH) & Right-hand(RH) side of current electrode for varying T_{oil} $/T_{over.}$ ratio in %.

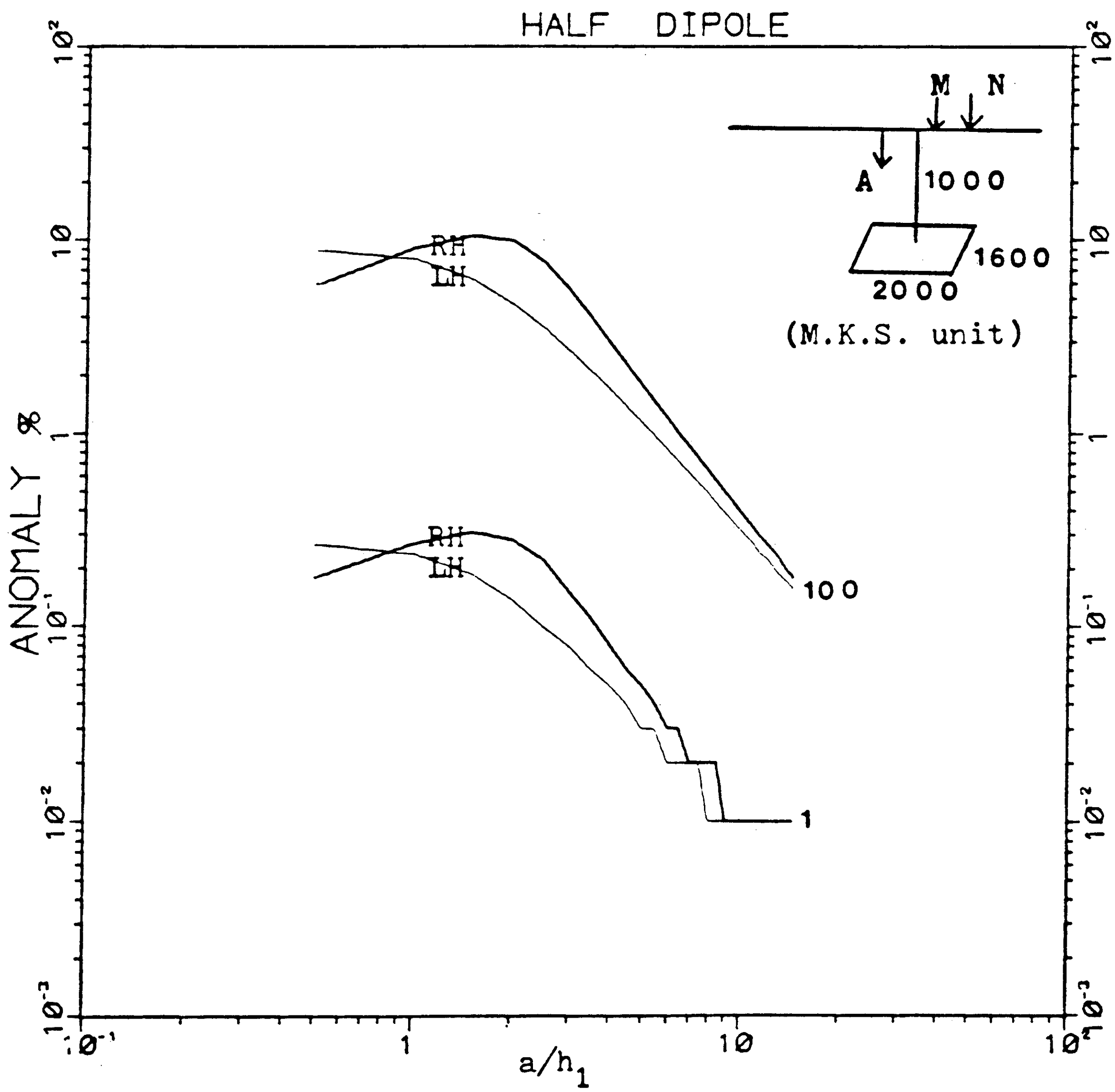

current electrodes are not symmetrically located with respect to the location of the finite-layer; the resulting anomaly curves are plotted as the potential electrode pair is moved on either side of the current electrode along the x-axis. The maximum anomaly value increases with increasing depth. For a depth of Z = 700 m, it is about 104 and 107% when the potential electrode pair is on the right hand side of current electrode of radial-dipole anomaly at the earth's surface. When the potential electrode pair is on the left side, it is about 91 and 93% for the same T values, respectively. Anomaly curves are also plotted in Figures 72, 73, and 74 for all the same depths when the current electrode is buried x = -1250 m. This time the maximum anomaly value corresponds to the depth Z = 10 m and then decreases with increasing depth because the current tends to flow parallel to this layer and is less distorted. The anomaly is about 65% for boh T values for the radial-dipole array at the earth's surface. For measuring the dipole on the left side, it is about 7% for both T values. Thus, the radial-dipole array is best for detecting a finite oil-layer and for a buried current electrode, we do not need to make measurements up the long separations normally needed in the DC soundings.

Figure 72 Anomaly plot over finite oil-layer for fixed buried current electrode at x= -1250 m & z=10 m and moving potential electrode pair on Left-hand(LH) & Right-hand(RH) side of current electrode for varying $T_{oil}/T_{over.}$ ratio in %.

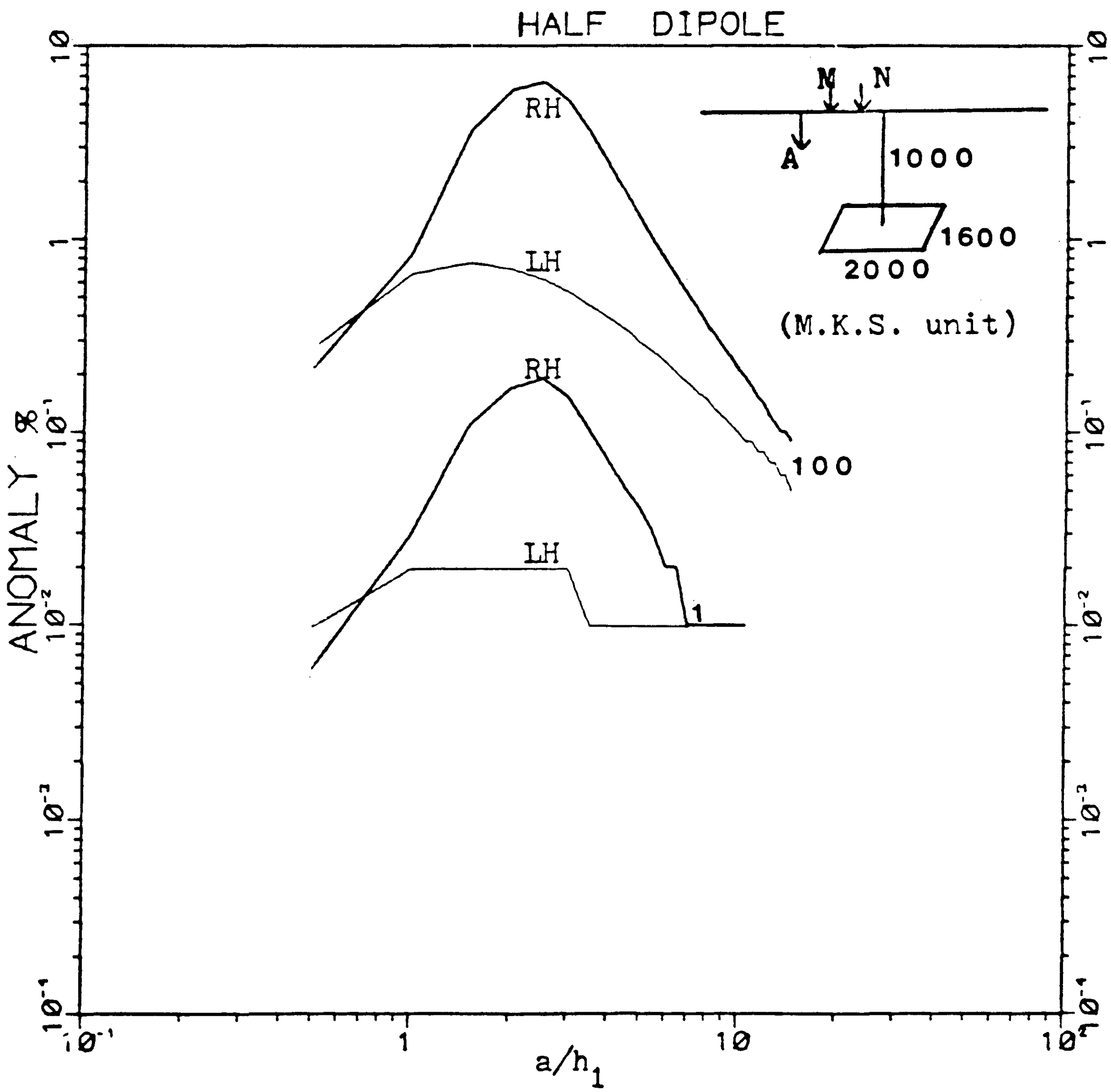

Figure 73 Anomaly plot over finite oil-layer for fixed buried current electrode at x= -1250 m & z=500 m and moving potential electrode pair on Left-hand(LH) & Right-hand(RH) side of current electrode for varying $T_{oil}/T_{over.}$ ratio in %.

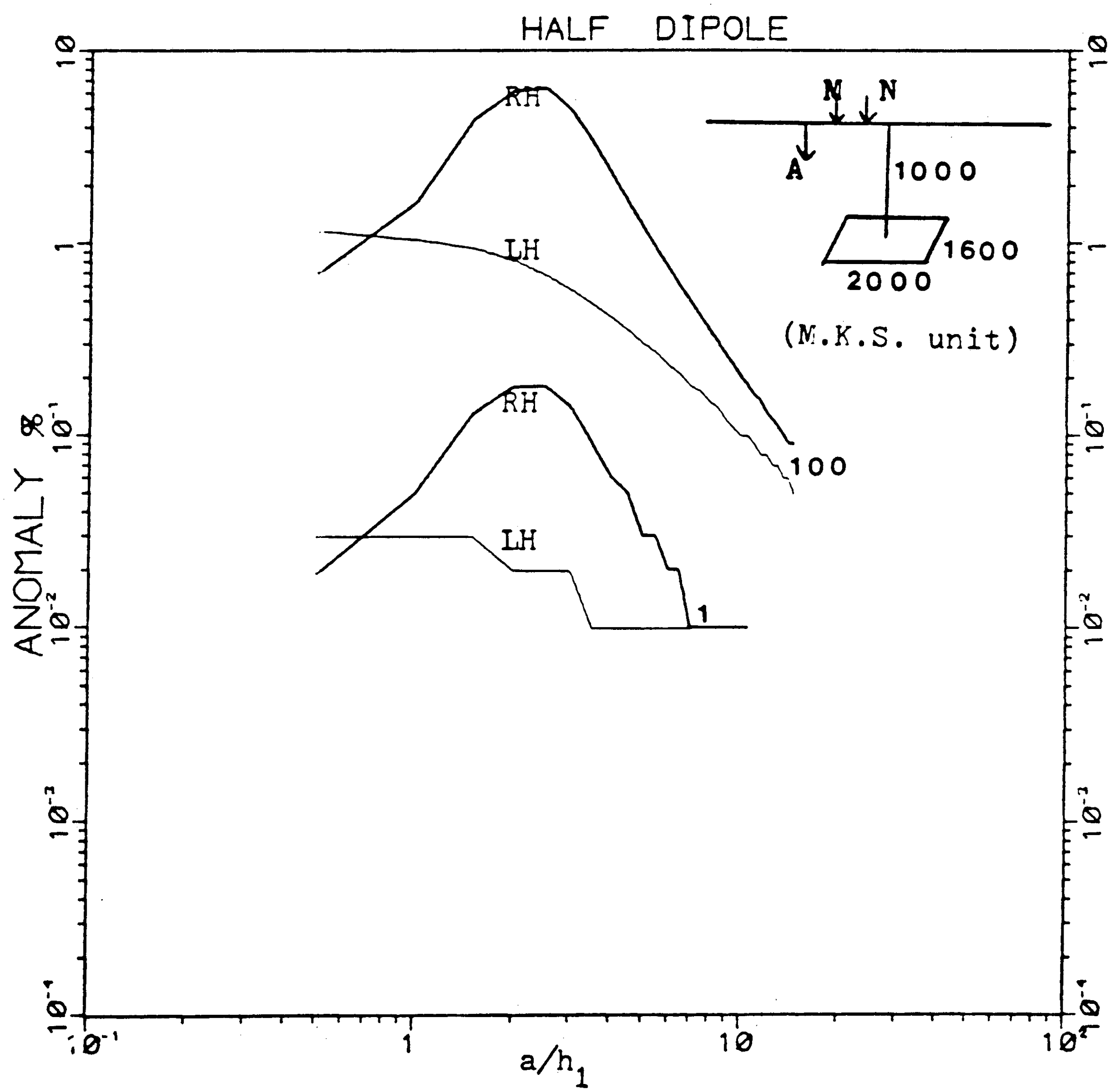

Figure 74 Anomaly plot over finite oil-layer for fixed buried current electrode at x= -1250 m & z=700 m and moving potential electrode pair on Left-hand(LH) & Right-hand(RH) side of current electrode for varying $T_{oil}/T_{over.}$ ratio in %.

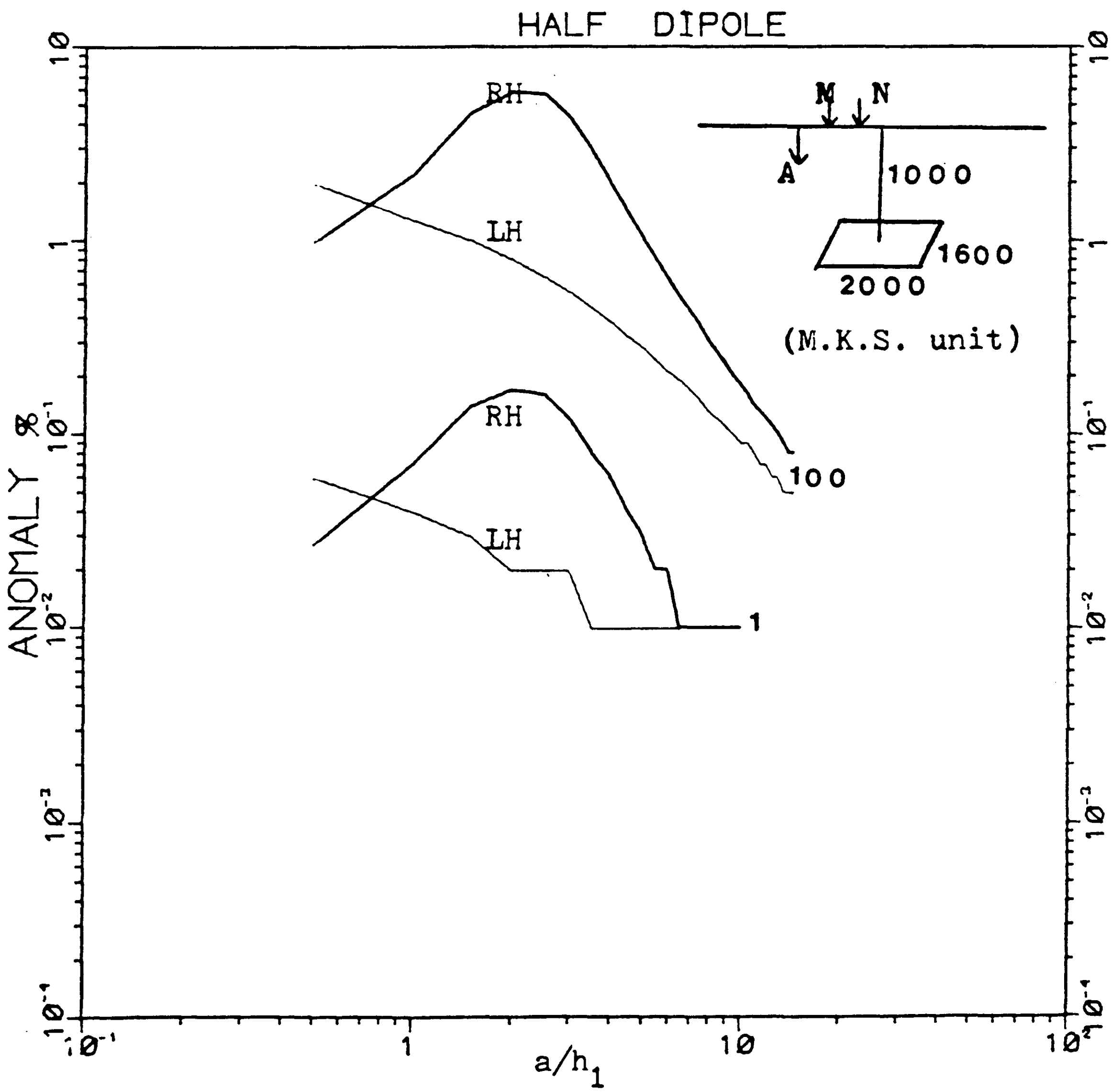

CONCLUSIONS

Study in the present work shows that:

1. Different oil-fields have different geoelectrical parameters. The geoelectrical parameters for the southern portion of San Joaquin Valley, Kern County, California, correspond to an H-type of curve. The geoelectrical parameters for Payne, Logan, Lincoln Counties, Oklahoma, and Lance Creek, Wyoming, correspond to an ascending type of curve with two and three layers, respectively.

2. The anomaly value depends upon the environmental geoelectric parameters in which the oil-layer is embedded.

3. The maximum anomaly value in an H-type of an environment with an oil-layer embedded between the first and second layers is almost the same as the transverse resistance contrast of oil-layer to the first layer when the radial-dipole array is considered. In a two-layer ascending type of environment, it is below 8% for T = 100%. In A-type of an environment, it is less than 2% for the same T values and arrays.

4. The radial-dipole array gives the best maximum anomaly value followed by the equatorial-dipole, Schlumberger and Wenner arrays over the same model.

5. The finite areal extent of an oil-layer does not

have any significant effect on the anomaly value for an infinite layer if its dimensions are about four times the depth.

6. Soundings carried out with one buried current electrode in the vicinity of oil-layer and a moving potential electrode pair, increase the maximum anomaly value over the same model and the maximum anomaly value appears at a separation comparable to the depth. Therefore, we do not need to make measurements at long separations compared to the depth as we generally do in DC soundings.

7. The direction of a dipping oil-layer along the geometrical spread line does not have any effect on the computed anomaly whether it is dipping downward or upward.

8. Finally, the anomaly should be greater than the expected lateral-resistivity variation in environmental-layers.

REFERENCES

California Oil and Gas Fields Maps and Data Sheets, 1960, Part 1, Division of Oil and Gas, San Francisco.

Frost, V.L., 1940, Ramsey Oil Pool, Payne County, Oklahoma, Bulletin AAPG, vol. 24, no. 11, pp. 1995-2005.

Garg, N.R., 1976, Direct detection of hydrocarbons through geoelectrical methods, M. Tech. Thesis, Roorkee University, India, pp. 1-84.

Ghosh, D.P., 1971, Inverse filter coefficients for the computation of apparent resistivity standard curves for a horizontally stratified earth, Geophysical Prospecting, vol. 19, pp. 769-775.

Keller, G.V., 1968, Electrical prospecting for oil, Quarterly of the Colorado School of Mines, vol. 63, no. 2, pp. 1-268.

Whan, W.J., 1979, Numerical modeling of the direct current resistivity for thin insulators, Ph.D. Thesis, T-2231, Colorado School of Mines, pp. 1-131.

Wyoming Oil and Gas Fields, 1957, Wyoming Geological Association Symposium.

APPENDIX 1 : Resistivity-integral plots & geoelectrical parameters,California.

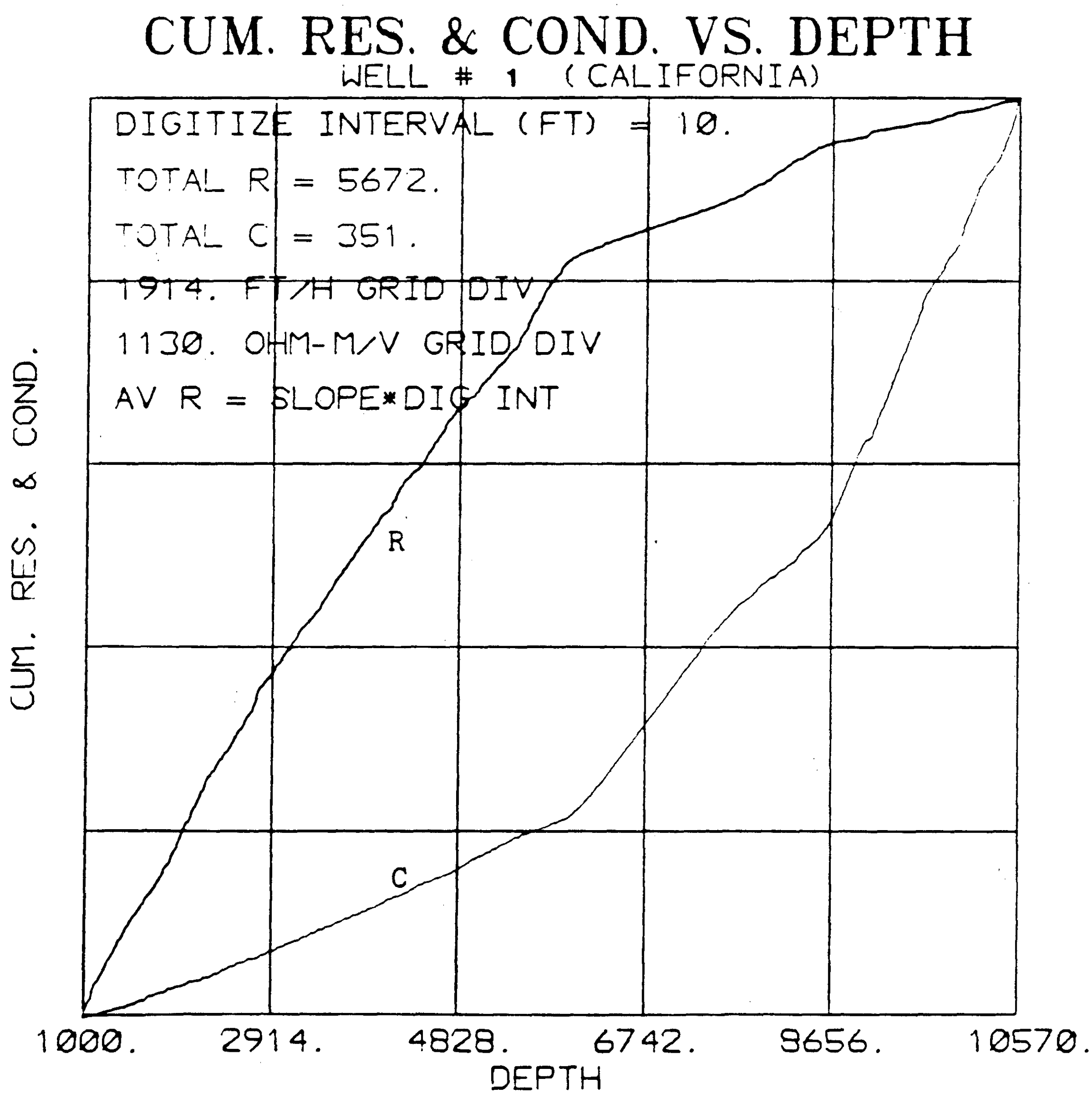

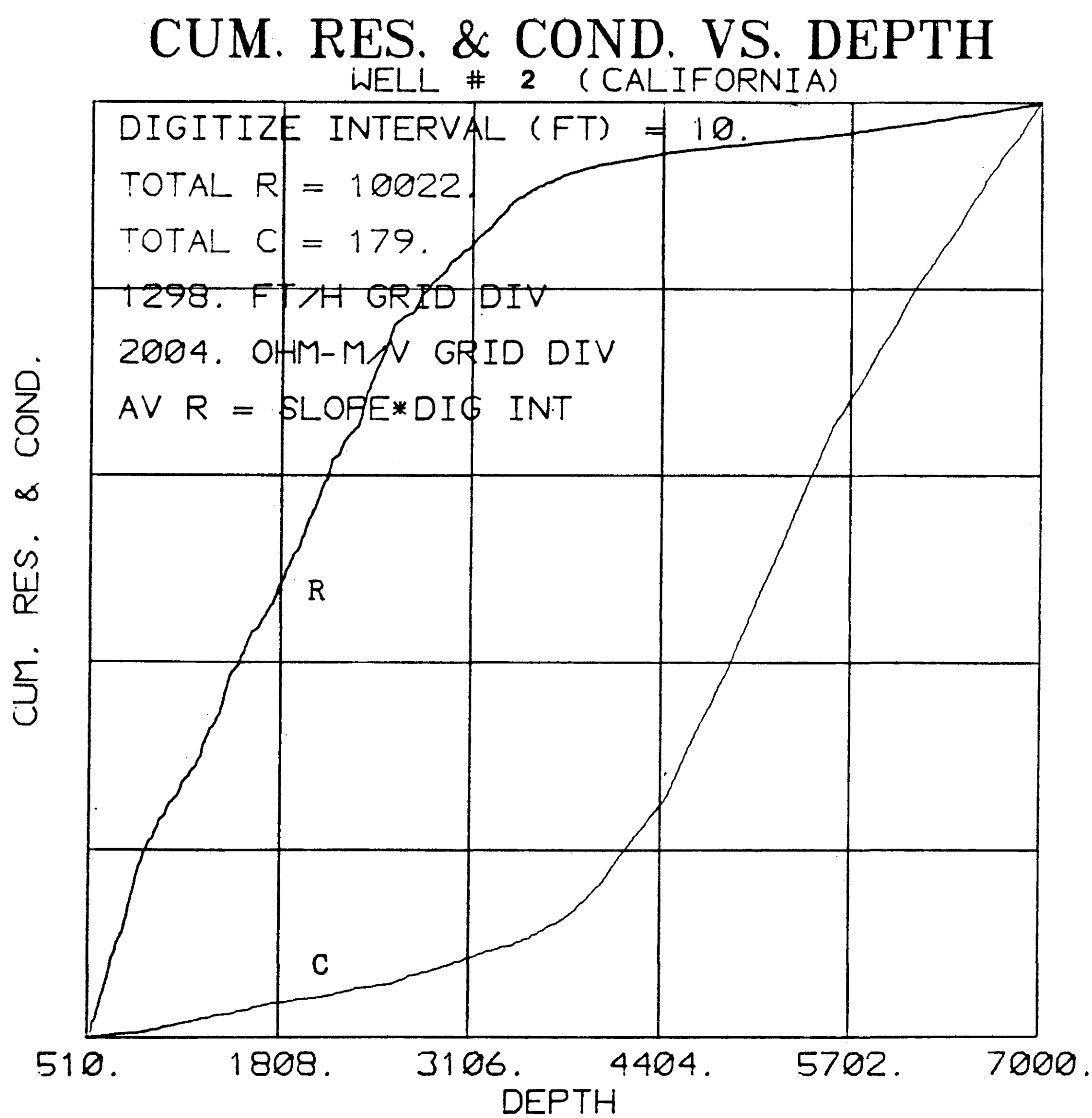
CUM. RES. & COND. VS. DEPTH
WELL # 2 (CALIFORNIA)
DIGITIZE INTERVAL (FT) = 10.
TOTAL R = 10022.
TOTAL C = 179.
1298. FT/H GRID DIV
2004. OHM-M/V GRID DIV
AV R = SLOPE*DIG INT
R
C
CUM. RES. & COND.
510.
1808.
3106.
4404.
5702.
7000.
DEPTH

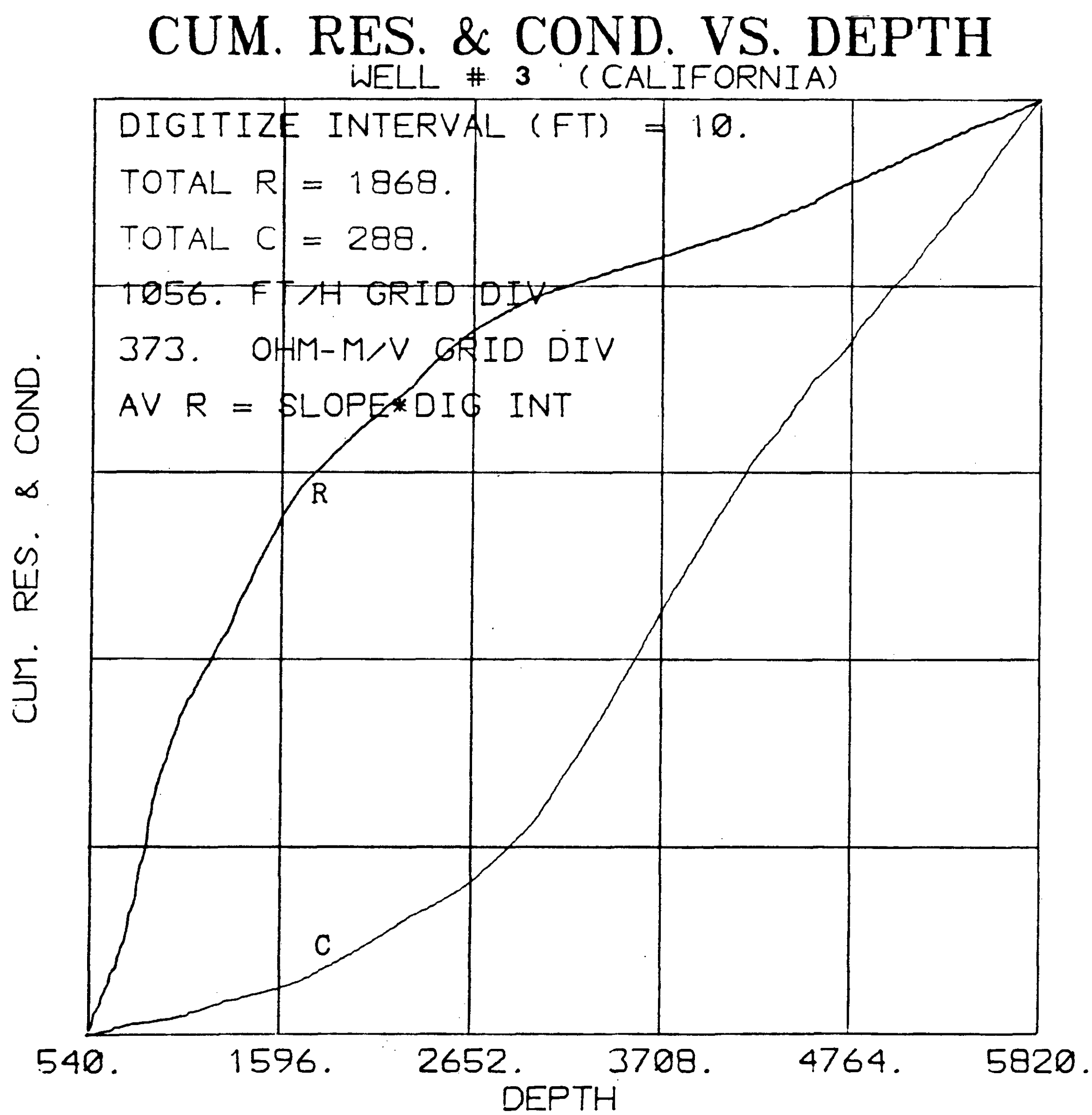
CUM. RES. & COND. VS. DEPTH
WELL # 3 (CALIFORNIA)
DIGITIZE INTERVAL (FT) = 10.
TOTAL R = 1868.
TOTAL C = 288.
1056. FT/H GRID DIV
373. OHM-M/V GRID DIV
AV R = SLOPE*DIG INT
R
C
CUM. RES. & COND.
540.
1596.
2652.
3708.
4764.
5820.
DEPTH

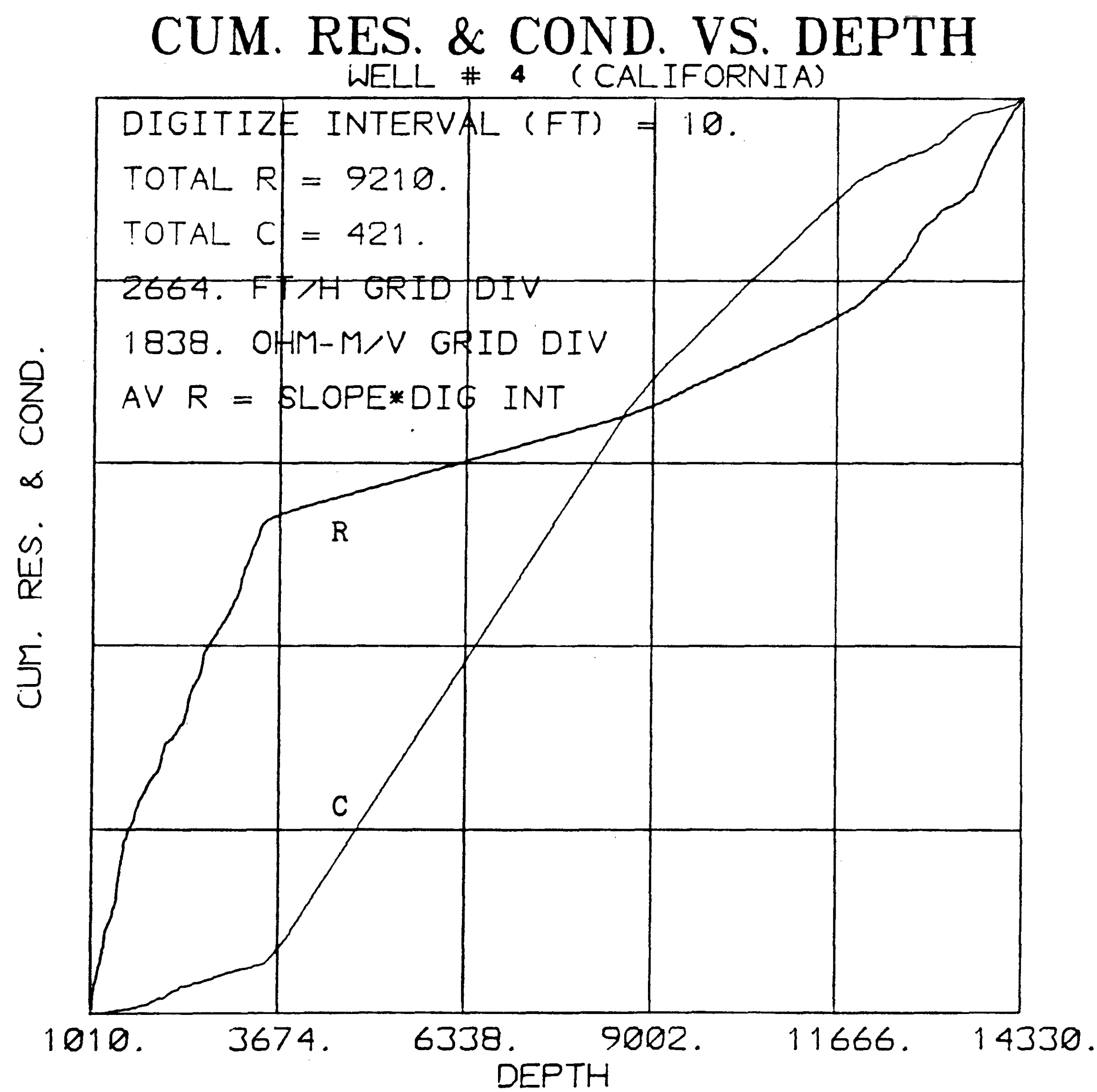
CUM. RES. & COND. VS. DEPTH
WELL # 4 (CALIFORNIA)
DIGITIZE INTERVAL (FT) = 10.
TOTAL R = 9210.
TOTAL C = 421.
2664. FT/H GRID DIV
1838. OHM-M/V GRID DIV
AV R = SLOPE*DIG INT
R
C
CUM. RES. & COND.
1010.
3674.
6338.
9002.
11666.
14330.
DEPTH

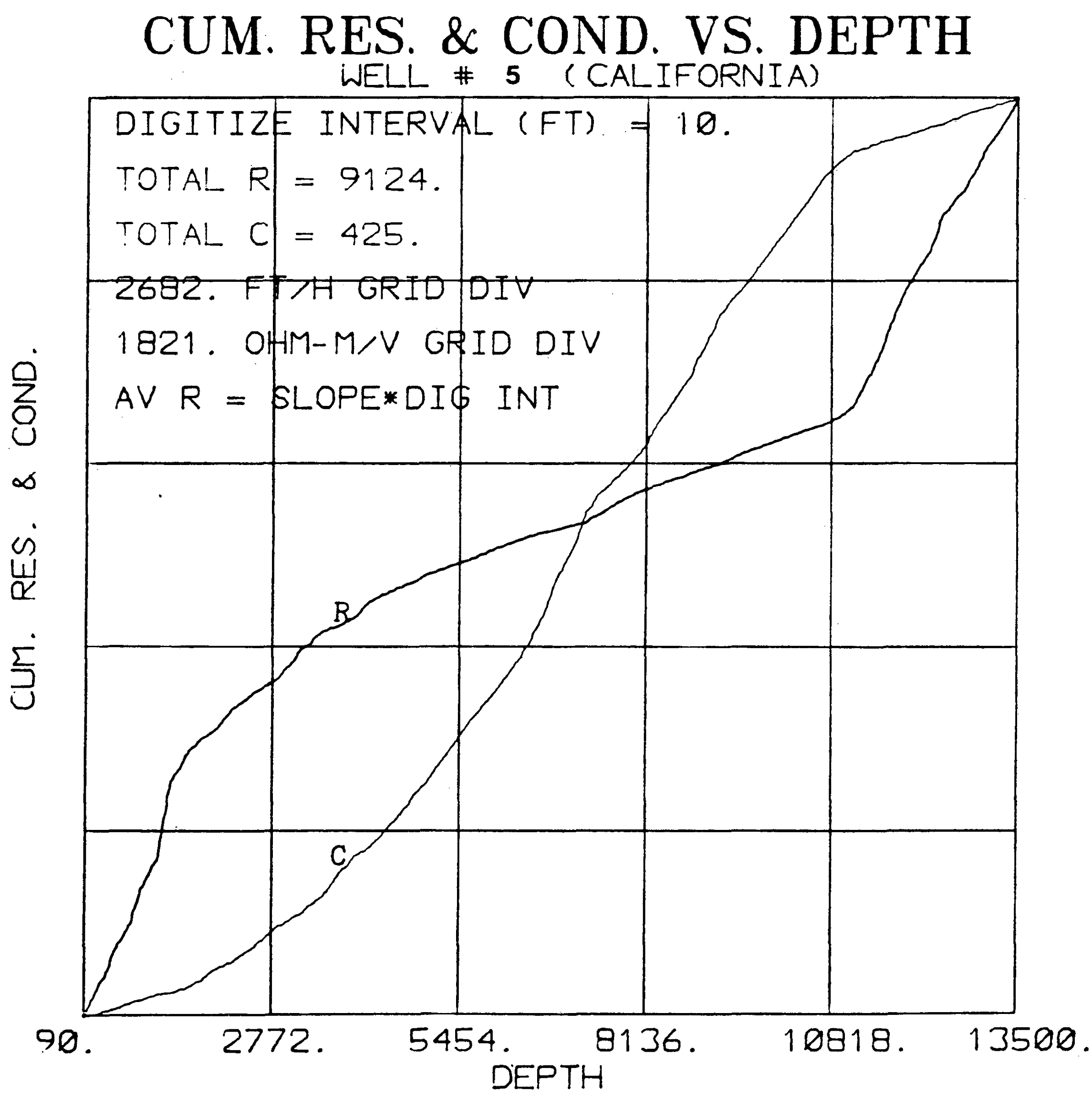
CUM. RES. & COND. VS. DEPTH
WELL # 5 (CALIFORNIA)
DIGITIZE INTERVAL (FT) = 10.
TOTAL R = 9124.
TOTAL C = 425.
2682. FT/H GRID DIV
1821. OHM-M/V GRID DIV
AV R = SLOPE*DIG INT
R
C
CUM. RES. & COND.
90.
2772.
5454.
8136.
10818.
13500.
DEPTH

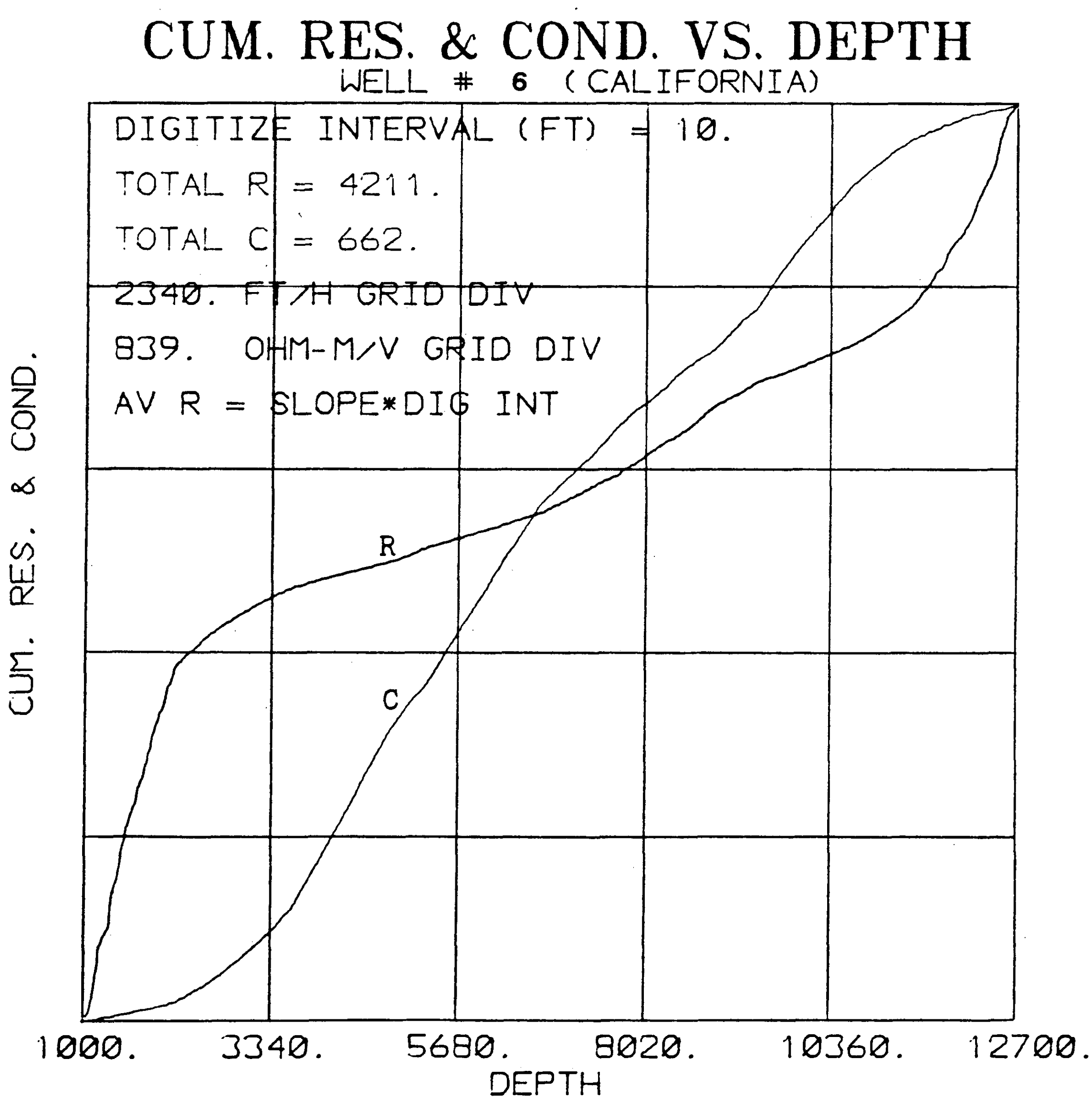
CUM. RES. & COND. VS. DEPTH
WELL # 6 (CALIFORNIA)
DIGITIZE INTERVAL (FT) = 10.
TOTAL R = 4211.
TOTAL C = 662.
2340. FT/H GRID DIV
839. OHM-M/V GRID DIV
AV R = SLOPE*DIG INT
R
C
CUM. RES. & COND.
1000.
3340.
5680.
8020.
10360.
12700.
DEPTH

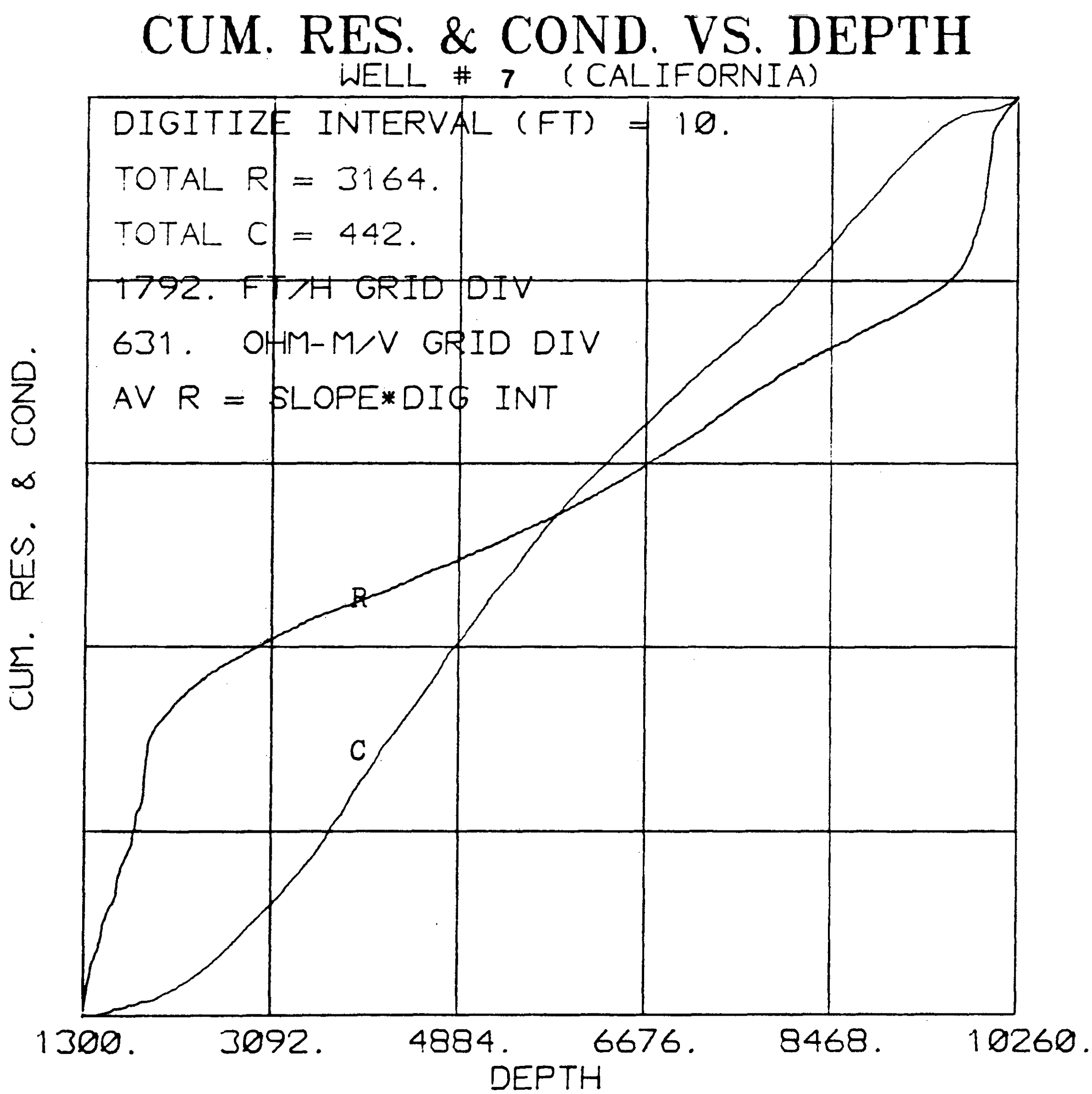
CUM. RES. & COND. VS. DEPTH
WELL # 7 (CALIFORNIA)
DIGITIZE INTERVAL (FT) = 10.
TOTAL R = 3164.
TOTAL C = 442.
1792. FT/H GRID DIV
631. OHM-M/V GRID DIV
AV R = SLOPE*DIG INT
R
C
CUM. RES. & COND.
1300.
3092.
4884.
6676.
8468.
10260.
DEPTH

CUM. RES. & COND. VS. DEPTH

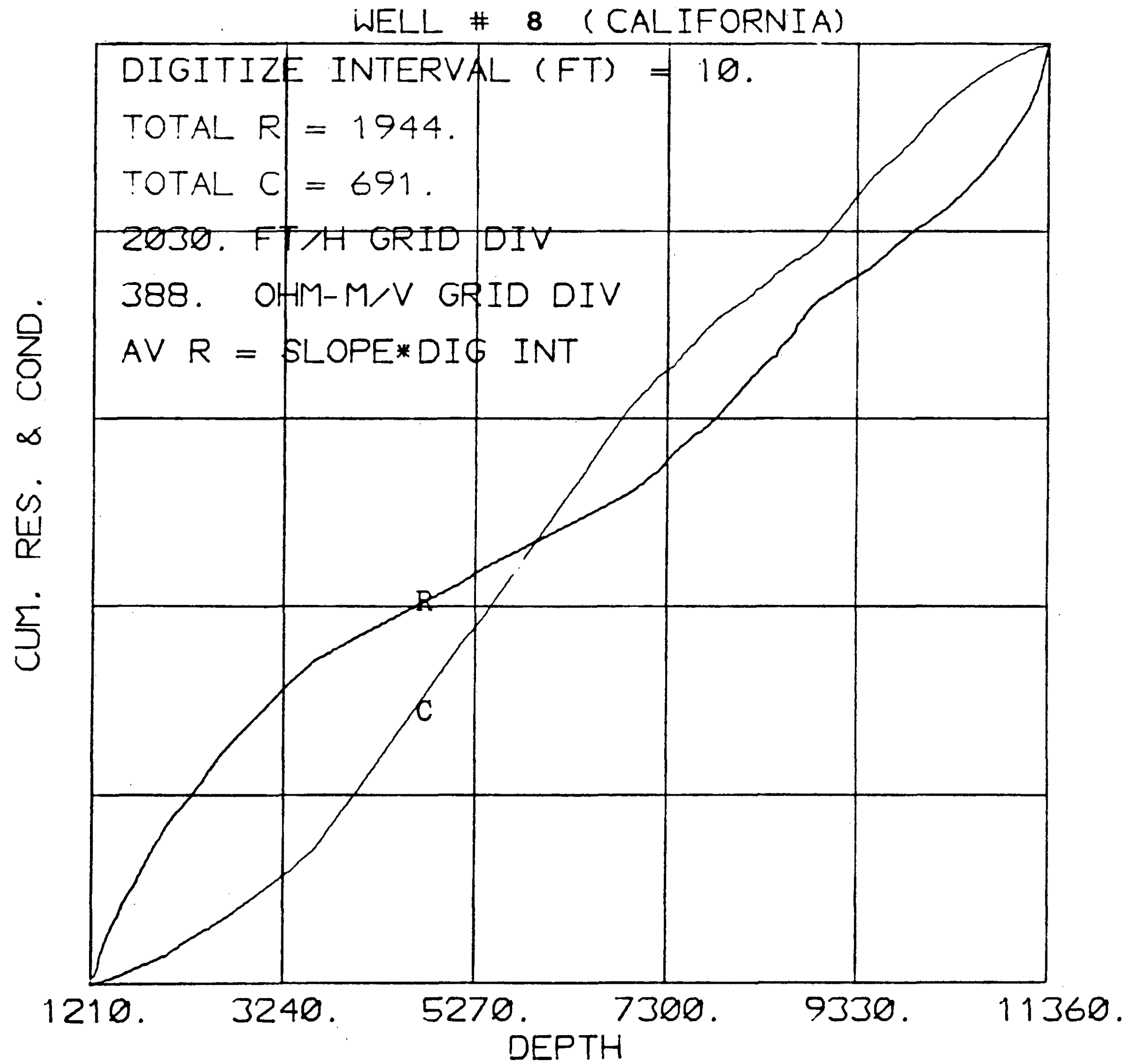

CUM. RES. & COND. VS. DEPTH

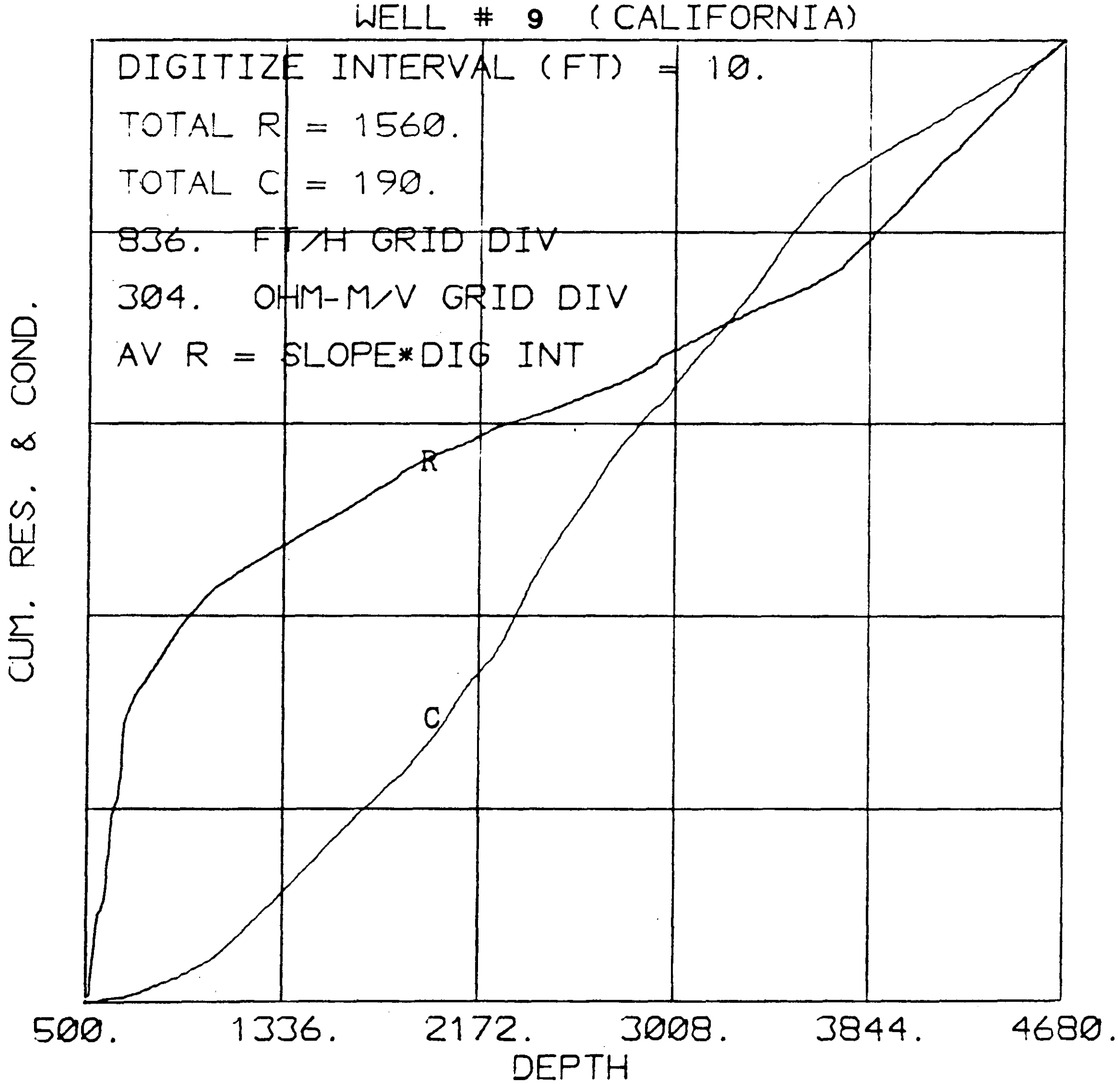

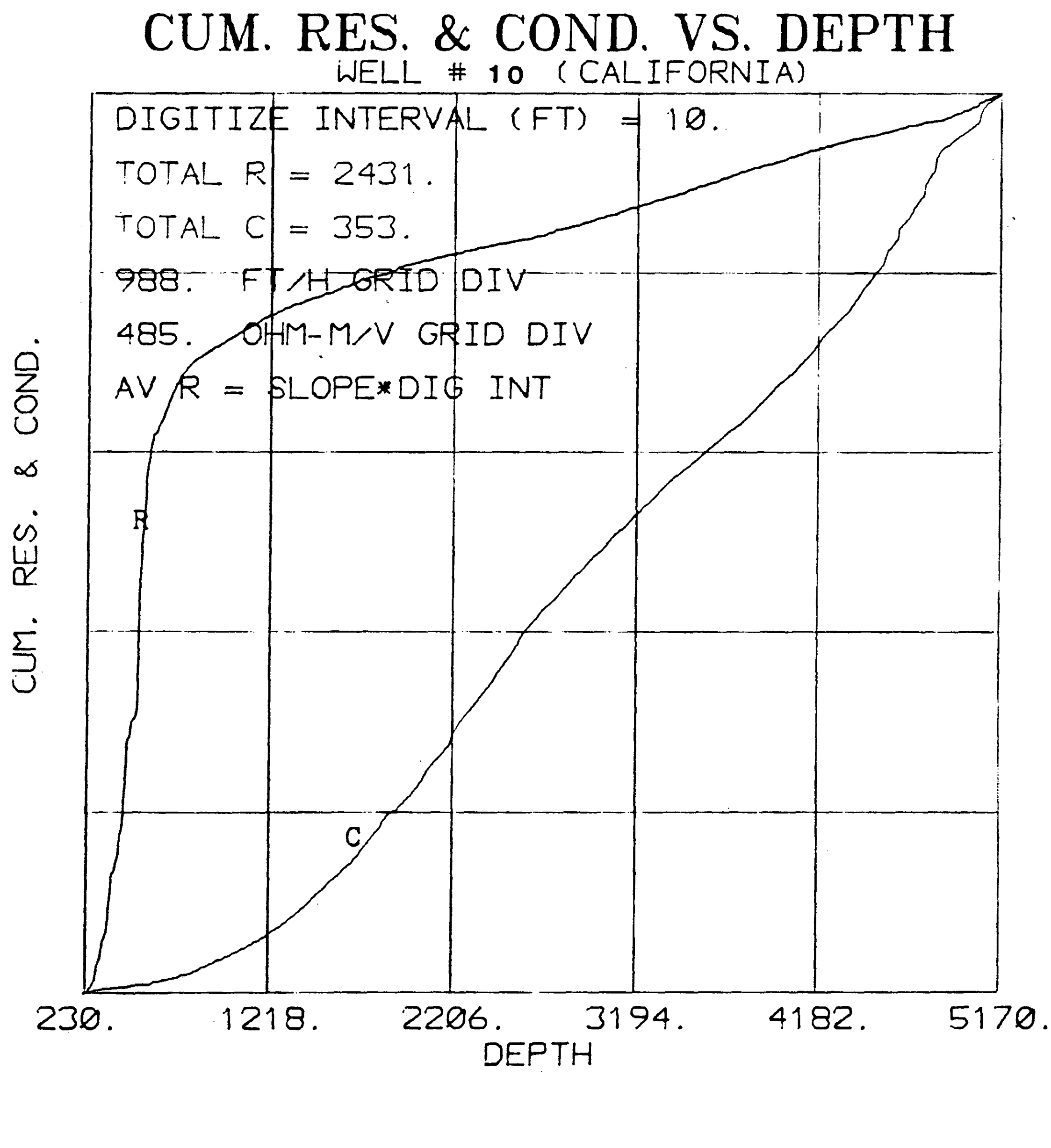
CUM. RES. & COND. VS. DEPTH
WELL # 10 (CALIFORNIA)
DIGITIZE INTERVAL (FT) = 10.
TOTAL R = 2431.
TOTAL C = 353.
988. FT/H GRID DIV
485. OHM-M/V GRID DIV
AV R = SLOPE*DIG INT
R
C
CUM. RES. & COND.
230.
1218.
2206.
3194.
4182.
5170.
DEPTH

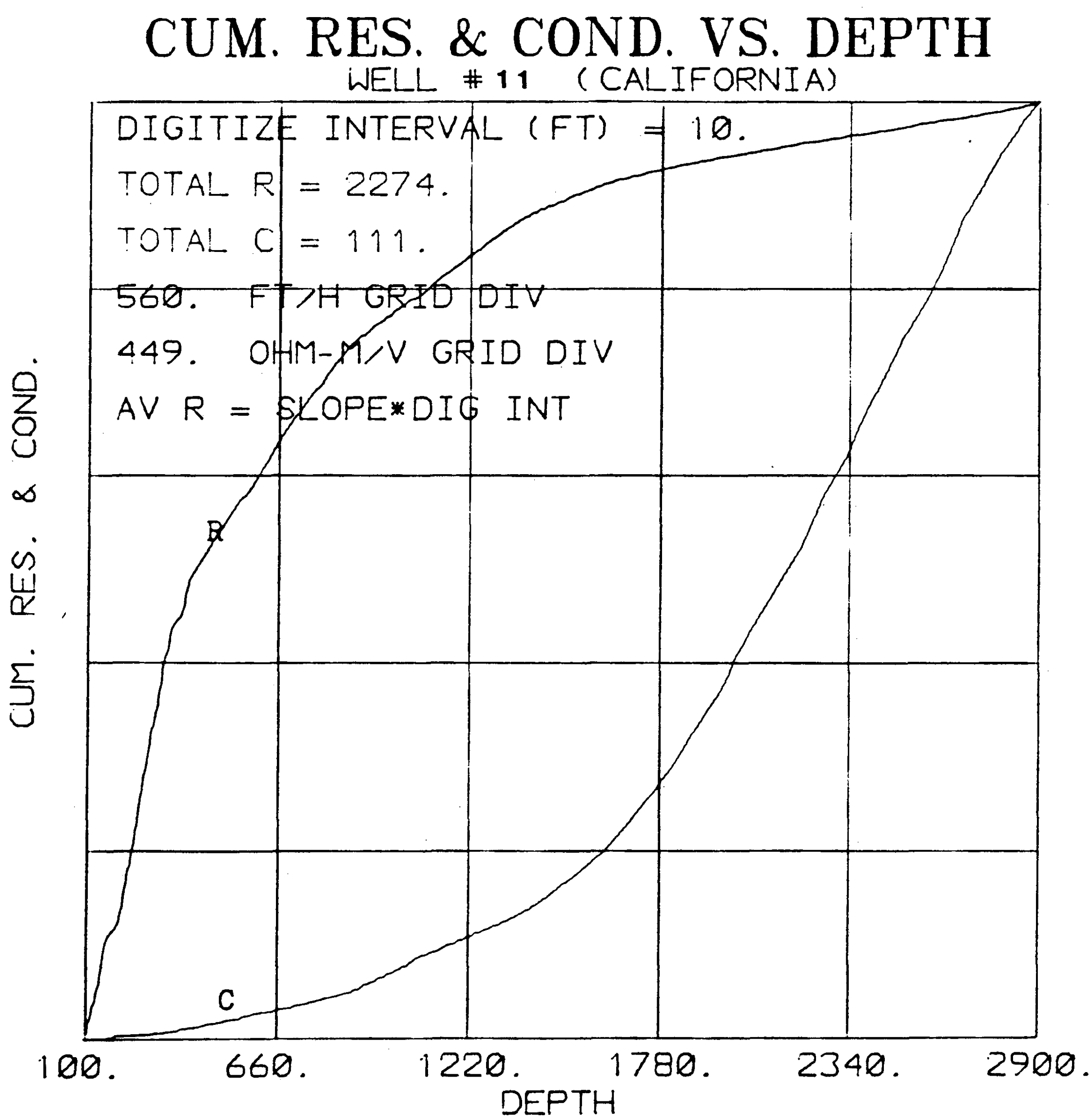
CUM. RES. & COND. VS. DEPTH
WELL # 11 (CALIFORNIA)
DIGITIZE INTERVAL (FT) = 10.
TOTAL R = 2274.
TOTAL C = 111.
560. FT/H GRID DIV
449. OHM-M/V GRID DIV
AV R = SLOPE*DIG INT
R
C
CUM. RES. & COND.
100.
660.
1220.
1780.
2340.
2900.
DEPTH

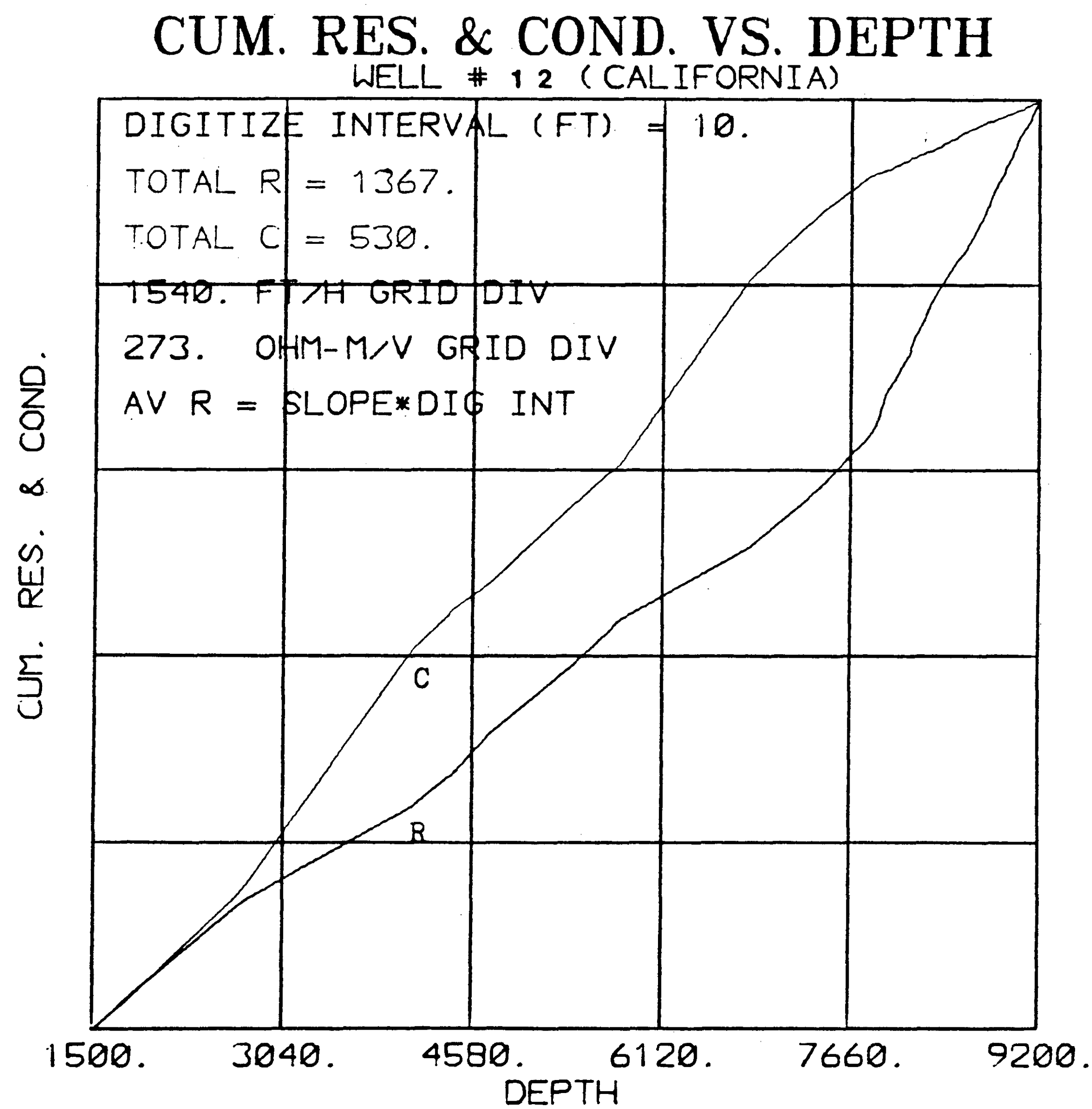
CUM. RES. & COND. VS. DEPTH
WELL # 12 (CALIFORNIA)
DIGITIZE INTERVAL (FT) = 10.
TOTAL R = 1367.
TOTAL C = 530.
1540. FT/H GRID DIV
273. OHM-M/V GRID DIV
AV R = SLOPE*DIG INT
C
R
CUM. RES. & COND.
1500.
3040.
4580.
6120.
7660.
9200.
DEPTH

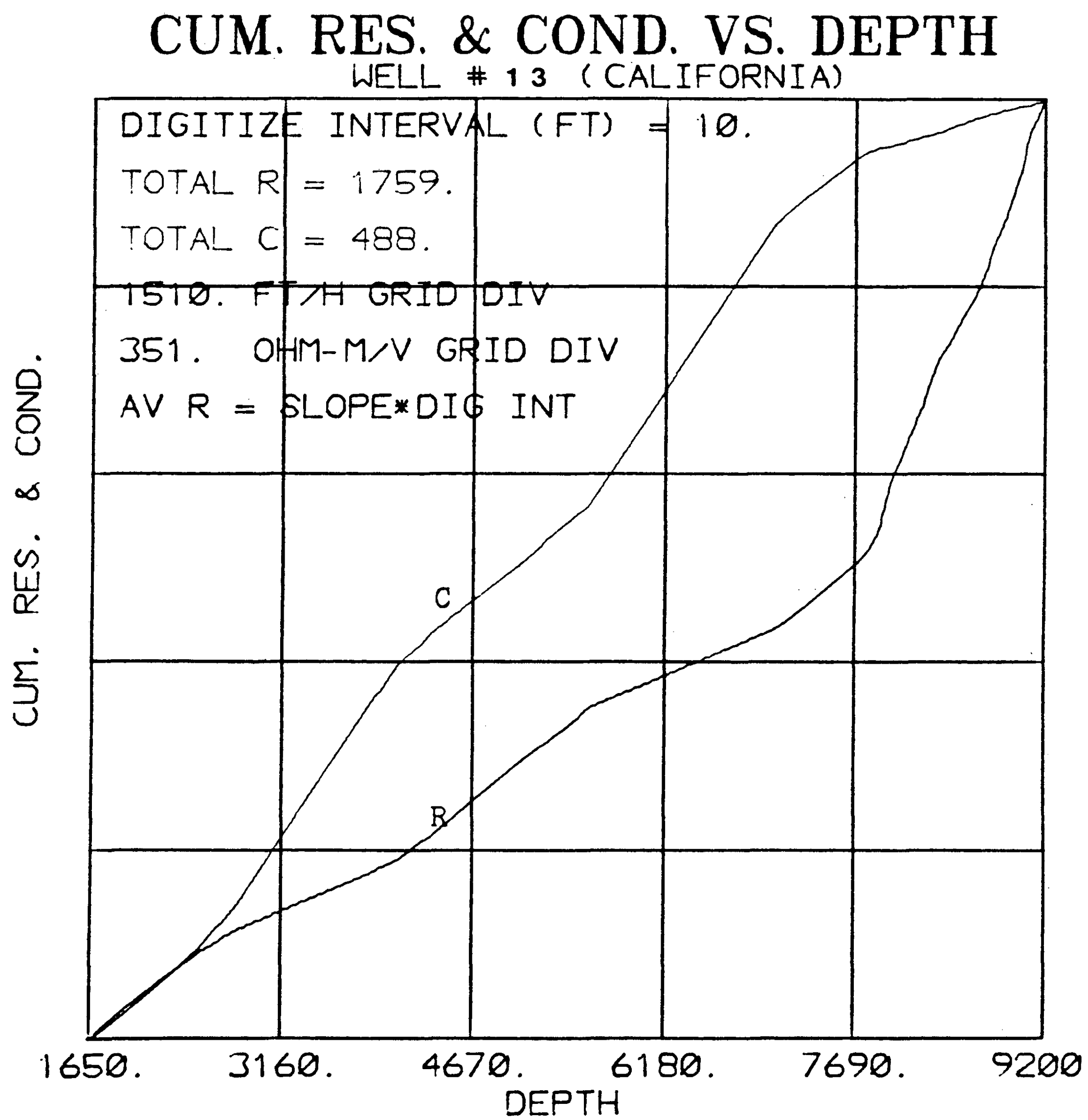
CUM. RES. & COND. VS. DEPTH
WELL # 13 (CALIFORNIA)
DIGITIZE INTERVAL (FT) = 10.
TOTAL R = 1759.
TOTAL C = 488.
1510. FT/H GRID DIV
351. OHM-M/V GRID DIV
AV R = SLOPE*DIG INT
C
R
CUM. RES. & COND.
1650.
3160.
4670.
6180.
7690.
9200.
DEPTH

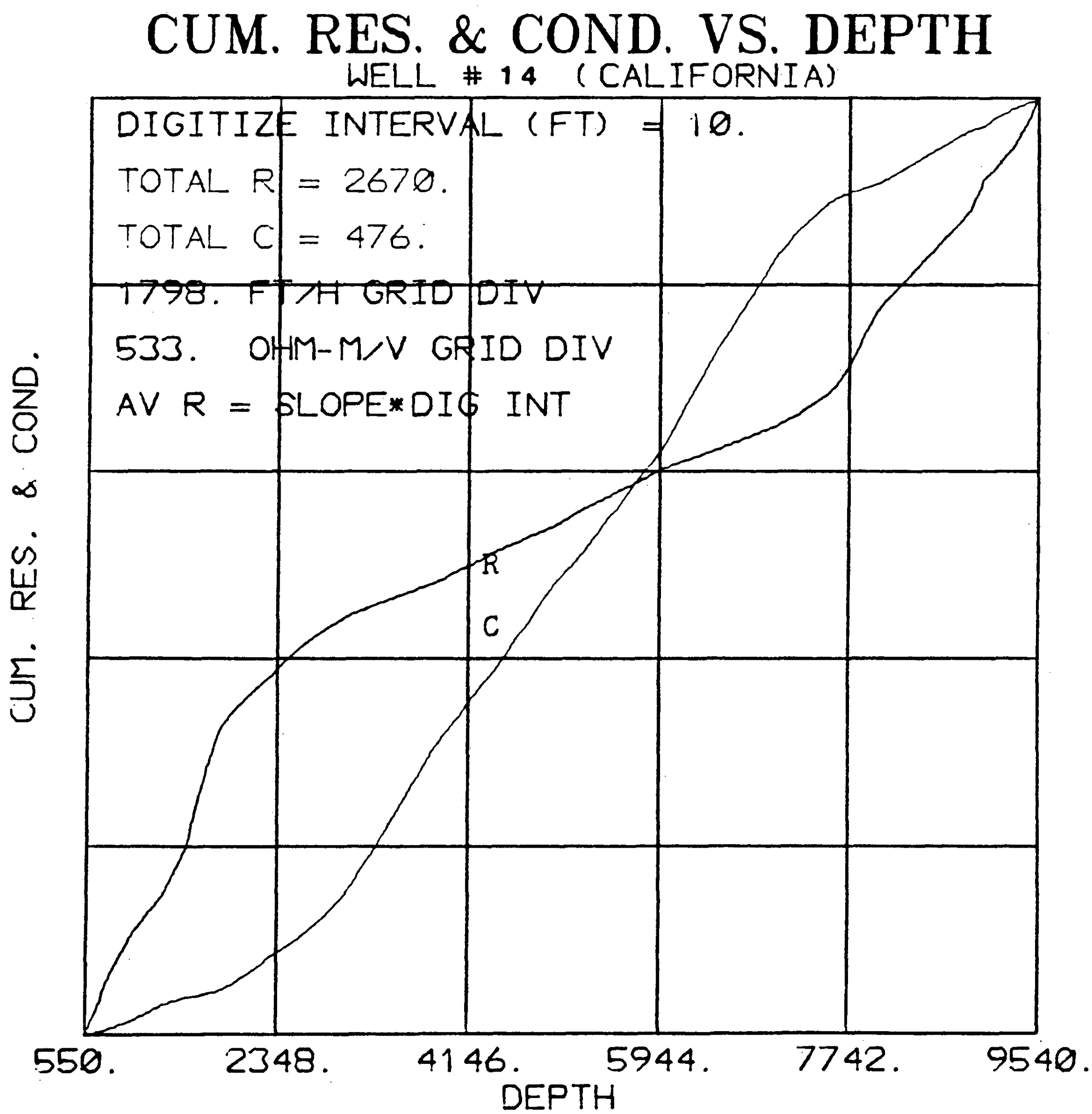
CUM. RES. & COND. VS. DEPTH
WELL # 14 (CALIFORNIA)
DIGITIZE INTERVAL (FT) = 10.
TOTAL R = 2670.
TOTAL C = 476.
1798. FT/H GRID DIV
533. OHM-M/V GRID DIV
AV R = SLOPE*DIG INT
R
C
550.
2348.
4146.
5944.
7742.
9540.
DEPTH
CUM. RES. & COND.

CUM. RES. & COND. VS. DEPTH

WELL # 15 (CALIFORNIA)

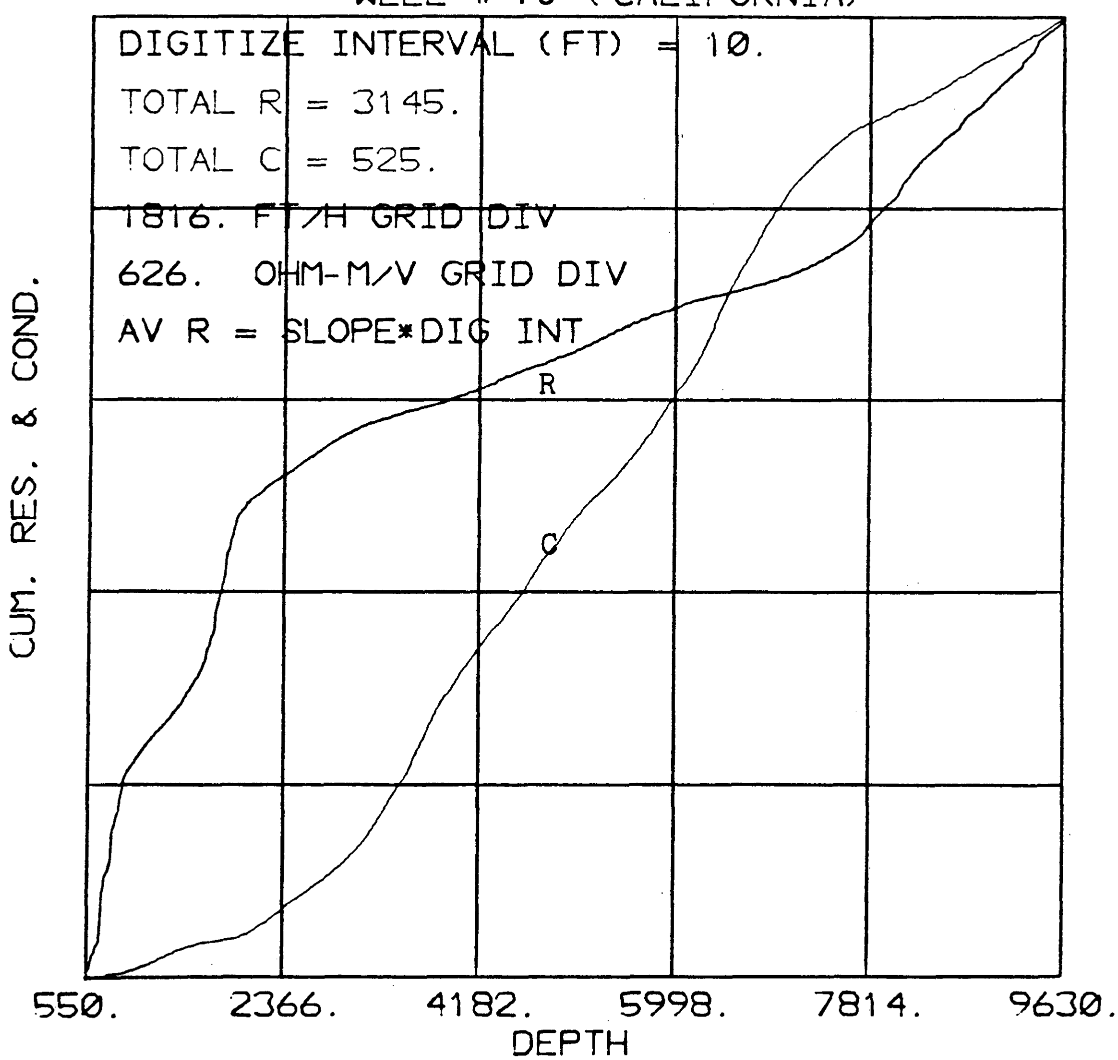

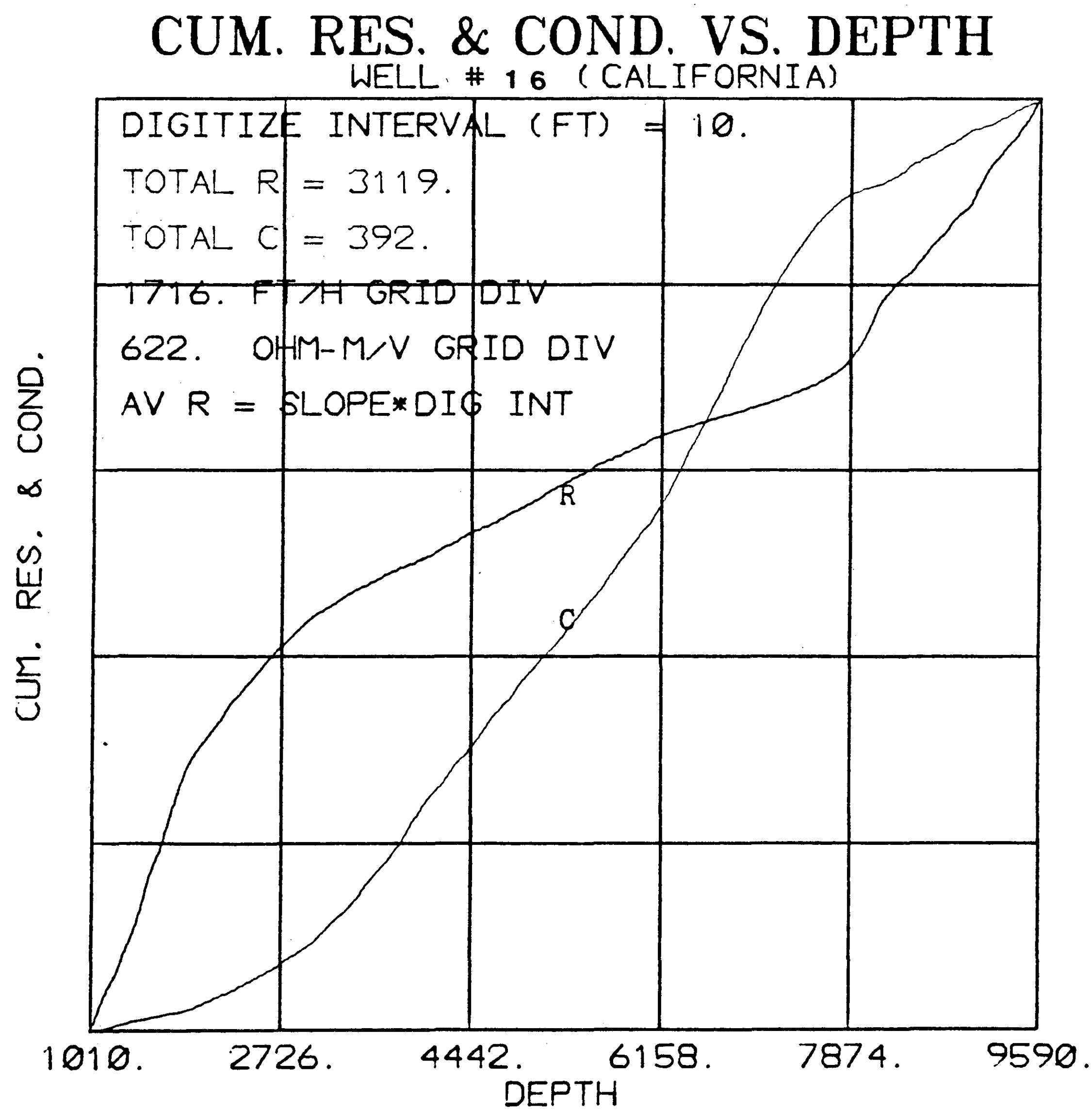
CUM. RES. & COND. VS. DEPTH
WELL # 16 (CALIFORNIA)
DIGITIZE INTERVAL (FT) = 10.
TOTAL R = 3119.
TOTAL C = 392.
1716. FT/H GRID DIV
622. OHM-M/V GRID DIV
AV R = SLOPE*DIG INT
R
C
CUM. RES. & COND.
1010.
2726.
4442.
6158.
7874.
9590.
DEPTH

CUM. RES. & COND. VS. DEPTH

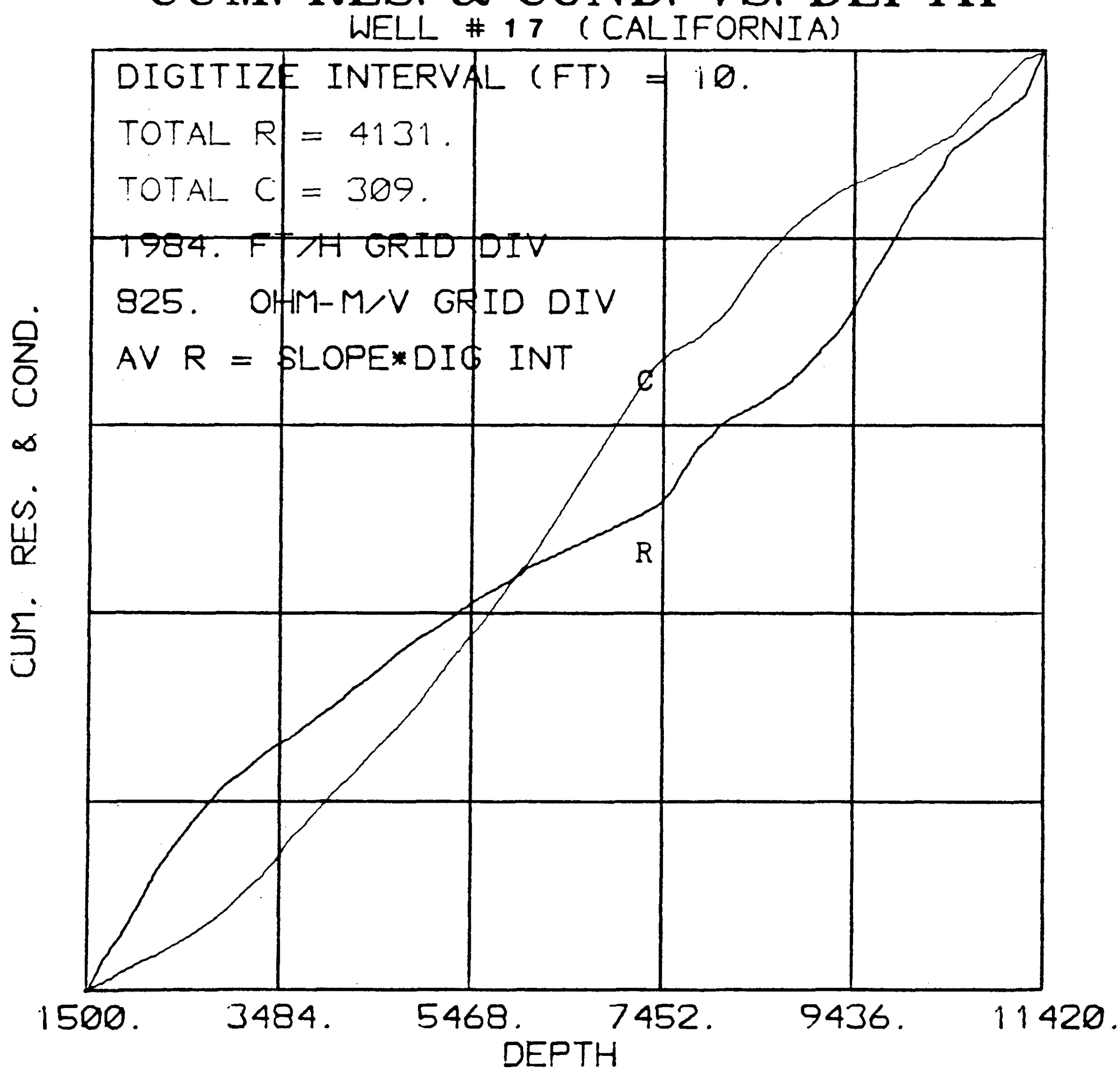

CUM. RES. & COND. VS. DEPTH

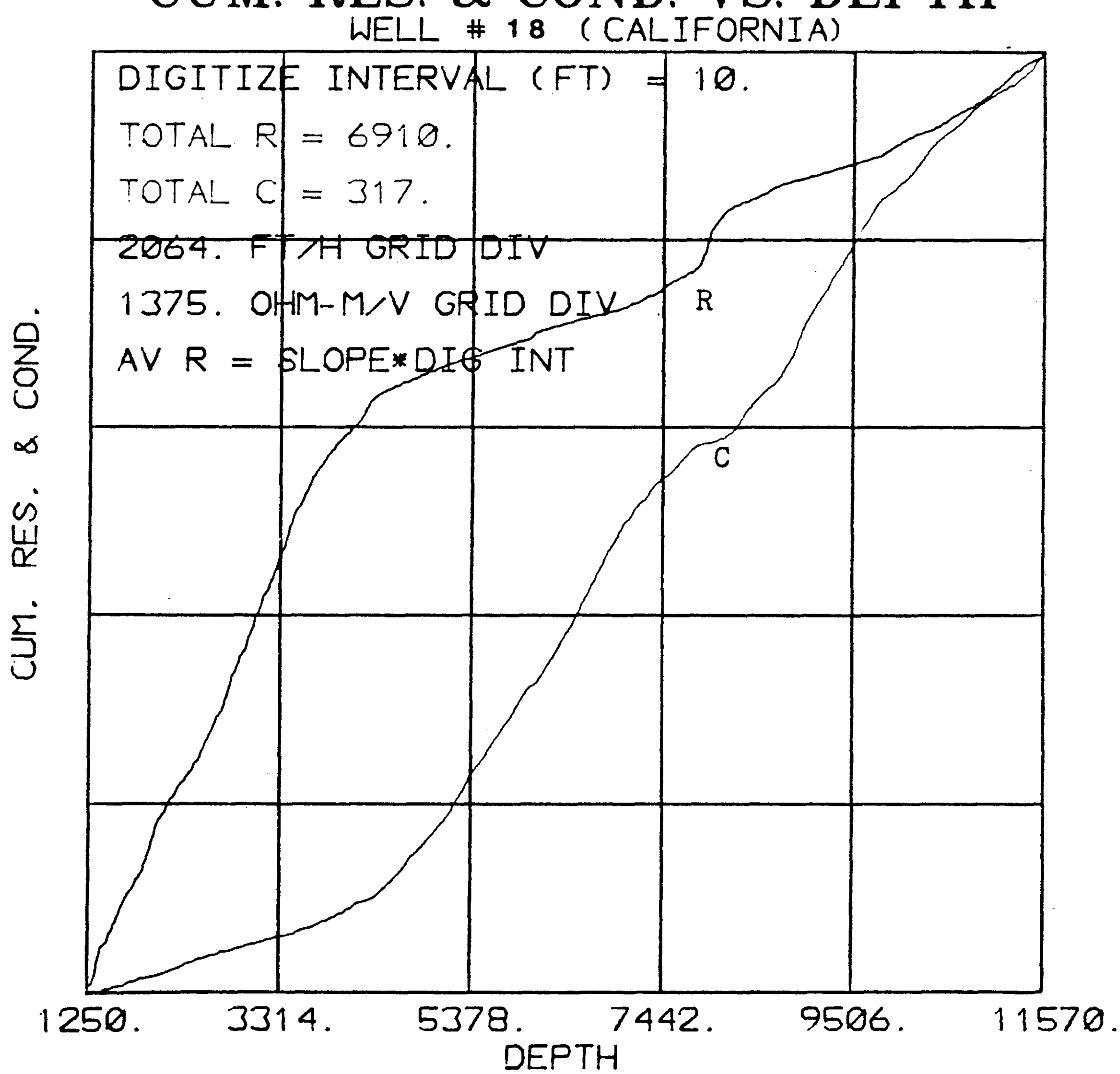

WELL # 1 (CALIFORNIA)

UNIT	DEPTH INTERVAL	AV.TRA.RES.	AV.LON.RES.	COEFF.ANISO.
1	1000.- 5900.	9.46	6.53	1.2033
2	5900.- 7880.	2.53	2.28	1.0541
3	7880.-10570.	1.99	1.43	1.1807

WELL # 2

1	510.- 3830.	27.92	13.59	1.4335
2	3830.- 7000.	2.29	2.06	1.0554

WELL # 3

1	540.- 3000.	5.97	3.81	1.2516
2	3000.- 5820.	1.39	1.27	1.0493

WELL # 4

1	1010.- 3470.	20.03	10.61	1.3742
2	3470.-11930.	2.57	2.35	1.0453
3	11930.-14330.	8.69	6.21	1.1834

WELL # 5

1	90.- 4330.	9.85	5.14	1.3848
2	4330.-10950.	2.69	2.11	1.1293
3	10950.-13500.	12.34	8.85	1.1813

WELL # 6

1	1000.- 3610.	7.62	3.22	1.5389
2	3610.-11200.	1.63	1.38	1.0850
3	11200.-12700.	6.50	4.64	1.1834

WELL # 7

1	1300.- 2420.	10.26	5.32	1.3889
2	2420.- 9700.	1.94	1.77	1.0480
3	9700.-10260.	10.49	6.37	1.2829
WELL # 8				
1	1210.- 1330.	6.00	4.17	1.1991
2	1330.-11180.	1.78	1.44	1.1117
3	11180.-11360.	6.55	5.77	1.0659
WELL # 9				
1	500.- 1060.	12.24	5.99	1.4293
2	1060.- 3710.	1.89	1.73	1.0429
3	3710.- 4680.	3.72	3.48	1.0338
WELL # 10				
1	230.- 1190.	18.85	4.46	2.0561
2	1190.- 5170.	1.52	1.20	1.1237
WELL # 11				
1	100.- 1460.	14.79	8.06	1.3550
2	1460.- 2900.	1.73	1.54	1.0602
WELL # 12				
1	1500.- 7820.	1.38	1.30	1.0323
2	7820.- 9200.	3.55	3.21	1.0517
WELL # 13				
1	1650.- 7840.	1.51	1.34	1.0602
2	7840.- 9200.	6.06	5.31	1.0680
WELL # 14				

1	550.- 2740.	5.21	3.84	1.1647
2	2740.- 7650.	1.46	1.33	1.0471
3	7650.- 9540.	4.27	3.78	1.0626
WELL # 15				
1	550.- 1940.	10.85	6.29	1.3139
2	1940.- 7680.	1.58	1.30	1.1033
3	7680.- 9630.	3.71	3.20	1.0754
WELL # 16				
1	1010.- 2900.	7.13	5.64	1.1240
2	2900.- 7780.	1.77	1.55	1.0710
3	7780.- 9590.	4.97	4.24	1.0827
WELL # 17				
1	1500.- 2760.	6.45	5.74	1.0603
2	2760.- 7480.	2.85	2.54	1.0595
3	7480.-11420.	4.99	3.92	1.1284
WELL # 18				
1	1250.- 4360.	14.13	9.47	1.2214
2	4360.- 7020.	2.42	2.13	1.0655
3	7020.-11570.	4.09	2.86	1.1953

AHHENDIX 2 : Resistivity-integral plots & geoelectrical parameters,Oklahoma.

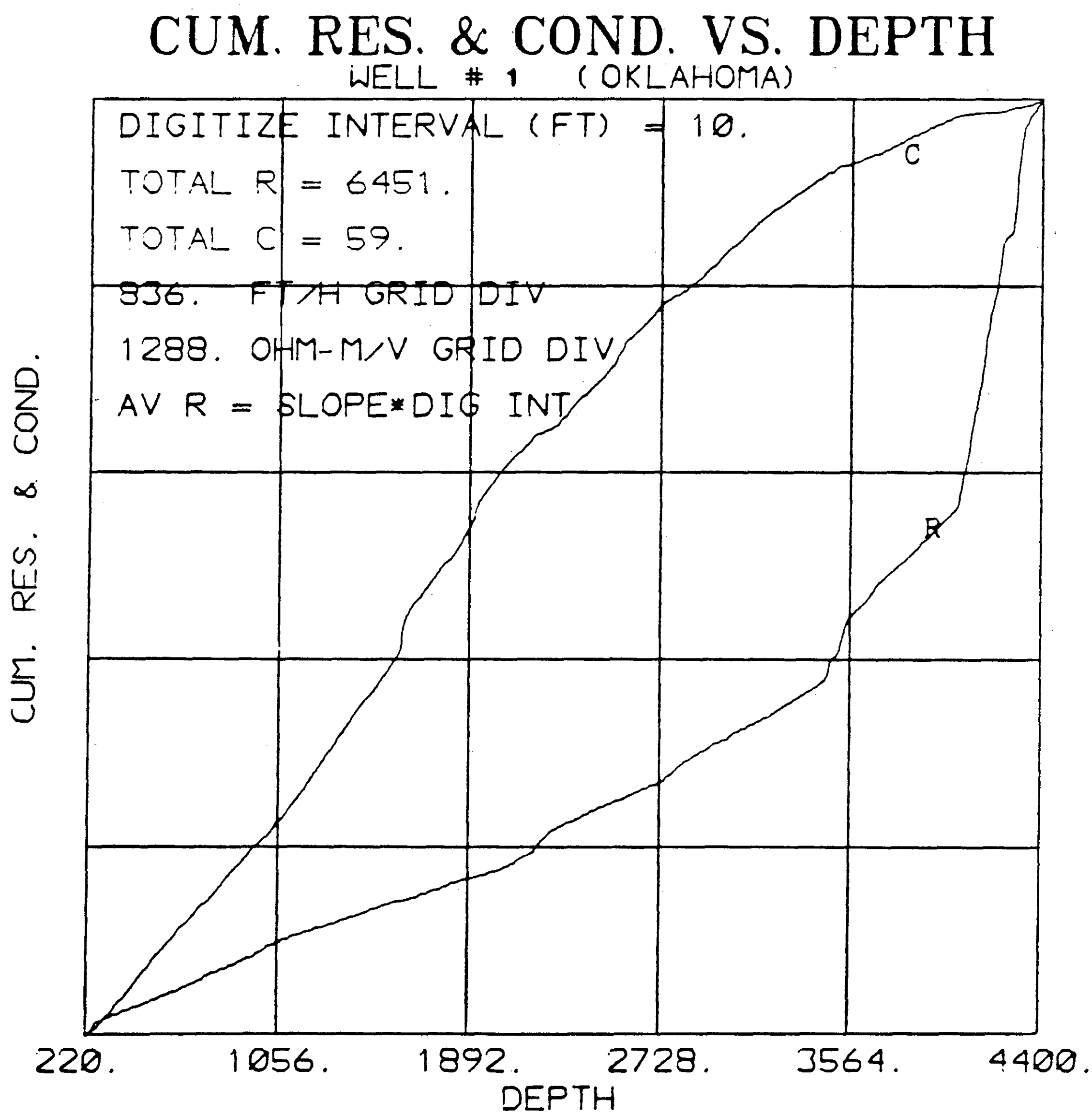

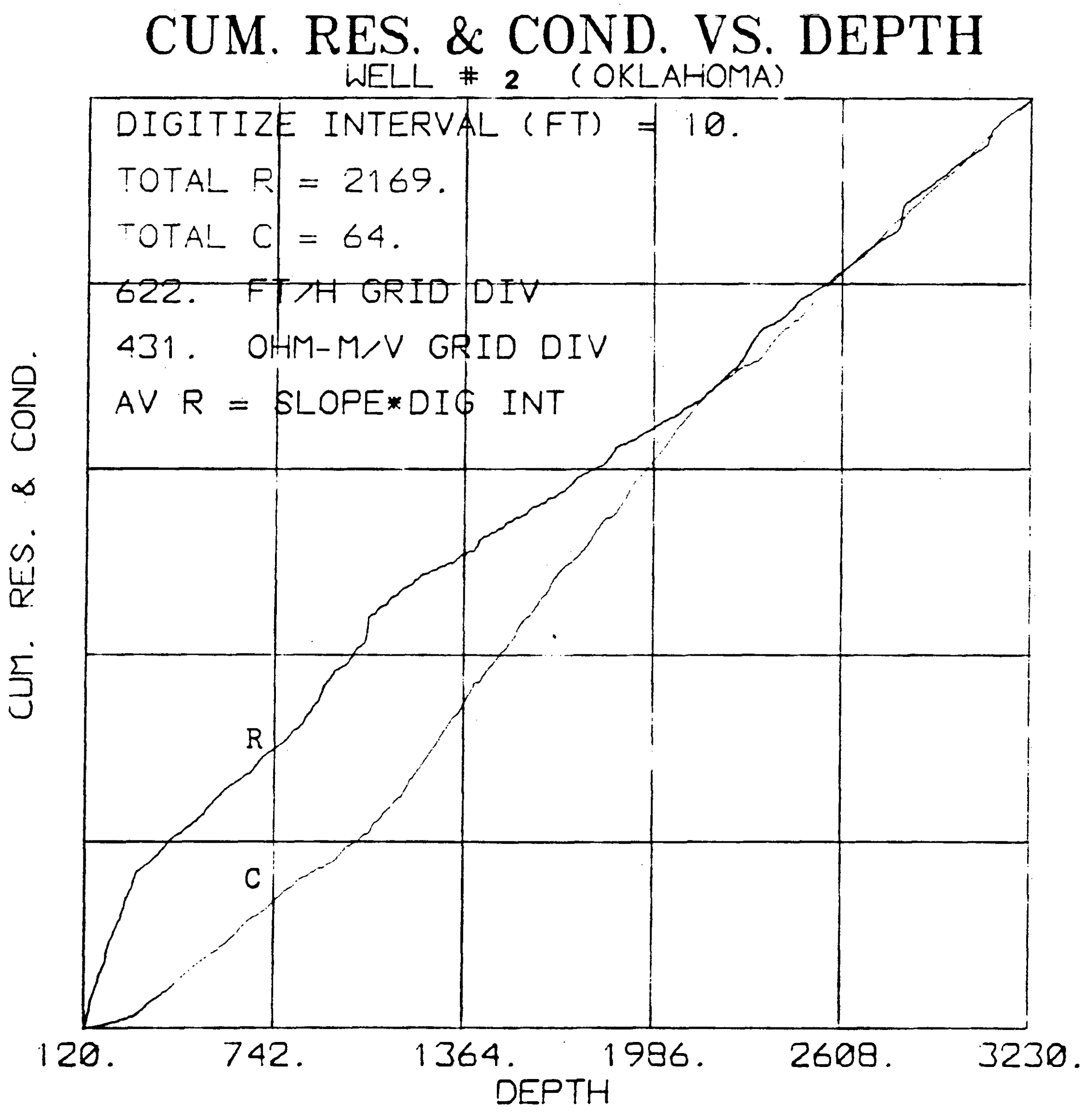
CUM. RES. & COND. VS. DEPTH
WELL # 2 (OKLAHOMA)
DIGITIZE INTERVAL (FT) = 10.
TOTAL R = 2169.
TOTAL C = 64.
622. FT/H GRID DIV
431. OHM-M/V GRID DIV
AV R = SLOPE*DIG INT
R
C
CUM. RES. & COND.
120.
742.
1364.
1986.
2608.
3230.
DEPTH

CUM. RES. & COND. VS. DEPTH

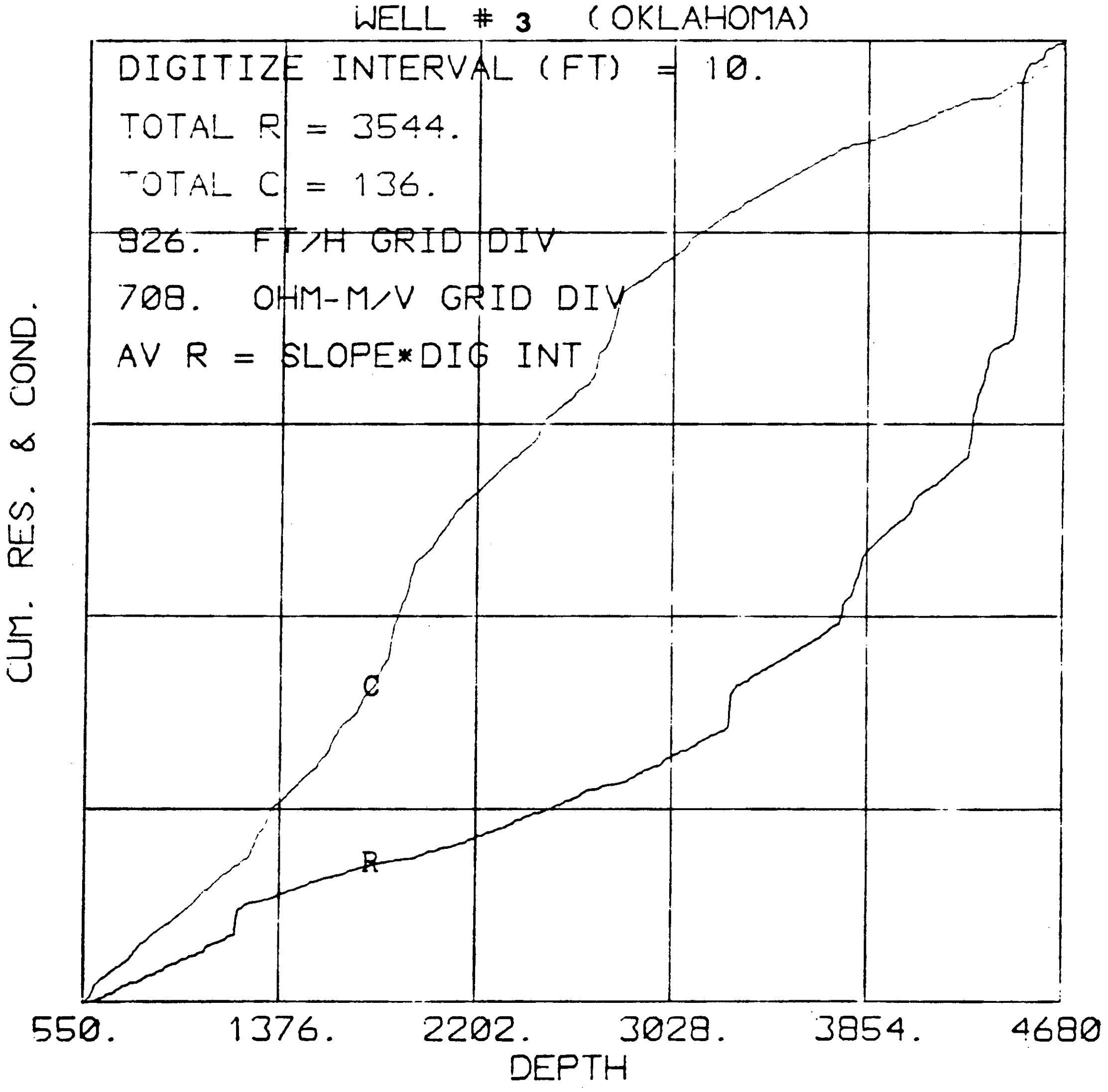

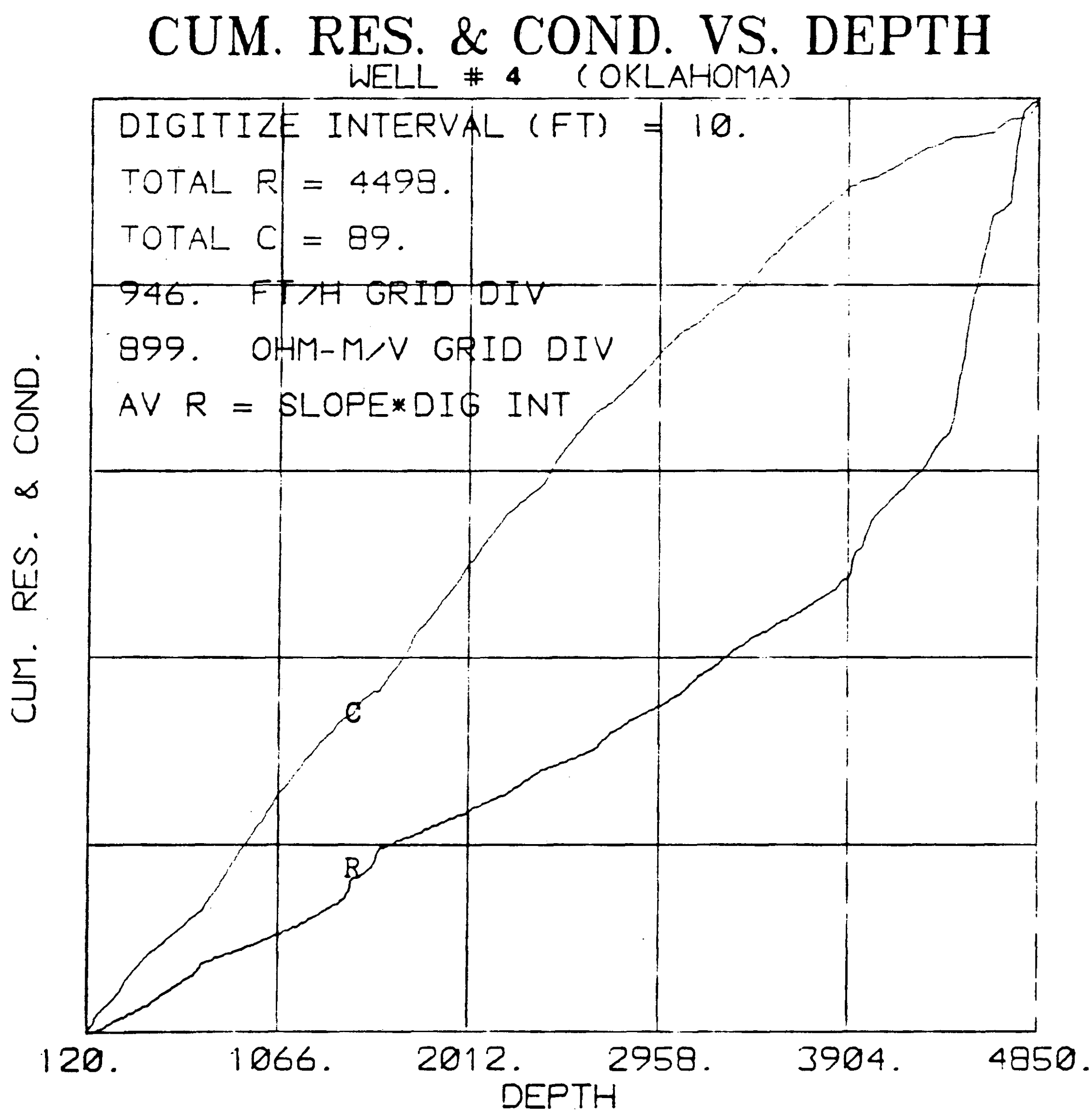
CUM. RES. & COND. VS. DEPTH
WELL # 4 (OKLAHOMA)
DIGITIZE INTERVAL (FT) = 10.
TOTAL R = 4498.
TOTAL C = 89.
946. FT/H GRID DIV
899. OHM-M/V GRID DIV
AV R = SLOPE*DIG INT
C
R
CUM. RES. & COND.
120.
1066.
2012.
2958.
3904.
4850.
DEPTH

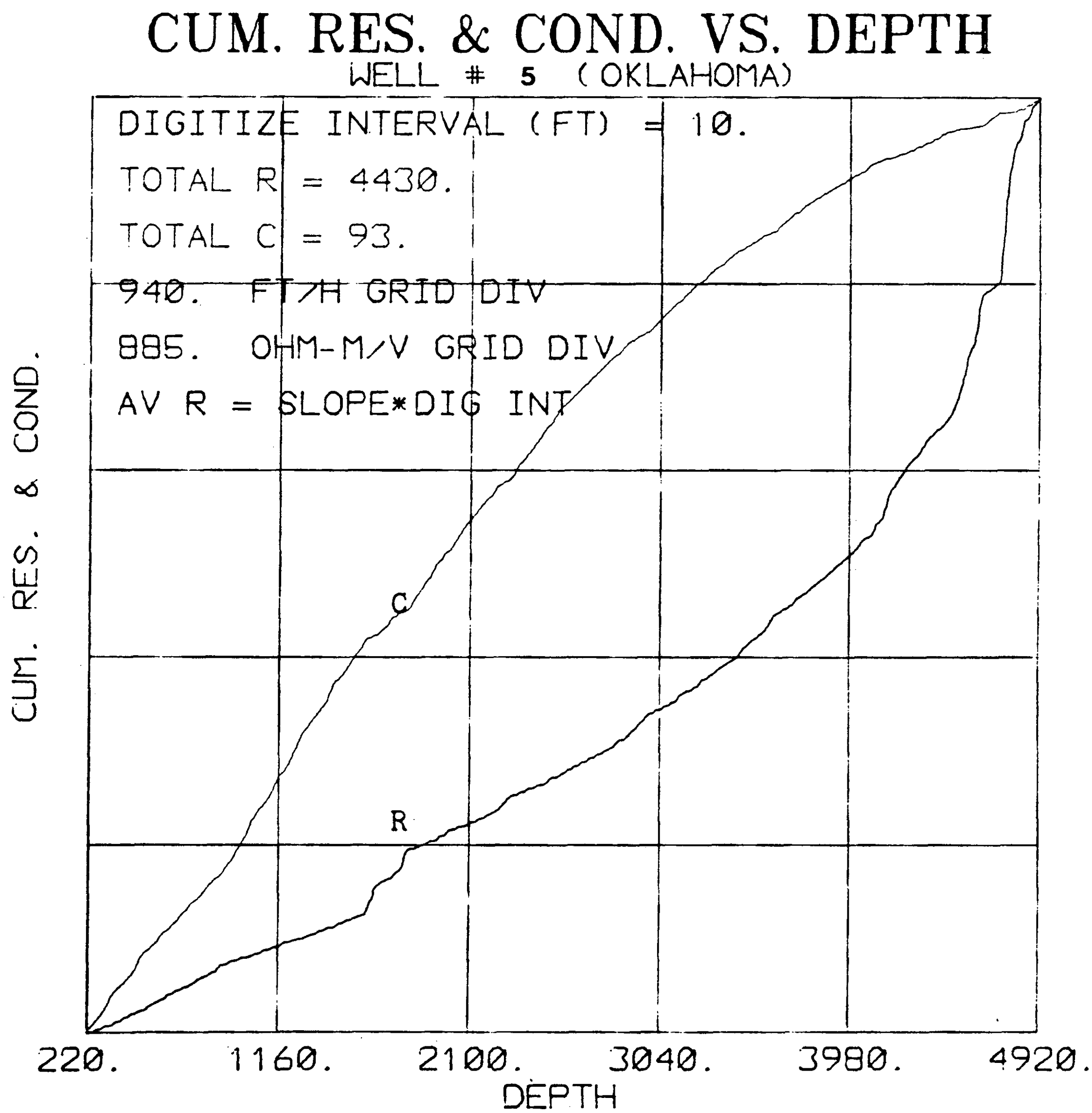
CUM. RES. & COND. VS. DEPTH
WELL # 5 (OKLAHOMA)
DIGITIZE INTERVAL (FT) = 10.
TOTAL R = 4430.
TOTAL C = 93.
940. FT/H GRID DIV
885. OHM-M/V GRID DIV
AV R = SLOPE*DIG INT
C
R
CUM. RES. & COND.
220.
1160.
2100.
3040.
3980.
4920.
DEPTH

CUM. RES. & COND. VS. DEPTH

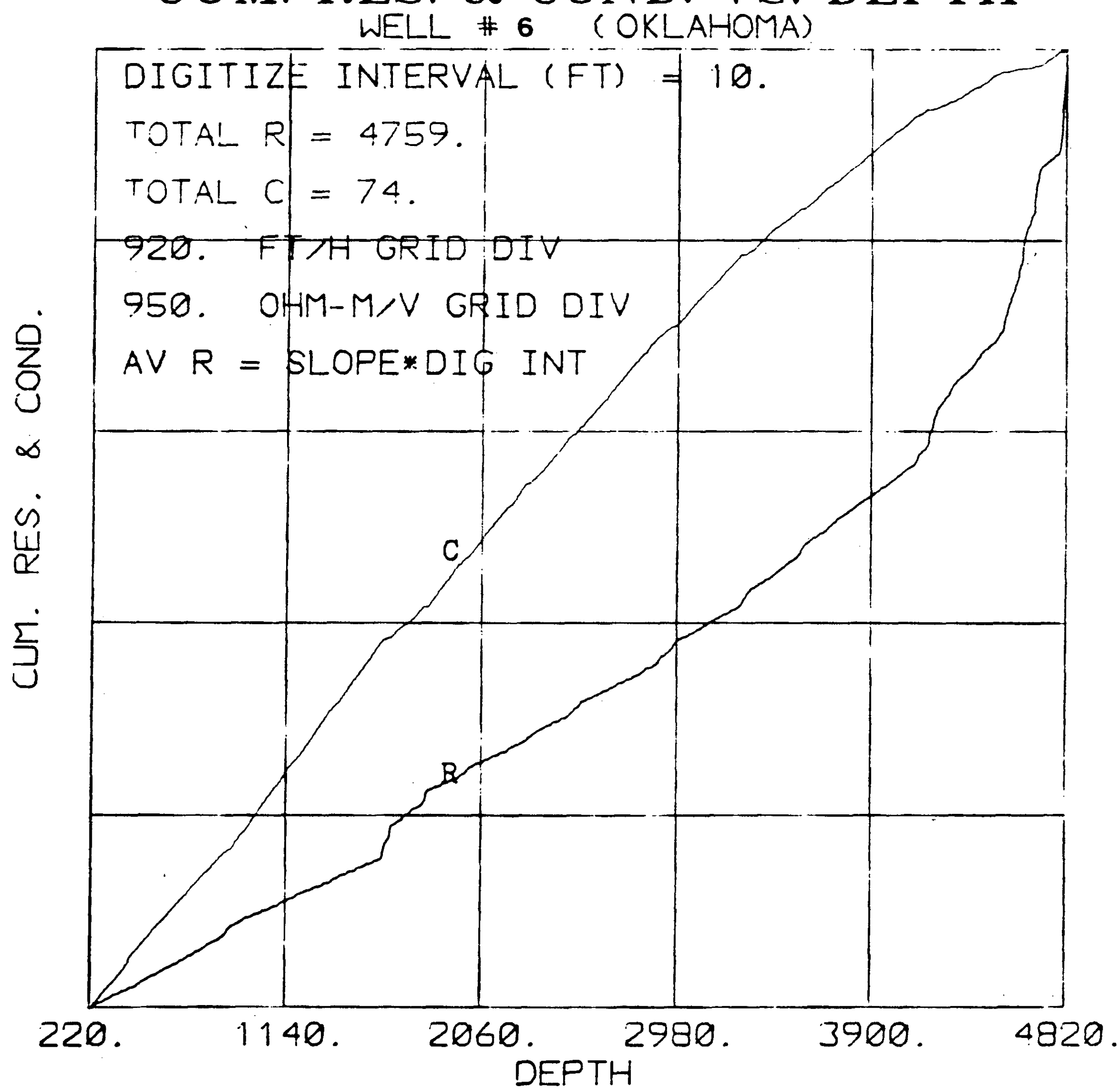

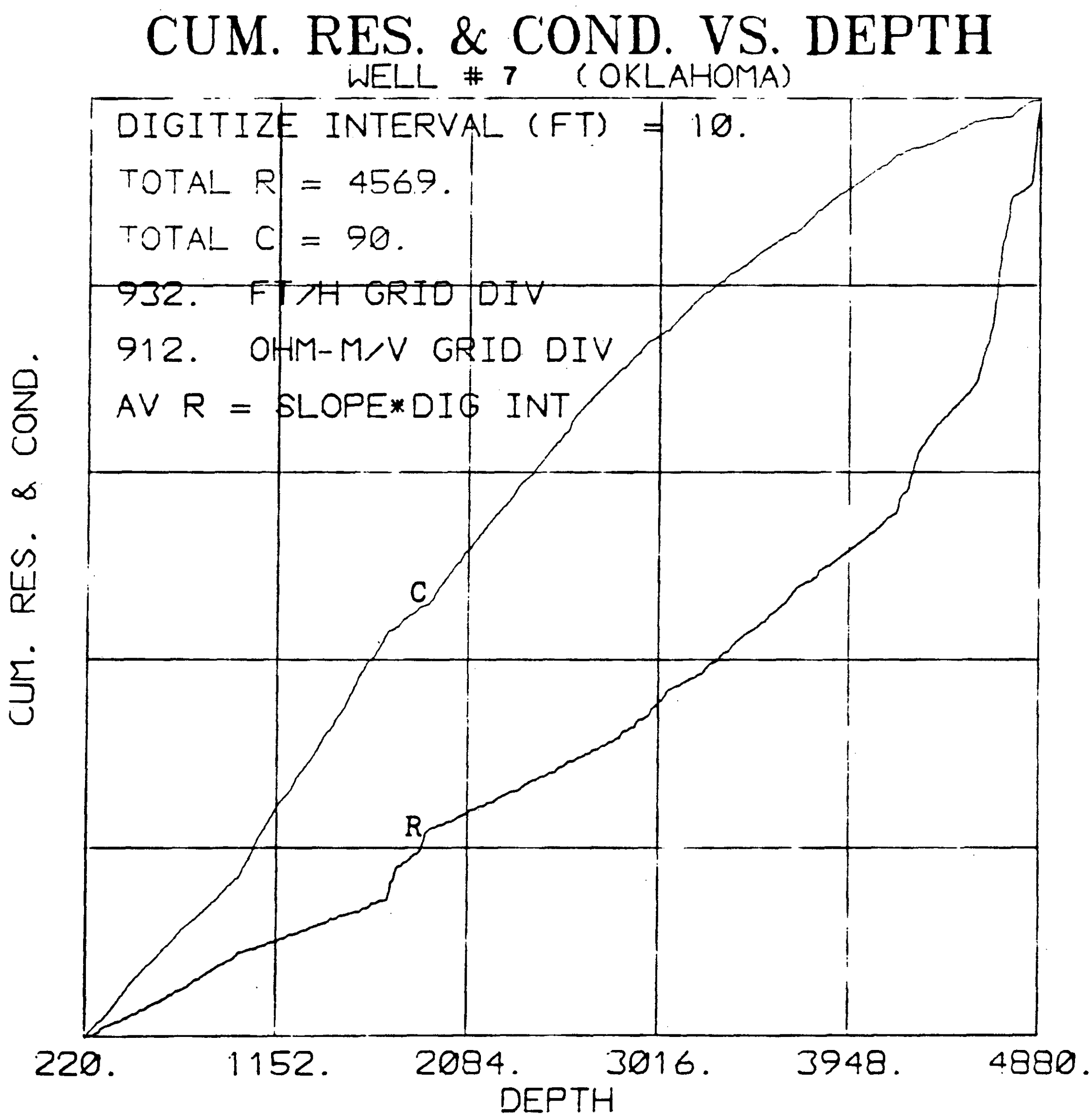
CUM. RES. & COND. VS. DEPTH
WELL # 7 (OKLAHOMA)
DIGITIZE INTERVAL (FT) = 10.
TOTAL R = 4569.
TOTAL C = 90.
932. FT/H GRID DIV
912. OHM-M/V GRID DIV
AV R = SLOPE*DIG INT
C
R
CUM. RES. & COND.
220.
1152.
2084.
3016.
3948.
4880.
DEPTH

CUM. RES. & COND. VS. DEPTH

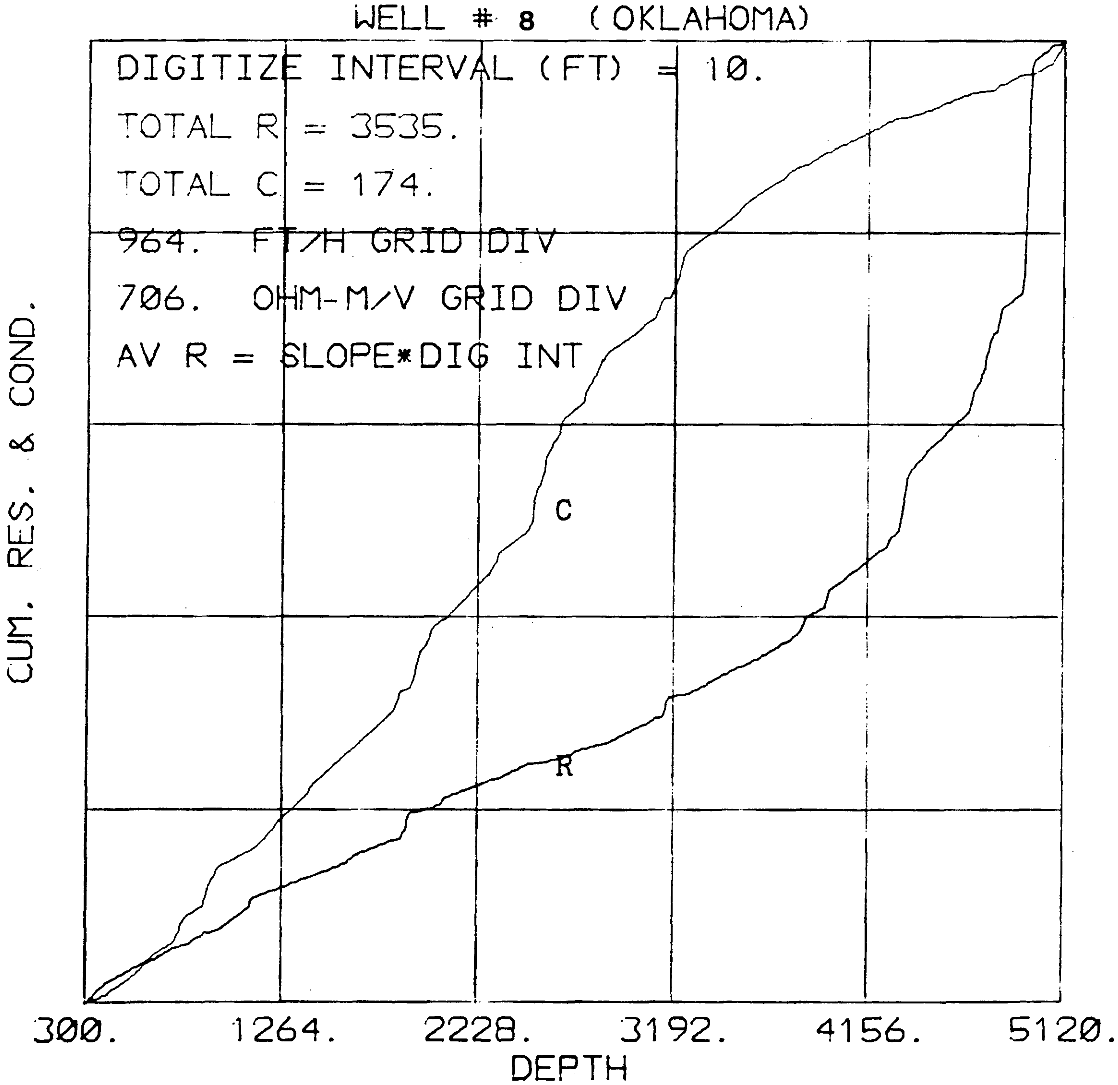

CUM. RES. & COND. VS. DEPTH

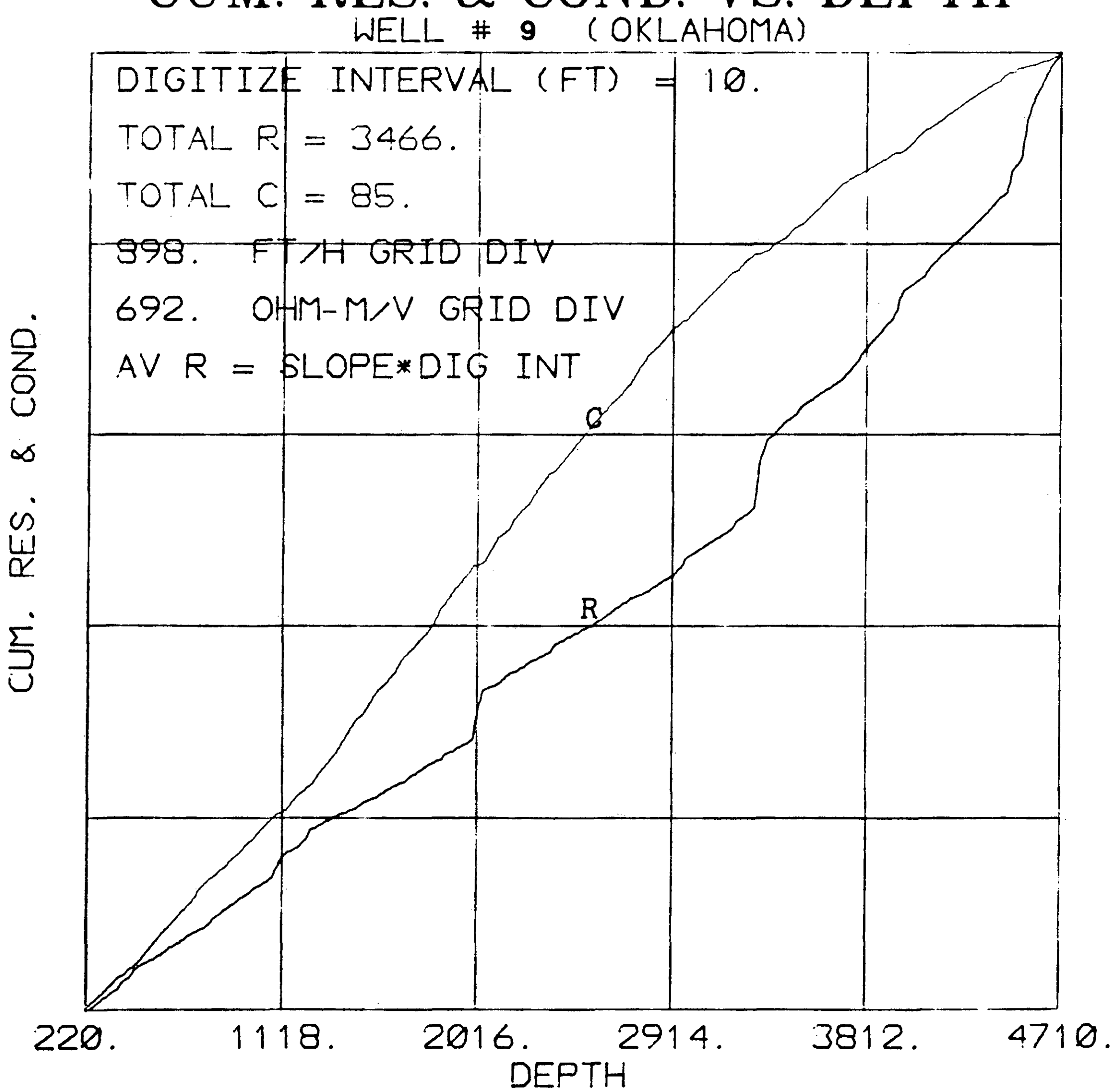

CUM. RES. & COND. VS. DEPTH

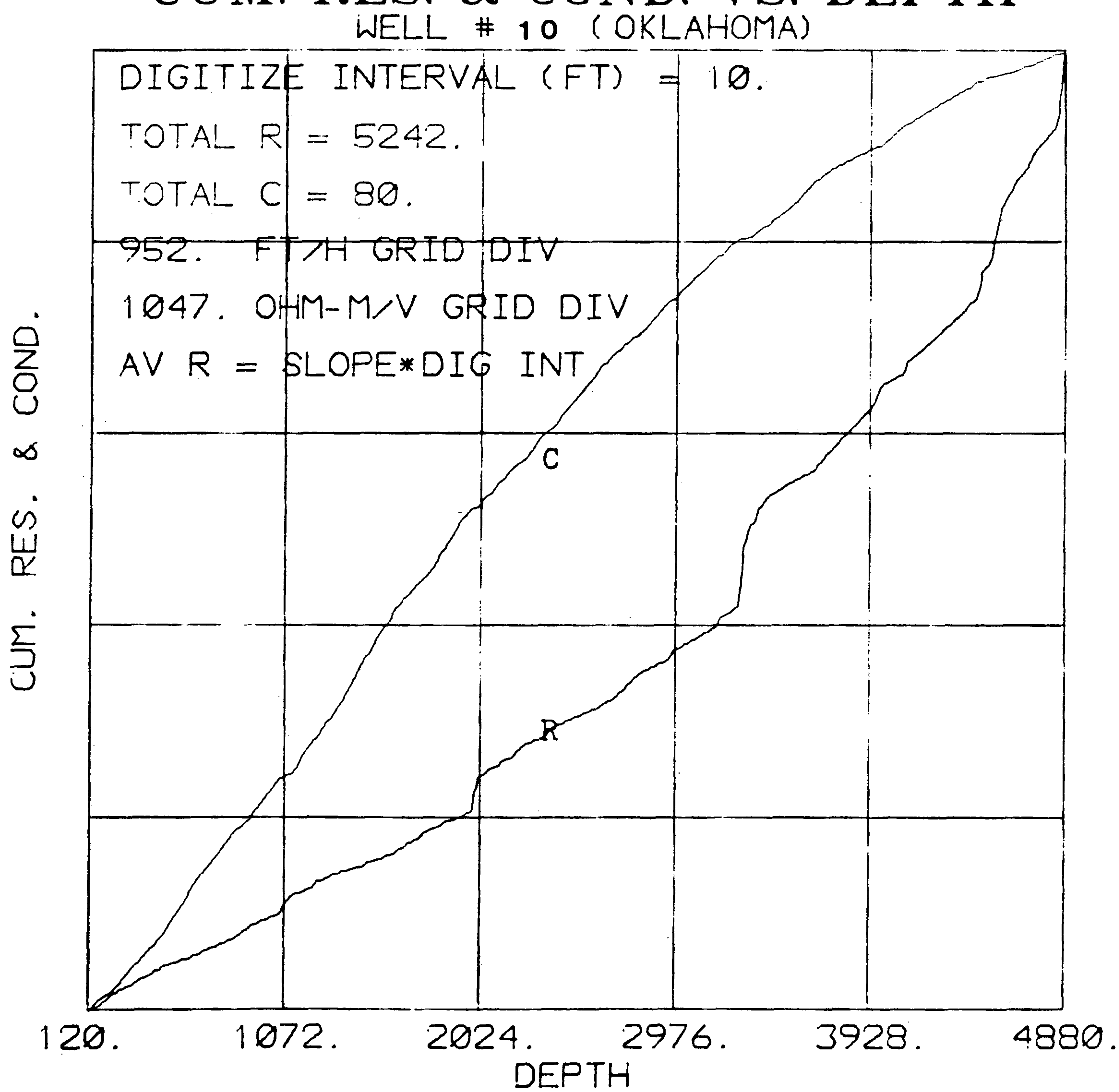

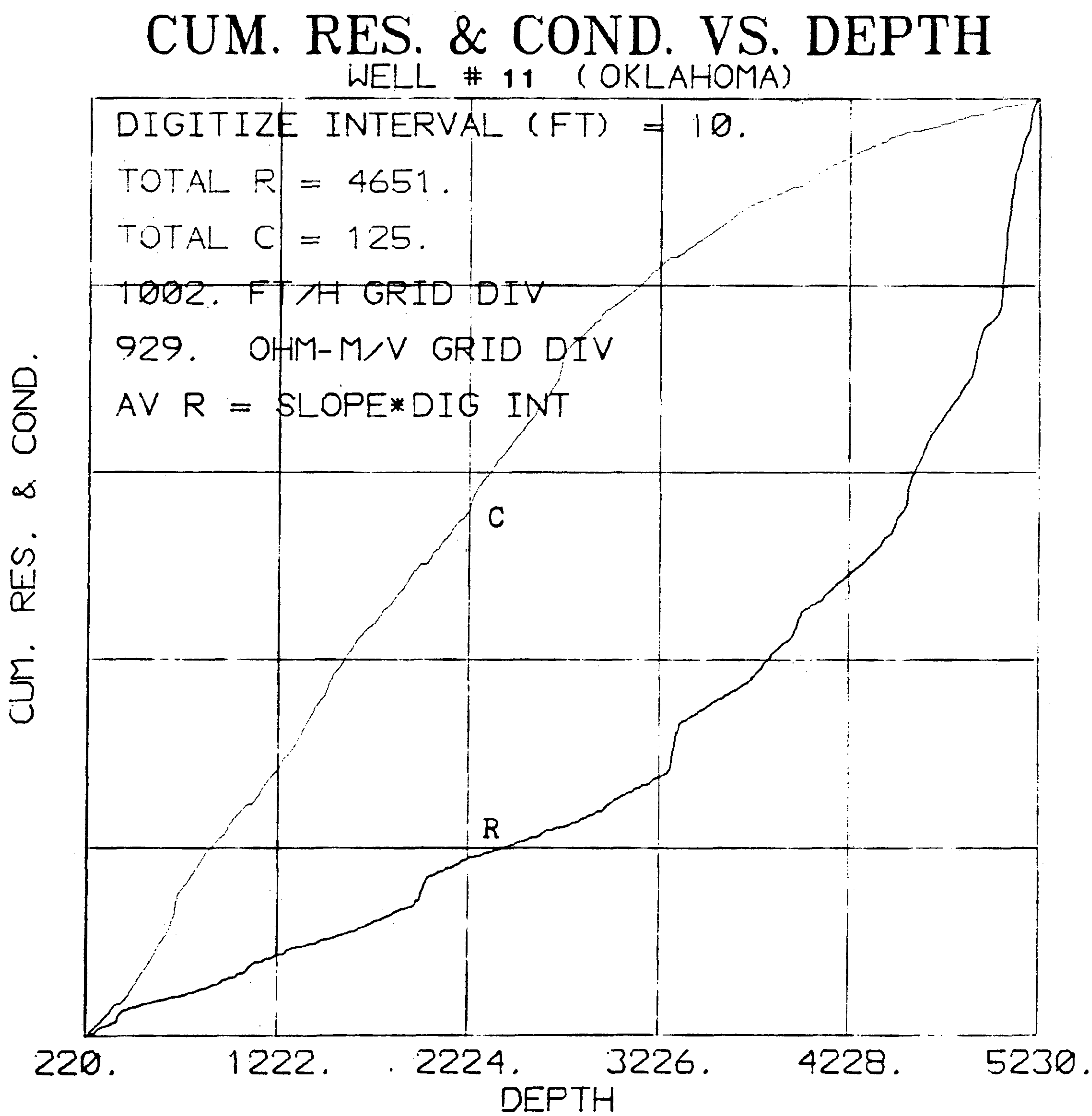
CUM. RES. & COND. VS. DEPTH
WELL # 11 (OKLAHOMA)
DIGITIZE INTERVAL (FT) = 10.
TOTAL R = 4651.
TOTAL C = 125.
1002. FT/H GRID DIV
929. OHM-M/V GRID DIV
AV R = SLOPE*DIG INT
C
R
CUM. RES. & COND.
220.
1222.
2224.
3226.
4228.
5230.
DEPTH

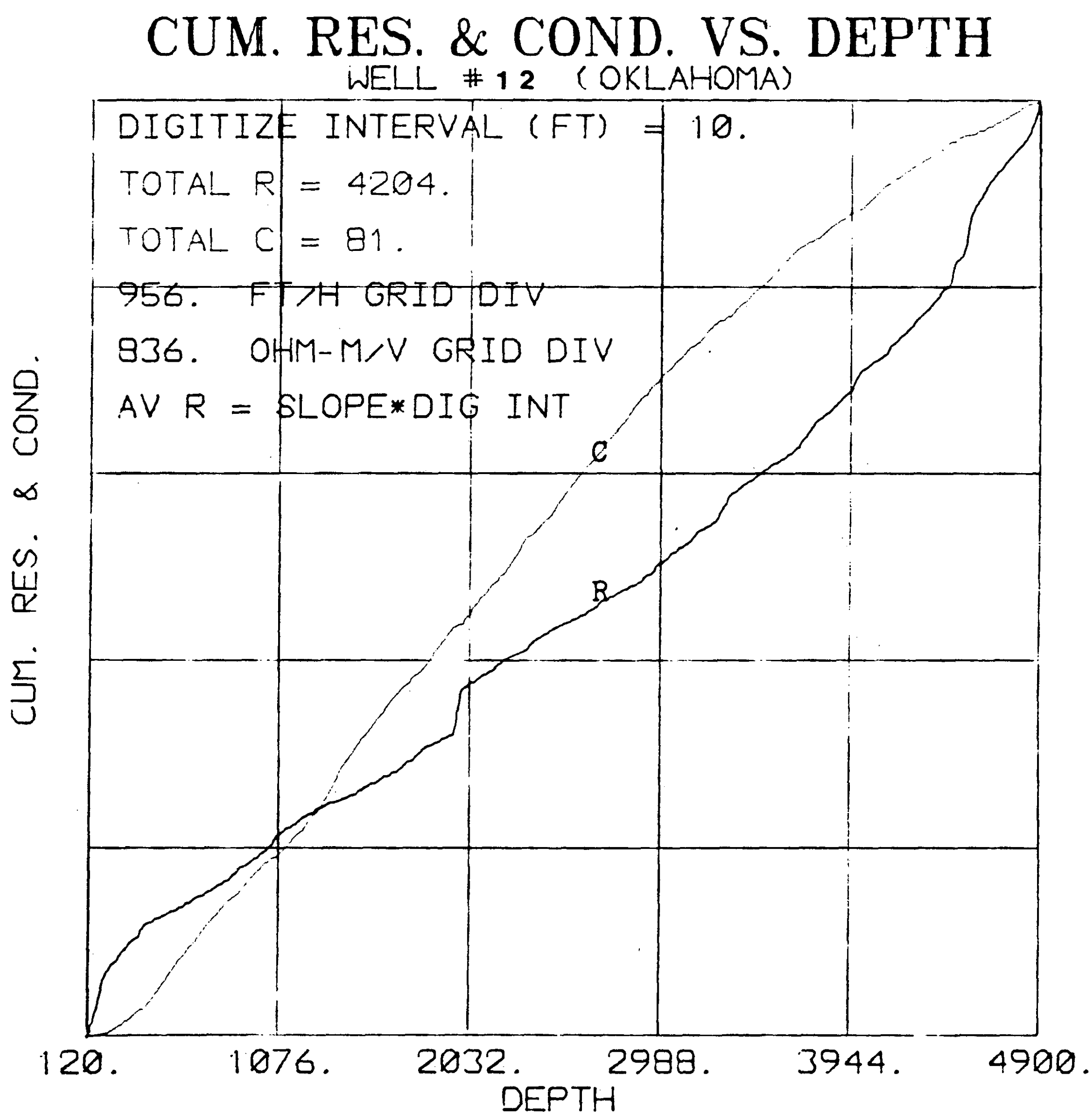
CUM. RES. & COND. VS. DEPTH
WELL #12 (OKLAHOMA)
DIGITIZE INTERVAL (FT) = 10.
TOTAL R = 4204.
TOTAL C = 81.
956. FT/H GRID DIV
836. OHM-M/V GRID DIV
AV R = SLOPE*DIG INT
C
R
CUM. RES. & COND.
120.
1076.
2032.
2988.
3944.
4900.
DEPTH

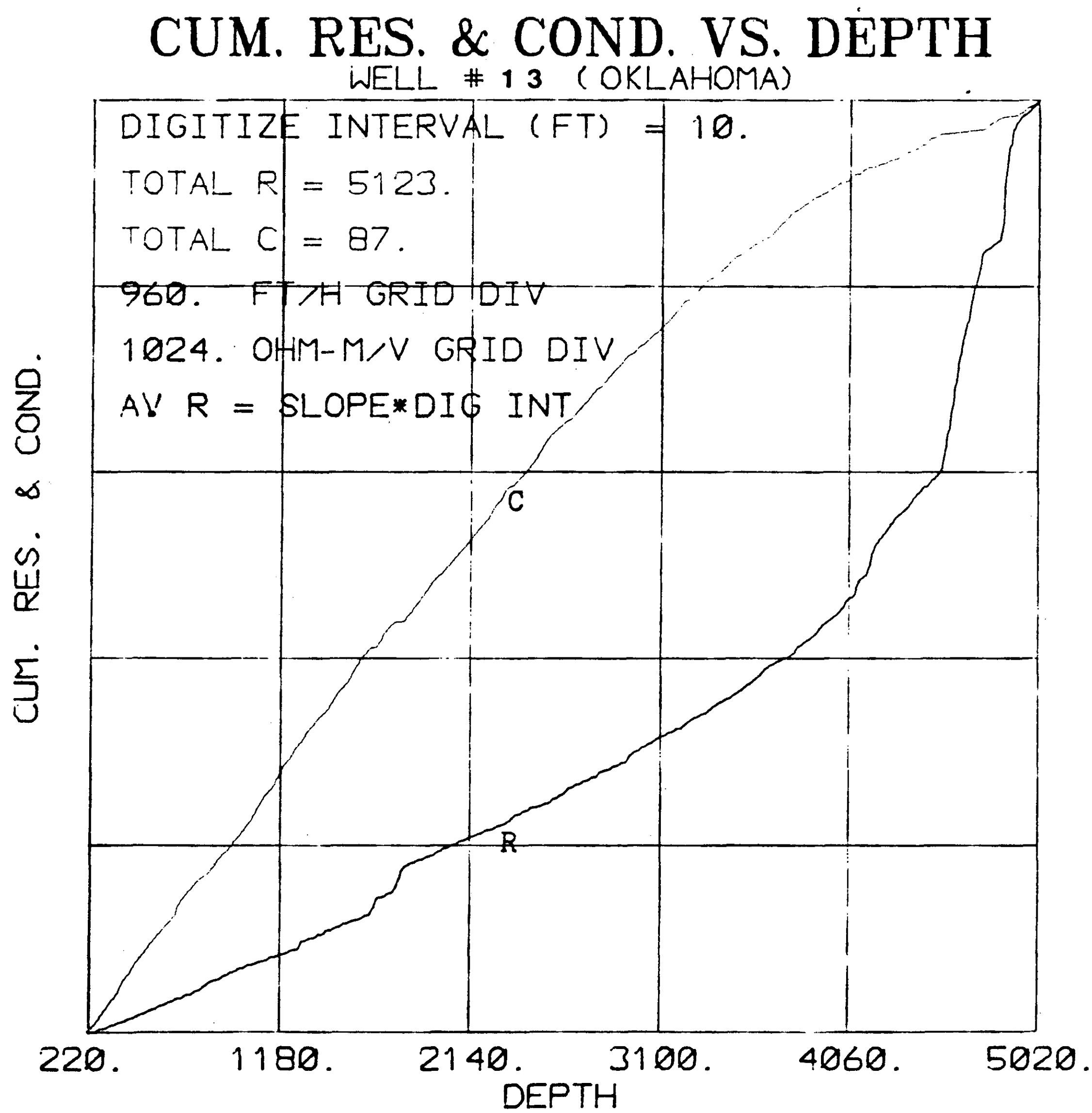
CUM. RES. & COND. VS. DEPTH
WELL # 13 (OKLAHOMA)
DIGITIZE INTERVAL (FT) = 10.
TOTAL R = 5123.
TOTAL C = 87.
960. FT/H GRID DIV
1024. OHM-M/V GRID DIV
AV R = SLOPE*DIG INT
C
R
CUM. RES. & COND.
220.
1180.
2140.
3100.
4060.
5020.
DEPTH

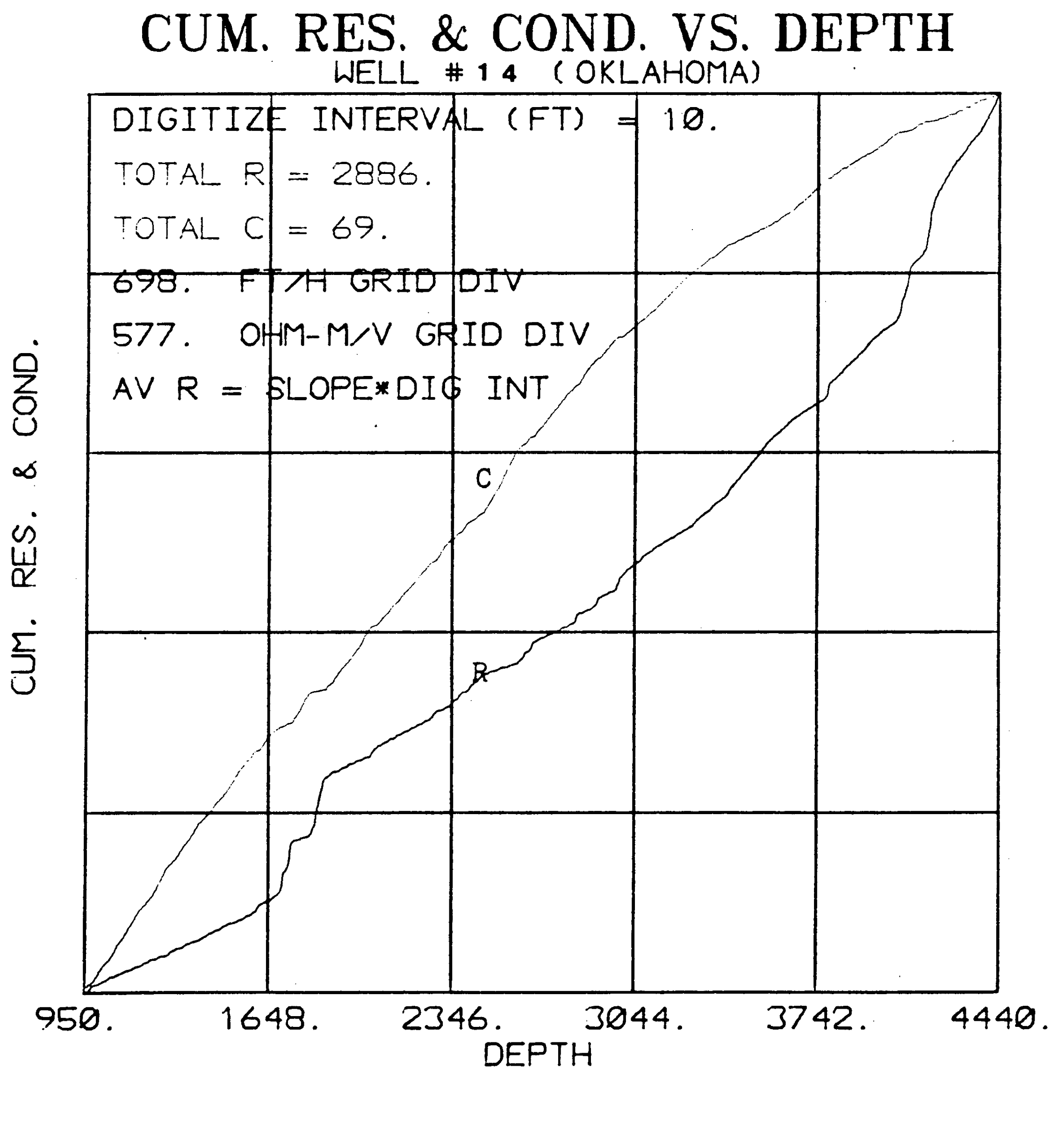
CUM. RES. & COND. VS. DEPTH
WELL #14 (OKLAHOMA)
DIGITIZE INTERVAL (FT) = 10.
TOTAL R = 2886.
TOTAL C = 69.
698. FT/H GRID DIV
577. OHM-M/V GRID DIV
AV R = SLOPE*DIG INT
C
R
CUM. RES. & COND.
950.
1648.
2346.
3044.
3742.
4440.
DEPTH

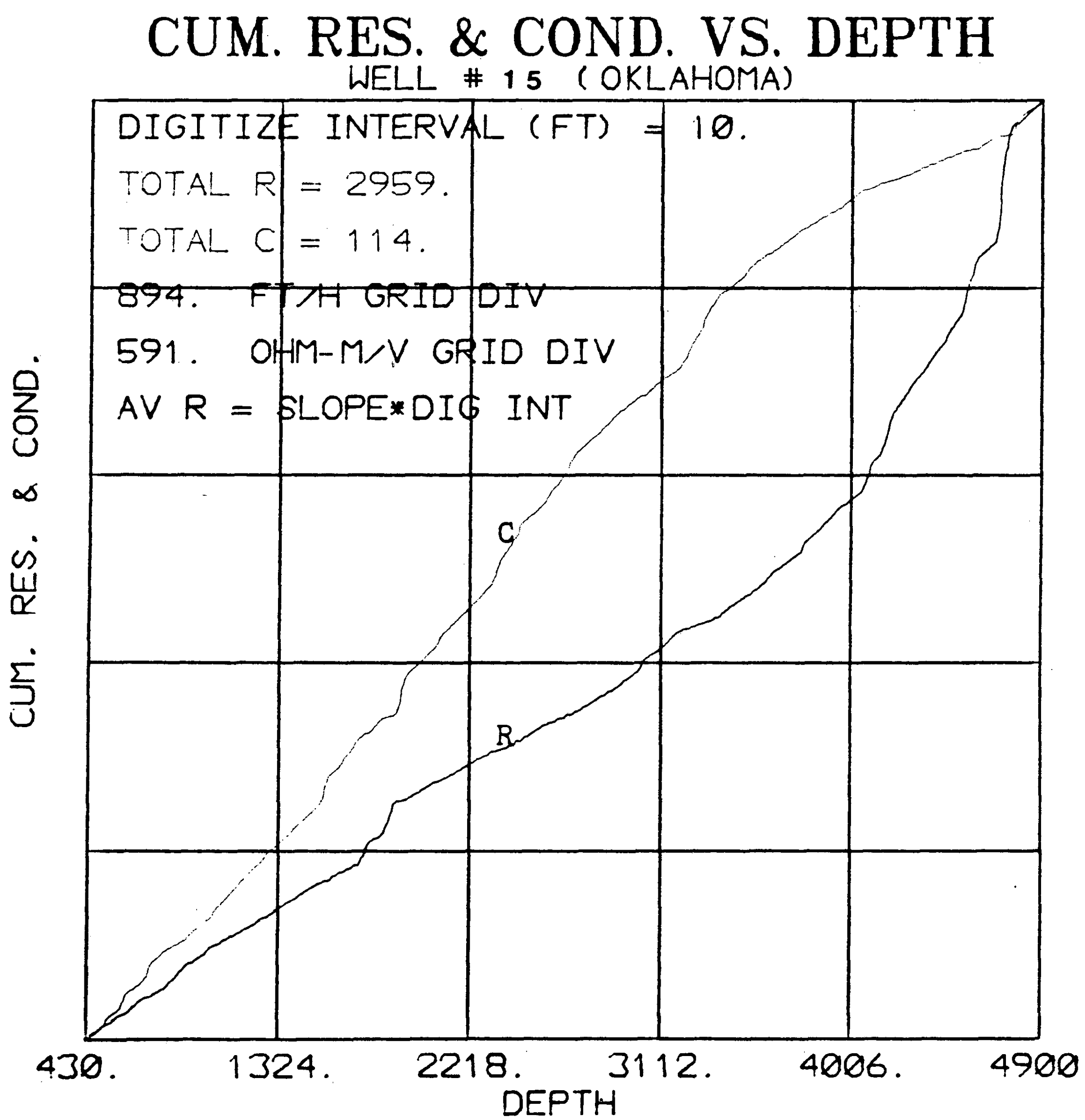
CUM. RES. & COND. VS. DEPTH
WELL # 15 (OKLAHOMA)
DIGITIZE INTERVAL (FT) = 10.
TOTAL R = 2959.
TOTAL C = 114.
894. FT/H GRID DIV
591. OHM-M/V GRID DIV
AV R = SLOPE*DIG INT
C
R
430.
1324.
2218.
3112.
4006.
4900.
DEPTH
CUM. RES. & COND.

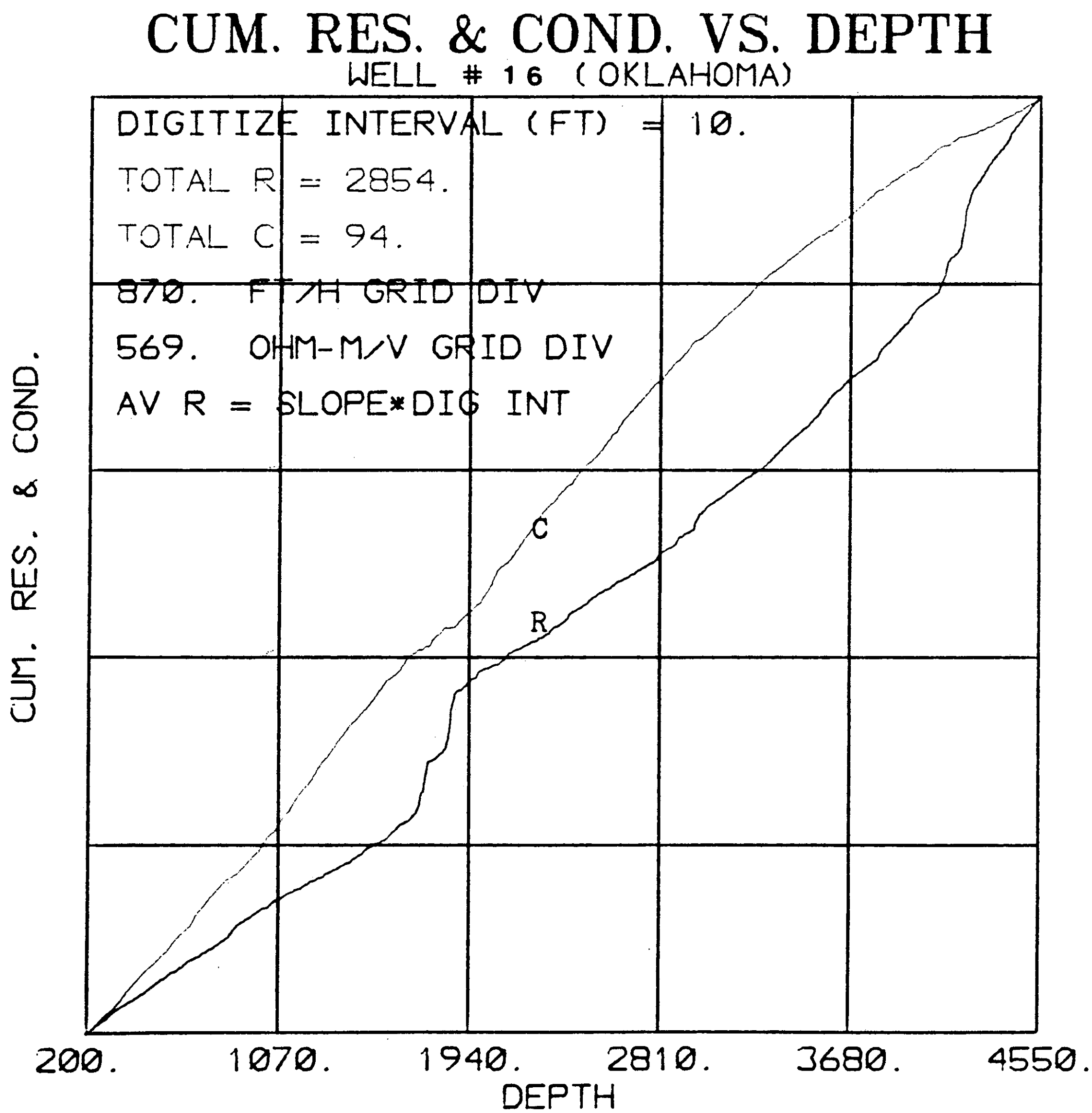
CUM. RES. & COND. VS. DEPTH
WELL # 16 (OKLAHOMA)
DIGITIZE INTERVAL (FT) = 10.
TOTAL R = 2854.
TOTAL C = 94.
870. FT/H GRID DIV
569. OHM-M/V GRID DIV
AV R = SLOPE*DIG INT
C
R
CUM. RES. & COND.
200.
1070.
1940.
2810.
3680.
4550.
DEPTH

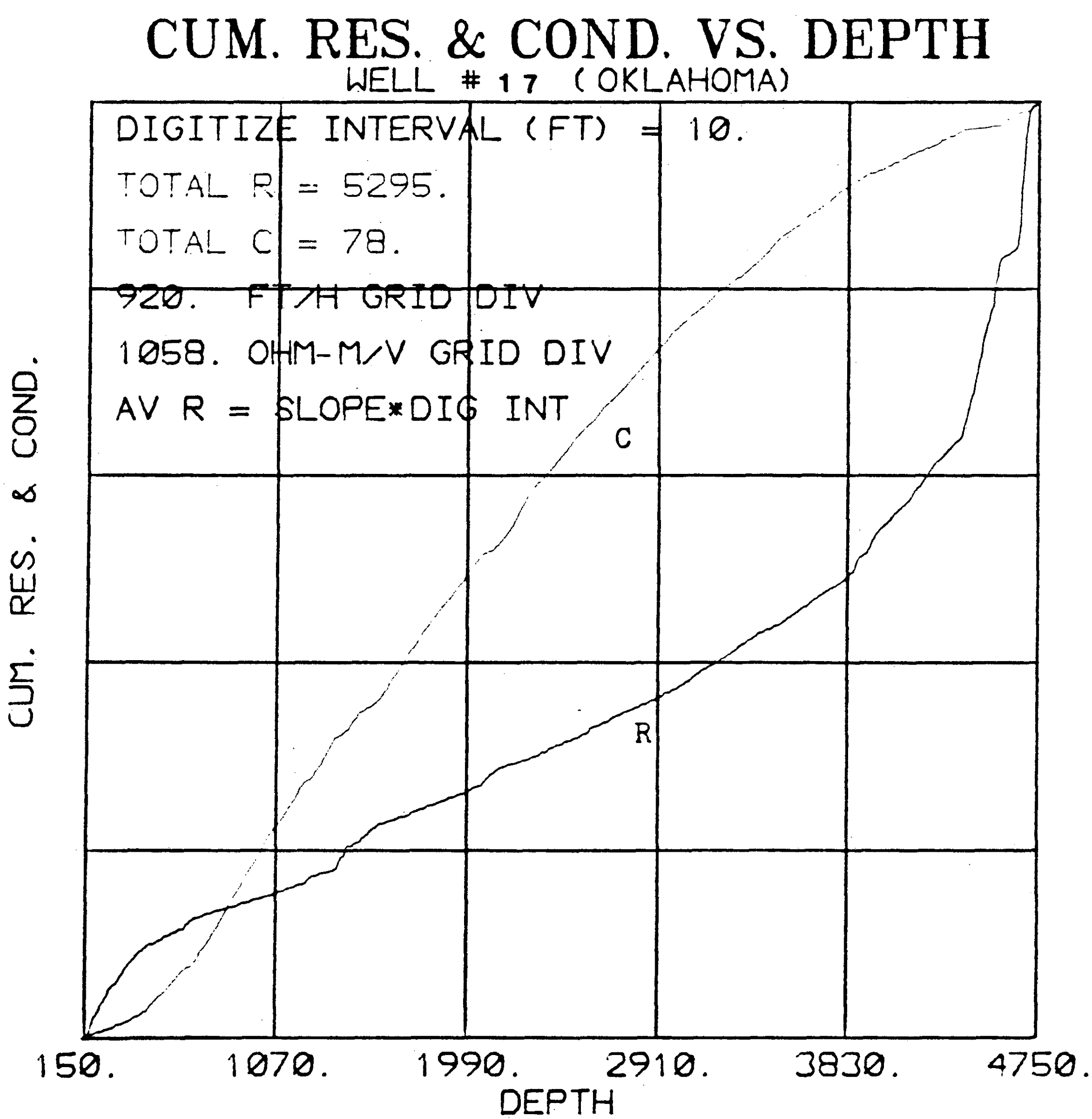
CUM. RES. & COND. VS. DEPTH
WELL # 17 (OKLAHOMA)
DIGITIZE INTERVAL (FT) = 10.
TOTAL R = 5295.
TOTAL C = 78.
920. FT/H GRID DIV
1058. OHM-M/V GRID DIV
AV R = SLOPE*DIG INT
C
R
CUM. RES. & COND.
150.
1070.
1990.
2910.
3830.
4750.
DEPTH

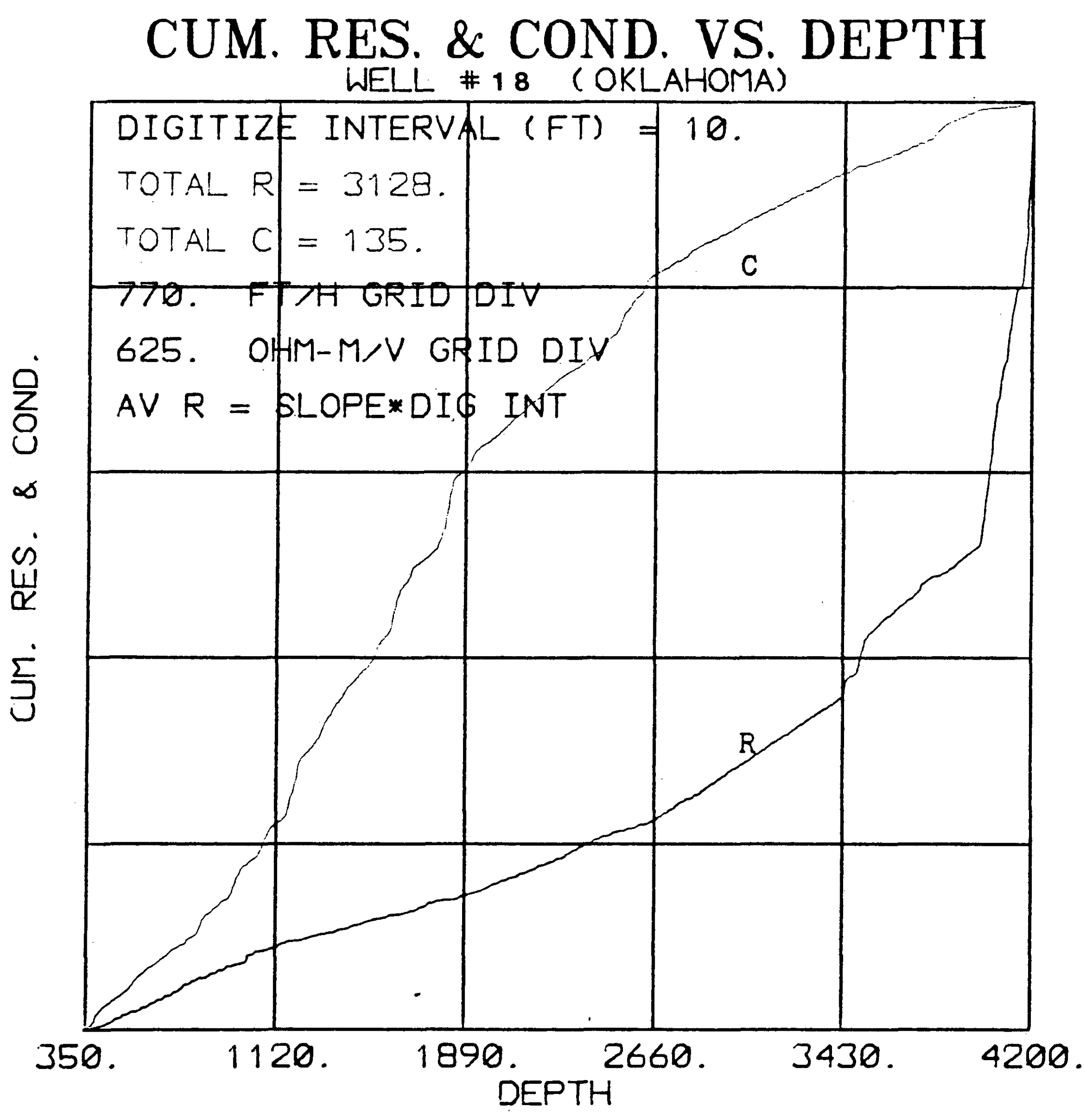
CUM. RES. & COND. VS. DEPTH
WELL #18 (OKLAHOMA)
DIGITIZE INTERVAL (FT) = 10.
TOTAL R = 3128.
TOTAL C = 135.
770. FT/H GRID DIV
625. OHM-M/V GRID DIV
AV R = SLOPE*DIG INT
C
R
350.
1120.
1890.
2660.
3430.
4200.
DEPTH
CUM. RES. & COND.

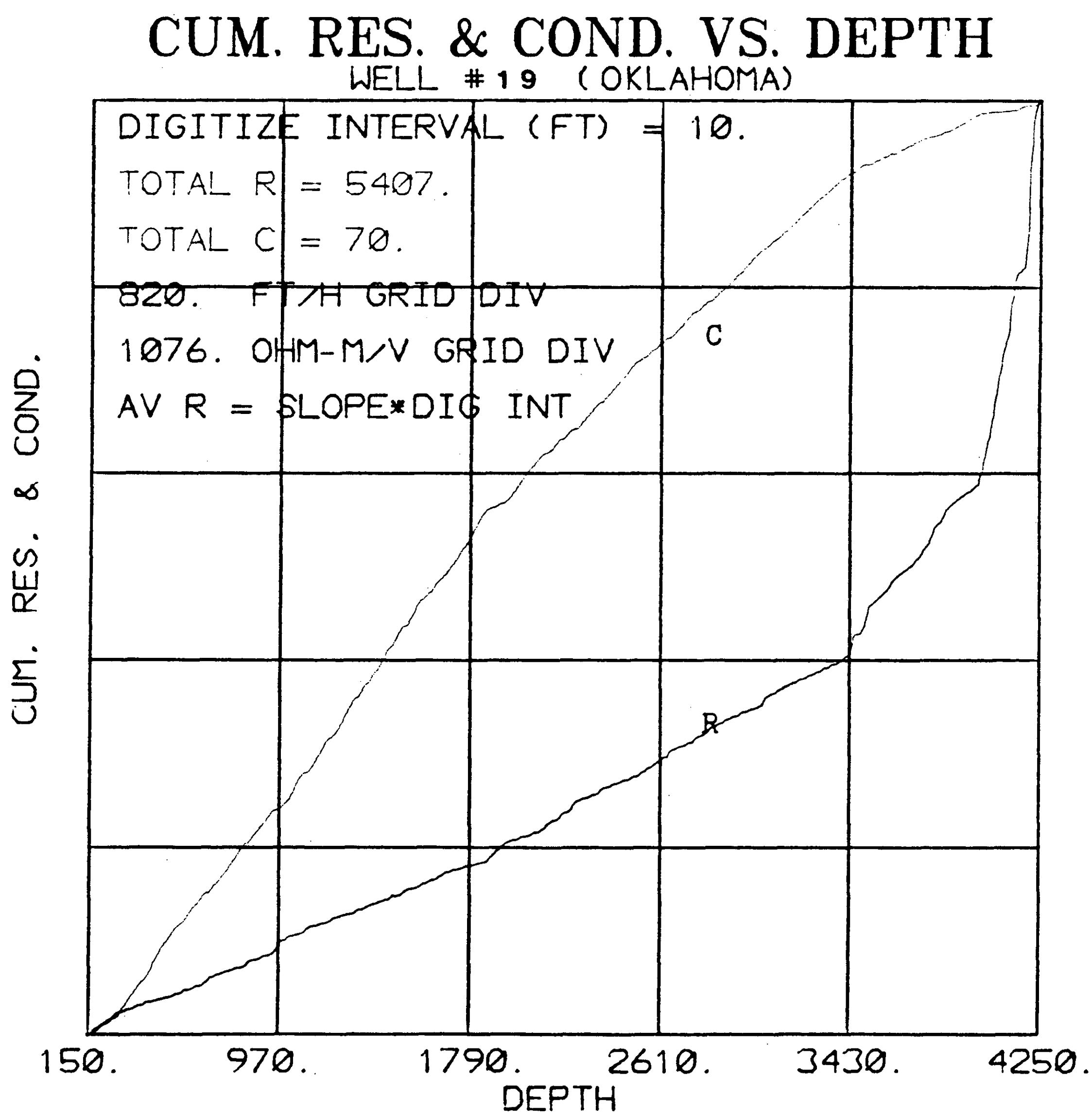
CUM. RES. & COND. VS. DEPTH
WELL #19 (OKLAHOMA)
DIGITIZE INTERVAL (FT) = 10.
TOTAL R = 5407.
TOTAL C = 70.
820. FT/H GRID DIV
1076. OHM-M/V GRID DIV
AV R = SLOPE*DIG INT
C
R
CUM. RES. & COND.
150.
970.
1790.
2610.
3430.
4250.
DEPTH

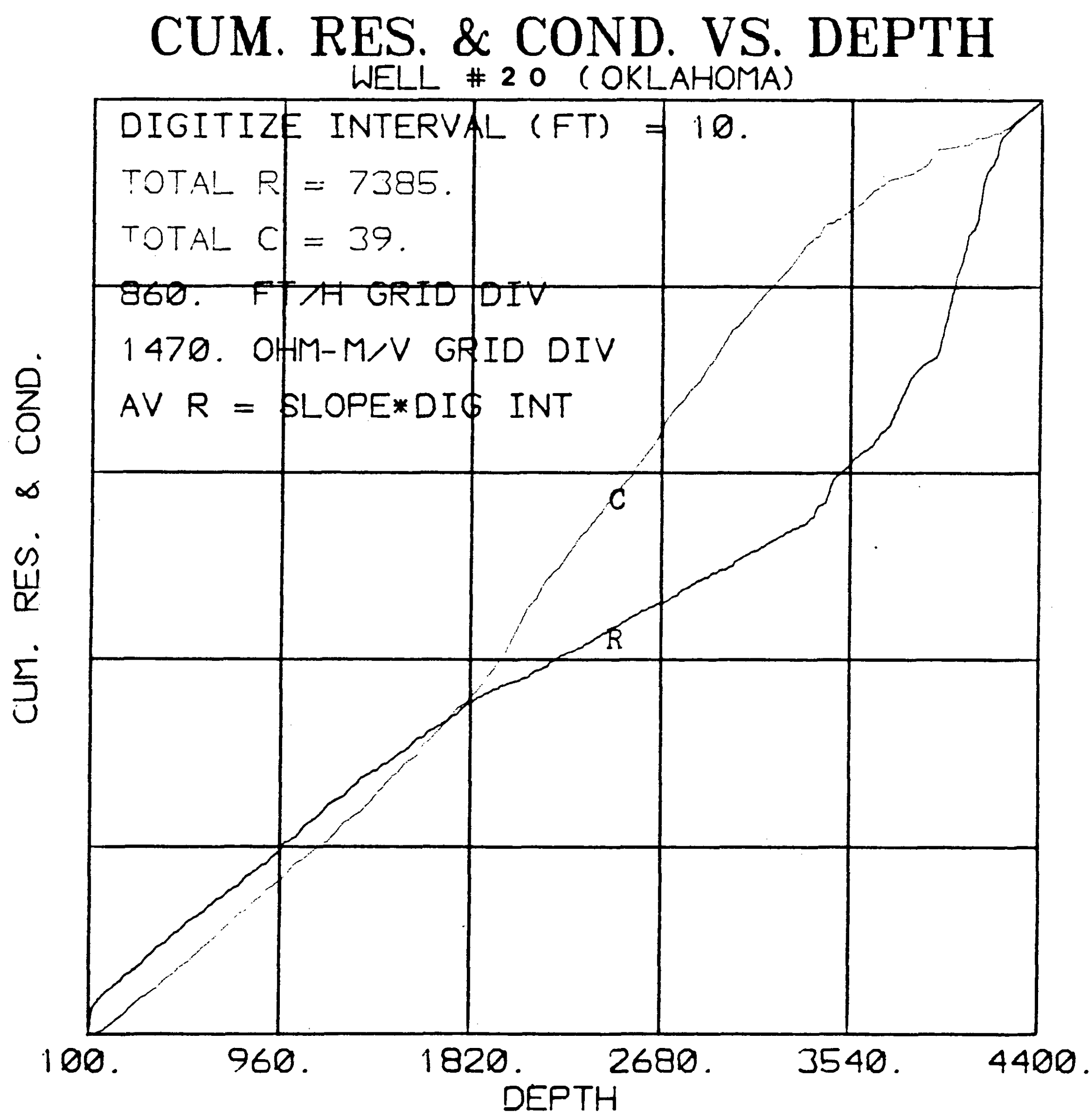
CUM. RES. & COND. VS. DEPTH
WELL # 20 (OKLAHOMA)
DIGITIZE INTERVAL (FT) = 10.
TOTAL R = 7385.
TOTAL C = 39.
860. FT/H GRID DIV
1470. OHM-M/V GRID DIV
AV R = SLOPE*DIG INT
C
R
CUM. RES. & COND.
100.
960.
1820.
2680.
3540.
4400.
DEPTH

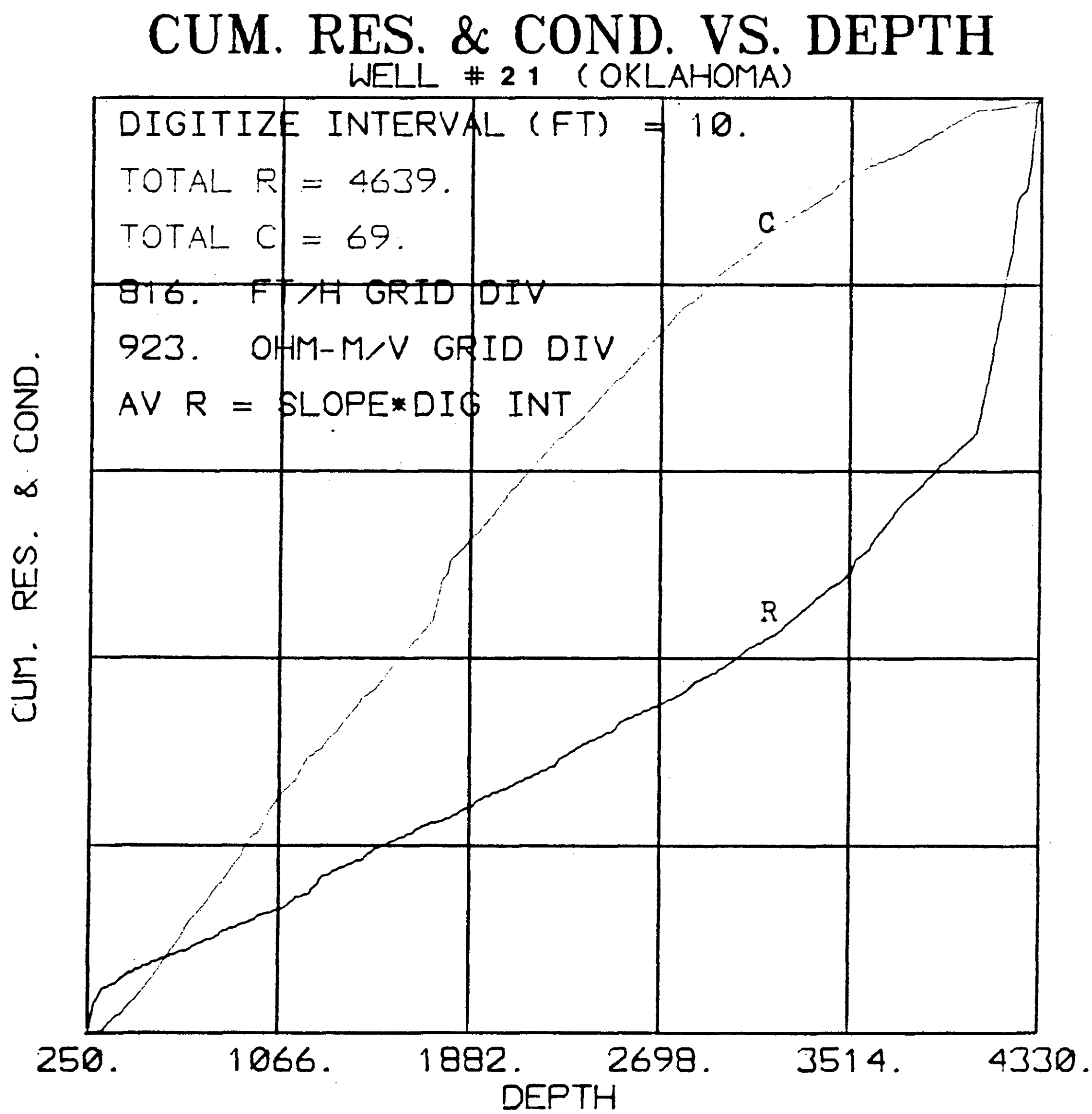
CUM. RES. & COND. VS. DEPTH
WELL # 21 (OKLAHOMA)
DIGITIZE INTERVAL (FT) = 10.
TOTAL R = 4639.
TOTAL C = 69.
816. FT/H GRID DIV
923. OHM-M/V GRID DIV
AV R = SLOPE*DIG INT
C
R
CUM. RES. & COND.
250.
1066.
1882.
2698.
3514.
4330.
DEPTH

CUM. RES. & COND. VS. DEPTH

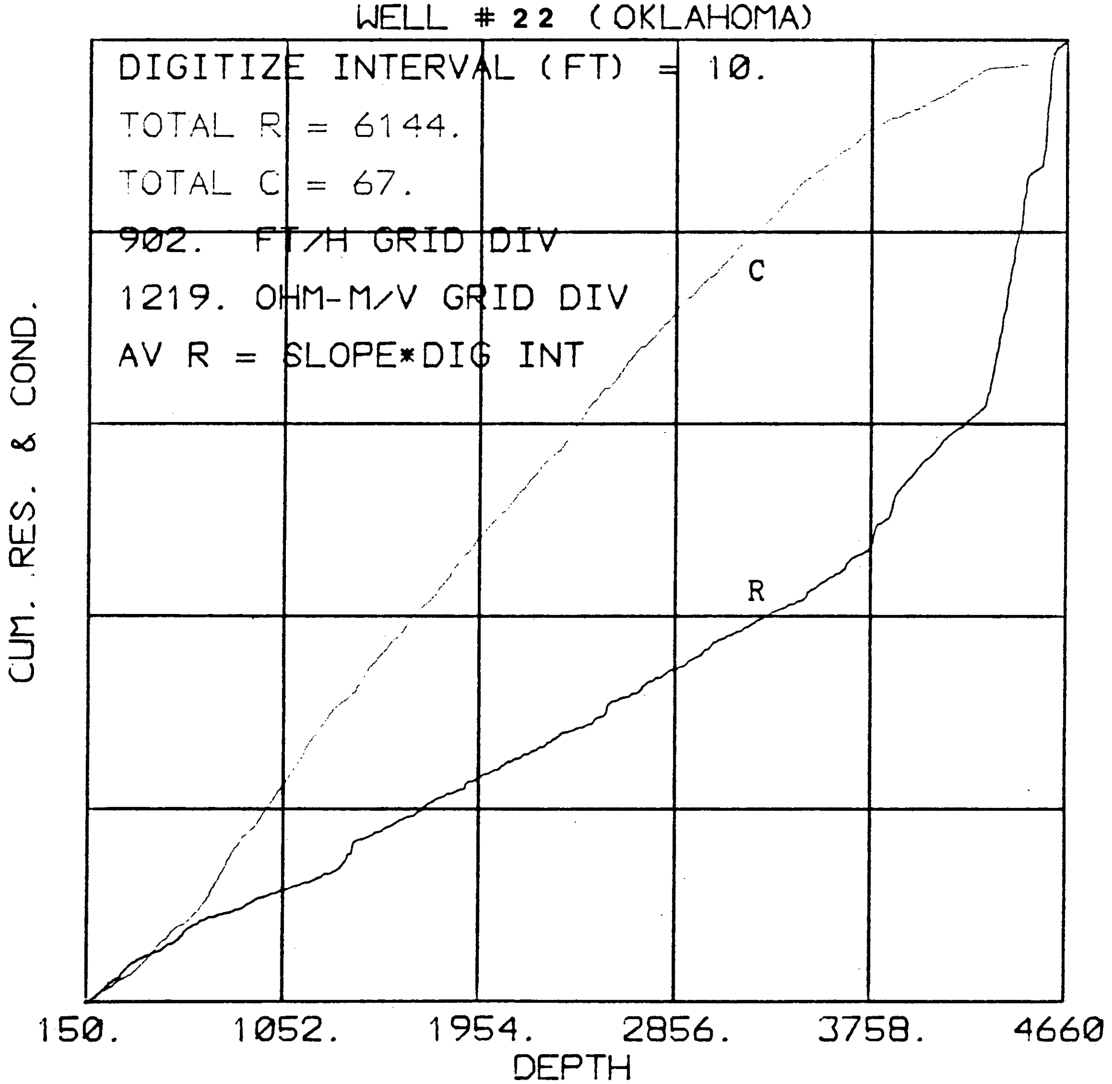

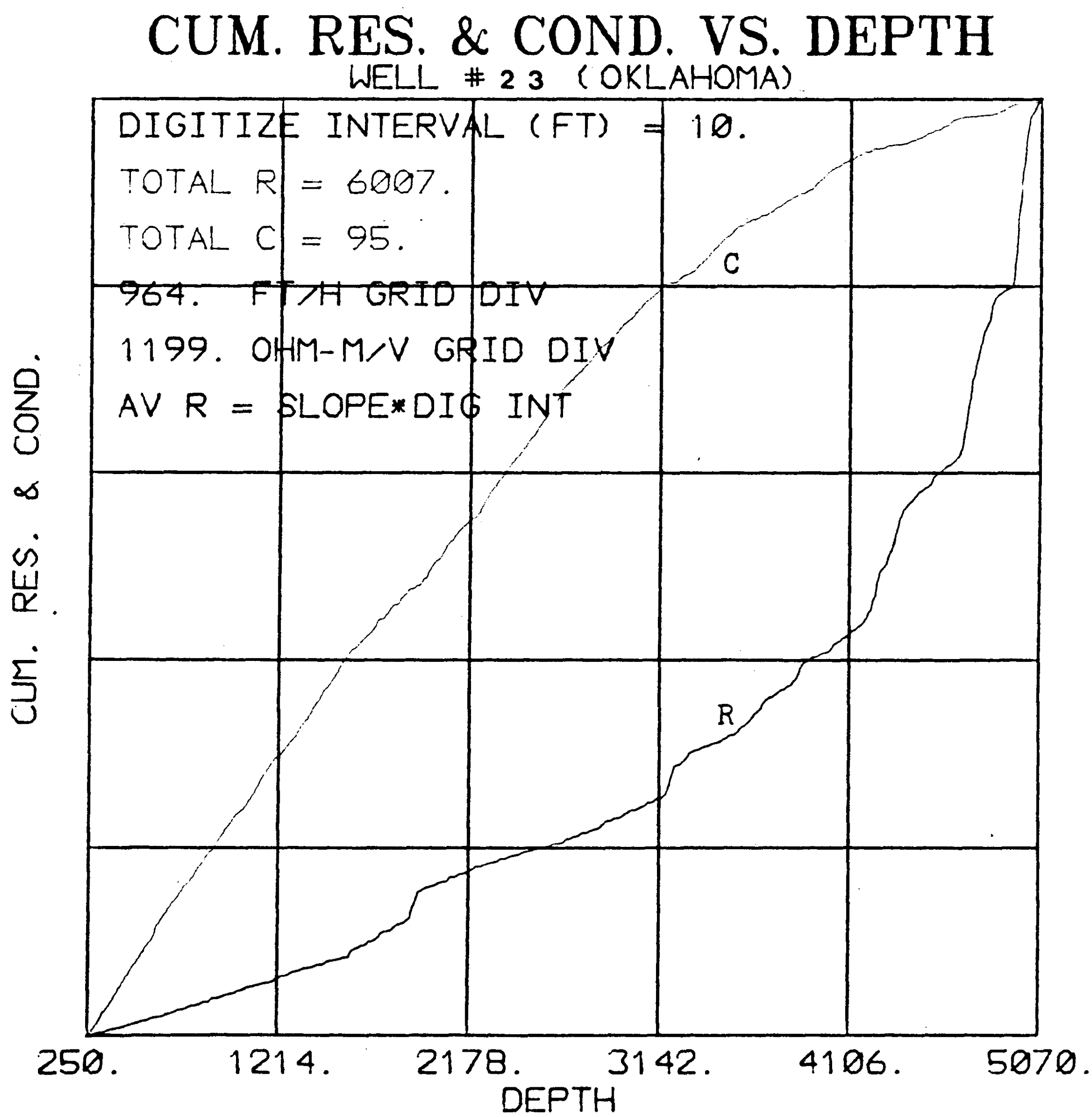
CUM. RES. & COND. VS. DEPTH
WELL # 23 (OKLAHOMA)
DIGITIZE INTERVAL (FT) = 10.
TOTAL R = 6007.
TOTAL C = 95.
964. FT/H GRID DIV
1199. OHM-M/V GRID DIV
AV R = SLOPE*DIG INT
C
R
CUM. RES. & COND.
250.
1214.
2178.
3142.
4106.
5070.
DEPTH

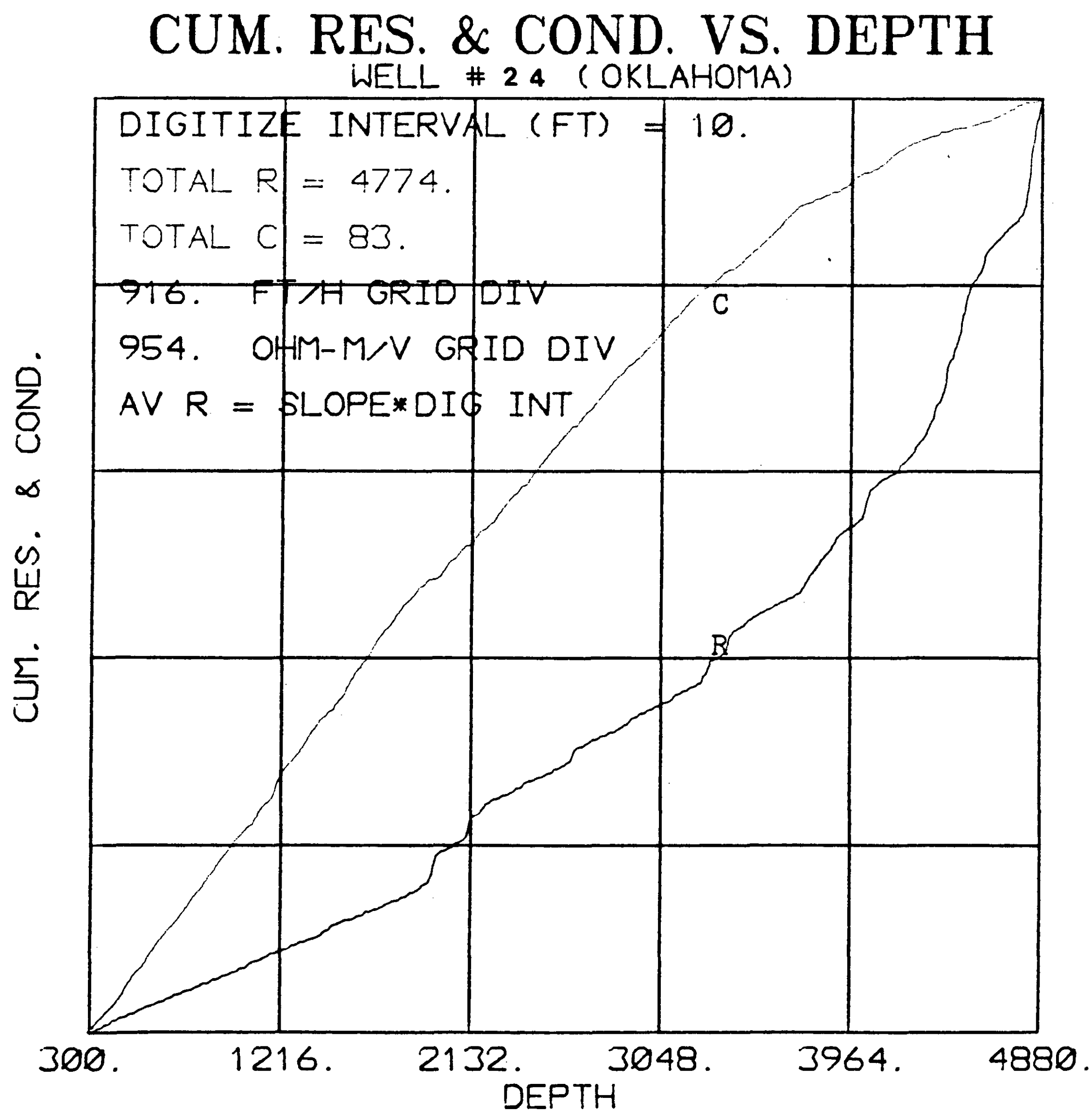
CUM. RES. & COND. VS. DEPTH
WELL # 24 (OKLAHOMA)
DIGITIZE INTERVAL (FT) = 10.
TOTAL R = 4774.
TOTAL C = 83.
916. FT/H GRID DIV
954. OHM-M/V GRID DIV
AV R = SLOPE*DIG INT
C
R
CUM. RES. & COND.
300.
1216.
2132.
3048.
3964.
4880.
DEPTH

WELL # 1 (OKLAHOMA)

UNIT	DEPTH INTERVAL	AV.TRA.RES.	AV.LON.RES.	COEFF.ANISO.
1	220.-3420.	7.52	5.94	1.1250
2	3420.-4400.	40.88	19.58	1.4449

WELL # 2

1	120.-3230.	6.95	4.88	1.1940

WELL # 3

1	550.-3700.	4.38	2.63	1.2920
2	3700.-4680.	21.88	6.16	1.8847

WELL # 4

1	120.-3850.	5.74	4.67	1.1087
2	3850.-4850.	23.34	10.80	1.4698

WELL # 5

1	220.-4030.	6.06	4.47	1.1637
2	4030.-4920.	23.62	12.01	1.4024

WELL # 6

1	220.-4050.	6.94	5.67	1.1064
2	4050.-4820.	26.97	13.00	1.4404

WELL # 7

1	220.-4120.	6.43	4.69	1.1713
2	4120.-4880.	26.82	12.26	1.4788

WELL # 8

1	300.-4340.	4.57	2.53	1.3442
2	4340.-5120.	21.54	5.84	1.9196

WELL # 9

1	220.-4420.	6.98	5.09	1.1708
2	4420.-4710.	17.97	11.67	1.2410

WELL # 10

1	120.-4390.	8.95	5.56	1.2689
2	4390.-4880.	28.46	15.75	1.3443

WELL # 11

1	220.-4390.	5.82	3.49	1.2907
2	4390.-5230.	26.21	14.54	1.3427

WELL # 12

1	120.-4390.	7.78	5.55	1.1841
2	4390.-4900.	17.02	11.87	1.1973

WELL # 13

1	220.-4010.	6.08	4.80	1.1259
2	4010.-5020.	27.66	13.30	1.4420

WELL # 14

1	950.-4050.	6.96	4.72	1.2140
2	4050.-4440.	18.22	13.18	1.1757

WELL # 15

1	430.-4040.	4.75	3.53	1.1606
2	4040.-4900.	14.30	7.72	1.3613

WELL # 16

1	200.-4080.	5.81	4.37	1.1532
2	4080.-4550.	12.46	9.15	1.1667

WELL # 17				
1	150.-3800.	7.05	5.17	1.1680
2	3800.-4750.	28.36	12.92	1.4819
WELL # 18				
1	350.-3400.	3.62	2.45	1.2159
2	3400.-4200.	25.00	7.53	1.8226
WELL # 19				
1	150.-3390.	6.70	5.05	1.1518
2	3390.-4250.	37.17	14.37	1.6086
WELL # 20				
1	100.-3340.	12.49	9.72	1.1338
2	3340.-4400.	31.16	17.42	1.3373
WELL # 21				
1	250.-3480.	6.95	5.18	1.1579
2	3480.-4330.	27.84	13.89	1.4155
WELL # 22				
1	150.-3610.	7.98	5.89	1.1641
2	3610.-4660.	31.91	13.25	1.5519
WELL # 23				
1	250.-4170.	6.74	4.38	1.2399
2	4170.-5070.	37.00	16.68	1.4894
WELL # 24				
1	300.-4270.	7.44	5.02	1.2179
2	4270.-4880.	29.37	15.76	1.3651

AHHENDIX 3 : Resistivity-integral plots & geoelectrical parameters,Wyoming.

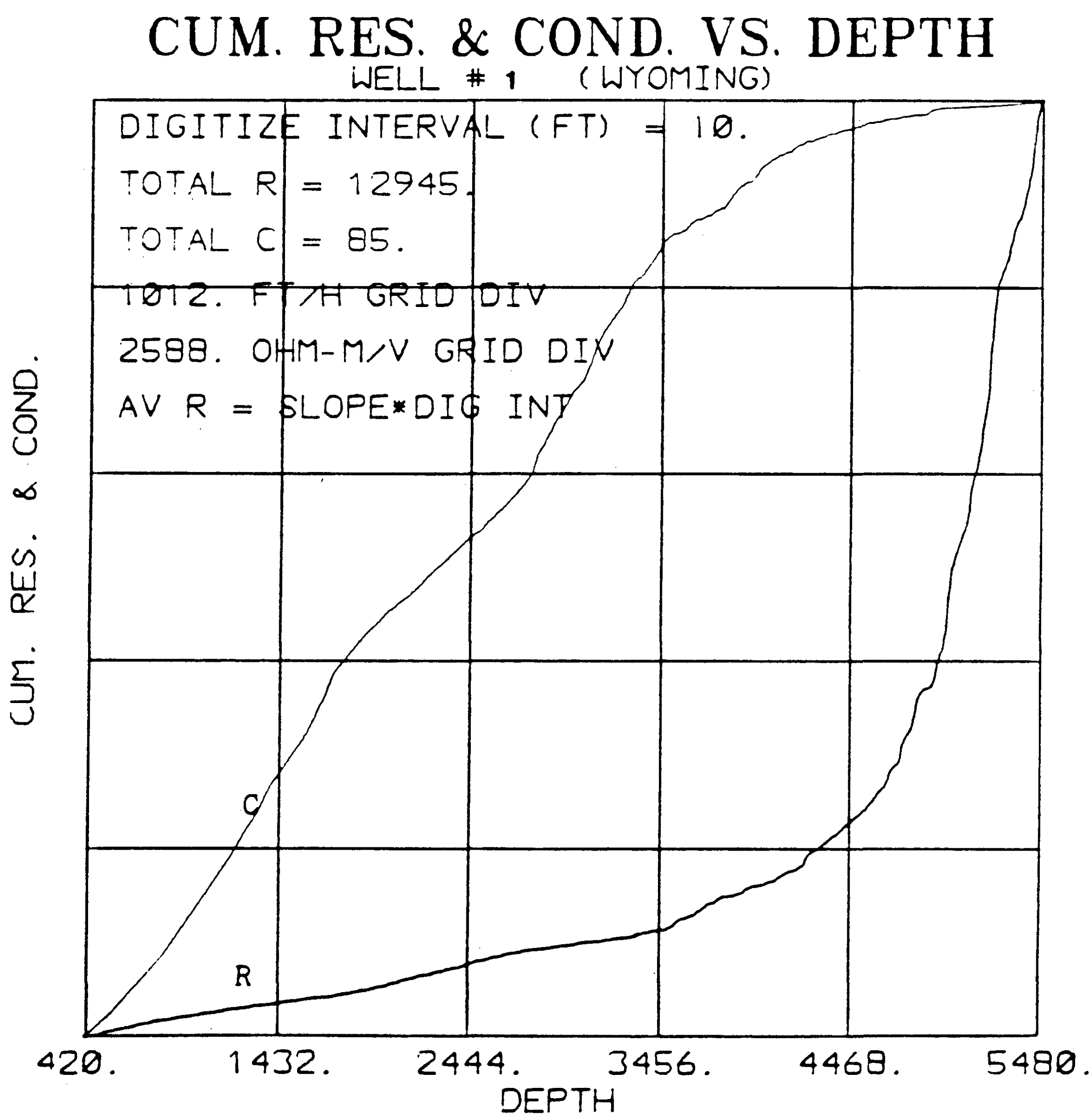

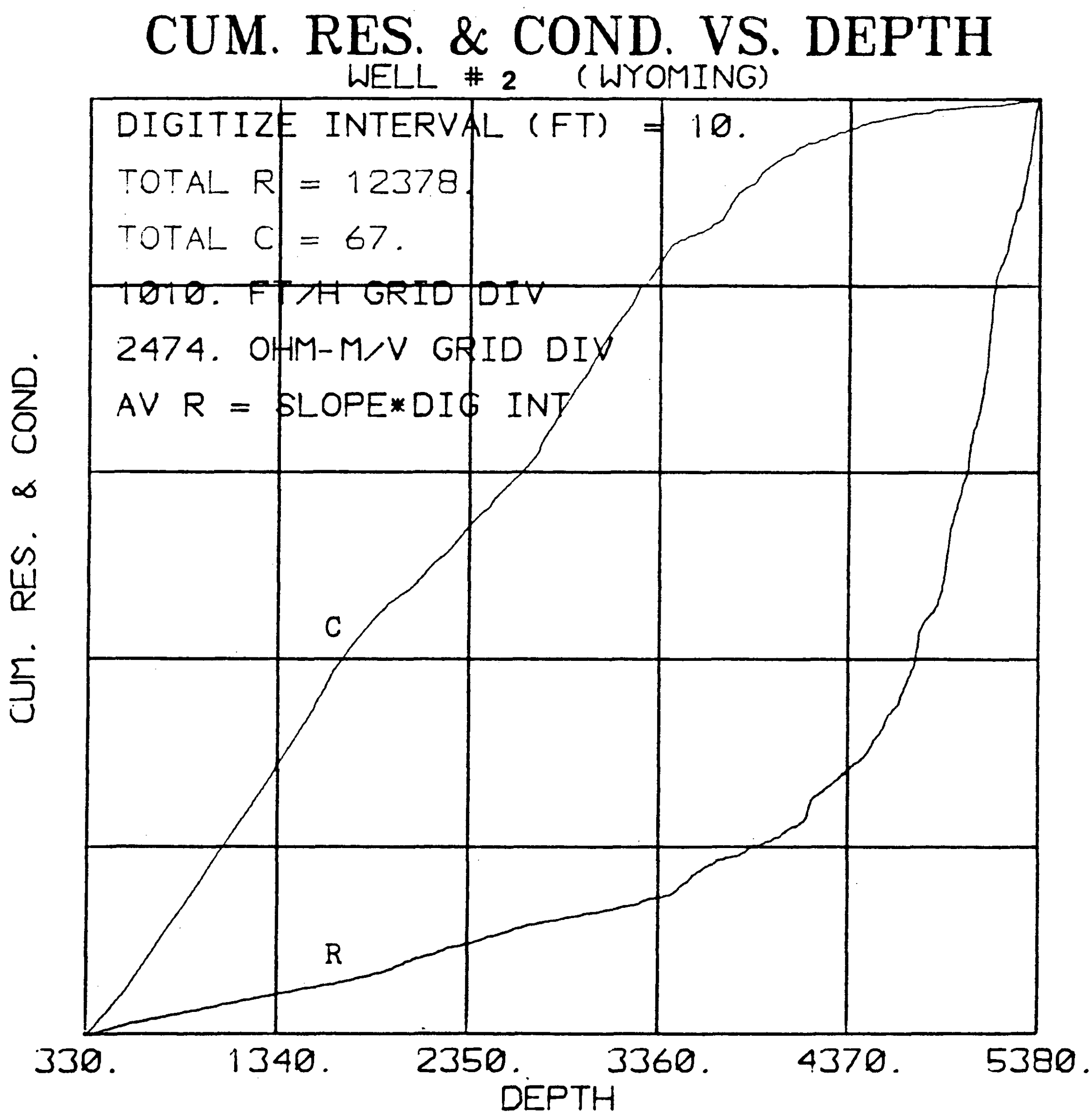
CUM. RES. & COND. VS. DEPTH
WELL # 2 (WYOMING)
DIGITIZE INTERVAL (FT) = 10.
TOTAL R = 12378.
TOTAL C = 67.
1010. FT/H GRID DIV
2474. OHM-M/V GRID DIV
AV R = SLOPE*DIG INT
C
R
CUM. RES. & COND.
330.
1340.
2350.
3360.
4370.
5380.
DEPTH

CUM. RES. & COND. VS. DEPTH

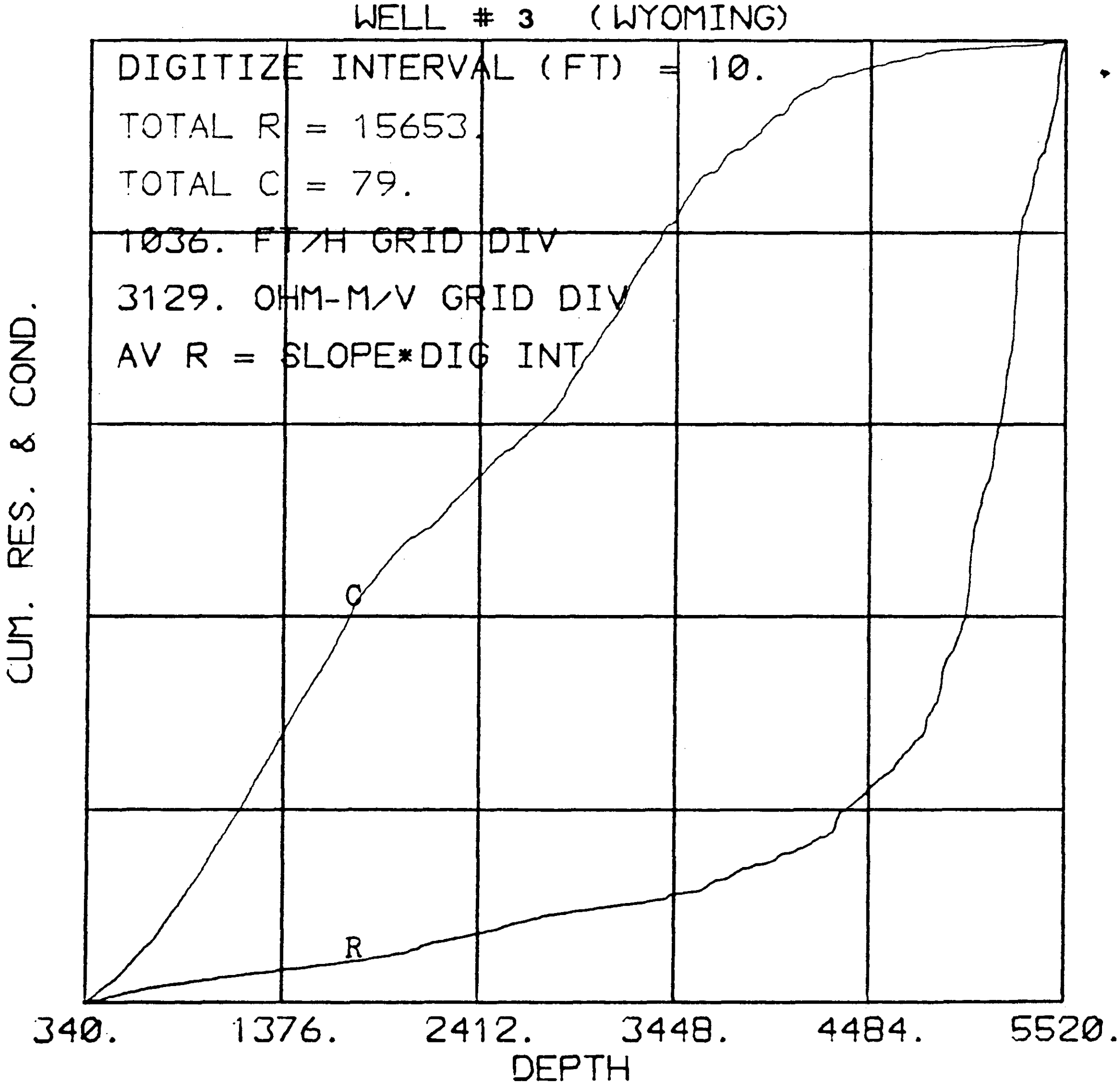

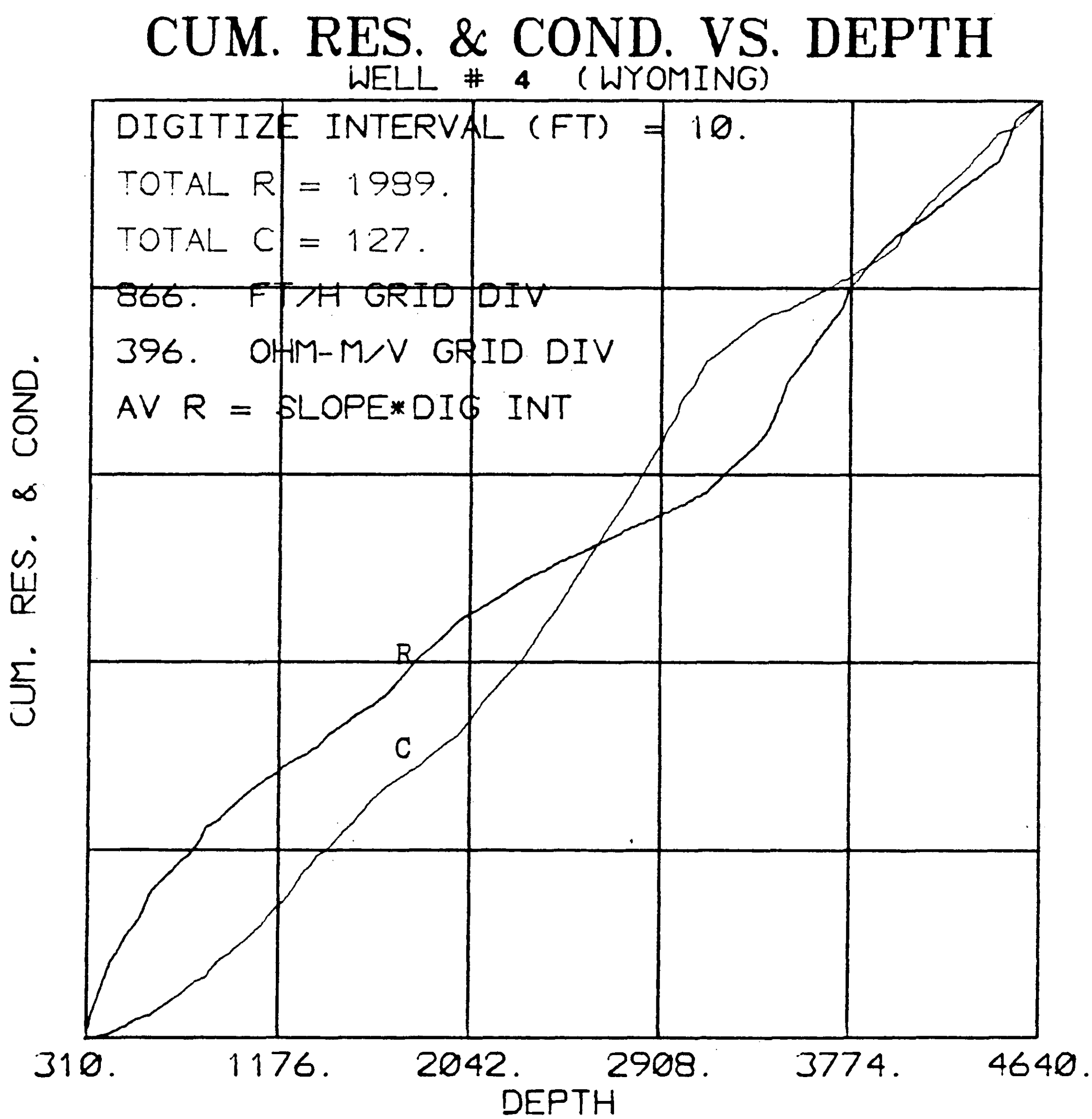
CUM. RES. & COND. VS. DEPTH
WELL # 4 (WYOMING)
DIGITIZE INTERVAL (FT) = 10.
TOTAL R = 1989.
TOTAL C = 127.
866. FT/H GRID DIV
396. OHM-M/V GRID DIV
AV R = SLOPE*DIG INT
R
C
CUM. RES. & COND.
310.
1176.
2042.
2908.
3774.
4640.
DEPTH

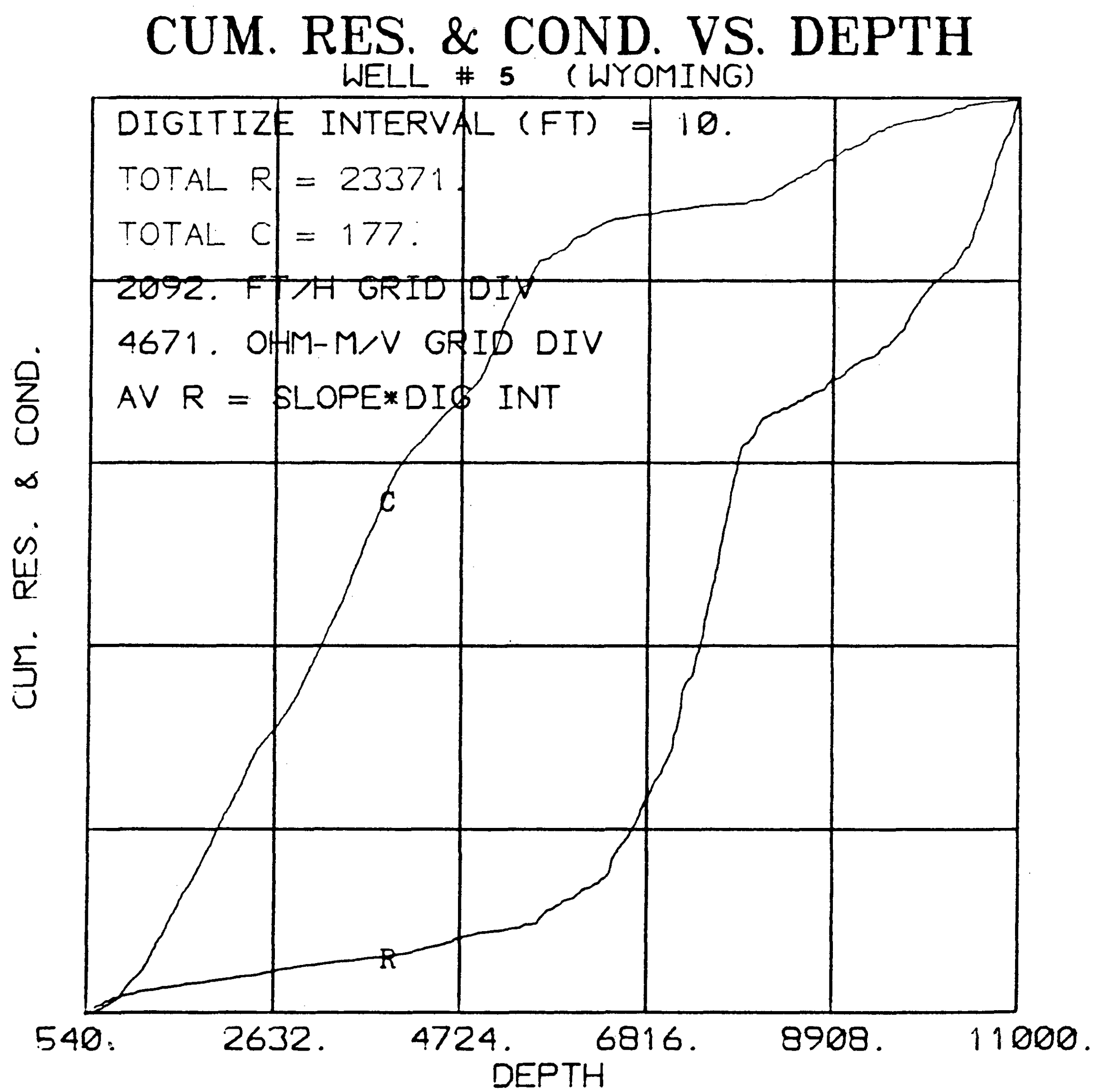
CUM. RES. & COND. VS. DEPTH
WELL # 5 (WYOMING)
DIGITIZE INTERVAL (FT) = 10.
TOTAL R = 23371.
TOTAL C = 177.
2092. FT/H GRID DIV
4671. OHM-M/V GRID DIV
AV R = SLOPE*DIG INT
C
R
CUM. RES. & COND.
540. 2632. 4724. 6816. 8908. 11000.
DEPTH

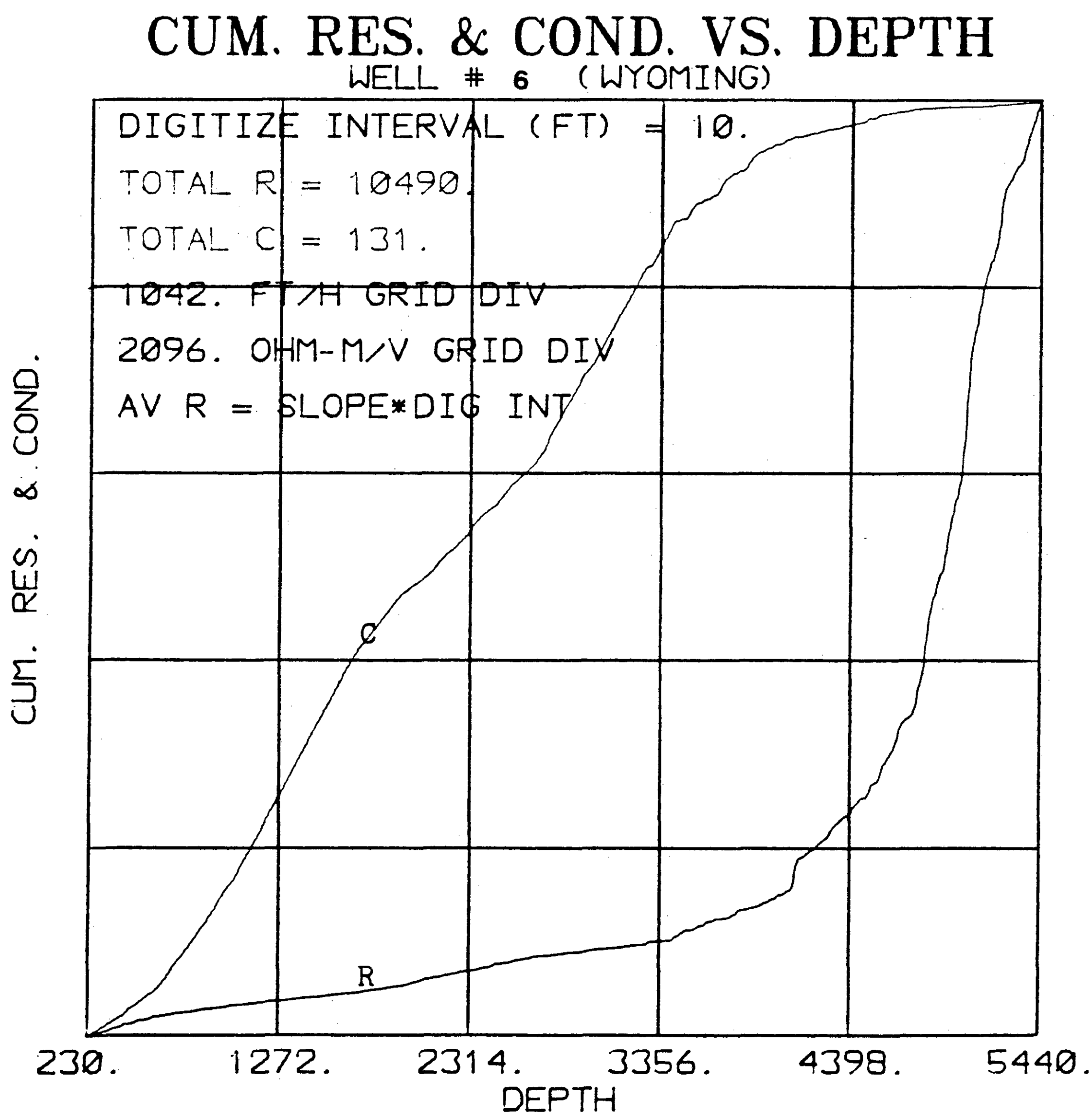
CUM. RES. & COND. VS. DEPTH
WELL # 6 (WYOMING)
DIGITIZE INTERVAL (FT) = 10.
TOTAL R = 10490.
TOTAL C = 131.
1042. FT/H GRID DIV
2096. OHM-M/V GRID DIV
AV R = SLOPE*DIG INT
C
R
CUM. RES. & COND.
230.
1272.
2314.
3356.
4398.
5440.
DEPTH

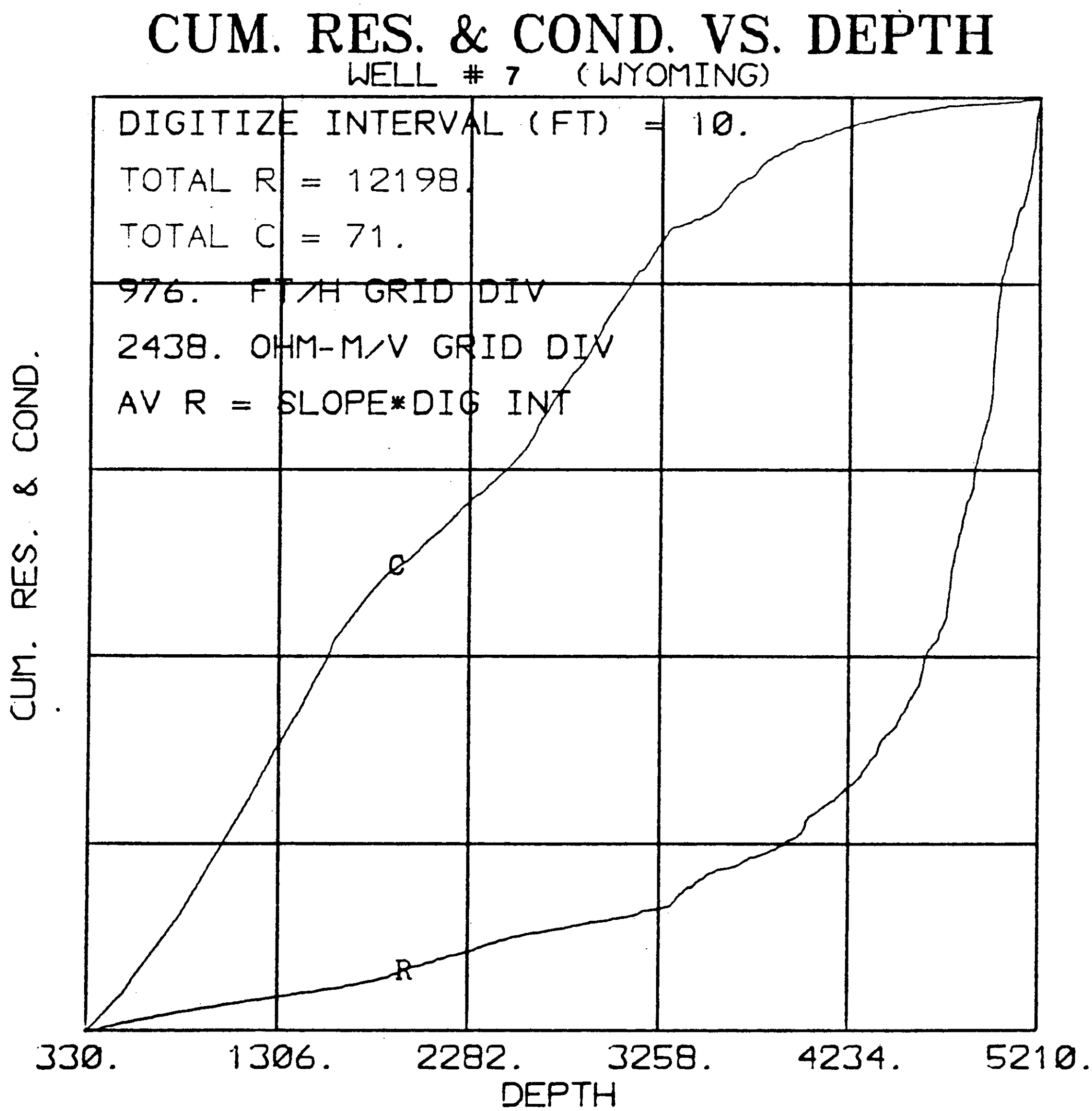
CUM. RES. & COND. VS. DEPTH
WELL # 7 (WYOMING)
DIGITIZE INTERVAL (FT) = 10.
TOTAL R = 12198.
TOTAL C = 71.
976. FT/H GRID DIV
2438. OHM-M/V GRID DIV
AV R = SLOPE*DIG INT
C
R
CUM. RES. & COND.
330.
1306.
2282.
3258.
4234.
5210.
DEPTH

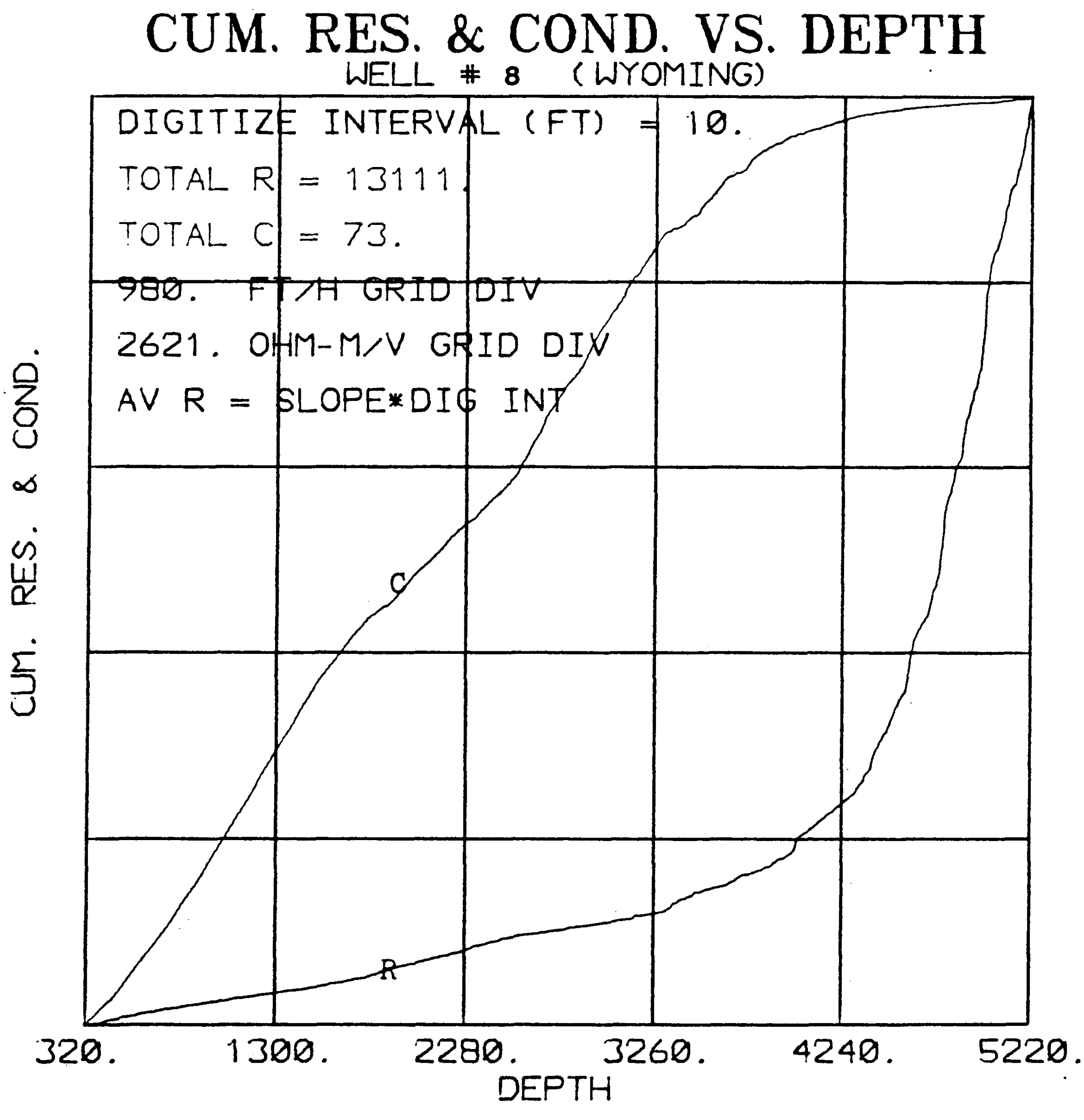
CUM. RES. & COND. VS. DEPTH
WELL # 8 (WYOMING)
DIGITIZE INTERVAL (FT) = 10.
TOTAL R = 13111.
TOTAL C = 73.
980. FT/H GRID DIV
2621. OHM-M/V GRID DIV
AV R = SLOPE*DIG INT
C
R
CUM. RES. & COND.
320.
1300.
2280.
3260.
4240.
5220.
DEPTH

CUM. RES. & COND. VS. DEPTH

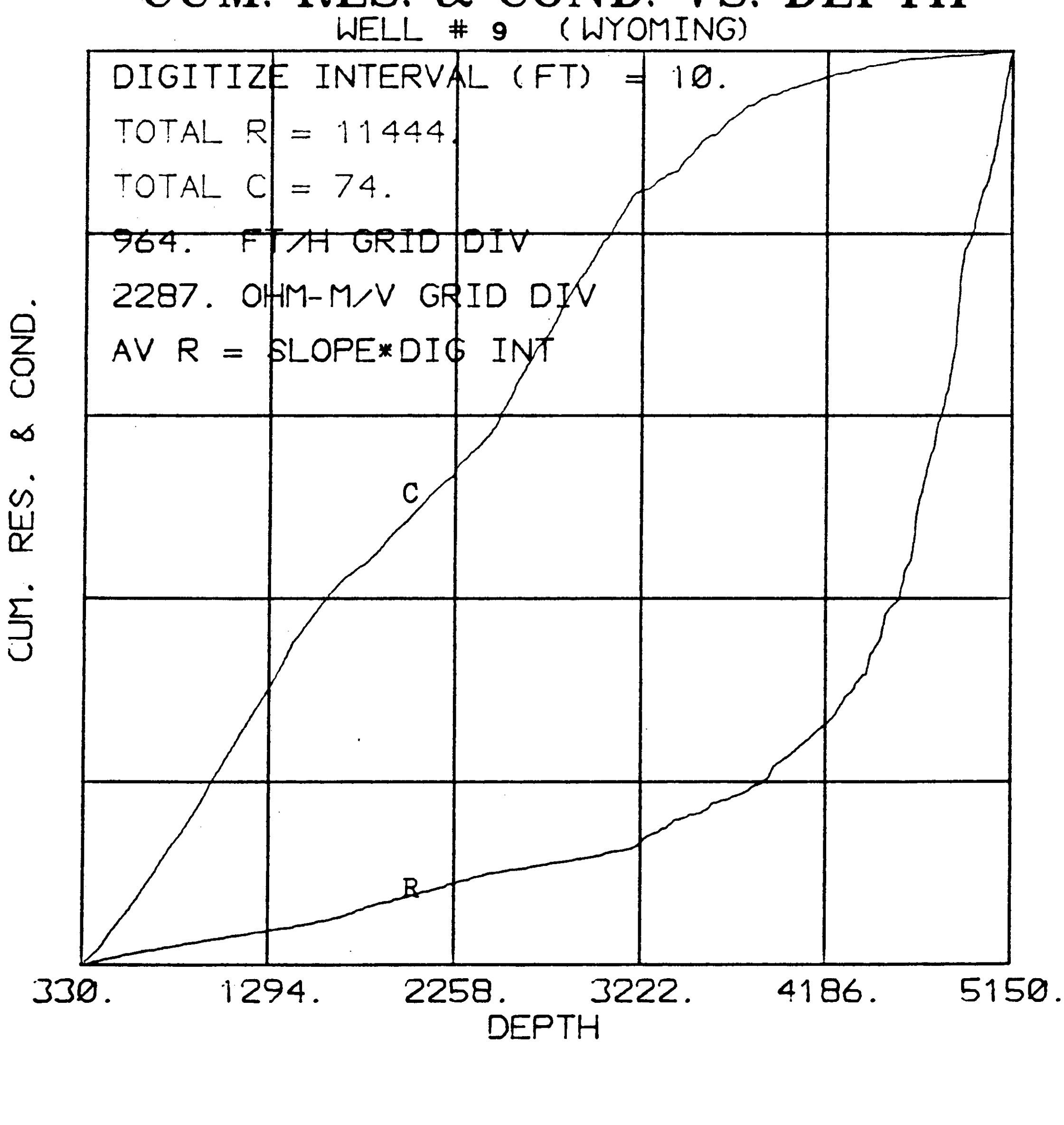

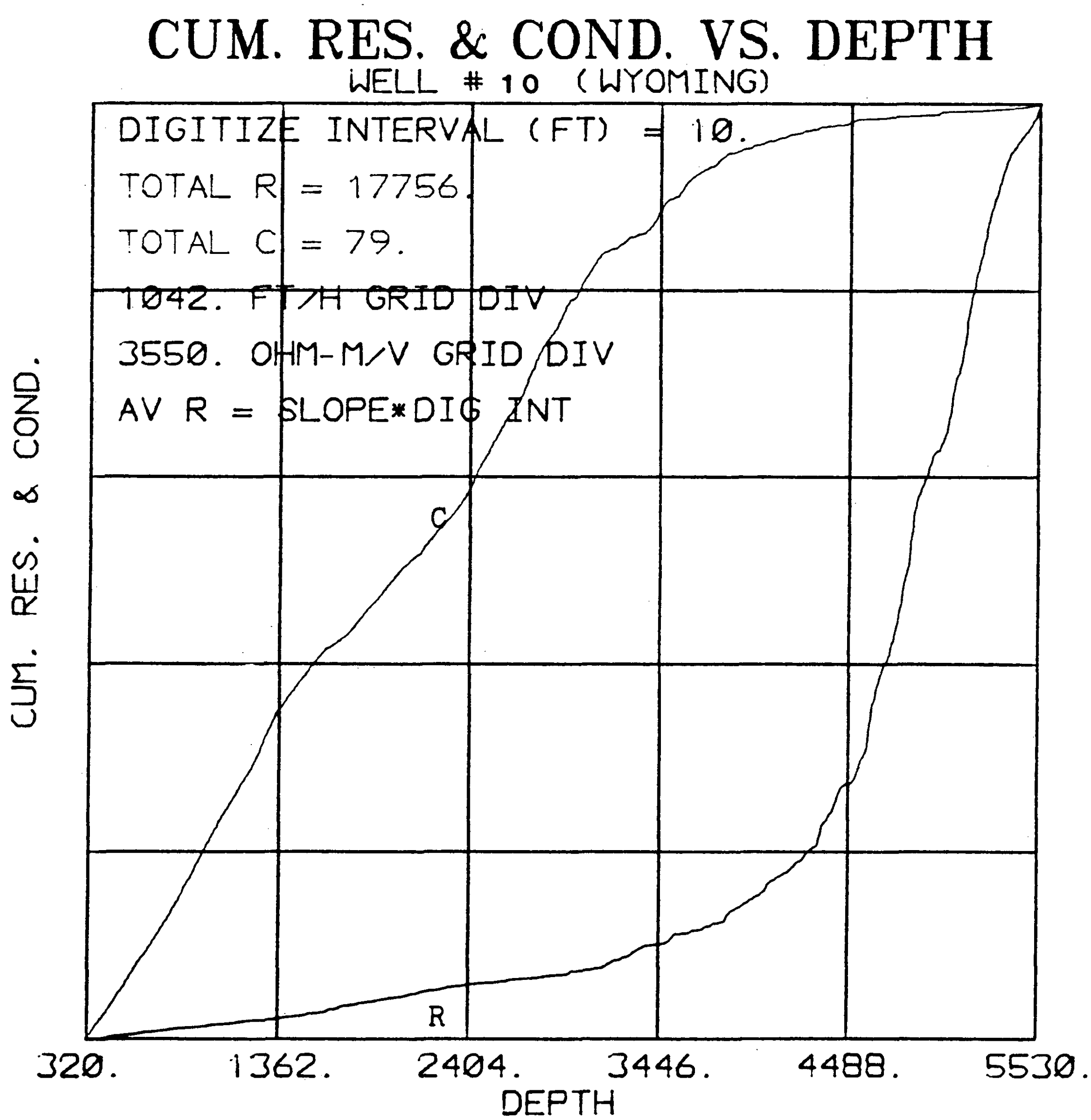
CUM. RES. & COND. VS. DEPTH
WELL # 10 (WYOMING)
DIGITIZE INTERVAL (FT) = 10.
TOTAL R = 17756.
TOTAL C = 79.
1042. FT/H GRID DIV
3550. OHM-M/V GRID DIV
AV R = SLOPE*DIG INT
C
R
CUM. RES. & COND.
320.
1362.
2404.
3446.
4488.
5530.
DEPTH

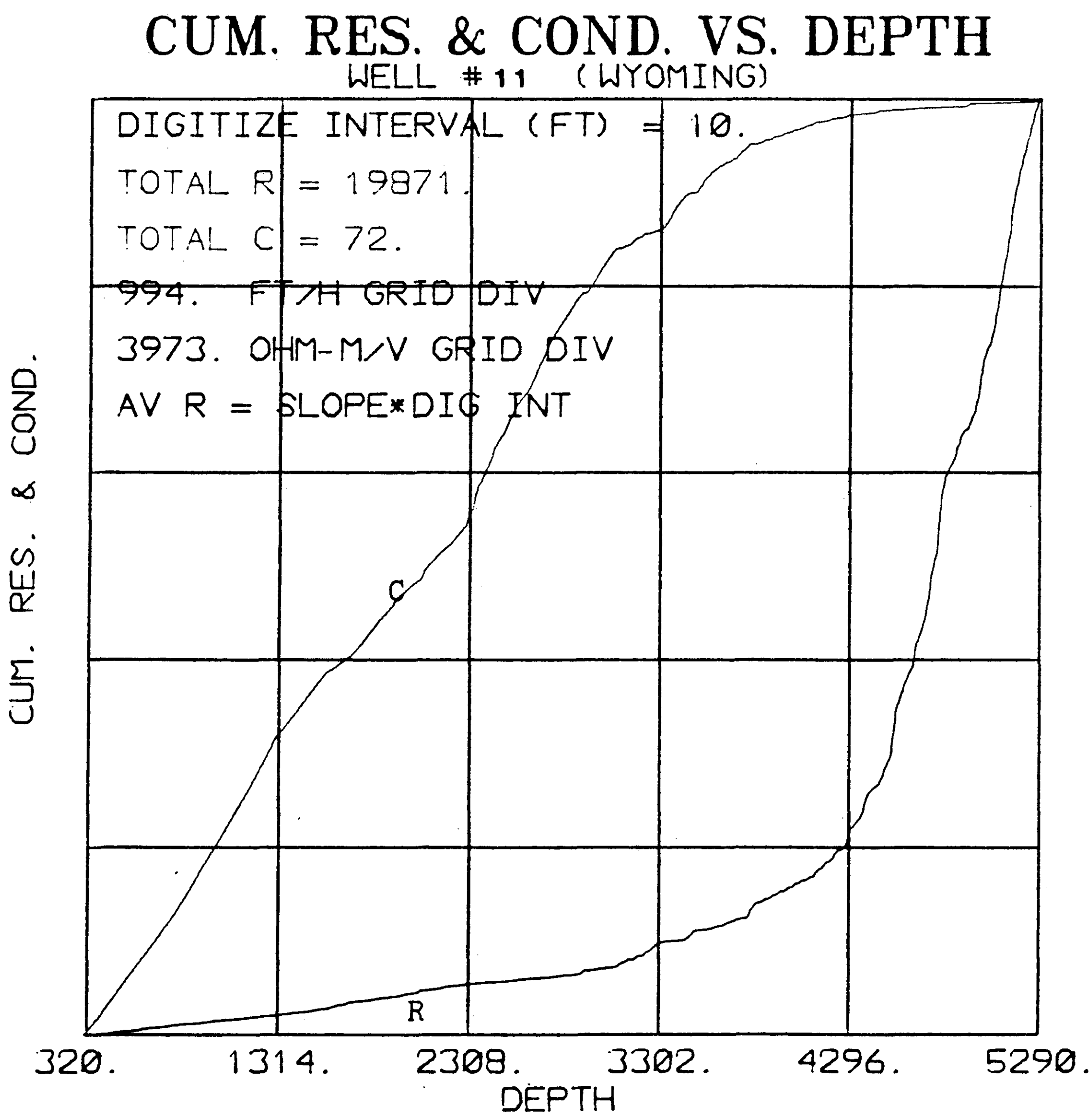
CUM. RES. & COND. VS. DEPTH
WELL #11 (WYOMING)
DIGITIZE INTERVAL (FT) = 10.
TOTAL R = 19871.
TOTAL C = 72.
994. FT/H GRID DIV
3973. OHM-M/V GRID DIV
AV R = SLOPE*DIG INT
CUM. RES. & COND.
C
R
320.
1314.
2308.
3302.
4296.
5290.
DEPTH

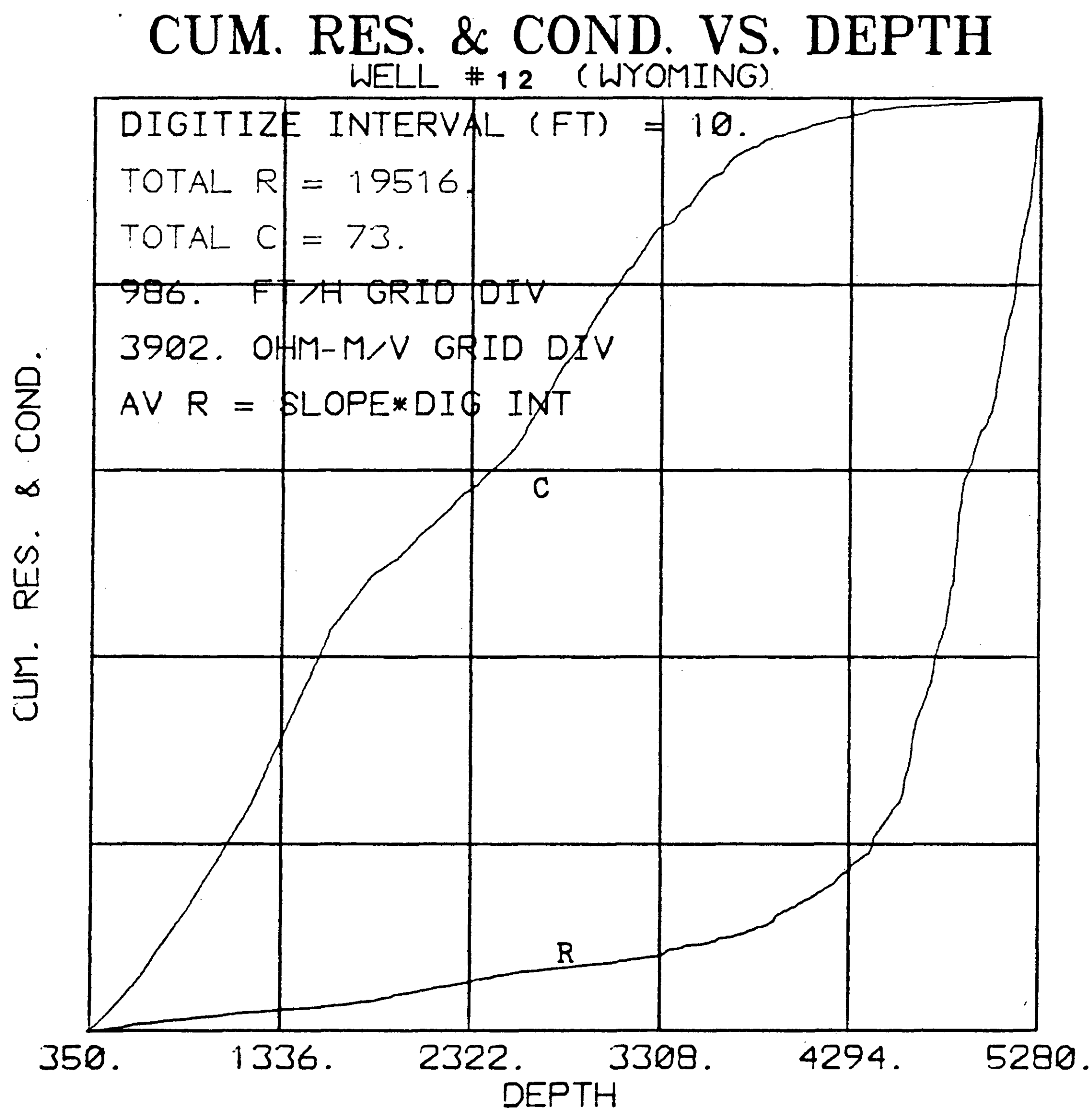
CUM. RES. & COND. VS. DEPTH
WELL # 12 (WYOMING)
DIGITIZE INTERVAL (FT) = 10.
TOTAL R = 19516.
TOTAL C = 73.
986. FT/H GRID DIV
3902. OHM-M/V GRID DIV
AV R = SLOPE*DIG INT
C
R
CUM. RES. & COND.
350.
1336.
2322.
3308.
4294.
5280.
DEPTH

CUM. RES. & COND. VS. DEPTH

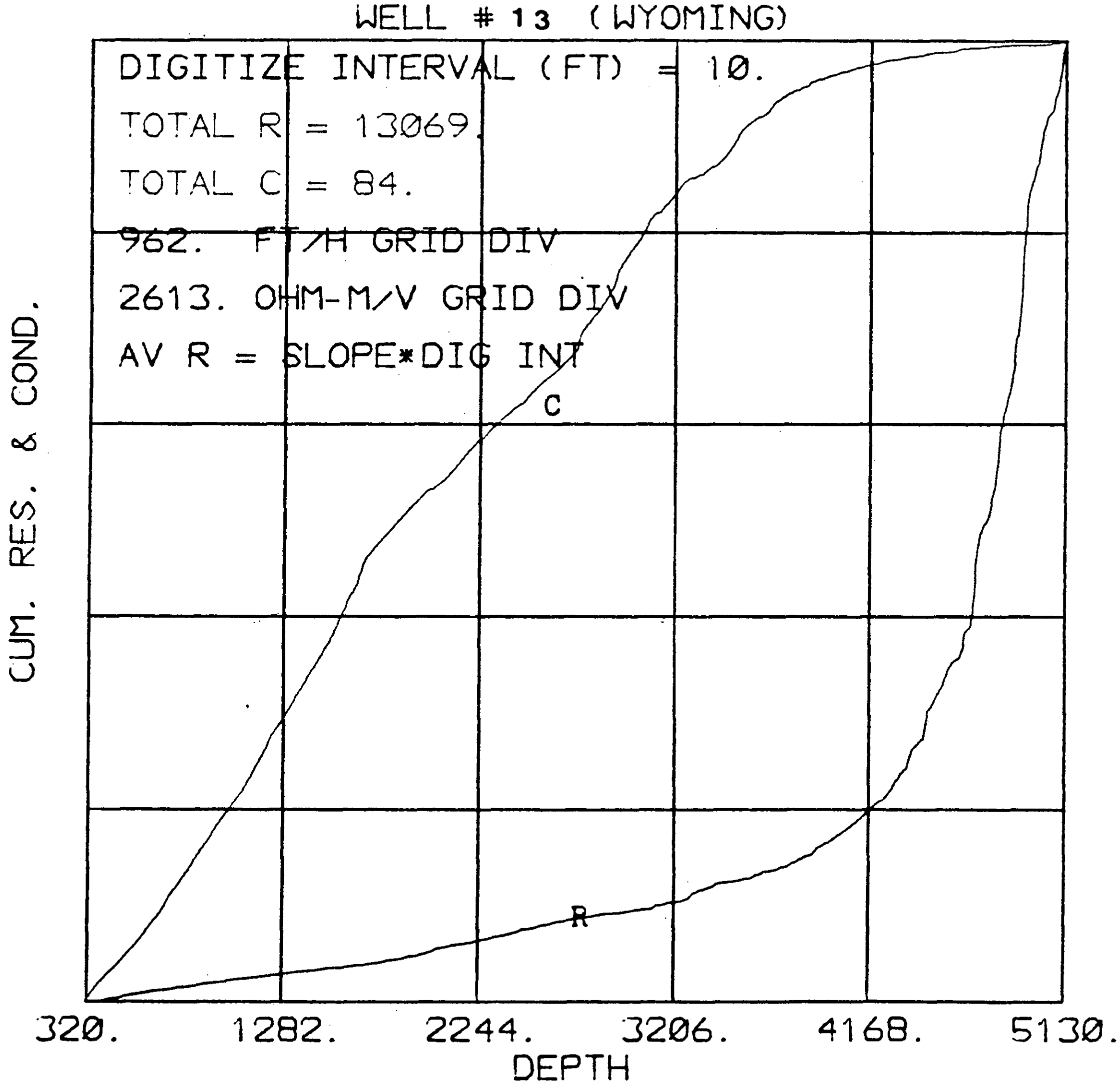

CUM. RES. & COND. VS. DEPTH

WELL # 14 (WYOMING)

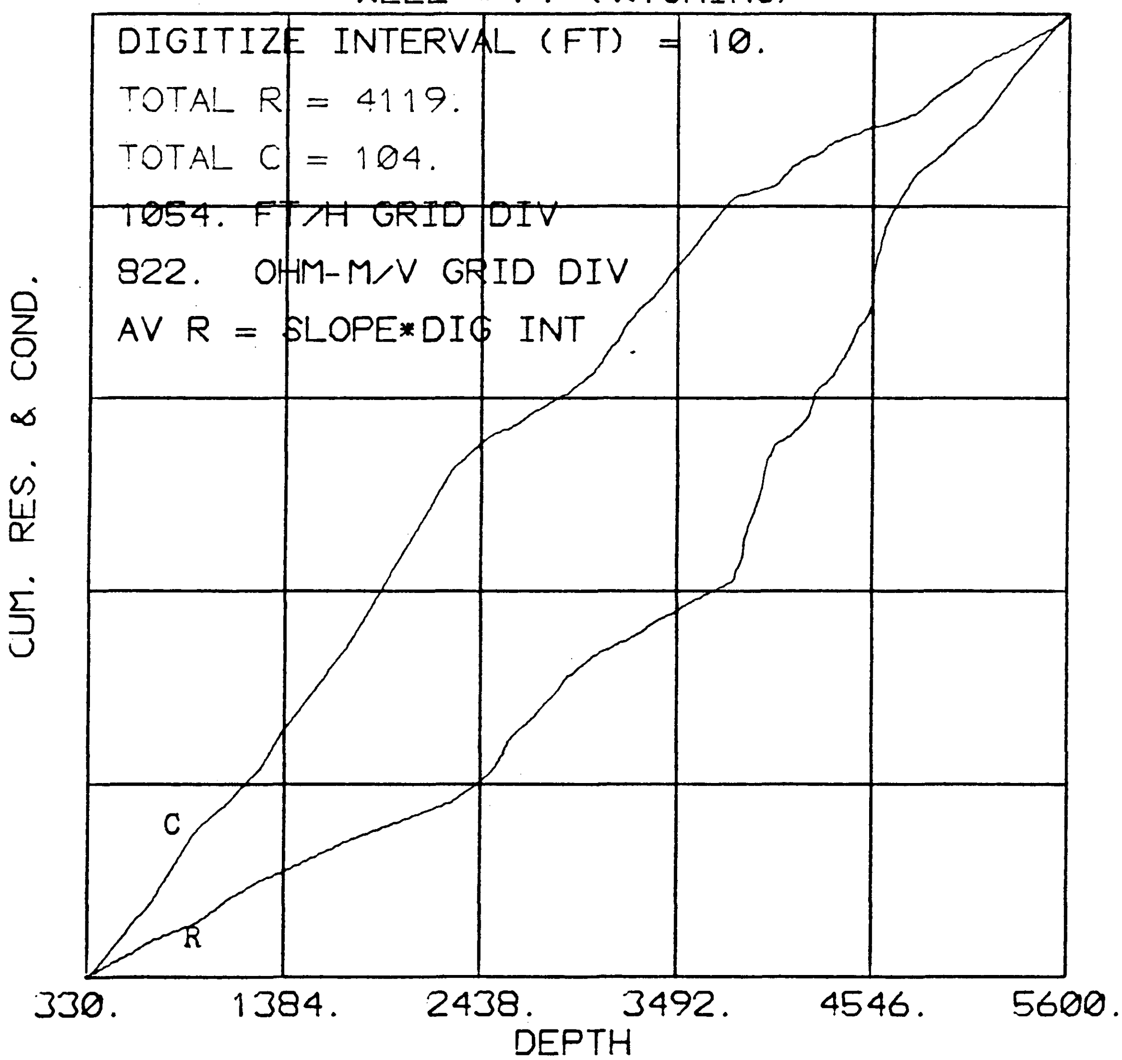

CUM. RES. & COND. VS. DEPTH

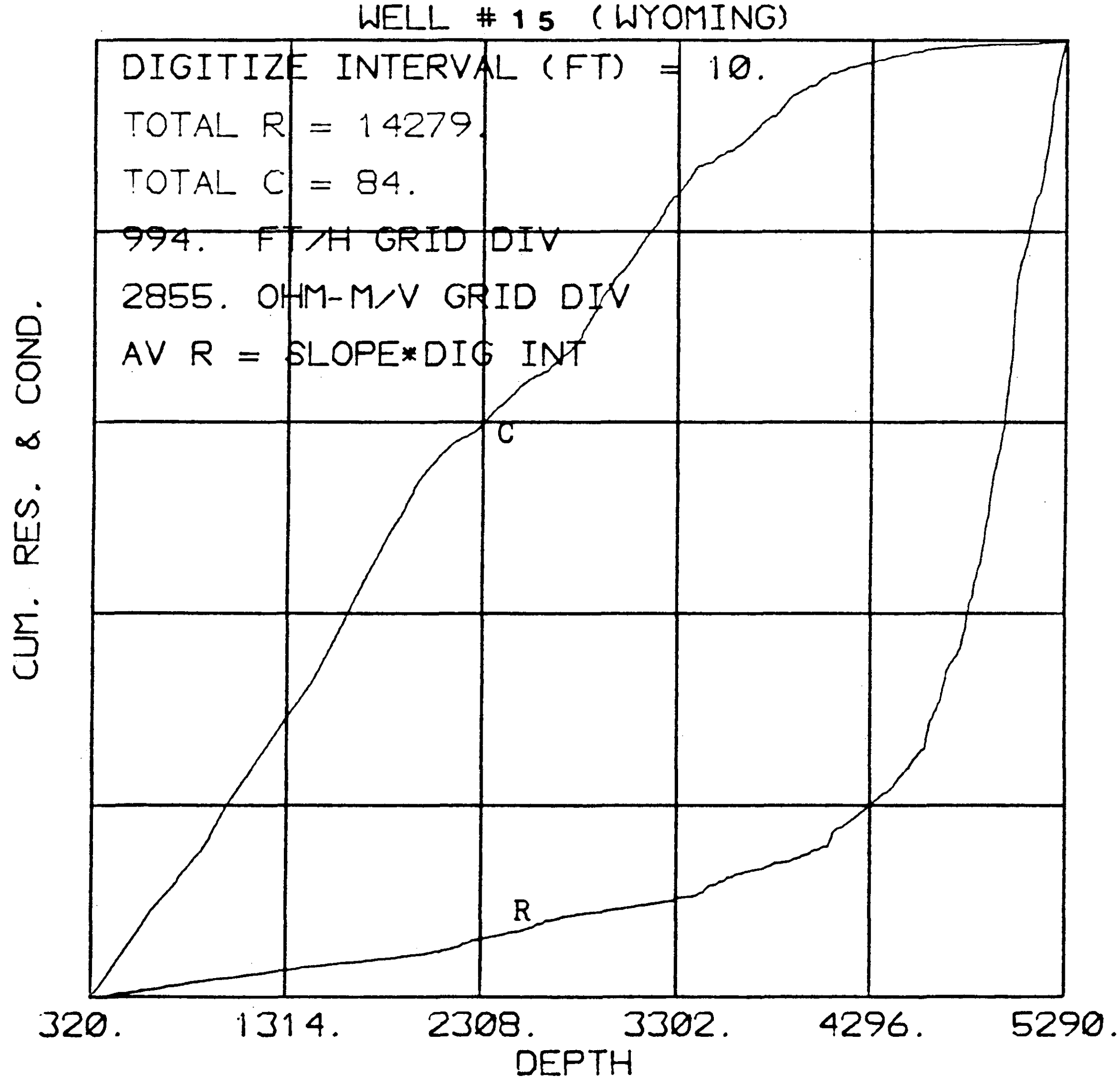

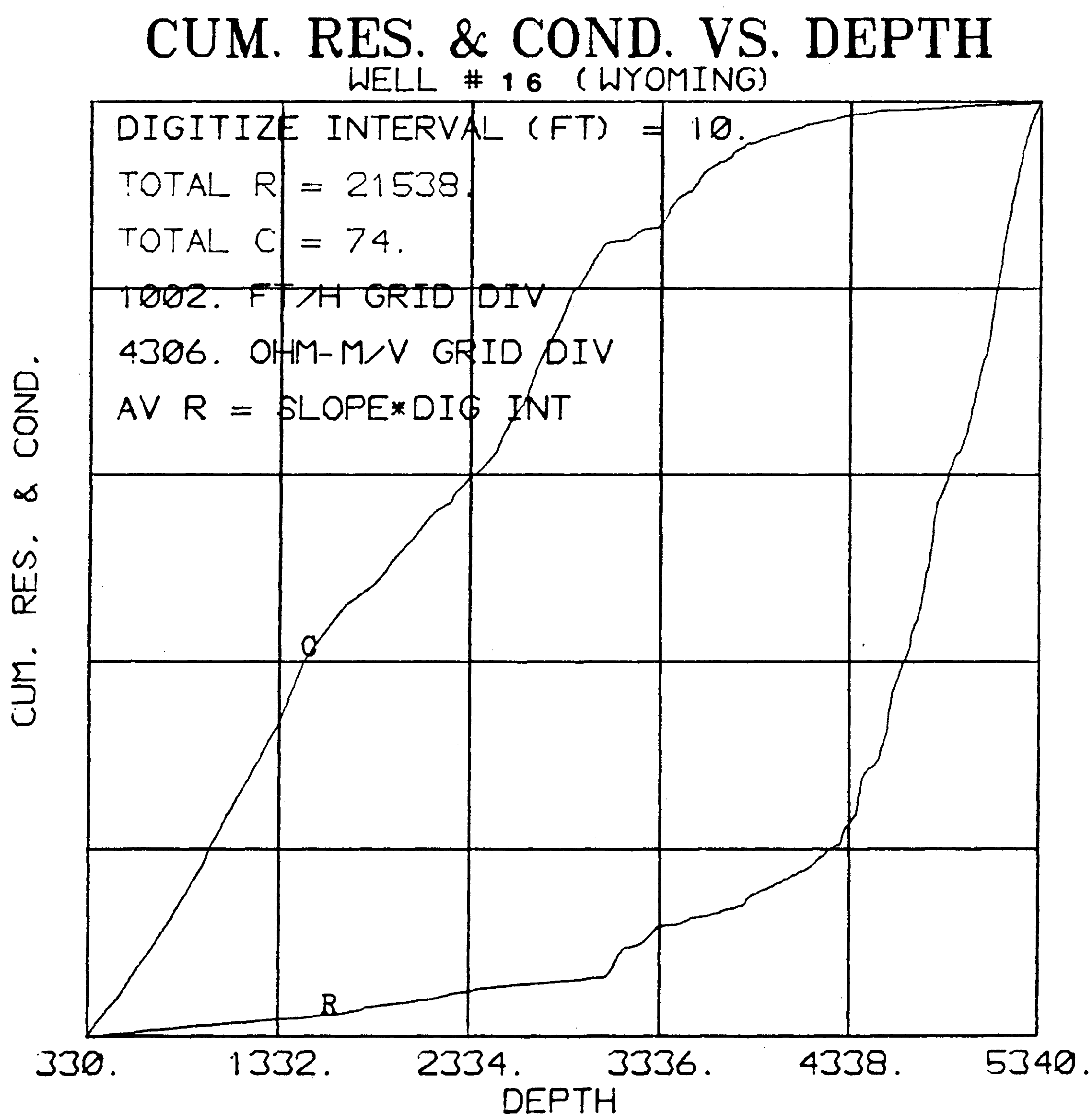
CUM. RES. & COND. VS. DEPTH
WELL # 16 (WYOMING)
DIGITIZE INTERVAL (FT) = 10.
TOTAL R = 21538.
TOTAL C = 74.
1002. FT/H GRID DIV
4306. OHM-M/V GRID DIV
AV R = SLOPE*DIG INT
C
R
CUM. RES. & COND.
330.
1332.
2334.
3336.
4338.
5340.
DEPTH

CUM. RES. & COND. VS. DEPTH

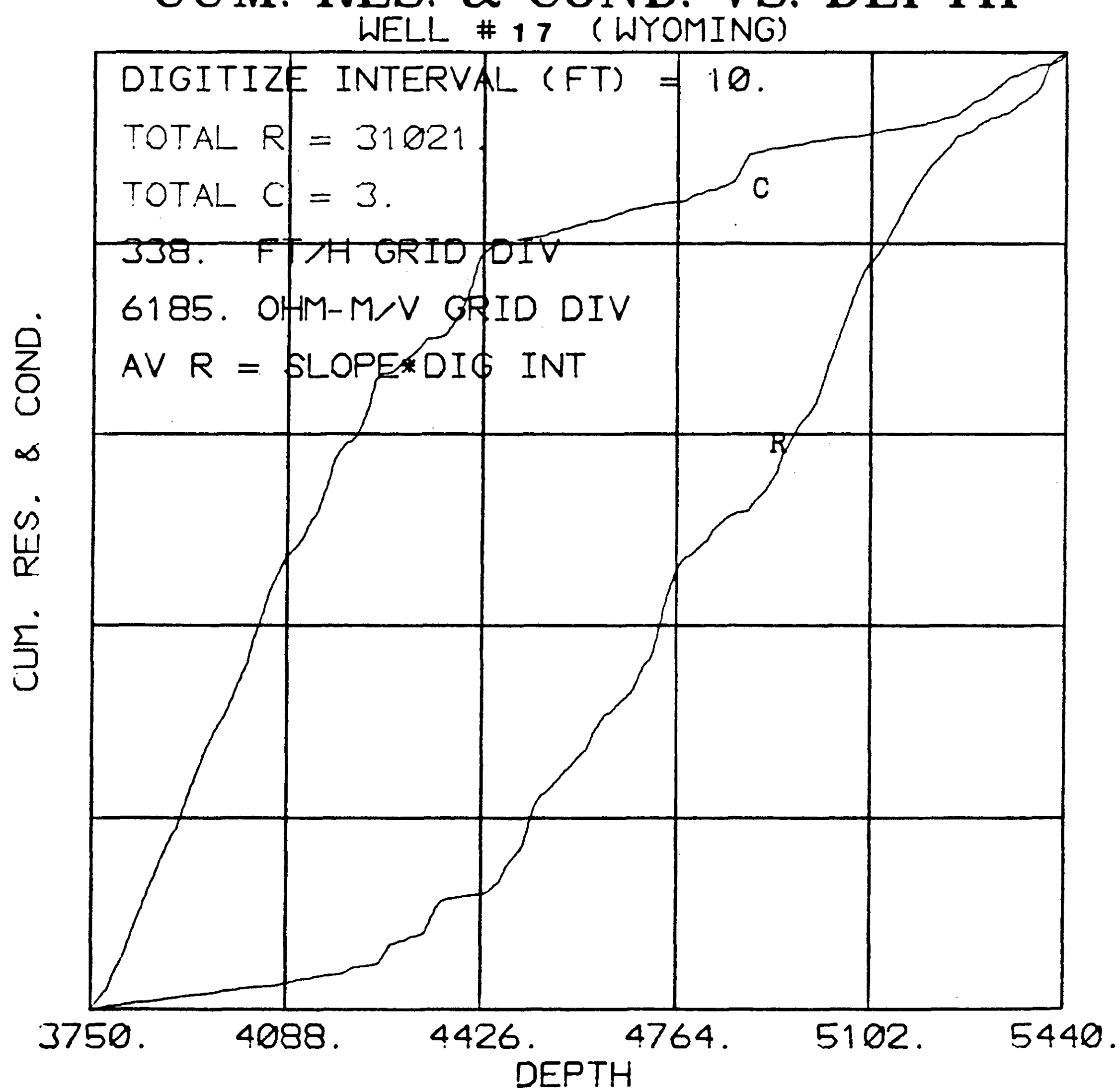

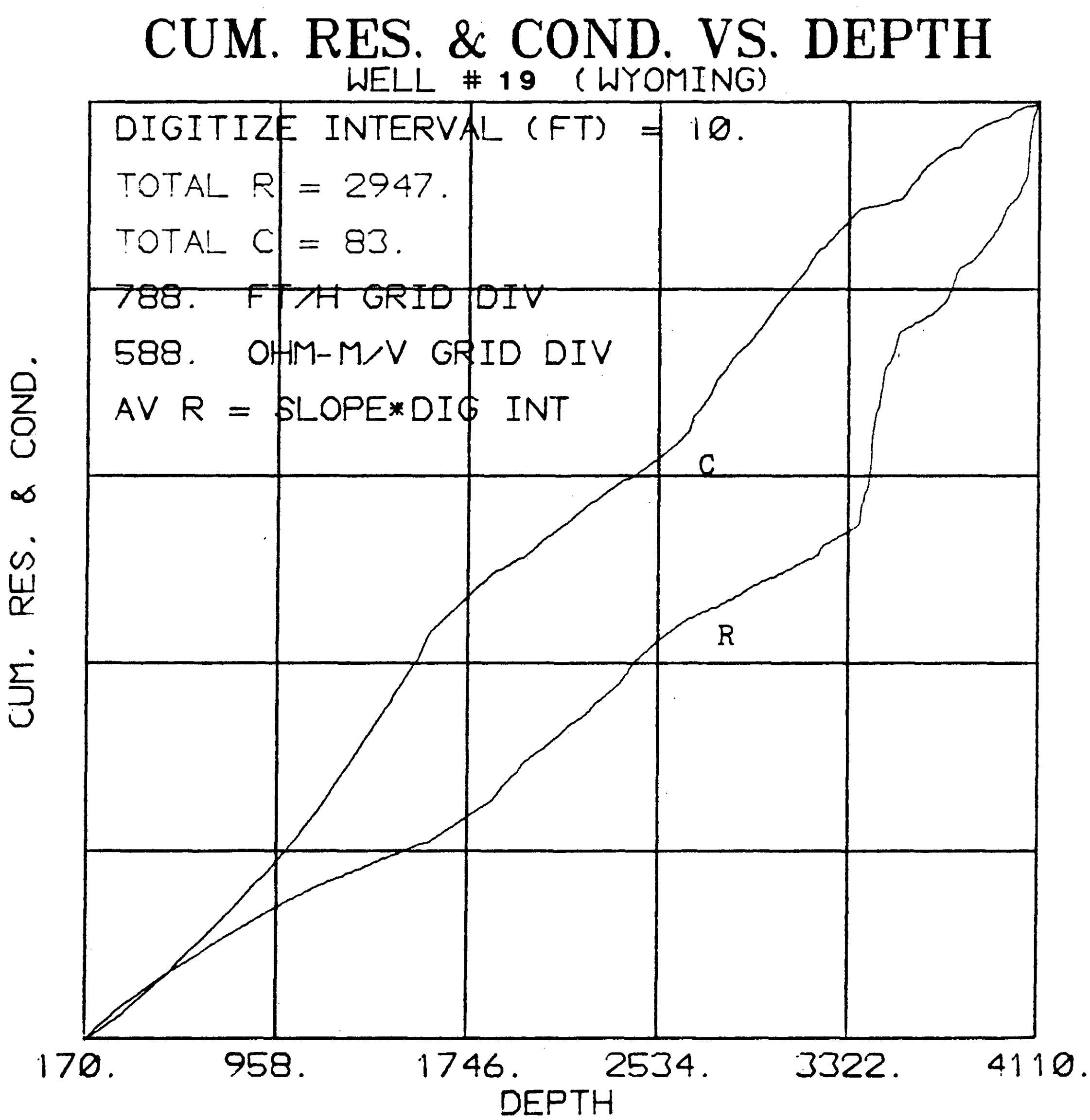
CUM. RES. & COND. VS. DEPTH
WELL # 19 (WYOMING)
DIGITIZE INTERVAL (FT) = 10.
TOTAL R = 2947.
TOTAL C = 83.
788. FT/H GRID DIV
588. OHM-M/V GRID DIV
AV R = SLOPE*DIG INT
C
R
CUM. RES. & COND.
170.
958.
1746.
2534.
3322.
4110.
DEPTH

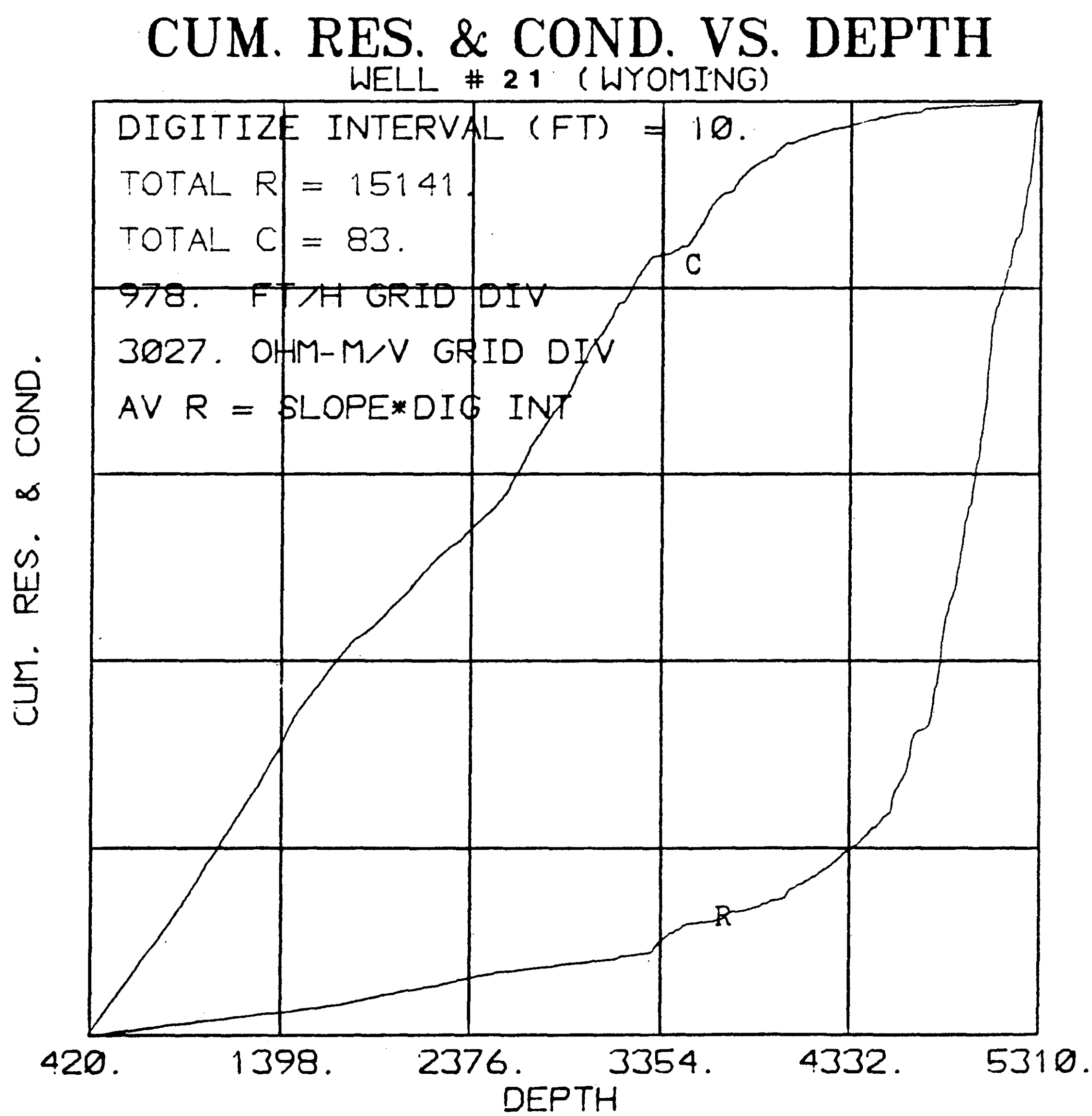
CUM. RES. & COND. VS. DEPTH
WELL # 21 (WYOMING)
DIGITIZE INTERVAL (FT) = 10.
TOTAL R = 15141.
TOTAL C = 83.
978. FT/H GRID DIV
3027. OHM-M/V GRID DIV
AV R = SLOPE*DIG INT
C
R
CUM. RES. & COND.
420.
1398.
2376.
3354.
4332.
5310.
DEPTH

CUM. RES. & COND. VS. DEPTH

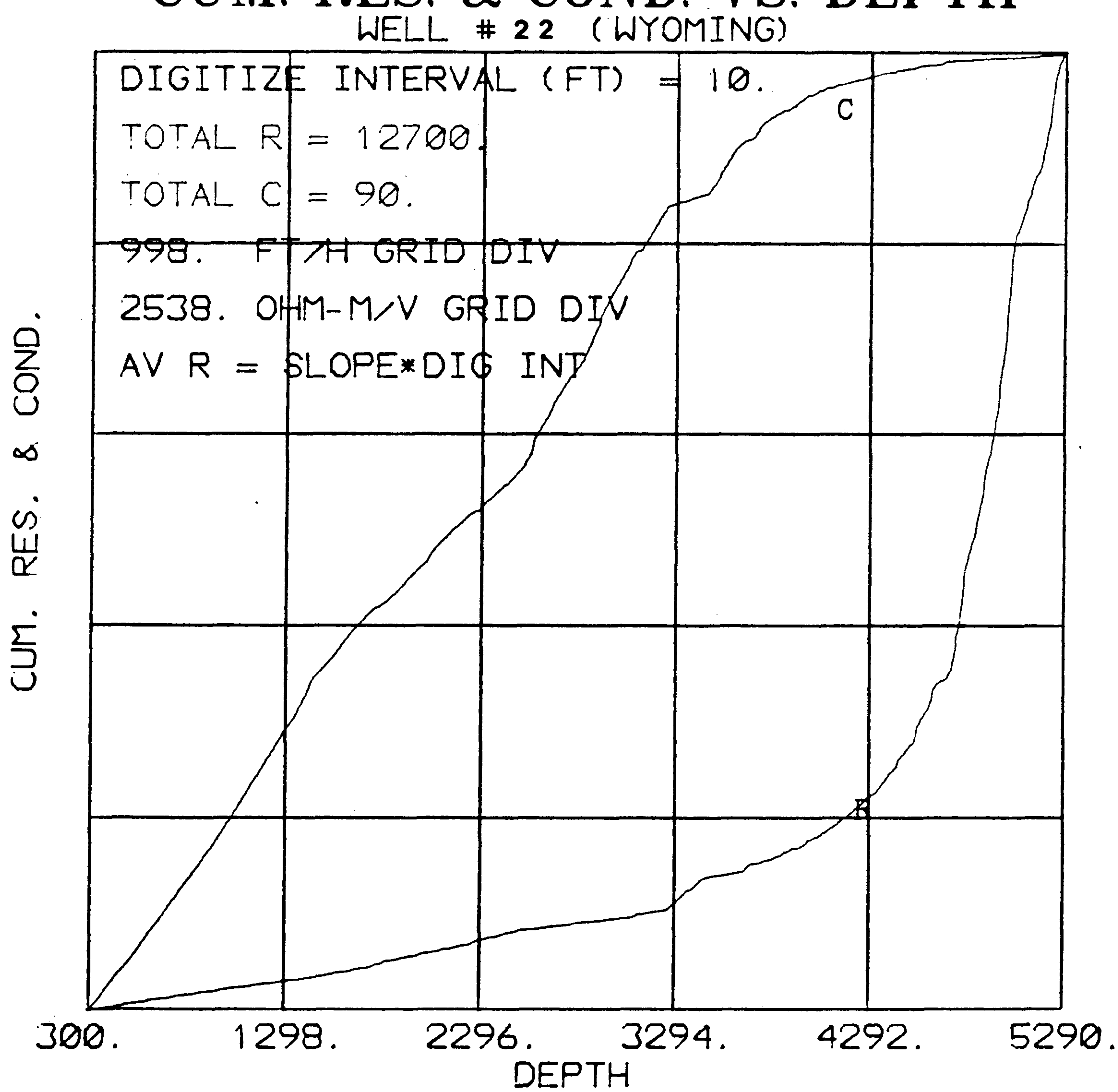

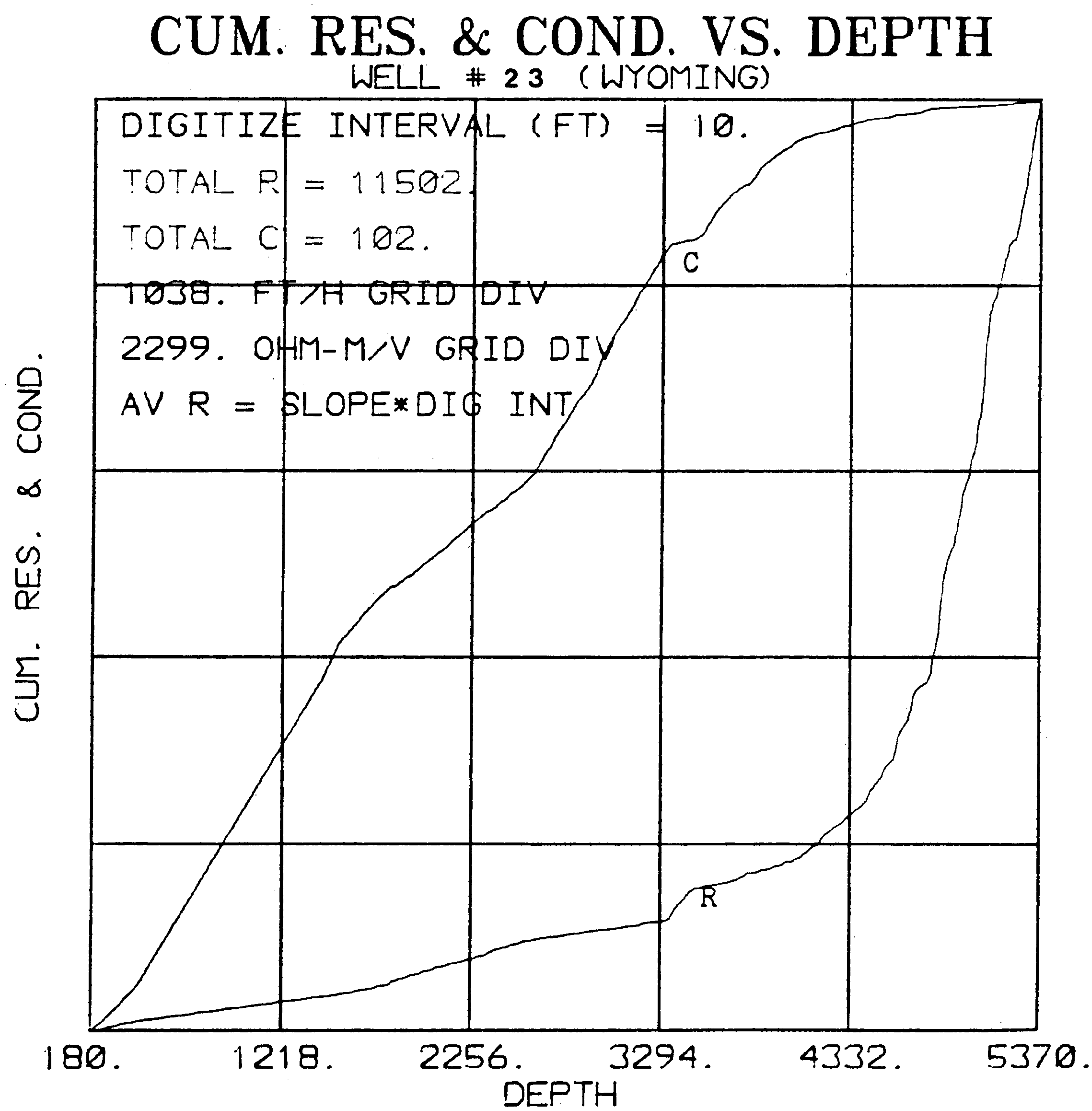
CUM. RES. & COND. VS. DEPTH
WELL # 23 (WYOMING)
DIGITIZE INTERVAL (FT) = 10.
TOTAL R = 11502.
TOTAL C = 102.
1038. FT/H GRID DIV
2299. OHM-M/V GRID DIV
AV R = SLOPE*DIG INT
C
R
CUM. RES. & COND.
180.
1218.
2256.
3294.
4332.
5370.
DEPTH

CUM. RES. & COND. VS. DEPTH

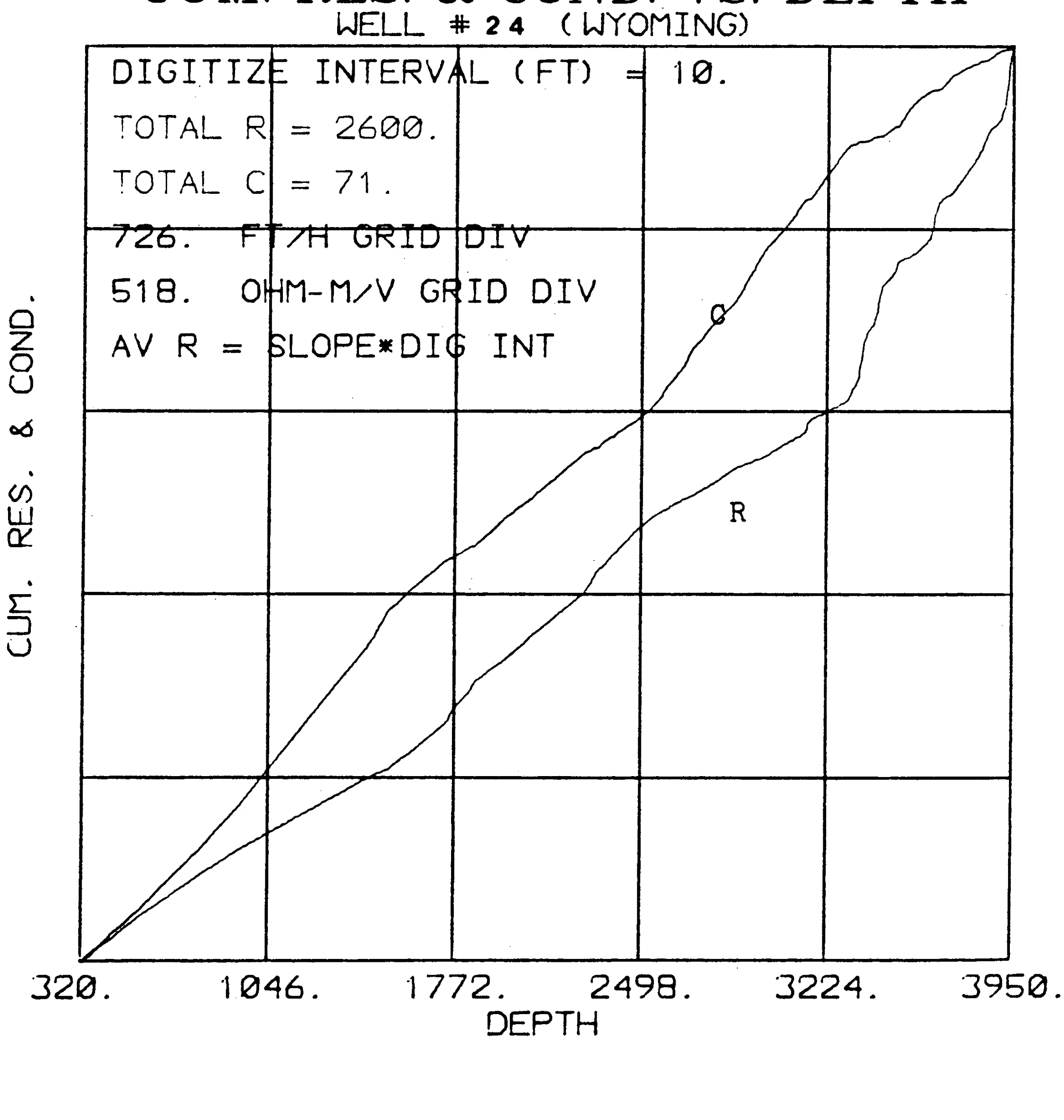

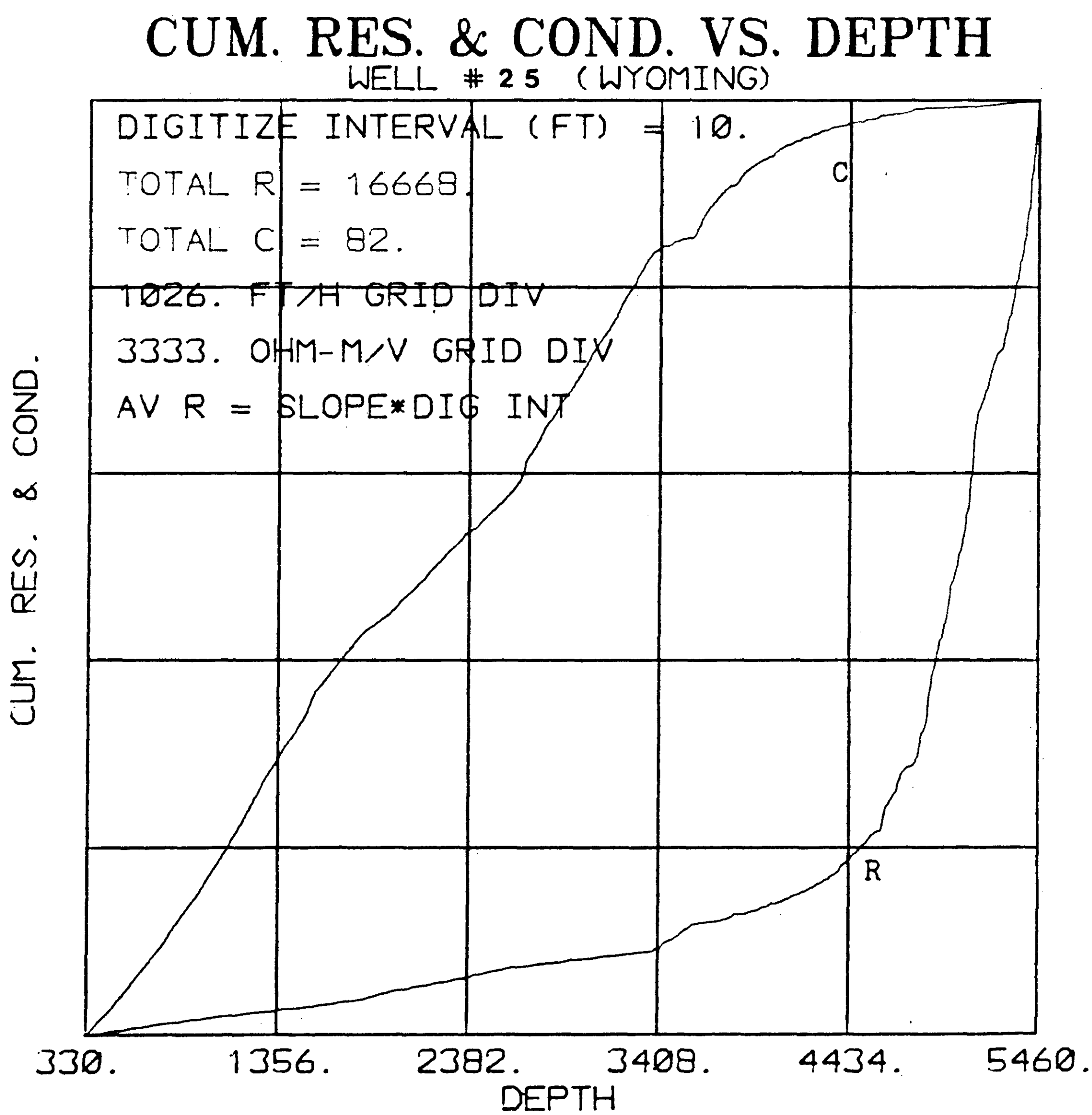
CUM. RES. & COND. VS. DEPTH
WELL # 25 (WYOMING)
DIGITIZE INTERVAL (FT) = 10.
TOTAL R = 16668.
TOTAL C = 82.
1026. FT/H GRID DIV
3333. OHM-M/V GRID DIV
AV R = SLOPE*DIG INT
C
R
CUM. RES. & COND.
330.
1356.
2382.
3408.
4434.
5460.
DEPTH

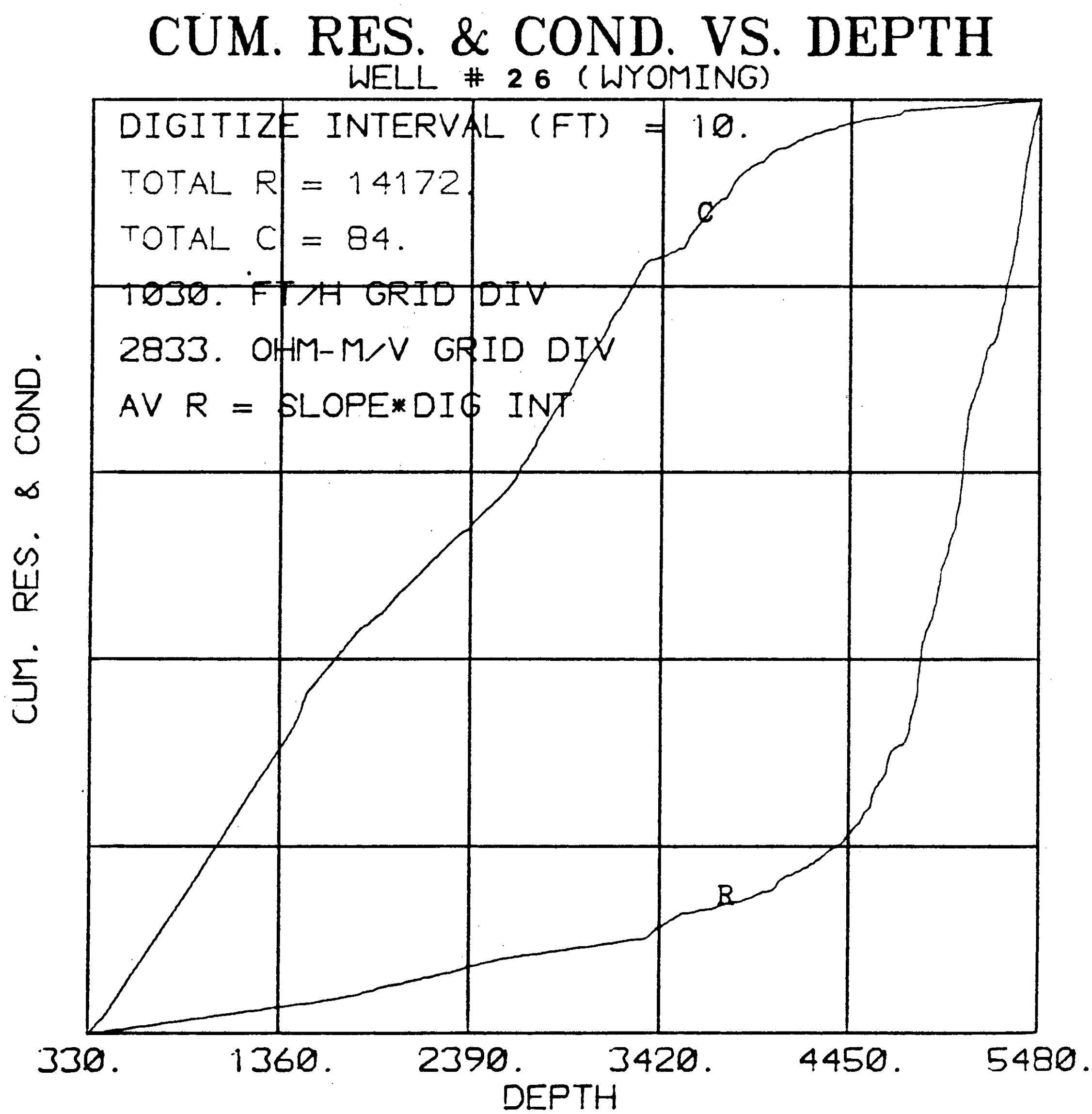
CUM. RES. & COND. VS. DEPTH
WELL # 26 (WYOMING)
DIGITIZE INTERVAL (FT) = 10.
TOTAL R = 14172.
TOTAL C = 84.
1030. FT/H GRID DIV
2833. OHM-M/V GRID DIV
AV R = SLOPE*DIG INT
C
R
CUM. RES. & COND.
330.
1360.
2390.
3420.
4450.
5480.
DEPTH

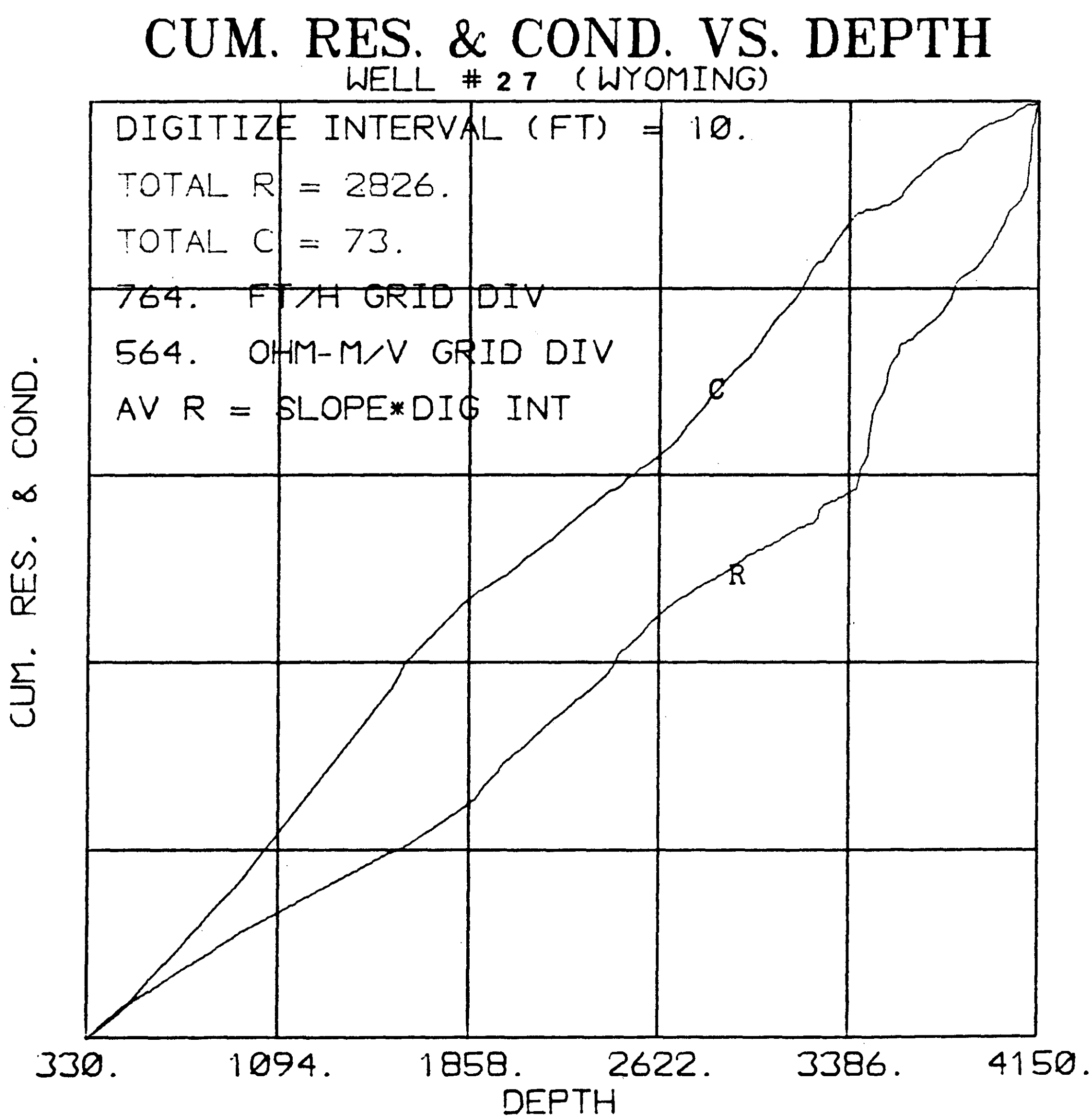
CUM. RES. & COND. VS. DEPTH
WELL # 27 (WYOMING)
DIGITIZE INTERVAL (FT) = 10.
TOTAL R = 2826.
TOTAL C = 73.
764. FT/H GRID DIV
564. OHM-M/V GRID DIV
AV R = SLOPE*DIG INT
C
R
CUM. RES. & COND.
330.
1094.
1858.
2622.
3386.
4150.
DEPTH

CUM. RES. & COND. VS. DEPTH

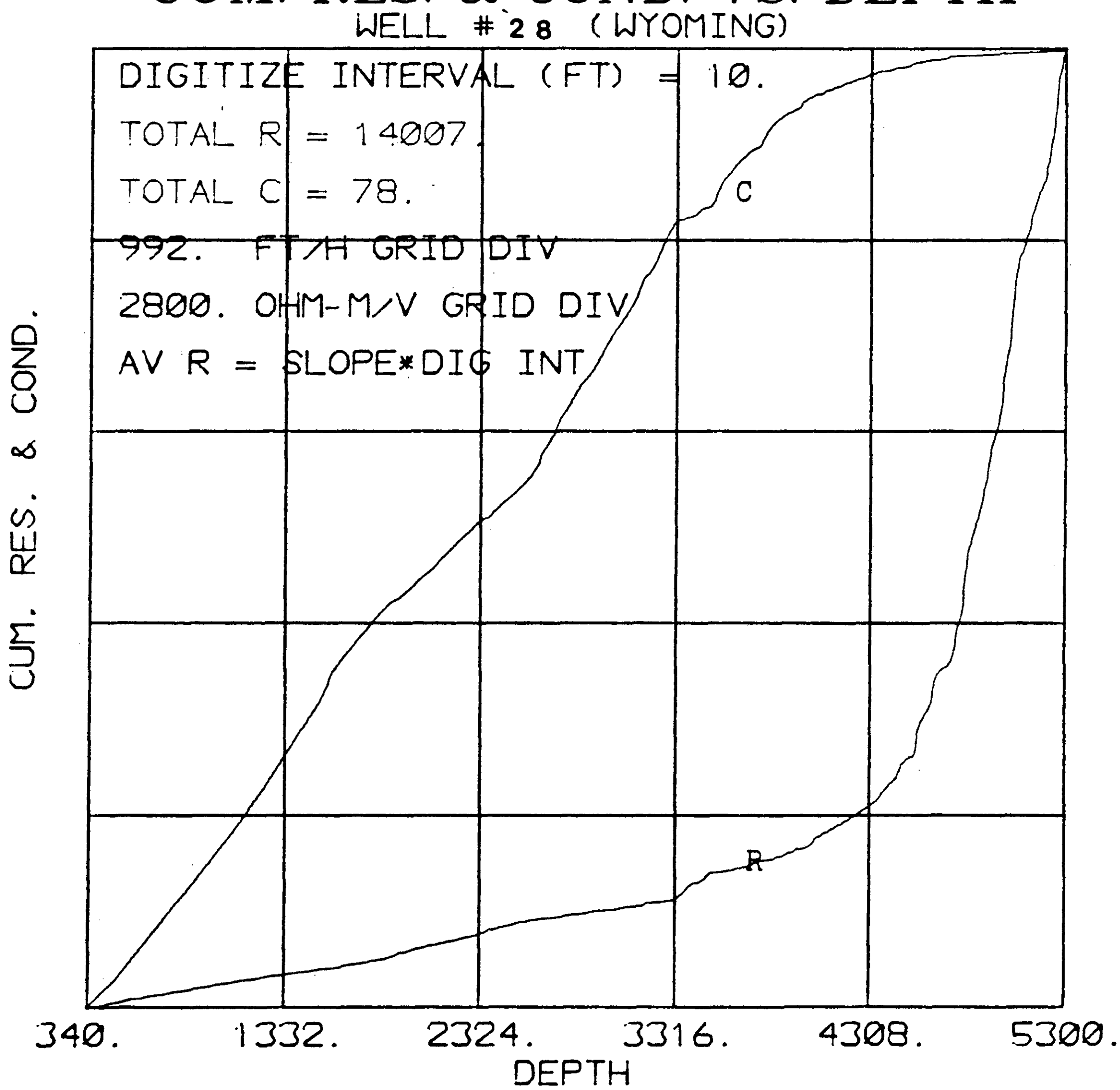

CUM. RES. & COND. VS. DEPTH

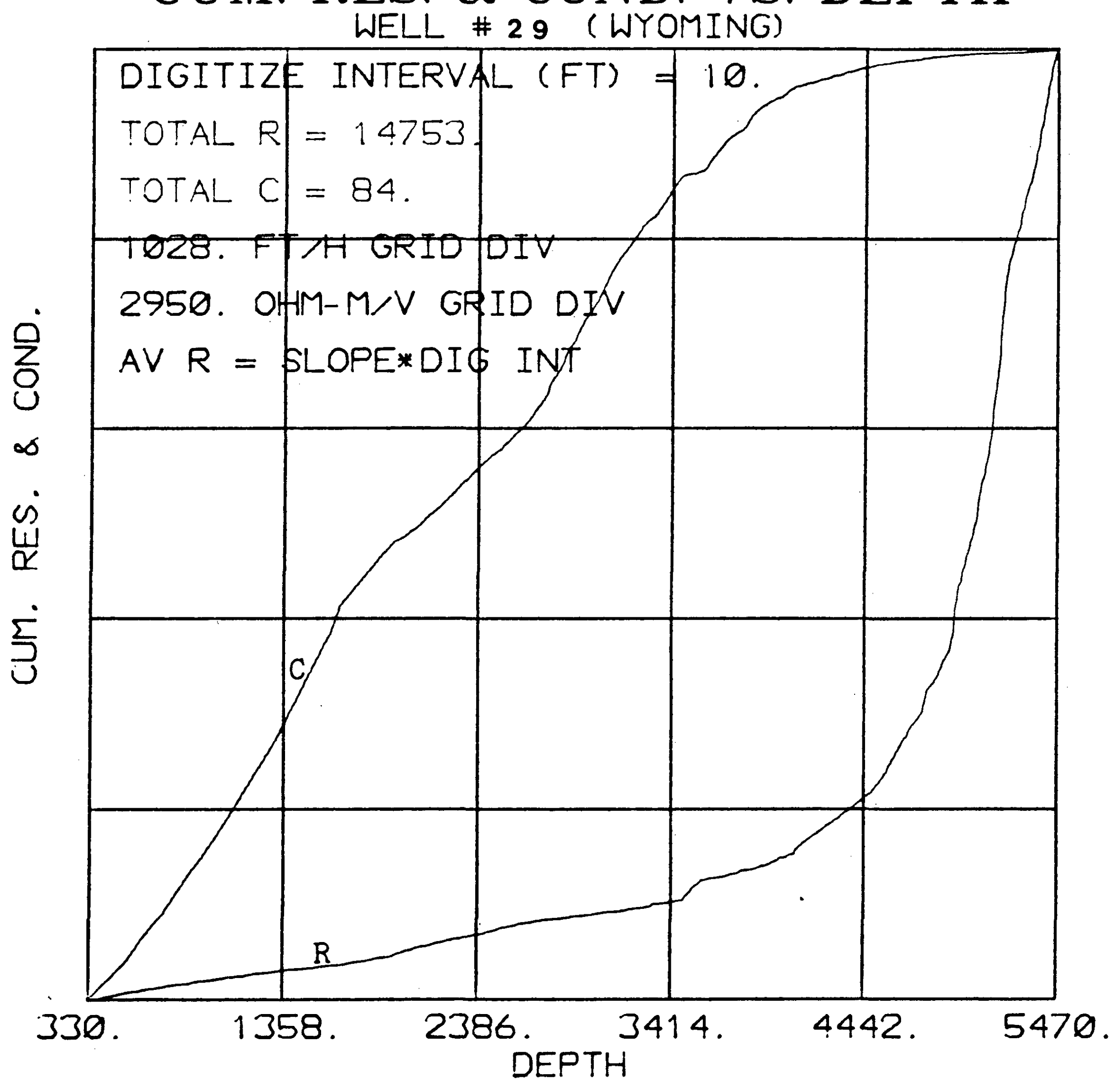

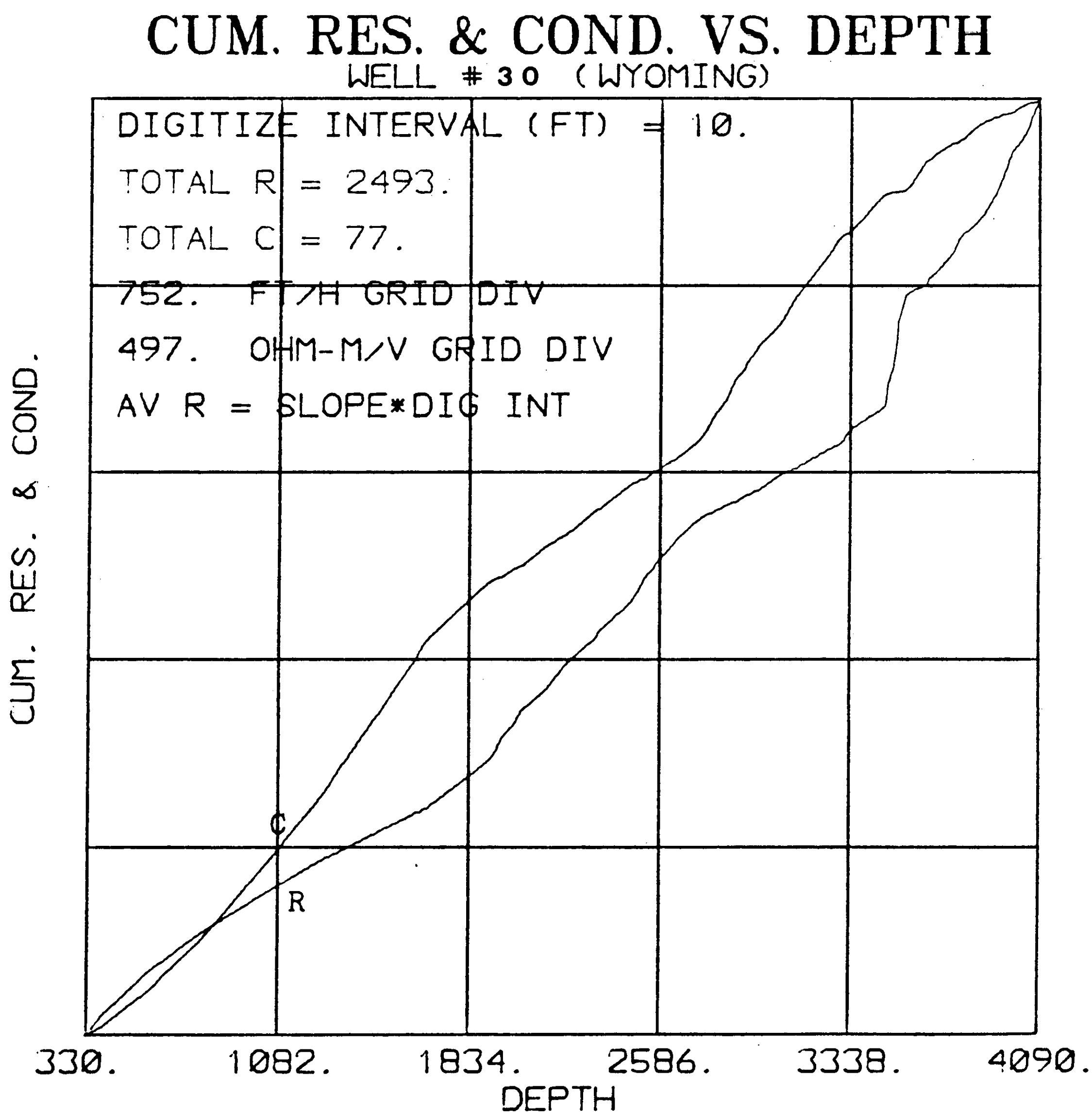
CUM. RES. & COND. VS. DEPTH
WELL # 30 (WYOMING)
DIGITIZE INTERVAL (FT) = 10.
TOTAL R = 2493.
TOTAL C = 77.
752. FT/H GRID DIV
497. OHM-M/V GRID DIV
AV R = SLOPE*DIG INT
C
R
CUM. RES. & COND.
330.
1082.
1834.
2586.
3338.
4090.
DEPTH

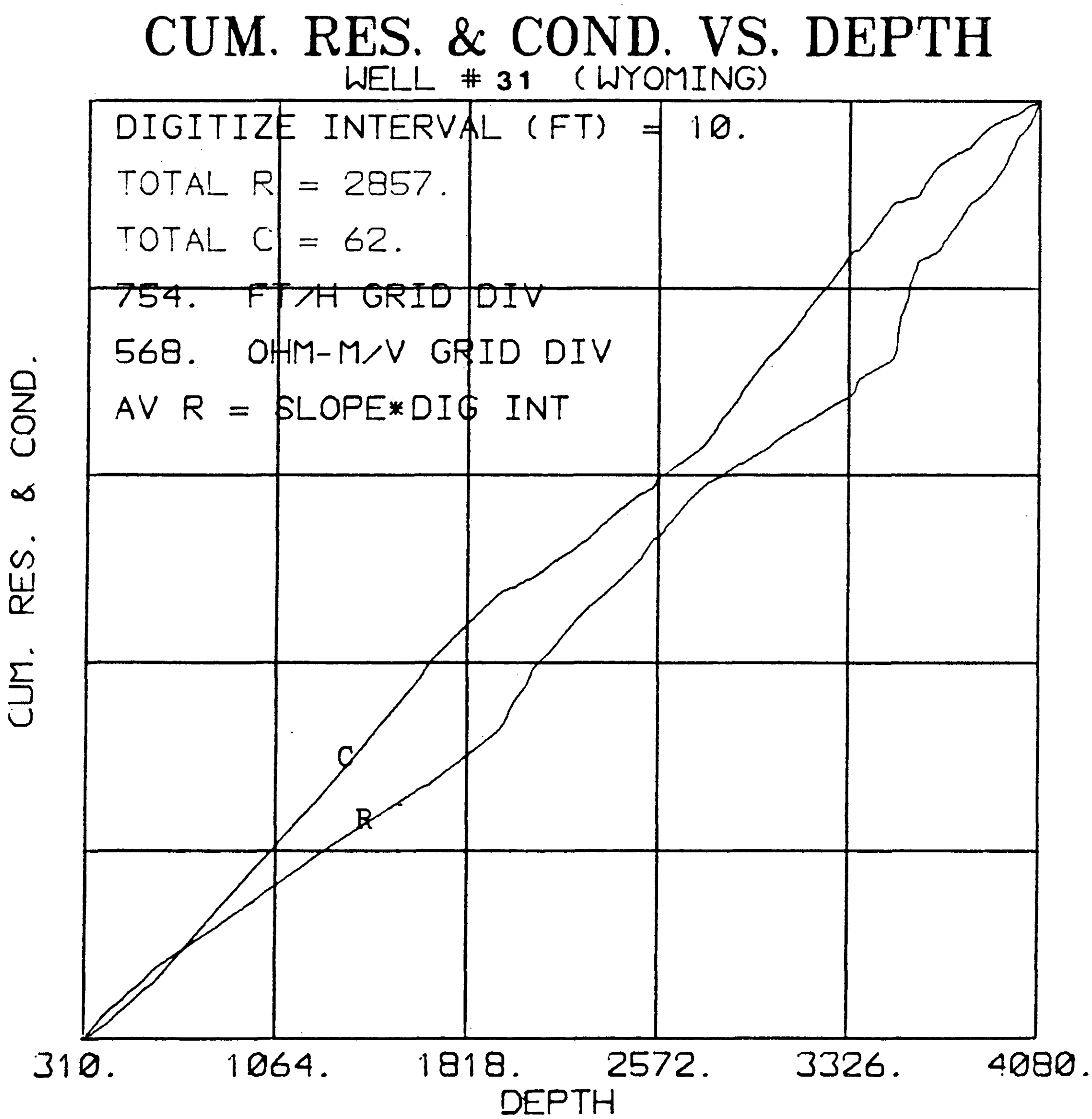
CUM. RES. & COND. VS. DEPTH
WELL # 31 (WYOMING)
DIGITIZE INTERVAL (FT) = 10.
TOTAL R = 2857.
TOTAL C = 62.
754. FT/H GRID DIV
568. OHM-M/V GRID DIV
AV R = SLOPE*DIG INT
C
R
CUM. RES. & COND.
310.
1064.
1818.
2572.
3326.
4080.
DEPTH

CUM. RES. & COND. VS. DEPTH

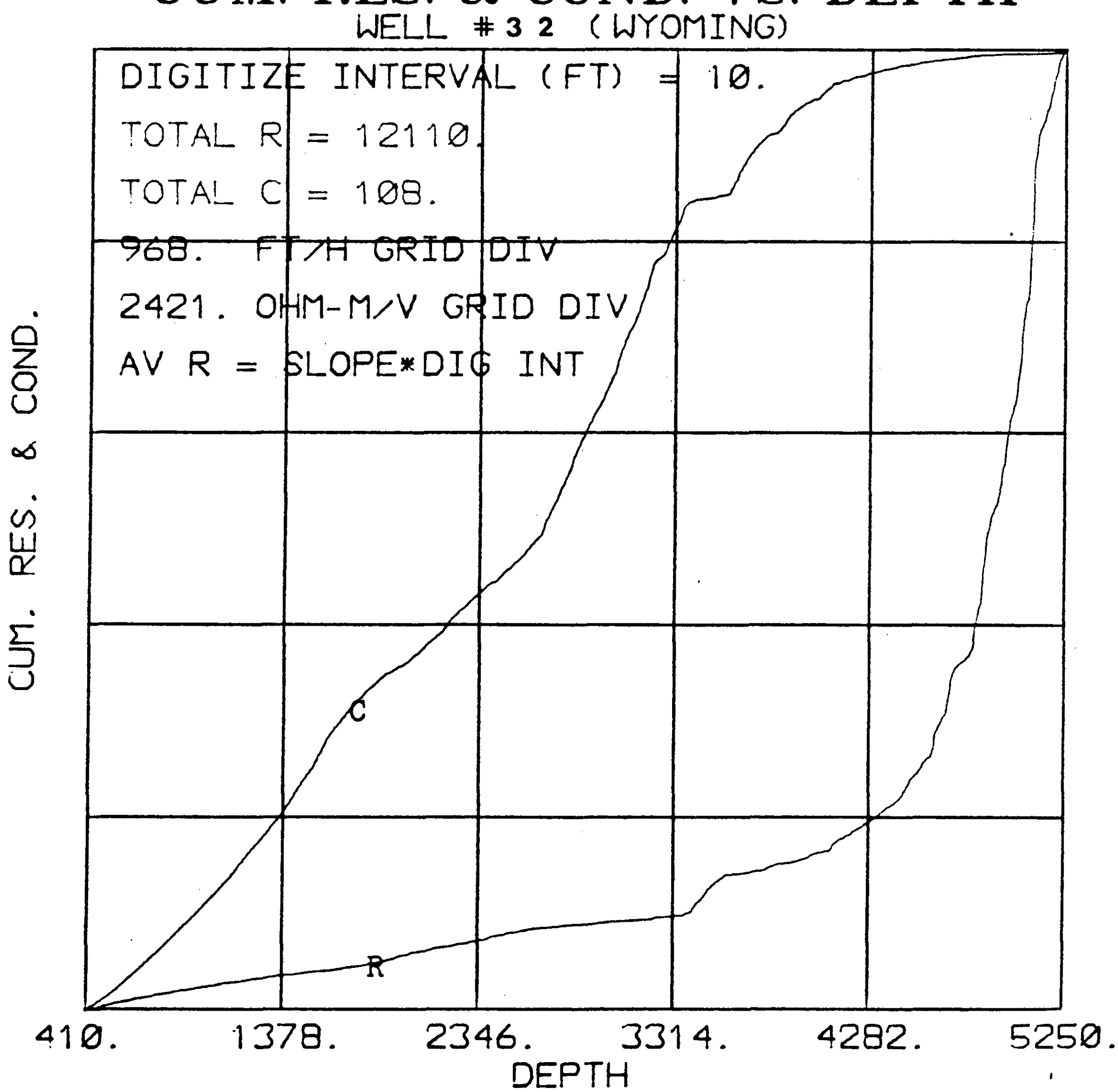

CUM. RES. & COND. VS. DEPTH

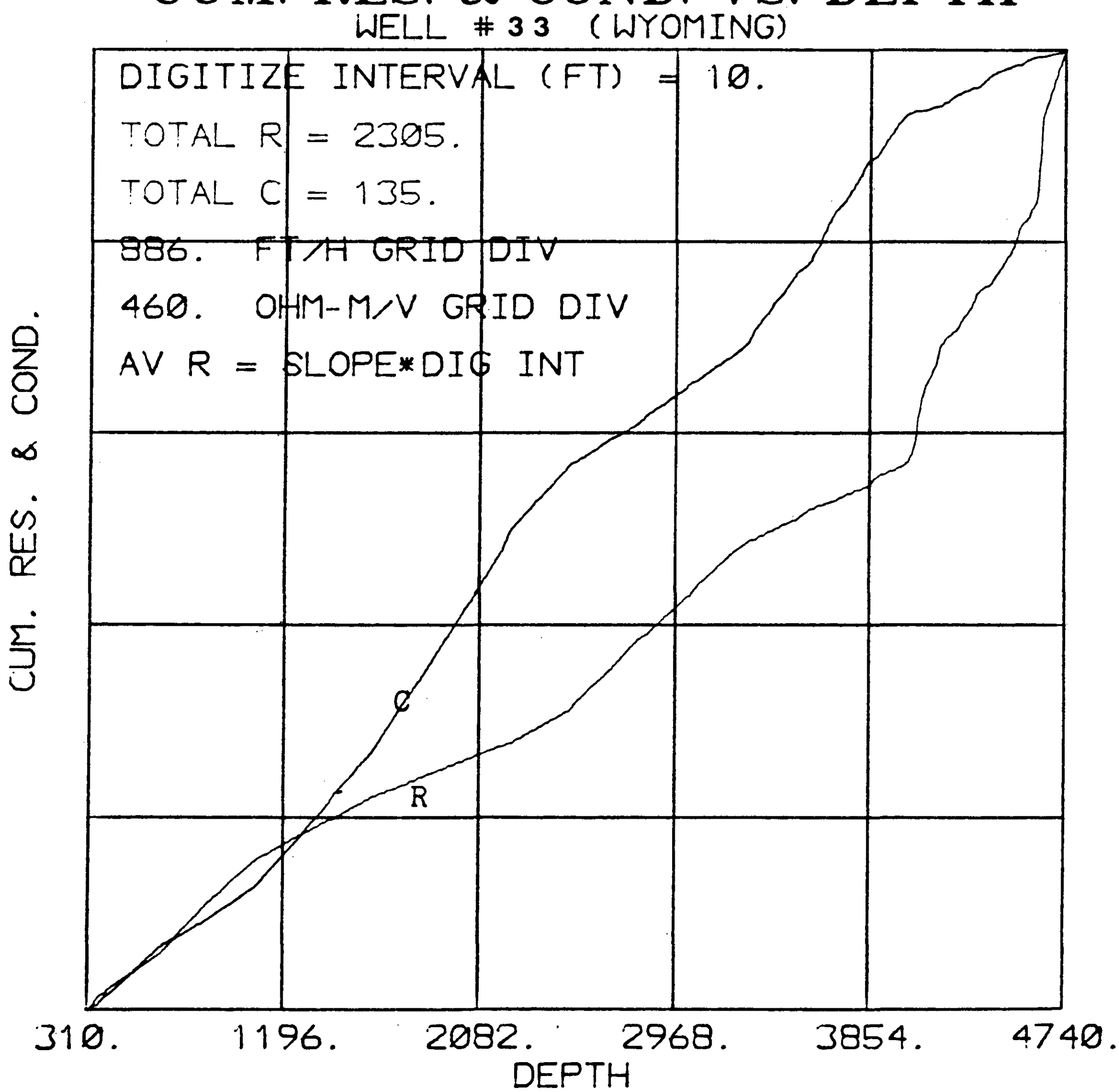

WELL # 1 (WYOMING)

UNIT	DEPTH INTERVAL	AV.TRA.RES.	AV.LON.RES.	COEFF.ANISO.
1	420.- 3510.	4.87	4.27	1.0678
2	3510.- 4560.	15.40	10.27	1.2241
3	4560.- 5480.	105.69	46.17	1.5130

WELL # 2

1	330.- 3430.	5.99	5.50	1.0438
2	3430.- 4450.	17.57	11.70	1.2258
3	4450.- 5380.	92.91	55.67	1.2919

WELL # 3

1	340.- 3580.	5.64	4.81	1.0827
2	3580.- 4610.	18.71	10.65	1.3252
3	4610.- 5520.	129.37	57.69	1.4976

WELL # 4

1	310.- 4640.	4.58	3.43	1.1566

WELL # 5

1	540.- 5600.	4.60	3.48	1.1498
2	5600.- 6380.	15.37	9.99	1.2404
3	6380.- 7210.	51.45	36.36	1.1896
4	7210.- 7910.	96.68	64.20	1.2271
5	7910.- 9690.	16.34	11.36	1.1991
6	9690.-10390.	30.10	23.69	1.1271
7	10390.-11000.	61.89	39.87	1.2459

WELL # 6

1	230.- 3430.	3.40	2.81	1.0993
2	3430.- 4400.	14.31	6.92	1.4382
3	4400.- 5440.	76.28	32.10	1.5415
WELL # 7				
1	330.- 3310.	5.48	4.86	1.0625
2	3310.- 4290.	16.94	11.91	1.1923
3	4290.- 5210.	95.77	49.94	1.3849
WELL # 8				
1	320.- 3300.	5.37	4.80	1.0577
2	3300.- 4300.	16.41	10.48	1.2514
3	4300.- 5220.	106.15	62.89	1.2992
WELL # 9				
1	330.- 3190.	5.16	4.59	1.0605
2	3190.- 4230.	15.67	10.82	1.2033
3	4230.- 5150.	89.92	49.84	1.3432
WELL # 10				
1	320.- 3120.	4.84	4.26	1.0666
2	3120.- 4150.	17.38	10.05	1.3148
3	4150.- 5530.	105.10	52.69	1.4123
WELL # 11				
1	320.- 3070.	5.31	4.55	1.0800
2	3070.- 4120.	18.16	10.62	1.3077
3	4120.- 5290.	139.86	66.67	1.4483
WELL # 12				

1	350.- 3300.	5.38	4.68	1.0723
2	3300.- 4220.	16.23	10.61	1.2367
3	4220.- 5280.	153.65	70.17	1.4798
WELL # 13				
1	320.- 3240.	4.73	4.10	1.0744
2	3240.- 4260.	13.89	9.17	1.2307
3	4260.- 5130.	116.81	53.85	1.4728
WELL # 14				
1	330.- 3810.	4.90	4.15	1.0867
2	3810.- 5600.	13.43	9.14	1.2121
WELL # 15				
1	320.- 3400.	4.94	4.26	1.0776
2	3400.- 4420.	15.83	10.20	1.2460
3	4420.- 5290.	126.76	68.21	1.3632
WELL # 16				
1	330.- 3040.	5.14	4.35	1.0863
2	3040.- 4120.	22.78	11.31	1.4193
3	4120.- 5340.	143.75	70.59	1.4270
WELL # 17				
1	3750.- 4080.	27.79	24.00	1.0761
2	4080.- 5440.	219.72	82.39	1.6331
WELL # 18				
1	3970.- 4030.	14.57	14.51	1.0020
2	4030.- 5290.	175.50	65.42	1.6378

WELL # 19

1	170.- 3360.	5.06	4.36	1.0770
2	3360.- 4110.	17.51	7.81	1.4970

WELL # 20

1	2700.- 3340.	3.77	2.93	1.1340
2	3340.- 3950.	12.69	7.44	1.3059
3	3950.- 5330.	136.14	65.58	1.4409

WELL # 21

1	420.- 3300.	4.63	4.16	1.0549
2	3300.- 4380.	16.17	8.88	1.3494
3	4380.- 5310.	128.31	49.73	1.6063

WELL # 22

1	300.- 3250.	4.52	3.90	1.0763
2	3250.- 4330.	14.27	8.44	1.3001
3	4330.- 5290.	101.34	48.87	1.4400

WELL # 23

1	180.- 3330.	4.36	3.68	1.0887
2	3330.- 4410.	13.15	7.74	1.3030
3	4410.- 5370.	89.84	45.08	1.4116

WELL # 24

1	320.- 3310.	5.34	4.70	1.0659
2	3310.- 3950.	15.43	8.30	1.3635

WELL # 25

1	330.- 3380.	4.95	4.44	1.0560

2	3380.- 4370.	13.94	8.94	1.2487
3	4370.- 5460.	125.32	50.63	1.5733
WELL # 26				
1	330.- 3340.	4.84	4.35	1.0555
2	3340.- 4410.	13.35	8.63	1.2440
3	4410.- 5480.	104.56	49.41	1.4548
WELL # 27				
1	330.- 3420.	5.38	4.80	1.0584
2	3420.- 4150.	15.74	8.43	1.3664
WELL # 28				
1	340.- 3320.	5.31	4.67	1.0660
2	3320.- 4350.	13.86	8.45	1.2803
3	4350.- 5300.	114.57	52.42	1.4784
WELL # 29				
1	330.- 3470.	4.93	4.34	1.0659
2	3470.- 4500.	16.57	10.32	1.2671
3	4500.- 5470.	117.46	73.63	1.2631
WELL # 30				
1	330.- 3470.	5.32	4.56	1.0802
2	3470.- 4090.	13.06	7.80	1.2941
WELL # 31				
1	310.- 3500.	6.48	5.75	1.0613
2	3500.- 4080.	13.36	8.34	1.2658

WELL # 32

1	410.-	3360.	4.07	3.26	1.1175
2	3360.-	4430.	13.30	6.60	1.4194
3	4430.-	5250.	114.30	49.74	1.5159

WELL # 33

1	310.-	4040.	3.57	2.95	1.0996
2	4040.-	4740.	13.86	8.14	1.3048